UAB
Universitat Autònoma de Barcelona

Advanced Corrosion Modelling: an Atomistic Approach to Describe the Corrosion Inhibition Process

José María Castillo Robles

Universitat Autònoma de Barcelona

Institut Català de Nanociència i Nanotecnologia

Advanced Corrosion Modelling: an Atomistic Approach to Describe the Corrosion Inhibition Process

José María Castillo Robles

A Thesis submitted in fulfillment of the requirements
for the degree of Doctor of Philosophy in Material Science

Theory and Simulation Group
Catalan Institute of Nanoscience and Nanotechnology
Autonomous University of Barcelona

Director
Dr. Ernane de Freitas Martins

Prof. Ivan Cole

Prof. Pablo Ordejón

Tutor
Prof. Pablo Ordejón

May 2024

Contents

List of Figures

List of Tables

Abstract

Toxic inorganic compounds, usually used as corrosion inhibitors within paint films, are being replaced by more environmentally friendly compounds in coatings across aerospace, automotive and infrastructure industries. However, the corrosion inhibition mechanism behind these compounds must be better understood. Molecular modelling can provide insights by analyzing the metal-inhibitor-water interface, but a realistic representation of the electrochemical processes is crucial. In this thesis, six critical aspects (A) must be considered to realistically describe the corrosion inhibition process in modelling: (A1) the electronic properties of isolated inhibitors, (A2) the interaction of the inhibitor with the surface, (A3) the surface model, (A4) the effect of the anodic and cathodic zones on the surface, (A5) the solvent effects, and (A6) the electrodes' potential effects. While aspects A1-A3 are usually considered in the literature, aspects A4-A6 and some more complex surface models in A3 are not. Here, two main ones will be the focus: the applied electrode potential and solvent effects.

The system chosen to showcase these two aspects is the adsorption of 2-mercapto-benzoimidazole (MBI) on Cu(111) surfaces. First, molecular modelling based on Density Functional Theory (DFT) combined with the Non-Equilibrium Green's Functions (NEGF) formalism was used to address the effect of the applied electrode potential in the MBI adsorption under different coverage and voltages. Both coverage and voltage play crucial

roles in the adsorption of the inhibitor. The coverage determines the extent of the surface area protected from corrosion by the inhibitor. On the other hand, the voltage is essential to describe the cathodic and anodic zones within the material. It induces the system's polarization, potentially influencing the inhibitor's orientation towards adsorption and its charge distribution. Our results show that the system becomes more stable as the coverage of molecules increases, forming a self-assembled monolayer (SAM). The electronic structure, characterized through the analysis of the charge density difference ($\Delta\rho$) and density of states (DOS), is sensitive to the applied voltage, inducing a charge redistribution in the system, where the MBI is acting as a metal and accumulates the induced charge at the molecule's edge.

The final step addressed the solvent effects in the MBI adsorption, where the methodology combining the NEGF formalism and the Quantum Mechanics/Molecular Mechanics (QM/MM) method was used in a 5×6 Cu surface slab under varying coverage conditions: bare surface, a low-coverage with one MBI adsorbed, and a high-coverage case with six MBI adsorbed, and under different applied voltages (-1, 0 and $+1$ V). The dynamics explicitly included water molecules, with their quantity adjusted to match the density of liquid water under standard pressure and temperature conditions (1 g/cm^3). Classical molecular dynamics were performed for the NPT (isothermal-isobaric ensemble) and NVT (canonical ensemble) ensembles to calibrate the system's pressure and temperature. The reference temperature and pressure were 300 K and 1 bar, respectively.

After the classical molecular dynamics calibration, the QM/MM-NEGF molecular dynamics were performed on the systems under varying coverage and voltages from the equilibrated geometries. Structural descriptors such as the water's density profiles, water dipole moment and angular distributions were evaluated for the different concentrations and applied voltages. The electronic structure was analyzed through the evolution of the net Hirshfeld charges along the dynamics.

The results suggest that a stable SAM is formed in the high-coverage case. It prevails along the dynamics and acts as a physical barrier between the water molecules and the sur-

face, preventing their interaction with the metallic surface. The results in the bare surface and with one MBI adsorbed showed a water layer directly in contact with the Cu surface, contrary to the case with a SAM adsorbed, where the first water layer is located at the end of the SAM structure. The results also indicated an induced polarization in the system due to the applied voltage on the system, which is reflected in the electronic structure and the structural descriptions evaluated. In this sense, the net Hirshfeld charges of the left and right Cu surface change according to the voltage, besides the charges in the MBI. The dipole moments and angular distribution revealed the water molecules' polarization, primarily with the ones located at the inhibitor-surface interface. The water molecules aligned according to the voltage sign, and in the case of positive voltages, their hydrogen atoms pointed out towards the left Cu surface. Negative potentials induced the opposite effect. Even at 0 V, the simulations with the SAM adsorption showed a polarization, which is evident in the angular distributions and indicates the outstanding charge redistribution caused by the SAM upon adsorption on the surface.

Finally, a collaboration with experimental parters in RMIT University was performed to investigate the adsorption of 2-mercaptobenzothiazole (2-MBT) and 2-aminobenzothiazole (2-ABT) on galvanized steel, using a Zn(0001) model surface. Two concentrations at the surface were investigated: a low (1 molecule/nm_2) and high (3 molecules/nm_2) concentration cases, identifying the most stable adsorption modes. The findings aligned with experimental data using X-ray Photoelectron Spectroscopy (XPS), which revealed the bonding between 2-ABT and the Zn through the endo S and the 2-MBT through the endo N and exo S. Electronic structure analysis revealed the inhibitor's charge density donation to the Zn surface. The experimental data also highlighted the strong interaction between 2-MBT and the surface, potentially forming complexes with Zn^{2+} ions.

Therefore, this thesis highlighted the importance of the six critical aspects of CI modelling and demonstrated that the proposed QM/MM-NEGF approach significantly advances modelling electrochemistry and can be successfully applied in corrosion inhibition studies. From these critical aspects, this thesis focused on two fundamental ones: the

solvent and electrode potential effects and how the inclusion of these effects allows us to understand the role of the inhibitor in the protection of the materials, in this case by the formation of stable films with the applied voltages, and the charge redistribution at the inhibitor structure.

The results from this QM/MM-NEGF approach differentiate from the usual CI modelling, which lacks a precise description of the atomistic process occurring at the metallic-inhibitor-aqueous interface. Instead, the QM/MM-NEGF approach provides an accurate and predictive way to simulate fundamental interactions that lead to CI properties. Furthermore, the results from this approach can potentially be used to feed artificial intelligence (AI) methods and multiscale models, which can bridge the gap between nanoscale CI modelling and the continuum scale of CI processes. This could enhance our understanding of corrosion inhibition and lead to more effective solutions.

Acknowledgements

Esta tesis es especial porque representa la culminación de años de esfuerzo, dedicación y perseverancia.

Agradezco a mis padres por siempre ser ese sostén en todo lo que hago y por apoyarme siempre en lo que necesito. Sin ustedes, definitivamente no hubiera llegado a estas instancias.

Agradezco a mi hermana, tíos y tías que siempre han estado pendientes de mí.

A mis asesores Ernane, Pablo e Iván por sus invaluables enseñanzas y los apoyos otorgados en el desarrollo de este proyecto. En particular, me gustaría agradecerte, Ernane, por toda la paciencia y dedicación que le pusiste para que este proyecto saliera adelante.

Agradezco a mis compañeros y amigos con quienes tuve el privilegio de compartir durante este tiempo entre dos continentes.

Y principalmente a mi amada esposa Nathalie. Agradezco a la vida que nuestros caminos se hayan entrelazado para siempre de una manera tan bella, especial y única.

Section 1

Introduction

1.1 Corrosion of metals

The corrosion process is the degradation of materials, typically metals and alloys, due to the interaction with the environment. The degradation occurs by chemical reactions that change the composition and structure of the material. This corrosion process leads to the loss of the material properties and represents economic and industrial losses, safety hazards, environmental impact, and critical technology deterioration [1, 2].

Corrosion can appear in all metals, and the corrosion extension depends on the metal's intrinsic properties. Not all metals suffer degradation at the same rate. Some metals are more likely to get corroded, while others, known as noble metals, present higher corrosion resistance. One example of a noble metal is copper. Copper and its alloys are widely used in various industries because of their exceptional physical and chemical properties. They exhibit high thermal conductivity ($400\ W/(mK)$) and electrical conductivity ($58\times10^6\ S/m$), mechanical workability, malleability, and corrosion resistance [3]. Copper is an important

material in manufacturing wires, water pipelines, sheets, power stations, heat exchangers, and radiators [4]. However, copper (and other noble metals) can degrade under certain conditions. These conditions include exposure to the atmosphere, moisture or water, salts, acidic-basic media, liquid chemicals and some gases.

Even if copper presents a corrosion resistance due to the passivated layer (copper oxides) formed when exposed to some chemical environments, the presence of oxygen and some aggressive anions, such as chloride and sulfate ions, promotes its corrosion [5, 6]. In Figure 1.1, the corrosion process in copper is depicted, under the effect of the Cl^- in dissolution. In this context, copper protection has been important for several fields over the years [7].

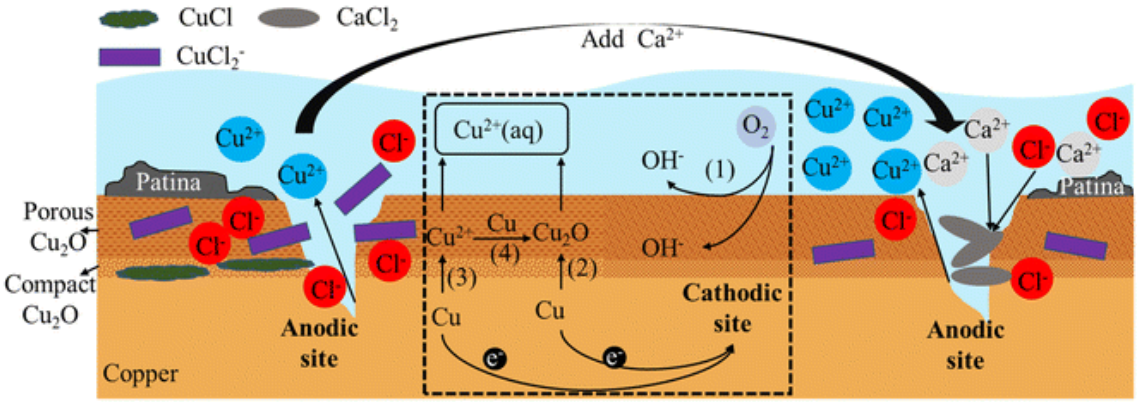

Figure 1.1: A sketch of the copper corrosion process in the presence of Cl^- in dissolution, showing the two processes related to the copper dissolution and formation of a passivation layer composed by compact and porous Cu_2O. The cathodic reaction is the oxygen reduction process, while the anodic reaction involves the formation of slightly soluble Cu_2O and its subsequent oxidation to soluble Cu(II) species. Also, the anodic reaction involves the by-product-release-redeposition mechanism, where Cu(II) is formed, followed by a disproportionation between Cu(0) and Cu(II) to form Cu_2O. Adapted from [8] with authorization.

1.2 Corrosion inhibitors

There are some alternatives to prevent the corrosion process, and inhibitors have been one of the most used ones. The inhibitors restrict the reactions that lead to the material's degradation: the anodic and cathodic reactions. In this case, inhibitors reduce the reaction

rates and prevent corrosion. Depending on which reactions they limit, particularly the electrochemical mechanism, they can be classified as anodic, cathodic or mixed-type. The anodic inhibitors reduce the anodic copper dissolution, inducing the passivation of the surface by the formation of an oxide layer on it. The cathodic inhibitors reduce the cathodic reactions, e.g., the oxygen or hydrogen reduction on the copper surface. When the inhibitor controls both anodic and cathodic reactions, the inhibitor is a mixed-type. The inhibitors can also be inorganic or organic compounds; both have shown high efficiency in corrosion inhibition (CI) [5, 9].

Inorganic inhibitors

In the case of inorganic compounds, commonly chromates (CrO_4^{-2}), molybdates (MoO_4^{-2}), nitrates (NO_3^{-1}), tetraborate ($B_4O_7^{-2}$), silicates (SiO_3^{-2}), cerium salts, among others, are used as efficient corrosion inhibitors for copper. The inhibition mechanism depends on the compound, which can be anodic, cathodic, or mixed-type. One of the main features of the inorganic corrosion inhibitors is their enduring stability with time and different temperatures. Chromates are typically used due to its high CI efficiency, where the anion promotes the formation of oxide layers on the surface. It can also form Cr-hydroxides due to the reduction to Cr^{+3}, which precipitates on the surface and protects it, as suggested by the decrease of the corrosion current density. However, the main problem with chromates (and most inorganic inhibitors) is their environmental impact and toxicity. Cr^{+6} is a highly toxic cation for humans and the environment [10].

Organic inhibitors

Organic inhibitors are more benign compounds for the environment with relatively low toxicity and high inhibition properties, and they are being used extensively in the industry. However, one of their main drawbacks is their less endurability with time and temperature, in contrast to the inorganic counterparts [5, 11, 12]. They are usually constituted

by elements such as C, O, N, P, or S, and/or aromatic rings with delocalized π electrons or contain functional groups such as amines (NH_2), carboxylic acids (-COOH), alcohols (-OH), phenols, amino acids, among others [13, 14]. These functional groups are electron-rich centres, which usually form coordinate covalent bonds with the metal surfaces via the unoccupied d-orbitals of the surfaces and the lone pair/π electrons in the inhibitor, as well as electron back-bonding between the free electrons of the metal and the orbitals of the inhibitor. The bonding between the inhibitor and the surface can be a physisorption or a chemisorption process [15].

In Figure 1.2, the adsorption process of the organic inhibitor on the surface is depicted. In the figure, the electrostatic interactions between the metal and inhibitor are illustrated, as well as the interaction between the vacant d-orbitals of metal atoms and the lone pair atoms of the inhibitor and its π-electrons. The adsorption of the organic inhibitors on the surface induces the formation of a protective layer, which affects both cathodic and anodic reactions. However, the precise CI mechanism is still not entirely clear.

1.3 Inhibition mechanism

Generally, it is accepted that the inhibitor's adsorption on the surface determines the protection of the material from corroding. Nonetheless, as mentioned before, the precise mechanism is unkown. In this section, we focus on the inhibition mechanism of organic inhibitors.

It is commonly believed that organic inhibitors adsorbed on the surface and form a protective film [16–21]. During this process, the organic inhibitor, along with its charge and potential variations, moves from the bulk of the solution towards the surface at a mixed potential (established by the various anodic and cathodic zones). It then interacts with the electric double-layer (EDL), replacing the existing shielding of water and solute, finally binding to the surface, and leading to subsequent changes in the charge and potential distributions at the surface and within the molecule. Both inhibitor-surface and inhibitor-

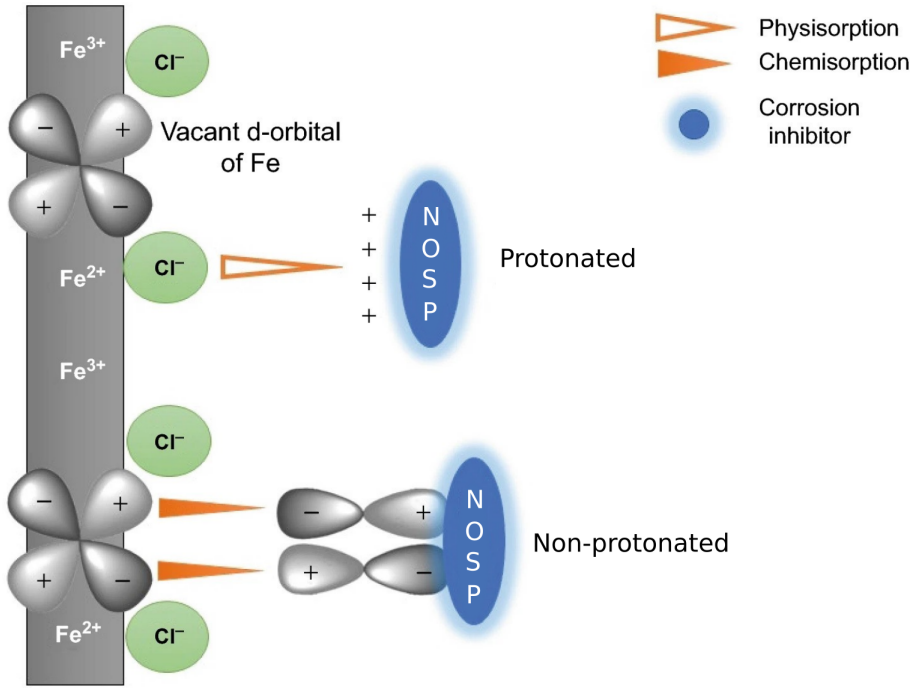

Figure 1.2: The physical and chemical adsorption process of organic inhibitors, in a protonated or non-protonated form, on the metallic surface, represented by an iron surface, which has some Cl^- anions adsorbed from the saline dissolution. During the physisorption process, the protonated inhibitors and the adsorbed Cl^- interact through their charges without forming a chemical bond. In the chemisorption case, the inhibitor and the surface form a chemical bond with the lone-pair electrons from the heteroatoms and the vacant *d* orbitals of Fe. Adapted from [12] with authorization.

inhibitor interactions present in the first and subsequent inhibitor layers determine the nature of the anodic and cathodic zones, as well as the growth of inhibitor films.

To describe all these processes, molecular modelling emerges as an excellent tool to deepen our understanding of each stage and help develop new strategies. However, realistic models must incorporate six key aspects: (A1) the electronic properties of isolated inhibitors, (A2) the interaction of the inhibitor with the surface, (A3) the surface model, (A4) the effect of the anodic and cathodic zones on the surface, (A5) the solvent effects, and (A6) the electrodes' potential effects. In Figure 1.3, an example of this molecular modelling is depicted for the adsorption of self-assembled monolayers (SAM) of n-alkyl carboxylic acids on oxidized Al surface models. Because of the complex nature of the corrosion process, our models should aim to consider all these essential aspects, which will be discussed in detail in the chapter 3 chapter of this thesis. Considering these critical

aspects in the CI modelling represents a step forward to more realistic simulations of the corrosion process.

In summary, the corrosion of metals represents a significant technological and industrial issue which leads to economic losses and safety issues. There are ways to prevent it, and in this case, the protection by organic molecules emerges as an efficient and environmentally friendly alternative. However, their inhibition mechanism needs to be better understood. Molecular modelling is an essential tool that can provide crucial insights into the CI process. However, it should include some critical aspects to provide realistic information. That is the overall objective of this thesis.

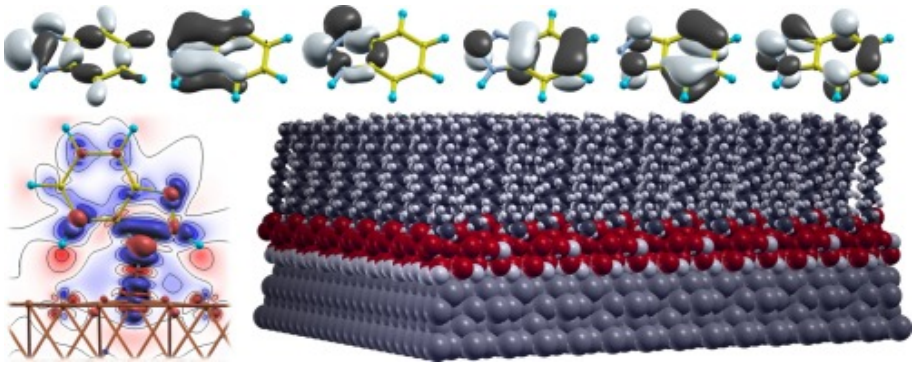

Figure 1.3: Atomistic model of self-assembled monolayers of n-alkyl carboxylic acids on oxidized Al surface. At the top of the figure, the different inhibitor's molecular orbitals are shown, which will induce a particular adsorption configuration on the surface. The induced electronic charge density between the inhibitor and the surface is depicted on the left part of the figure, where the blue and red regions mean the accumulation and depletion of the charge in that area. Finally, in the bottom-right part of the figure, the representation of the oxidized Al surface, with the n-alkyl carboxylic acids adsorbed on top, is shown. Adapted from [15] with authorization.

1.4 Outline of thesis

From the previous essential aspects of CI modelling, this thesis aims to set the ground for as-reallistic-as-possible simulations of the CI process. A significant lack in current simulations is on the effect of the solvent and the electrode potential effects and their interaction. So this thesis presents a novel molecular dynamics technique applied for the

first time in corrosion modelling: the coupling between Quantum Mechanics/Molecular Mechanics (QM/MM) and non-equilibrium Green's Function formalism (NEGF), which we named QM/MM-NEGF molecular dynamics to provide such potential and solvent interaction. This methodology is implemented in the SIESTA [22–24] code and is available under a free license.

The main system used in this thesis to apply this novel methodology was the adsorption of 2-mercaptobenzimidazole on the Cu(111) surface. In order to understand the CI mechanism in similar inhibitors, 2-mercaptobenzothiazole (MBT) and 2-aminobenzothiazole (ABT) were also investigated as corrosion inhibitors for electro-galvanized steel (ZE), a collaboration with experimental partners at RMIT University. The adsorption of the inhibitors was considered using different coverages on the ZE surface, which was simulated using a Zn(0001) slab because in ZE, Zn is used to coat the steel for protection. In the collaboration, the main questions regarding how the inhibitor is bonded to the surface were clarified by the comparison between the adsorption energies and the X-ray Photoelectron Spectra (XPS). The outcome of this collaboration was one article published in the Molecular Systems Design & Engineering journal.

In this thesis, the addressed research questions were the following ones:

RQ1. What is the interaction between the inhibitor and the metallic surface?

- How does the inhibitor concentration impact the protection of the surface from the H_2O molecules?

RQ2. What is the effect of the electrode potential in the corrosion inhibition process?

- How does it affect the inhibitor absorption mechanism?
- How does it change the electronic structure of the system?

RQ3. How does the solvent affect the interaction between the inhibitor and the surface?

RQ4. Can the results obtained for a given system (MBI on Cu in aqueous solution) be extrapolated to other corrosion inhibitors and surfaces?

RQ5. What are the scope, advantages, and limitations of the proposed multiscale approach (QM/MM-NEGF molecular dynamics), to simulate corrosion inhibition?

- Is it enough to consider the electrode potential and solvent effects to simulate the corrosion inhibition process?
- How do the experiments correlate with the modelling?

In chapter 2, a summary of the underlying theory and methods used in this thesis is presented. The essential concepts for Density Functional Theory (DFT), NEGF formalism, Classical Molecular Dynamics, QM/MM method and SIESTA are explained. In chapter 3, a literature review with the six critical aspects of the CI modelling is presented, including the gaps in CI modelling, which was accepted for publication in npj Materials Degradation. In chapter 4, the adsorption of the MBI on the Cu surface is described, considering the effect of the coverage in the adsorption, as well as the electrode potential effects, in vacuum. This chapter represents a proof of test about the possible implications of the applied voltage on the electronic structure of the adsorbed MBI. In this chapter, the research questions **RQ1.** and **RQ2.** are addressed. In chapter 5, the results of the complete methodology: QM/MM-NEGF molecular dynamics on the MBI adsorption, which introduces the solvent and electrode potential effects are presented. This chapter tackled **RQ1.** and **RQ3.**. In chapter 6, the collaboration between experimental patterns about the adsorption of 2-MBT and 2-ABT on the Zn surface is shown. The importance of this chapter lies in the possible validation of the adsorption modes of the inhibitors at the surface by comparing the adsorption energies and the experimental XPS. This chapter responded to **RQ4.**. Finally, in chapter 7, the primary outcomes and findings of this PhD project are outlined, which responded to **RQ5.**, and includes future plans in regards to this project.

Section 2

Theory

This chapter will briefly introduce the basic methodology used in this thesis. First, the Density Functional Theory (DFT) will be discussed, whose importance lies in the description of the electronic structure of systems, especially atoms, molecules, and solids through the electronic charge density $\rho(\vec{\mathbf{r}})$. Following this, the Non-equilibrium Green's Functions (NEGF) formalism will be described, a theoretical framework used in quantum mechanics to describe systems out of equilibrium, allowing us to introduce the effect of the electrode potential in our simulations. Subsequently, the classical molecular dynamics technique is used to simulate the time evolution of the system, allowing us to account for thermodynamic effects in our simulations. After that, a hybrid methodology that combines the low computational cost of molecular mechanics and the high predictive power of quantum mechanics, the Quantum Mechanics/Molecular Mechanics (QM/MM) method, will be described. This methodology is typically used in biological systems, and here it is applied to account for the solvent effects dynamically in electrochemistry. Finally, a description of the SIESTA [22–24] code, the computational method used in this thesis, is

presented.

The Schrödinger equation

Molecules and materials are formed by nuclei, which have a positive charge, and electrons, which are way lighter and negatively charged. If the system is formed by N nuclei with charge Z, the total number of interacting particles will be $2N$, in this case, interacting electrostatically. This is a quantum many-body problem of particles interacting. The equation that describes all the interatomic interactions is the Schrödinger equation:

$$\hat{H}|\Phi_i(\vec{\mathbf{x}})\rangle = E_i|\Phi_i(\vec{\mathbf{x}})\rangle \,, \tag{2.1}$$

where $|\Phi_i(\vec{\mathbf{x}})\rangle$ are the wavefunctions, $\vec{\mathbf{x}}$ are the generalized position vector for all nuclei and electrons, $\hat{H}$ is the Hamiltonian operator, and E_i its eigenvalues. Equation 2.1 is the time-independent version of Schrödinger's equation, which is a simplification considered here to allow us to focus on stationary states and energy levels of the systems investigated. Besides, time-dependent processes can be investigated through the time evolution of the stationary states or the adiabatic approximation, where electrons are assumed to be in their instantaneous ground state.

The Hamiltonian that describes the system can be expressed as a sum of kinetic ($\hat{T}$) and potential ($\hat{V}$) contributions:

$$\begin{aligned} \hat{H} &= \hat{T} + \hat{V}, \\ &= \hat{T}_e + \hat{T}_n + \hat{V}_{ee} + \hat{V}_{en} + \hat{V}_{nn}, \end{aligned} \tag{2.2}$$

where $\hat{T}_e$ and $\hat{T}_n$ are the operators for the kinetic energy of the electrons and the nuclei, respectively. The operators $\hat{V}_{ee}$, $\hat{V}_{en}$, and $\hat{V}_{nn}$ correspond to the potential energies of the electron-electron, electron-nuclei, and nuclei-nuclei interactions. These contributions can be expressed as:

$$\hat{H} = \underbrace{-\frac{\hbar^2}{2}\sum_i \frac{\nabla_i^2}{m}}_{\hat{T}_e} \underbrace{-\frac{\hbar^2}{2}\sum_\alpha \frac{\nabla_\alpha^2}{M_\alpha}}_{\hat{T}_n} + \underbrace{\sum_{j\neq i} \frac{e^2}{|\vec{\mathbf{r}_i} - \vec{\mathbf{r}_j}|}}_{\hat{V}_{ee}} \underbrace{-\sum_{i,\alpha} \frac{e^2 Z_\alpha}{|\vec{\mathbf{R}_\alpha} - \vec{\mathbf{r}_i}|}}_{\hat{V}_{en}} + \underbrace{\sum_{\alpha\neq\beta} \frac{e^2 Z_\alpha Z_\beta}{|\vec{\mathbf{R}_\beta} - \vec{\mathbf{R}_\alpha}|}}_{\hat{V}_{nn}}, \tag{2.3}$$

where i and j indicate the electron indices and α and β the nuclei indices. M_α is the mass of the nucleus α at $\vec{\mathbf{R}_\alpha}$, m is the mass of the electron located at $\vec{\mathbf{r}_i}$, and Z_α is the charge of nucleus α on units of the electron charge. Considering all these interactions the solution of Equation 2.1 becomes unfeasible even for the simplest molecular systems due to the complexity of solving it for many body systems. This is because Equation 2.2 considers the coupled variables $3N_i + 3N_\alpha$, with N_i and N_α as the number of electrons and nuclei, respectively. To simplify it, a series of approximations are needed. One of them is the Born-Oppenheimer approximation [25].

Born-Oppenheimer approximation

The movement of a nucleus is much slower than the one of an electron because of the nucleus mass, which is around three orders of magnitude the one of the electron ($M_\alpha \approx 2000 m_i$). This difference in mass between the nucleus and the electron makes the electron see the same static configuration of the nucleus. Because of this slow movement of the nuclei compared to the electrons, it is assumed that the electrons are always in the same stationary state of the electronic Hamiltonian. The electrons will adjust instantaneously their wave function to follow the one from the nuclei, without changing their electronic state. In this way, we can decouple the electronic movement from the nuclear one, and this is known as the Born-Oppenheimer or adiabatic approximation [25]. Considering the Born-Oppenheimer approximation, the many-body wave function can be express as:

$$\Psi_{BO}(\vec{\mathbf{R}}, \vec{\mathbf{r}}, t) = \Theta_n(\vec{\mathbf{R}}, t)\Phi_n(\vec{\mathbf{R}}, \vec{\mathbf{r}}), \tag{2.4}$$

where $\Theta_n(\vec{\mathbf{R}}, t)$ is the nuclear wave function, and $\Phi_n(\vec{\mathbf{R}}, \vec{\mathbf{r}})$ the electronic wave function, which is the solution of Equation 2.1. Each electronic state corresponds to a particular nuclear configuration:

$$\hat{H}_e \Phi_n(\vec{\mathbf{R}}, \vec{\mathbf{r}}) = \epsilon_n \Phi_n(\vec{\mathbf{R}}, \vec{\mathbf{r}}), \tag{2.5}$$

where $\hat{H}_e$ is the electronic hamiltonian, which is expressed as:

$$\hat{H}_e = -\sum_{i=1}^{N_e} \frac{\hbar^2}{2m} \nabla_i^2 + \frac{e^2}{2} \sum_{i=1}^{N_e} \sum_{j \neq i}^{N_e} \frac{1}{|\vec{\mathbf{r}}_i - \vec{\mathbf{r}}_j|} - e^2 \sum_{\alpha=1}^{N_n} \sum_{i=1}^{N_e} \frac{Z_\alpha}{|\vec{\mathbf{R}}_\alpha - \vec{\mathbf{r}}_i|}. \tag{2.6}$$

Once $\Phi_n(\vec{\mathbf{R}}, r)$ is determined for all the nuclear positions, $\Theta_n(\vec{\mathbf{R}}, t)$ can be obtained by the substitution of the wave function Equation 2.4 in the Schrödinger equation for the system, expressed by:

$$i\hbar \frac{\delta \Psi_{BO}(\vec{\mathbf{R}}, \vec{\mathbf{r}}, t)}{\delta t} = \hat{H} \Psi_{BO}(\vec{\mathbf{R}}, \vec{\mathbf{r}}, t), \tag{2.7}$$

where the time evolution can be obtained for the nuclear system.

The Born-Oppenheimer approximation simplifies Equation 2.5, but it is still too difficult to solve even for the simplest molecules, and more approximations have to be made. Quantum chemistry [26] provides some methods with different approximations to the many-body electronic wavefunctions, with increasing levels of accuracy, from the simple Hartree-Fock (HF) method to sophisticated Configuration Interaction approaches. However, in most of the methods, the approaches are still too expensive computationally to deal with the typical sizes involved in CI, which limits their applicability and impact in this field. An alternative to overcome the cost of the wavefunctions methods is the Density Functional Theory (DFT). Here one abandons any attempt to approximate the electronic many-body wavefunction $\Psi_n(\vec{\mathbf{r}})$, and focuses on the electronic charge density ($\rho(\vec{\mathbf{r}})$). In the next section, a brief review of the main concepts in DFT will be provided.

2.1 Density Functional Theory

In DFT, the solution of Equation 2.5 is based on the electronic charge density rather than on finding the wave functions. In this sense, the energy of the ground state is expressed as a functional of the electronic charge density $\rho(\vec{\mathbf{r}})$, that can be expressed as:

$$\rho(\vec{\mathbf{r}}) = N \int d\vec{\mathbf{r}}_2 \cdots \int d\vec{\mathbf{r}}_N \Psi^*(\vec{\mathbf{r}}, \vec{\mathbf{r}}_2, \ldots, \vec{\mathbf{r}}_N)\Psi(\vec{\mathbf{r}}, \vec{\mathbf{r}}_2, \ldots, \vec{\mathbf{r}}_N), \tag{2.8}$$

where N is the number of electrons. This theory originates in the Thomas-Fermi model [27], where a functional form for the kinetic energy of a gas of non-interacting electrons under an external potential is proposed as a function of its electronic charge density. The theoretical formalism on which DFT is based was established by Hohenberg and Kohn in 1964 [28] and later generalized by Levy [29].

Hohenberg-Kohn theorem

Hohenberg and Kohn proposed that the energy is a functional of the electronic charge density through the relation:

$$E_{HK}[\rho(\vec{\mathbf{r}})] = F[\rho(\vec{\mathbf{r}})] + \int d\vec{\mathbf{r}}\rho(\vec{\mathbf{r}})V_{ext}(\vec{\mathbf{r}}). \tag{2.9}$$

Here, $V_{ext}(\vec{\mathbf{r}})$ is the external potential, which includes the Coulomb potential between the nuclei and the electrons: $V_{ext}(\vec{\mathbf{r}}) = -\sum_{i,\alpha} \frac{e^2 Z_\alpha}{|\vec{\mathbf{R}}_\alpha - \vec{\mathbf{r}}_i|}$, and $F[\rho(\vec{\mathbf{r}})]$, which is known as the Hohenberg-Kohn functional, considers the kinetic energy of the electrons and the electron-electron interaction energy:

$$\begin{aligned} F[\rho(\vec{\mathbf{r}})] &= T\left[\rho(\vec{\mathbf{r}})\right] + E_{ee}\left[\rho(\vec{\mathbf{r}})\right], \\ &= T\left[\rho(\vec{\mathbf{r}})\right] + E_H\left[\rho(\vec{\mathbf{r}})\right] + E_Q\left[\rho(\vec{\mathbf{r}})\right], \end{aligned} \tag{2.10}$$

where E_H and E_Q are the classical Coulomb energy (also known as Hartree) and the non-classical part, which is denoted by Q.

In 1964, Hohenberg and Kohn proposed two theorems:

Theorem 1. *The external potential $V_{ext}(\vec{\mathbf{r}})$ is (to within a constant) a unique functional of $\rho(\vec{\mathbf{r}})$.*

This theorem implies that there is a one-to-one mapping between $V_{ext}(\vec{\mathbf{r}})$ and the electron charge density $\rho(\vec{\mathbf{r}})$. However, the exact form of this Hohenberg-Kohn functional is unknown. In this case, the second theorem can provide us with a clue about finding a form of this functional.

Theorem 2. *A universal functional for the energy $E[n]$ of the density $\rho(\vec{\mathbf{r}})$ can be defined for all electron systems. The exact ground state energy E_{gs} is the global minimum for a given external potential $V_{ext}(\vec{\mathbf{r}})$, and the density $\rho(\vec{\mathbf{r}})$ that minimizes this functional is the exact ground state density $\rho_{GS}(\vec{\mathbf{r}})$.*

This theorem proposes that the variational principle can be used to find the electron charge density, implying that the resulting energies will always be greater than or equal to the ground state energy E_{GS}:

$$F[\rho(\vec{\mathbf{r}})] = \min_{\vec{\Psi}\to\rho(\vec{\mathbf{r}})} \langle\vec{\Psi}|\hat{T} + \hat{V}_{ee}|\vec{\Psi}\rangle, \tag{2.11}$$

which leads to $E[\rho(\vec{\mathbf{r}})] \geq E[\rho_{GS}(\vec{\mathbf{r}})]$.

The two theorems indicate finding the ground state energy using the variational principle to minimize the energy of the different trial $\rho(\vec{\mathbf{r}})$. In this sense, both theorems are reformulating the many-body wave function problem to a three-dimensional problem ($\rho(\vec{\mathbf{r}})$). However, the exact form of $F[\rho(\vec{\mathbf{r}})]$ is unknown, and therefore, Hohenberg and Kohn do not solve anything yet but reformulate the many-body problem. Kohn and Sham [30] proposed in 1965 a solution to it.

Kohn-Sham method

With the Hohenberg-Kohn (HK) theorem, the existence of an energy functional that only depends on the electronic density is demonstrated, but no concrete expression is given for this functional (Equation 2.11). Kohn and Sham [30] proposed a reformulation of the problem of the unknown $F[\rho]$ in 1965, in which the problem of a system of many interacting particles is transformed into one of non-interacting electrons with the same density $\rho(\mathbf{r})$ and moving under an effective local potential, which simulates interactions with the other electrons. The electronic charge density for this non-interacting system is written as:

$$\rho(\vec{\mathbf{r}}) = \sum_i \left|\psi_i^{KS}(\vec{\mathbf{r}})\right|^2 , \tag{2.12}$$

and the approximation T_{KS} for its kinetic energy T:

$$T_{KS}[\rho(\vec{\mathbf{r}})] = -\frac{1}{2}\sum_i \langle\psi_i^{KS}(\vec{\mathbf{r}})|\nabla^2|\psi_i^{KS}(\vec{\mathbf{r}})\rangle, \tag{2.13}$$

where ψ_i^{KS} are the single-particle wave functions or Kohn-Sham orbitals. Considering this approximation for the kinetic energy, the energy functional (Equation 2.9) can be rearranged as:

$$E[\rho(\vec{\mathbf{r}})] = T_s[\rho(\vec{\mathbf{r}})] + E_H[\rho(\vec{\mathbf{r}})] + E_{ext}[\rho] + E_{xc}[\rho(\vec{\mathbf{r}})], \tag{2.14}$$

where a new term is introduced: the exchange-correlation functional $E_{xc}[\rho(\vec{\mathbf{r}})]$, which is written as:

$$\begin{aligned} E_{xc}[\rho(\vec{\mathbf{r}})] &= T[\rho(\vec{\mathbf{r}})] - T_s[\rho(\vec{\mathbf{r}})] + E_{ee}[\rho(\vec{\mathbf{r}})] - E_H[\rho(\vec{\mathbf{r}})], \\ &= T[\rho(\vec{\mathbf{r}})] - T_s[\rho(\vec{\mathbf{r}})] + E_Q[\rho(\vec{\mathbf{r}})]. \end{aligned} \tag{2.15}$$

This new term $E_{xc}[\rho(\vec{\mathbf{r}})]$ contains all the non-classical information of our system, and it represents the missing energy because of the non-interacting electron's approximation

instead of the exact result. In this case, if the exact exchange-correlation functional were known, the solution would be exact: we would obtain the ground state and density.

The minimization of the Kohn-Sham density functional gives

$$\left[-\frac{1}{2}\nabla^2 + v_{ext}(\vec{\mathbf{r}}) + v_H(\vec{\mathbf{r}}) + v_{xc}(\vec{\mathbf{r}})\right]\psi_i^{KS}(\vec{\mathbf{r}}) = \epsilon_i\psi_i^{KS}(\vec{\mathbf{r}}), \tag{2.16}$$

where $V_{xc}(\vec{\mathbf{r}})$ can be written as:

$$v_{\mathrm{xc}}(\vec{\mathbf{r}}) = \frac{\delta E_{\mathrm{xc}}[\rho(\vec{\mathbf{r}})]}{\delta\rho(\vec{\mathbf{r}})}. \tag{2.17}$$

Equations 2.16 are self-consistent and can be solved by an iterative approach. The Kohn-Sham equations present the form of an eigenvalue problem in which each wave function $\psi_i^{KS}(\vec{\mathbf{r}})$ has an associated eigenvalue ϵ_i, with an occupation number n_i. The Janak's theorem provides a relationship between the total energy and these eigenvalues, written as:

$$\epsilon_i = \frac{\partial E}{\partial n_i}, \tag{2.18}$$

Therefore, the eigenvalues ϵ_i are the total energy change with the occupation number change. However, a more physical interpretation of these eigenvalues is needed. The one-electron picture of ϵ_i has been widely used in solid state physics, for example, in the distinction between materials, i.e., metals and insulators, which is based on the analysis of the energy bands, that are one-electron energies plotted in the reciprocal space.

The explicit form of Equation 2.17 will depend on the approximation used in the exchange-correlation functional, always considering that its exact form is unknown. The first approximation and the simplest one is the Local Density Approximation (LDA), where the value of $E_{xc}[\rho(\vec{\mathbf{r}})]$ is approximated by the exchange-correlation energy of an electron in a homogeneous electron gas of the same density $\rho(\vec{\mathbf{r}})$:

$$E_{XC}^{LDA}[\rho(\vec{\mathbf{r}})] = \int \rho(\vec{\mathbf{r}})\epsilon_{xc}^{LDA}(\rho(\vec{\mathbf{r}}))d\vec{\mathbf{r}}\,, \tag{2.19}$$

where $\epsilon_{xc}^{LDA}(\rho(\vec{\mathbf{r}}))$ can be obtained from Quantum Monte Carlo calculations. This approximation is particularly accurate for systems where the charge density varies slowly. However, LDA has the tendency to favour more homogeneous systems and overbinds molecules and solids. An improvement in the LDA can be achieved by introducing gradient corrections, where the exchange-correlation functional is expressed as a function of the local density and of a local gradient of the density, usually as an enhancement factor F_{xc}, which is multiplying the homogeneous electron density:

$$E_{XC}^{GGA}[\rho(\vec{\mathbf{r}})] = \int \epsilon_{xc}(\rho(\vec{\mathbf{r}})F_{xc}(\rho(\vec{\mathbf{r}}), |\nabla\rho(\vec{\mathbf{r}})|))\rho(\vec{\mathbf{r}})d\vec{\mathbf{r}}\,. \tag{2.20}$$

The enhancement factor can be written in terms of r_s and of a dimensionless reduced density gradient $s(\vec{\mathbf{r}})$:

$$\begin{aligned} F_{xc}(\rho(\vec{\mathbf{r}}), |\nabla\rho(\vec{\mathbf{r}})|) &\rightarrow F_{xc}(r_s, s), \\ s(\vec{\mathbf{r}}) &= \frac{|\nabla\rho(\vec{\mathbf{r}})|}{2k_F\rho(\vec{\mathbf{r}})}. \end{aligned} \tag{2.21}$$

Within these gradient-corrected functionals, one common approximation is the generalized gradient approximation (GGA), which usually performs better than LDA functionals for describing atomic energies and binding energies but mostly fails for van der Waals interactions. Yet, the computational cost for GGA functionals is similar to that of LDA. One of the most popular GGAs functional is PBE [31], which was proposed in 1996 by Perdew, Burke, and Ernzerhof.

Even if GGA functionals can significantly enhance the LDA ones, they cannot capture van der Waals interactions, which are essential for intermolecular interactions that lead to the formation, structure, and stability of molecules and materials, especially for molecule adsorption studies. The main issue with LDA and GGA functionals, which are local and semi-local functionals, respectively, is that they do not account for long-range electronic

correlation. Although there are some approaches to include it, such as using non-local correlation functionals, one of the most straightforward and effective ways is to incorporate empirical potentials to correct the total energy. This approach is known as dispersion-corrected DFT, and several options are available in the literature. In this thesis, we focus on DFT-D2, which was proposed by Grimme [32]. This method introduces the correction through a damped function and pairwise atomic parameters. In the DFT-D2 approach, the total energy is corrected as follows:

$$E_{DFT-D2} = E_{KS-DFT} + E_{disp}^{D2}, \tag{2.22}$$

where E_{disp}^{D2} is the empiral dispersion potential defined by:

$$E_{disp}^{D2} = -s_6 \sum_{i}^{N} \sum_{i \neq j}^{N} \left(\frac{C_{6,ij}}{R_{ij}^6} \right) f_{damp}^{D2}(R_{ij}), \tag{2.23}$$

where s_6 is the global scaling parameter which depends on the DFT functional used, i and j the atom index, $C_{6,ij}$ the dispersion coefficient for the atom pair ij, R_{ij} the distance between the atom i and j, and $f_{damp}^{D2}(R_{ij})$ the damping function, which is defined by:

$$f_{damp}^{D2}(R_{ij}) = [1 + e^{-d\frac{R_{ij}}{R_{0,ij}-1}}]^{-1}, \tag{2.24}$$

where d is a damping parameter and $R_{0,ij}$ is the sum of the van der Waals radii for the atoms i and j.

2.2 Green's Functions formalism

The Green's function formalism is a mathematical tool which can be use as response functions, i.e, how a quantum mechanical system responds to an external perturbation, such as electric or magnetic fields. It is commonly used in nanoelectronics and quantum transport to calculate the current and charge densities under a bias, thus allowing for out-of-equilibrium simulations. In this case, the problem to be simulated is the electron transport

in a system that comprises two or more contacts or electrodes (a source and drain), coupled to a central region, usually named scattering region, contact, or channel. Each electrode has a chemical potential: μ_L and μ_R for the left-electrode and right-electrode, respectively. The source electrode will send electrons through the channel towards the drain electrode. This is a scattering process, where the electron from the source will be scattered through the contact region and then transmitted to the drain electrode. If we apply a voltage V, and considering the Fermy energy (E_F) at equilibrium, the chemical potentials are expressed as:

$$\mu_{L/R} = E_F \pm \frac{V}{2}. \tag{2.25}$$

In the equilibrium case, all the chemical potentials are equal, so in order to solve this problem, we can simulate the two contacts as two semi-infinite electrodes (periodic in the transversal plane but not in the transport direction) and the central region, which is also not periodic in the transport direction. The Hamiltonian and wavefunction of our electrodes will be H_L and $|\psi_L\rangle$ for the left-electrode and H_R and $|\psi_R\rangle$ for the right-electrode. For the central region, the Hamiltonian and wavefunction will be H_C and $|\psi_C\rangle$. From the time-independent Schrödinger equation:

$$H|\Psi\rangle = E|\Psi\rangle, \tag{2.26}$$

and dividing between the subspaces for the electrodes ($H_{L,R}$, $|\psi_{L,R}\rangle$) and the contact region (H_C, $|\psi_C\rangle$):

$$\begin{pmatrix} H_L & \eta_L & 0 \\ \eta_L^\dagger & H_C & \eta_R^\dagger \\ 0 & \eta_R & H_R \end{pmatrix} \begin{pmatrix} |\psi_L\rangle \\ |\psi_C\rangle \\ |\psi_R\rangle \end{pmatrix} = ES \begin{pmatrix} |\psi_L\rangle \\ |\psi_C\rangle \\ |\psi_R\rangle \end{pmatrix}, \tag{2.27}$$

where $\eta_{L,R}$ considers the interaction between the electrodes and the central region. Within the Green's functions formalism, the problem can be expressed in terms of the retarded

single-particle Green's function ($G(E)$), defined by:

$$[(E + i\delta)\, S - H]\, G(E) = I, \qquad \text{with } \delta \to 0^{+}, \tag{2.28}$$

where S is the overlap matrix, H is the Hamiltonian, E is the energy, and I is the identity matrix. If the limit $\delta \to 0^{+}$ is taken, the retarded G is obtained. The limit $\delta \to 0^{-}$ gives the advanced G. From the definition of the retarded Green's function, we write:

$$\begin{pmatrix} ES_L - H_L & ES_{LC} - \eta_L & 0 \\ ES_{CL} - \eta_L^{\dagger} & ES_C - H_C & ES_{CR} - \eta_R^{\dagger} \\ 0 & ES_{RC} - \eta_L & ES_R - H_R \end{pmatrix} \begin{pmatrix} G_L & G_{LC} & G_{LR} \\ G_{CL} & G_C & G_{CR} \\ G_{RL} & G_{RC} & G_R \end{pmatrix} = \begin{pmatrix} \mathbf{I} & 0 & 0 \\ 0 & \mathbf{I} & 0 \\ 0 & 0 & \mathbf{I} \end{pmatrix}, \tag{2.29}$$

where E denotes $E + i\delta$ and considering that the basis set used is orthogonal, the overlap $S_{LC} = S_{CL}$ and $S_{RC} = S_{CR}$ are zero. In this case, Equation 2.29 is written as:

$$\begin{pmatrix} E - H_L & -\eta_L & 0 \\ -\eta_L^{\dagger} & E - H_C & -\eta_R^{\dagger} \\ 0 & -\eta_R & E - H_R \end{pmatrix} \begin{pmatrix} G_L & G_{LC} & G_{LR} \\ G_{CL} & G_C & G_{CR} \\ G_{RL} & G_{RC} & G_R \end{pmatrix} = \begin{pmatrix} \mathbf{I} & 0 & 0 \\ 0 & \mathbf{I} & 0 \\ 0 & 0 & \mathbf{I} \end{pmatrix}. \tag{2.30}$$

To solve this problem, we can select three equations from the second matrix, in the second column:

$$\begin{aligned} (E - H_L)\, G_{LC} - \eta_L G_C &= 0, \\ -\eta_L^{\dagger}\, G_{LC} + (E - H_C) G_C - \eta_R^{\dagger} G_{RC} &= \mathbf{I}, \\ (E - H_R)\, G_{RC} - \eta_R G_C &= 0, \end{aligned} \tag{2.31}$$

and solving for G_{LC} and G_{RC}:

$$\begin{aligned} G_{LC} = (E - H_L)^{-1} \eta_L G_C &= g_L \eta_L G_C, \\ G_{RC} = (E - H_R)^{-1} \eta_R G_C &= g_R \eta_R G_C, \end{aligned} \tag{2.32}$$

where $g_{L,R} = (E - H_{L,R})^{-1}$. For the Green's function in the contact region, G_C, it can be ob-

tained from Equation 2.31, using the Green's functions for the electrodes in Equation 2.32:

$$-\eta_L^\dagger\, g_L \eta_L G_C + (E - H_C)G_C - \eta_R^\dagger g_R \eta_R G_C = \mathbf{I}, \tag{2.33}$$

and solving for G_C:

$$G_C = (E - H_C - \eta_L^\dagger\, g_L \eta_L - \eta_R^\dagger g_R \eta_R)^{-1} \quad = (E - H_C - \Sigma_L - \Sigma_R)^{-1}, \tag{2.34}$$

where $\Sigma_L = \eta_L^\dagger\, g_L \eta_L$ and $\Sigma_R = \eta_R^\dagger\, g_R \eta_R$ are known as the self-energies.

In general terms, the effect of the electrodes on the contact region is to incorporate the self-energies into the contact Hamiltonian. Finally, from the retarded Green's function $G(E)$, one can obtain properties such as the density of states (DOS) and the local density of states (LDOS) by applying the following:

$$\mathrm{DOS}(E) = -\frac{1}{\pi}\mathrm{Tr}[\Im\, G_k(E)], \tag{2.35}$$

and

$$\mathrm{LDOS}(E) = -\frac{1}{\pi}\Im\, G_{k,\{ii\}}(E), \qquad \text{local at site } i, \tag{2.36}$$

where k represents the periodicity in the Brillouin zone. In the following the non-equilibrium Green's Functions formalism (NEGF) will be described within the TranSIESTA [33, 34] implementation available in the SIESTA [22–24] code.

TranSIESTA module

The TranSIESTA module [33, 34] is a DFT+NEGF code implemented within SIESTA [24], which allows us to introduce the electrode potential effects in the simulation, will be discussed. TranSIESTA has been widely used in the electron transport problem to calculate a variety of physical properties where there is a net flow of electrons due to an applied voltage or temperature gradient, such as electrical and heat conductivity, heat

dissipation, electron transmission and conductance in materials, current-voltage curves, among other [33].

The central point of TranSIESTA formalism is to obtain a self-consistent description of the electron density $\rho(\vec{\mathbf{r}})$ and the Kohn-Sham Hamiltonian $\mathbf{H}$ for an open quantum system coupled with two (or more) electrodes, and where the size in the electrodes should be large enough to avoid perturbations due to the scattering region. In our case, we will focus in the solution for the case of two electrodes.The retarded Green's function $\mathbf{G}$ at energy ϵ is expressed as:

$$\mathbf{G}(z) = \left[z\mathbf{S} - \mathbf{H} - \sum_{e} \Sigma_e(z) \right]^{-1}, \tag{2.37}$$

where $z \equiv \epsilon + i\eta$, e denotes the electrodes and Σ_e their corresponding self-energy.

The broadening function Γ_e is expressed as:

$$\Gamma_e(z) = i \left[\Sigma_e(z) - \Sigma_e^{\dagger}(z) \right], \tag{2.38}$$

and the spectral function A_e as:

$$A_e(z) = \mathbf{G}(z)\Gamma(z)\mathbf{G}^{\dagger}(z). \tag{2.39}$$

Finally, the non-equilibrium density matrix ρ is defined as:

$$\rho = \frac{1}{2\pi} \int \mathrm{d}\epsilon \sum_{e} A_e(z)\, n_{F,e}(\epsilon), \tag{2.40}$$

where $n_{F,e}$ denotes a Fermi distribution function. In this case, Equation 2.40 is the density matrix for both equilibrium and non-equilibrium. Another central quantity for the NEGF is the energy density matrix $\mathfrak{E}$, which enables the force calculations and in TranSIESTA is obtained by:

$$\mathfrak{E} = \frac{1}{2\pi} \int \mathrm{d}\epsilon\epsilon \sum_{e} A_{e,}(z)\, n_{F,e}(\epsilon). \tag{2.41}$$

Equilibrium case (EGF)

In the equilibrium case, when all the chemical potentials are equal, Equation 2.40 can be expressed as:

$$\rho_{eq} = \frac{1}{2\pi} \int \mathrm{d}\epsilon \, n_F(\epsilon), \tag{2.42}$$

where ρ_{eq} is the equilibrium density matrix corresponding to the chemical potential n_F.

Non-equilibrium case (NEGF)

When in the system there is a difference between the electrode electronic distributions $n_{F,e}$, the system is out-of-equilibrium. This situation can appear when the electrodes have different chemical potentials or temperatures. Defining the non-equilibrium density for the electrode e as ρ^e_{neq}:

$$\rho^e_{neq} = \rho^e_{eq} + \sum_{e' \neq e} \Delta^e_{e'}, \tag{2.43}$$

where $\Delta^e_{e'}$ is a non-equilibrium correction term for the equilibrium density of the electrode e due to the electrode e'. $\Delta^e_{e'}$ can be written in terms of the two chemical potentials as:

$$\Delta^e_{e'} = \frac{1}{2\pi} \int \mathrm{d}\epsilon A_{e'}(z)[n_{F,e'}(\epsilon) - n_{F,e}(\epsilon)]. \tag{2.44}$$

The triple matrix product needed it for the evaluation of $A_{e'}$, the evaluation of ρ^e_{neq} and the inversion of Γ make more computationally demanding the NEGF case than the EGF one.

2.3 Classical potentials

While quantum mechanics methods, such as DFT, provide a description of the electronic states from fundamental laws of physics without requiring any previous information about the system or empirical parameters, when the number of atoms involved is beyond a few hundred or the time scales involved are longer than a few picoseconds, their computational cost becomes too high, and one has to resort to less expensive approaches. One approach is the classical potentials, which maintains an atomistic system description but does not derive interatomic forces directly from electronic structures. Instead, these forces are parameterized within a classical interatomic potential $V(\vec{\mathbf{r}})$. This parameterization enables classical MD to simulate large-scale systems, typically comprising thousands of atoms and longer time scales. In MD, either using forces computed through classical or quantum mechanics, the dynamics of the atoms is controlled by Newton's equation of motion:

$$\vec{\mathbf{F}}_\mathbf{i} = m_i \frac{\partial^2 \vec{\mathbf{r}}_\mathbf{i}}{\partial t^2},\ i = 1, 2,\ ...\ N, \tag{2.45}$$

where $\vec{\mathbf{F}}_\mathbf{i}$ is the force on atom i, m_i is the mass of atom i, $\vec{\mathbf{r}}_\mathbf{i}$ is its position vector, and N is the total number of atoms in the system. The interacting potential, in this case, is related to the atom's forces by:

$$\vec{\mathbf{F}}_\mathbf{i} = -\frac{\partial V(\vec{\mathbf{r}_1}, \vec{\mathbf{r}_2}..., \vec{\mathbf{r}_N})}{\partial \vec{\mathbf{r}}_\mathbf{i}}, \tag{2.46}$$

where $V(\vec{\mathbf{r}_1}, \vec{\mathbf{r}_2}..., \vec{\mathbf{r}_N})$ is the interacting potential that depends on the atoms positions. The interacting potential in classical MD is also known as the force field (FF), and it basically consists of intramolecular and intermolecular potentials, defined as:

$$V(\vec{\mathbf{r}}) = V_{\text{intramolecular}}(\vec{\mathbf{r}}) + V_{\text{intermolecular}}(\vec{\mathbf{r}}), \tag{2.47}$$

where the intramolecular interactions consider the chemical bonding interactions within

a molecule: bond stretching, bond angles, and torsion around bonds (dihedrals). On the other hand, the intermolecular interactions or nonbonded interactions consider the van der Waals and Coulombic interactions. A typical FF can be expressed as:

$$V(\vec{\mathbf{r}}) = \sum_i K_i^b (b_i - b_0)^2 + \sum_j K_j^\theta (\theta_j - \theta_0)^2 + \sum_k K_k^{dihe.} (1 + \cos[n_k \varphi_k - \varphi_0]) + \sum_{lm} \left[\frac{A_{lm}}{\vec{r}_{lm}^{12}} - \frac{B_{lm}}{\vec{r}_{lm}^{6}} + \frac{1}{4\pi\epsilon_0} \frac{q_l q_m}{\vec{r}_{lm}} \right], \tag{2.48}$$

where each sum runs over all i bonds, j angles, k dihedrals, and l, m atom pairs. The three first terms of Equation 2.48 represent the intramolecular interactions, while the last two are the intermolecular ones. The equilibrium values for the bonds (b_0), angles (θ_0) and dihedrals (ϕ_0), as well as the corresponding spring constants (K_i^b, K_j^θ, and $K_k^{dihe.}$) for each different bond/angle/dihedral (i, j, and k) must be provided. Generally, the parameter values of a FF are determined by either QM calculations or experimental data. Finally, n_k is the multiplicity number, A_{lm} and B_{lm} are the Lennard-Jones constants for each l, m atom pair, $\vec{r}_{lm}$ is the distance between the l, m atoms, q are the charges, and ϵ_0 is the permittivity of vacuum. The positions ($\vec{\mathbf{r}}_\mathbf{i}$) and velocities ($\vec{\mathbf{v}}_\mathbf{i}$) of the atom in the system are then obtained by integrating over time the equations of motion Equation 2.45.

However, for a system with N atoms, the problem becomes a $3N$ second-order ordinary differential equations coupled, which cannot be solved analytically but numerically using a solver or numerical integrator [35]. The first quantity to be discretized is the time. In this case, we do not obtain the trajectory for continuous t, but for a set of discrete t_i, separated by dt. One of the most common and simple numerical integrators is the Verlet algorithm. In this algorithm, the atom velocities that are one time step ahead are calculated from the positions at the current and the previous time step. First, a Taylor expansion is performed around time t for one atom's coordinate at time $t + \delta t$:

$$\vec{\mathbf{r}}(t + \delta t) = \vec{\mathbf{r}}(t) + \frac{d}{dt}\vec{\mathbf{r}}\delta t + \frac{1}{2!}\frac{d^2}{dt^2}\vec{\mathbf{r}}\delta t^2 + \cdots + O(\delta t^4). \tag{2.49}$$

The Taylor expansion is also performed for the time $t - \delta t$, and it is expressed by:

$$\vec{\mathbf{r}}(t - \delta t) = \vec{\mathbf{r}}(t) - \frac{d}{dt}\vec{\mathbf{r}}\delta t + \frac{1}{2!}\frac{d^2}{dt^2}\vec{\mathbf{r}}\delta t^2 + \cdots + O(\delta t^4). \tag{2.50}$$

Combining both Equation 2.49 and Equation 2.50, we obtain the following:

$$\vec{\mathbf{r}}(t + \delta t) = -\vec{\mathbf{r}}(t - \delta t) + 2\vec{\mathbf{r}}(t) + \frac{d^2}{dt^2}\vec{\mathbf{r}}\delta t^2 + \cdots + O(\delta t^4). \tag{2.51}$$

The velocity $\vec{\mathbf{v}}(t)$ is derived by subtracting Equation 2.50 from Equation 2.49:

$$\vec{\mathbf{v}}(t) = \frac{d}{dt}\vec{\mathbf{r}}(t) = \frac{1}{2\delta t}[\vec{\mathbf{r}}(t + \delta t) - \vec{\mathbf{r}}(t - \delta t) + O(\delta t^2)]. \tag{2.52}$$

The trajectories derived of the Verlet algorithm present an inherent error of $O(\delta t^2)$ and $O(\delta t^4)$ for the velocities and positions, respectively. The accuracy of the trajectory is increased using the Verlet leapfrog algorithm, where the velocities are updated at every half-integer time step:

$$\vec{\mathbf{v}}\left(t + \frac{\delta t}{2}\right) = \vec{\mathbf{v}}\left(t - \frac{\delta t}{2}\right) + \frac{\vec{\mathbf{F}}(t)}{m}\delta t, \tag{2.53}$$

and the positions are obtained as follows:

$$\vec{\mathbf{r}}(t + \delta t) = \vec{\mathbf{r}}(t) + \vec{\mathbf{v}}\left(t + \frac{\delta t}{2}\right)\delta t. \tag{2.54}$$

The velocity at time t is determined as:

$$\vec{\mathbf{v}}(t) = \frac{1}{2}\left[\vec{\mathbf{v}}\left(t - \frac{\delta t}{2}\right) + \vec{\mathbf{v}}\left(t + \frac{\delta t}{2}\right)\right]. \tag{2.55}$$

However, because the positions and velocities are not simultaneously defined in the Verlet leapfrog algorithm, it is not possible to compute the kinetic, potential, and total energies at the same time. An alternative is the velocity-Verlet algorithm, one of the most common choices in MD simulations, where the velocity and positions are expressed as:

$$\vec{\mathbf{v}}\left(t+\frac{\delta t}{2}\right)=\vec{\mathbf{v}}(t)+\frac{1}{2}\frac{\vec{\mathbf{F}}(t)}{m}\delta t, \qquad \vec{\mathbf{v}}(t+\delta t)=\vec{\mathbf{v}}\left(t+\frac{\delta t}{2}\right)+\frac{1}{2}\frac{\vec{\mathbf{F}}(t+\delta t)}{m}\delta t \tag{2.56}$$

and

$$\vec{\mathbf{r}}(t+\delta t)=\mathbf{r}(\vec{t})+\vec{\mathbf{v}}\left(t+\frac{\delta t}{2}\right)\delta t. \tag{2.57}$$

In all the algorithms, it is essential to choose the right time interval δt, which determines the balance between the precision in the simulation and the computational efficiency. Smaller time intervals improve the accuracy but demand more computational efforts. However, large time intervals result in greater numerical errors. Typically, the time interval is chosen to be smaller than the shortest characteristic time scale of motion within the system.

2.4 Quantum Mechanics/Molecular Mechanics

When describing chemical processes, especially in complex environments such as the ones found in electrochemistry, it is often necessary to use different levels of theory to find the correct balance between accuracy and computational efficiency. As mentioned in section 2.3, QM calculations can be too computationally expensive for extensive systems, so classical MD simulations are often used instead. However, sometimes, a pure classical MD simulation is insufficient for capturing the main processes occurring in the system. In this case, an alternative strategy is employing hybrid approaches, such as the quantum mechanics/molecular mechanics (QM/MM) method. QM/MM combines the low computational cost of classical MD with the high accuracy/predictability of QM calculations.

Warshel and Levitt [36] first developed the QM/MM method for large systems where

a QM calculation was not feasible, but a detailed description of bond-forming/breaking or charge transfer was necessary. In QM/MM runs, the system is divided into two subsystems, one described using QM and the other using MM. The QM subsystem is chosen for the part requiring higher accuracy/predictability, like where the charge transfer occurs, while the MM subsystem includes the remaining atoms (in the case of this work, the solvent atoms). This way, larger time scales and a realistic number of atoms can be considered, making the method popular in biological systems and biosensors [37–44].

In this thesis, the QM/MM method used was described by [38, 45] and implemented using the DFT formalism of SIESTA [22–24] for the QM part, and the Wang et al. [46] FF parametrization within the AMBER scheme [47]. In this implementation, the total energy of the combined system is given by:

$$E^{tot} = E_{QM} + E_{MM} + E_{QM/MM}, \tag{2.58}$$

where E_{QM} is the Kohn-Sham energy of the QM subsystem calculated by SIESTA, E_{MM} the classical term which includes the two-, three-, and four-body bonded terms as well as the non-bonded terms (van de Waals and Coulomb interactions between the MM atoms), and the $E_{QM/MM}$ includes the mixed interactions between the QM and MM regions, which are van der Waals and Coulomb interactions between the classical and quantum atoms. E_{QM} is defined in the SIESTA formalism as:

$$E_{KS} = \sum_{\mu\nu} P_{\mu\nu} H_{\mu\nu} - \frac{1}{2} \int V^H(\vec{\mathbf{r}}) \rho(\vec{\mathbf{r}}) \mathrm{d}\vec{\mathbf{r}} + \int (\epsilon^{xc}(\vec{\mathbf{r}}) - V^{xc}(\vec{\mathbf{r}})) \rho(\vec{\mathbf{r}}) \mathrm{d}\vec{\mathbf{r}} + \frac{1}{2} \sum_{\alpha\beta} \frac{Z_\alpha Z_\beta}{r_{\alpha\beta}}, \tag{2.59}$$

where $P_{\mu\nu}$ are the density matrix elements, $H_{\mu\nu}$ the Hamiltonian matrix elements, $V^H(\vec{\mathbf{r}})$ the Hartree potential, $\rho(\vec{\mathbf{r}})$ the electronic charge density, $\epsilon^{xc}(\vec{\mathbf{r}})\rho(\vec{\mathbf{r}})$ the exchange-correlation energy density, $V^{xc}(\vec{\mathbf{r}})$ the exchange-correlation potential, $Z_{\alpha,\beta}$ the core's charge, and $r_{\alpha,\beta} = |\vec{\mathbf{r}_\beta} - \vec{\mathbf{r}_\alpha}|$ the distance between the cores.

The E_{MM}, which is the energy of the MM subsystem, has the form of a FF under the

parametrization of Wang et al. [46], and can be defined in the same way as Equation 2.48.

Finally, the coupling between QM and MM regions is taken into account as follows:

$$E_{QM/MM} = \sum_{i}^{C} q_i \int \frac{\rho(\vec{\mathbf{r}})}{|\vec{\mathbf{r}} - \vec{\mathbf{r}_i}|} \mathrm{d}\vec{\mathbf{r}} + \sum_{i}^{C} \sum_{\alpha}^{A} \frac{q_i Z_\alpha}{|\vec{\mathbf{R}_\alpha} - \vec{\mathbf{r}_i}|} + E^{LJ}, \tag{2.60}$$

where the first term of the equation represents the electrostatic interaction between the electrons (through the electronic charge density $\rho(\vec{\mathbf{r}})$ and the classical atoms i with partial charge q_i, the next term the electrostatic interaction between the nucleus α with charge Z_α and the classical atoms, and the last term stands for the van der Waals interactions between the quantum and classical atoms through a 6-12 Lennard-Jones potential, which was taken from the Wang et al. [46] force field parametrization, as appears in the before last term of Equation 2.48.

The effect of the classical atoms on the charge density, and hence in the QM subsystem, is introduced in a self-consistent way by the addition of the point charge potential to the Hartree potential as follows:

$$\delta V^H(\vec{\mathbf{r}}) = \delta V^H(\vec{\mathbf{r}}) + \sum_{i}^{C} V_i^{MM}(\vec{\mathbf{r}}), \tag{2.61}$$

where

$$V_i^{MM}(\vec{\mathbf{r}}) = \frac{q_i}{|\vec{\mathbf{r}_i} - \vec{\mathbf{r}}|}. \tag{2.62}$$

In summary, in this thesis, the QM/MM method was coupled with NEGF to describe the solvent and electrode potential effects on the adsorption of MBI on the Cu surface using molecular dynamics: a QM/MM-NEGF molecular dynamics approach. The Cu and MBI atoms form the QM subsystem, and the H_2O molecules are the MM ones. Using QM/MM-NEGF molecular dynamics allowed us to have QM accuracy/predictability for Cu and MBI interaction while keeping an efficient description of liquid water. Yet, that approach allow us to keep a constant voltage applied between the electrodes, thus allowing for as-realistic-as-possible simulations being applied for the first time in the context of electrochemistry

to study CI.

2.5 SIESTA method

The Spanish initiative for Electronic Simulations with Thousands of Atoms (SIESTA) is a self-consistent DFT code [22–24], based on the linear combination of atomic orbitals (LCAO) basis set, and norm-conserving pseudopotentials, which enables the $O(N)$ scaling. This choice of LCAO with pseudopotentials enables SIESTA to perform very efficient simulations using a minimal basis set and very accurate calculations when a more complete and polarized basis set is used, reducing the storage and computational resources. Within SIESTA, the most basic approximations are considered for the DFT simulations, including the Born-Oppenheimer approximation, the electronic exchange-correlation treatment, and using pseudopotentials to represent the core electrons. In SIESTA, the Kohn-Sham one-electron Hamiltonian can be written as:

$$\hat{H} = \hat{T} + \sum_i \hat{V}_i^{KB} + \sum_i V_i^{NA}(\vec{\mathbf{r}}) + \delta V^H(\vec{\mathbf{r}}) + \delta V^{xc}(\vec{\mathbf{r}}), \tag{2.63}$$

where $\hat{T}$ is the kinetic energy operator, $V^H(\vec{\mathbf{r}})$ the Hartree potential, $V^{xc}(\vec{\mathbf{r}})$ the exchange-correlation potential, $V_i^{NA} = V_i^{local} + V_i^{atom}$ the local and $\hat{V}_i^{KB}$ the non-local parts of the pseudopotentials.

The basis set in SIESTA are strictly localized pseudoatomic orbitals, which are zero beyond a certain radius. The basis set is a product of a numerical radial function and a spherical harmonic:

$$\phi_{\alpha lmn}(\vec{\mathbf{r}}) = \phi_{\alpha ln}(\vec{\mathbf{r}} - \vec{\mathbf{R}_\alpha})\Upsilon_{lm}\left(\frac{\vec{\mathbf{r}} - \vec{\mathbf{R}_\alpha}}{|\vec{\mathbf{r}} - \vec{\mathbf{R}_\alpha}|}\right), \tag{2.64}$$

where α is the atomic index, l and m the angular momentum and n the index of the orbitals. In this case, if there are several orbitals with the same angular dependence but different radial shapes, the basis set is called a multiple-ζ. The accuracy in the basis set can be con-

trolled by increasing the radius, adding more ζ orbitals for the same angular moment but with different radial dependence, or adding polarization orbitals to consider the deformation induced by the bond formation. However, the accuracy is not a simple parameter. It can depend on multiple combinations of parameters, representing a disadvantage in using this basis set (and, in general, in the LCAO method).

The overlap matrix between the LCAO orbitals, $\mathbf{S}_{\mu\nu}$ is expressed as follows:

$$\mathbf{S}_{\mu\nu} = \langle \phi_\mu | \phi_\nu \rangle, \tag{2.65}$$

denoting that the basis set is non-orthogonal. The Kohn-Sham orbitals are expressed in terms of the SIESTA atomic orbitals as:

$$\psi_i(\vec{\mathbf{r}}) = \sum_\mu \phi_\mu(\vec{\mathbf{r}}) c_{\mu i}; \qquad c_{\mu i} = \langle \tilde{\phi_\mu} | \psi_i \rangle = \mathbf{S}^{-1}_{\nu\mu} \langle \phi_\mu | \psi_i \rangle, \tag{2.66}$$

where $\tilde{\phi_\mu}$ defines the dual orbital of ϕ_μ:

$$\langle \tilde{\phi_\mu} | \phi_\nu \rangle = \delta_{\mu\nu}. \tag{2.67}$$

Hence, the Kohn-Sham eigenproblem using this basis set is expressed as:

$$\sum_\nu \mathbf{H}_{\mu\nu} c_{\nu i} = \epsilon_i \sum_\nu \mathbf{S}_{\mu\nu} c_{\nu i}, \tag{2.68}$$

and, the electronic charge density is obtained as follows:

$$\rho(\vec{\mathbf{r}}) = \sum_i n_i |\psi(\vec{\mathbf{r}})|^2, \tag{2.69}$$

where n_i is the occupation state of ψ_i according to the Fermi-distribution. Combining Equation 2.69 with the definition of $\psi(\vec{\mathbf{r}})$, we obtain:

$$\psi(\vec{\mathbf{r}}) = \sum_i n_i |\psi(\vec{\mathbf{r}})|^2| = n_i \sum_i \sum_{\nu\mu} c^*_{\nu i} \phi^*_\nu(\vec{\mathbf{r}}) \phi_\mu(\vec{\mathbf{r}}) c_{\mu i}, \tag{2.70}$$

and the density matrix is defined as:

$$\rho_{\mu\nu} = \sum_i c_{\mu i} n_i c_{i\nu}, \tag{2.71}$$

and rewritten the electron density as:

$$\rho(\vec{\mathbf{r}}) = \sum_{\mu\nu} \rho_{\mu\nu} \phi^*_\nu(\vec{\mathbf{r}}) \phi_\mu(\vec{\mathbf{r}}). \tag{2.72}$$

As the atomic orbitals are confined within some confinement radius, limiting the orbital's range, that leads to a sparse Hamiltonian and overlap matrices; they present non-zero elements only when the two basis orbitals overlap. From Equation 2.72, we can observe that the only required elements are those where the overlap matrix is non-zero, thus also generating a sparse density matrix.

In summary, the SIESTA method provides a general and very efficient scheme to perform DFT calculations, from fast to very accurate simulations, and it can deal with thousands of atoms in the simulation [24].

Section 3

Literature Review

In the this section, a literature review of the topic of molecular modelling of corrosion inhibition is presented. This review has been put it in the form of a paper which has been recently accepted in npj Materials Degradation [48] journal. This review highlights the need to understand the fundamental mechanisms of organic corrosion inhibitors, where molecular modelling can provide important insights. That would allow for a detailed analysis of the corrosion inhibition (CI) process. However, CI modelling is often not explored in-depth and is usually applied to this field in a standardised way only to support experimental results. In this paper, six essential aspects (A) to consider when modelling CI are described: (A1) the electronic properties of isolated inhibitors, (A2) the interaction of the inhibitor with the surface, (A3) the surface model, (A4) the effect of the anodic and cathodic zones on the surface, (A5) the solvent effects, and (A6) the electrodes' potential effects. While the first three aspects are commonly considered, the latter three and more complex surface models are often neglected, creating gaps in the CI modelling literature. This literature review aims to discuss the main features of molecular modelling in CI, fo-

cusing on the key aspects mentioned above and the emerging approaches that aim to fill the gaps in the literature.

This review is organized as follows: section 3.1 discusses the theoretical background involved in the simulations commonly applied to CI and section 3.2 discusses the main aspects for the CI modeling, reviewing the most recent works for each of the aspects highlighted before. We also give a focus on the main gaps found in the CI literature to describe some critical phenomena, discussing the most recent works that somehow address those gaps.

3.1 Theoretical background

Molecular modeling is a very active research area with applications in many different fields, such as sensors [49], materials design [50], and drug discovery [51], to name just a few. With the advent of faster computers and optimized methodologies, molecular modeling has become a vital tool for investigating CI. Although molecular modeling is a versatile tool with many methods available, its use in CI is standardized and frequently limited to complement the experimental findings, often relying on QSAR (Quantitative Structure-Activity relationship), or on very simplified models of the structures and the physical and chemical processes. By standardized, we mean molecular modeling performed with over-simplified models, where the employed theory level is insufficient to provide significant insights about the CI.

However, the methodologies available for molecular modeling are very rich and diverse, and could contribute to a much deeper understanding if their full potential would be deployed to the study of the processes involved in CI. As it will be further discussed in section 3.2, the recent works applied to CI, especially those intended to develop methods, despite being scarce, provide important information about the molecular process that occurs during the CI.

From a molecular modeling point-of-view, we can, in principle, describe computation-

ally any atomistic process in materials if we have two basic ingredients. The first one is the knowledge of the interactions between atoms in the material (that is, the interatomic potentials). Those determine the equations of motion for the atoms and the physical evolution of the material at the atomic level. The second one is an algorithm to integrate the equations of motion and obtain physical properties (such as most stable structures, thermodynamic properties, reaction rates, and many others) from the atomic interactions. The variety of available choices for these two ingredients is overwhelming, and well beyond the scope of this review. Here we give a very broad and superficial account of the most popular approaches.

Concerning the interatomic interactions, one could obtain the forces on the atomic nuclei in any material from Quantum Mechanics (QM) by solving the Schrödinger equation[1] (SE) for its nuclei and electrons, as explained in Equation 2.1.

Normally, the electrons are considered to be in their ground state, so that their energy E_e is their ground state energy. The nuclear dynamics can be obtained considering the nuclei as quantum particles, thus incorporating all quantum effects in the model, or as classical particles (due to their large mass). The latter case is the most frequent one in the modeling of materials, and restricts the quantum effects to the description of the electrons. The nuclei, in this case, move following the Newton laws of classical mechanics, with forces defined by the derivatives of the PES:

$$\vec{\mathbf{F}}_i = -\frac{dE_\mathrm{e}(\{\vec{\mathbf{R}}\})}{dR_i} \,. \tag{3.1}$$

The electronic SE Equation 2.1 is still too difficult to be solved but for the simplest molecules, and approximations have to be made. Quantum Chemistry (QC) [26] provides a plethora of methods that propose approximations to the many-body electronic wavefunctions, with increasing levels of accuracy, from the simple Hartree-Fock (HF) method to sophisticated Configuration Interaction approaches. Quantum Monte Carlo methods

[1] Here we only present the time-independent Schrödinger equation as time dependent phenomena are usually described using the time evolution of stationary states, or through the adiabatic approximation where electrons are assumed to be in their (instantaneous) ground state.

(QMC) [52], on the other hand, do not propose explicit functional forms for the wavefunction, but directly compute averages of physical quantities (mainly the energy, typically for the ground state) numerically using stochastic methods by sampling the multidimensional space of the wavefunctions. The advantage of QMC over QC methods is that the scaling with system size is much more favourable, allowing to deal with larger systems, although they are usually restricted to simple properties such as the total energy, and to deal with the ground state. However, both kinds of approaches are usually too expensive computationally to deal with the typical sizes involved in CI, which limits their applicability and impact in this field.

A class of methods that is frequently used to solve the electronic problem is Density Functional Theory (DFT), as explained in section 2.1. Here one abandons any attempt to approximate the electronic many-body wavefunction $\Psi_n(\vec{\mathbf{r}})$, and focuses on the electronic charge density.

Using the Kohn-Sham formulation of DFT, the previous many-body problem is reduced to a one-electron problem which can be readily solved numerically, enabling the studying of much larger systems compared to the ones that can be investigated through wave-function-based electronic structure methods. This numerical efficiency and the capacity of DFT to reach systems of considerable size (even thousands of atoms in high performance computers) have made it the methods of choice in most computations in materials science and chemistry, and in most applications to CI modeling.

DFT provides a description of the electronic state and the nuclear dynamics (from the forces obtained from the electronic solution) that stem from the fundamental laws of QM and electromagnetism. As they do not require neither any previous knowledge of the system under study nor empirical parameters, they are usually referred to as first-principles methods. They are highly transferable and can be applied to any system, as they rely only on the fundamental laws of physics and do not require any previous knowledge or parameters fit to any particular system. Therefore, they have a high level of predictive power, and thus are of general applicability. Besides, they provide a detailed microscopic picture of

processes in materials. DFT in particular is the first-principles method of choice for practical CI studies, when the behavior of the electrons is a concern (like in the study of chemical reactions), and when one does not wish to use experimental or empirical parameters in the simulation.

Although DFT can be used in the study of large atomistic systems, when the number of atoms involved is beyond a few hundreds or the time scales involved are longer than a few picoseconds, DFT is too computationally demanding, and one has to resort to less expensive approaches. A popular one is Molecular Mechanics (MM), where one retains an atomistic description of the system, but the interatomic forces are not obtained from the electronic structure, but parameterized in the form of a classical interatomic potential $V(\{\vec{\mathbf{R}}\})$, commonly referred to as force field (FF), that depends on the positions of the atoms in the system. The FF can be more or less complex, and have different analytical or numerical forms and parametrizations, but have the common feature that they are parametrized and fit to known experimental or theoretical results. Commonly used forms of FFs for small molecules are OPLS-All-Atom (OPLS-AA) [53], OPLS3 [54], General AMBER Force Field (GAFF) [55, 56], CHARMM General force field [57–59], GROMOS [60–64], and Merck Molecular Force Field (MMFF) [65–69], which are implemented in software packages such as GROMACS [70], NAMD [71], LAMMPS [72], AMBER [73], CHARMM [74], and OpenMM [75], among others. These FFs contain molecular parameters for a wide range of chemical species [76, 77]. Nonetheless, a common issue of utilizing FF in CI modeling (and in other areas) is the indiscriminate use of unvalidated FFs.

Also, recently, other types of FFs are being developed which do not have an analytical expression and are parameterized using machine learning (ML) approaches [78]. The ML FFs learn about the system through the relationship between chemical descriptors and their properties from patterns in the data [79]. The patterns and structure in data are typically extracted by applying kernel methods, and neural networks based on the atomic representation of the system [80]. In this respect, ML FFs allow to explore efficiently the

chemical space and predict some properties of the system with good accuracy. Although the transferability of ML FFs poses a problem when going beyond the specific training conditions [78, 79], they are a promising approach that may provide in the near future first-principles accuracy at the cost of MM methods.

Once the method to compute the energies and forces is chosen (either using first-principles or classical potentials), one still must solve the equations of motion and obtain the physical properties of the system, like reaction energies, thermodynamics, phase stability, transport properties, etc. For this, two main methods have been used. The first one is Molecular Dynamics (MD) [81, 82], in which one essentially integrates the Newton's equations of motion for the atoms in the system:

$$\vec{\mathbf{F}}_i = m_i \frac{\partial^2 \vec{\mathbf{R}}_i}{\partial t^2},\ i = 1, 2,\ \ldots N, \tag{3.2}$$

obtaining their trajectories as a function of time: $\vec{\mathbf{R}}_i(t)$. This is done from the knowledge of the forces (derivatives of the system energy with respect to the atomic positions, as in Equation 3.1), discretizing time and approximating the derivatives using finite differences. The trajectories are then obtained for discrete values of time. Time averages over the integrated trajectories for the properties of interest are approximations to the thermodynamic averages. Different MD techniques allow to access different physical properties, over different thermodynamic ensembles: microcanonical (constant NVE), canonical (constant NVT), Grand canonical (constant μVT), etc.

The second class of methods commonly used to obtain the physical properties form the energy and interaction models are based on Monte Carlo approaches. Here, one does not attempt to follow the dynamics of the system, but to compute properties in equilibrium, from averages of the corresponding operator. The averages are computed using stochastic approaches. In these simulations, a system is evolved to a different state from an ensemble of possible future states, which is accepted or rejected with a certain probability and using some criterion. The equilibrium's state in the system is investigated as a function of the temperature (Metropolis Monte Carlo), or to advance the system's state through time

(kinetic Monte Carlo). In Metropolis Monte Carlo, the number of states can be seen as the number of geometries, which are accumulated, and then a potential energy function is calculated for each of them. Thus, a certain thermodynamic property can be computed through the integration:

$$A = \int A(\vec{\mathbf{r}})P(\vec{\mathbf{r}})\mathrm{d}\vec{\mathbf{r}}\,, \tag{3.3}$$

where A is the thermodynamic property, $P(\vec{\mathbf{r}})$ is the probability distribution function, and $\vec{\mathbf{r}}$ the coordinates. $P(\vec{\mathbf{r}})$ is given by:

$$P(\vec{\mathbf{r}}) = \frac{\exp(-\frac{E(\vec{\mathbf{r}})}{k_\mathrm{B}T})}{\int \exp(-\frac{E(\vec{\mathbf{r}})}{k_\mathrm{B}T})}\,, \tag{3.4}$$

where $E(\vec{\mathbf{r}})$ is the energy of the system with coordinates $\vec{\mathbf{r}}$ and the denominator is the partition function. $P(\vec{\mathbf{r}})$ can be calculated using two methods: a quadrature scheme or Metropolis [83].

In Kinetic Monte Carlo, the simulation proceeds with a list of all possible discrete reaction steps, and then a probabilistic method is used to select a reaction based on what will occur in a time step. In this case, reactions with a high rate will be preferably selected over those with a slower rate, and the reaction rates can be obtained from ab-initio simulations. The time step for the selected reaction is evolved based on all possible reaction rates for the current configuration. Once the system is updated, a list of reactions is created, and the probabilistic selection process continues. The main difference between MD and Kinetic Monte Carlo is that MD follows the evolution of the system with time in a continuous manner, whereas in Kinetic Monte Carlo, the events are discrete [83, 84].

3.2 Main aspects for the CI modeling

From a molecular point of view, CI modeling provides invaluable insights into all phenomena that occur during the corrosion process, e.g. oxidation/reduction of the metallic

surface and other chemical species present in solution, mass loss in the metallic surface, redistribution of the electronic charge in the inhibitor and the EDL, which functional groups are oriented toward the metal, how the molecule builds up layers on the metallic surface, etc. Those insights allow us to comprehend how atoms-molecules-surface-solvent interact, paving the way to investigating several degrees of freedom of a given problem, individually and collectively, a tricky task when doing experiments. In that manner, one can evaluate with atomistic detail the CI process, bringing light to the inhibition mechanisms.

The choice of the interaction model (mainly between QM and MM models) is related to the desired level of predictability in investigating the target property or phenomenon. However, in CI modeling, because of the system's size usually required in the simulations, often highly accurate methods are prohibitive. QM methods allow us to investigate the electronic and structural properties of the inhibitor, surface, and aqueous interface with more detail than the MM ones since the electrons are explicitly considered in those methods, besides being more transferable and general. In that manner, QM methods may provide important information about the adsorption mechanism of the inhibitor, where, for instance, the π-orbitals of the inhibitor will interact with the surface and with the other ones from other inhibitor molecules, and depending on the coverage and the strength of this interaction, the corrosion inhibitor will adopt a particular adsorption configuration, that potentially could lead to the formation of self-assembled monolayers (SAM) [21]. Nonetheless, the lack of computing power often limits the application of QM methods, where, for instance, the solvent effects are not always included. Modeling based on MM is very popular in the CI field, as it is reported in many works in the literature [85–108]. That is primarily because of its low computational cost compared to QM methods, allowing, for instance, the inclusion of solvent effects, one of the critical aspects in the CI field.

Many works reported in the literature use molecular modeling only to support experimental observations [98, 103, 109–115]. Most works use QM methods to compute molecular properties of isolated inhibitors [98, 103, 110–116] which are traditionally attempted to correlate with CI efficiency through electronic properties, such as the ones discussed in

the next section. In the following sections, we revise the main works available in the literature, presenting a detailed discussion of the six main aspects of CI modeling highlighted in the introduction.

3.2.1 Electronic properties of isolated inhibitors

The electronic properties of isolated inhibitors can give us a first insight into their CI properties. Most of the works reported in the literature attempt to correlate these properties with the experimental CI performances of the inhibitors. This approach is known as MEPTIC (molecular-electronic properties to inhibition-efficiency correlation) [117]. This is usually done through simple correlation methods (e.g., linear regression analysis) or more elaborated statistical models such as nonlinear methods (e.g., neural networks, polynomial regressions, ML techniques, etc.) [15]. The more elaborated methods correspond to the QSAR (Quantitative Structure-Activity Relationship) approach, which is usually applied in predicting biological activities or physicochemical properties of compounds, but in recent years has been applied to predict the CI properties of compounds.

MEPTIC

In the MEPTIC approach, trends in the electronic structure of the isolated inhibitors and their similarity with other inhibitors are attempted to correlate with the experimental CI performance, sometimes also aiming to provide insights into its interaction with the surface. Most of the time, the aforementioned molecular properties are calculated using DFT, but some works use wave-function-based methods, such as Møller-Plesset (MP), Coupled Cluster (CC), HF method, etc., and semiempirical methods [118–121]. The MEPTIC models can be expressed as follows:

$$f(x) = \alpha_1 x_1 + \alpha_2 x_2 + ... + \alpha_n x_n + \epsilon \ , \tag{3.5}$$

where $f(x)$ is the molecular property, x_n the n^{th} molecular parameter, α_n the coefficient (weight) of each parameter, and ϵ the associated error. For example, the CI performance, η, can be expressed as a combination of some coefficients and the energies of the frontier orbitals:

$$\eta = a + bE_{\text{HOMO}} + cE_{\text{LUMO}} + ..., \tag{3.6}$$

where a, b, and c are constants determined to fit the model, E_{HOMO} and E_{LUMO} the energies of the HOMO (highest occupied molecular orbital) and LUMO (lowest unoccupied molecular orbital) orbitals. Once these apparent correlations are determined for a given set of inhibitors and materials, the findings are extrapolated to other systems [19, 117, 122, 123]. However, this approach may result in erroneous associations, as many of these studies observed the correlations within a restricted set of molecules, or even to no correlation as shown in Figure 3.1. The inhibition efficiency (η) in Figure 3.1 was calculated as $\eta = (R_{\text{p}}^{\text{inh}} - R_{\text{p}}^{\text{blank}})/R_{\text{p}}^{\text{inh}}$, where $R_{\text{p}}^{\text{inh}}$ is the mean polarization resistance of the inhibited sample, and $R_{\text{p}}^{\text{blank}}$ the mean polarization of the blank (non-inhibited sample). When a more comprehensive dataset of inhibitors is employed, the apparent correlation might disappear or not be so apparent [15, 19, 124–129]. From MEPTIC approach, one can not have any information about the physical and chemical processes that occur during/after the adsorption process because of the lack of explicit interaction between inhibitors and the metallic surfaces, which is not considered in these studies [130–139].

Another problem that could appear in MEPTIC is the linear dependence between the variables (molecular properties) used. The linear dependence could appear using two related quantities (e.g., the fundamental gap and the HOMO and LUMO energies), but there might also be other ambiguous and unclear linear dependencies when many parameters are used in the models. To deal with that, there are statistical techniques to identify the causal correlations between the parameters or regularization techniques [15, 140, 141].

Among the electronic properties typically utilized in the MEPTIC approach, the frontier molecular orbitals HOMO and LUMO are the most commonly analyzed in the liter-

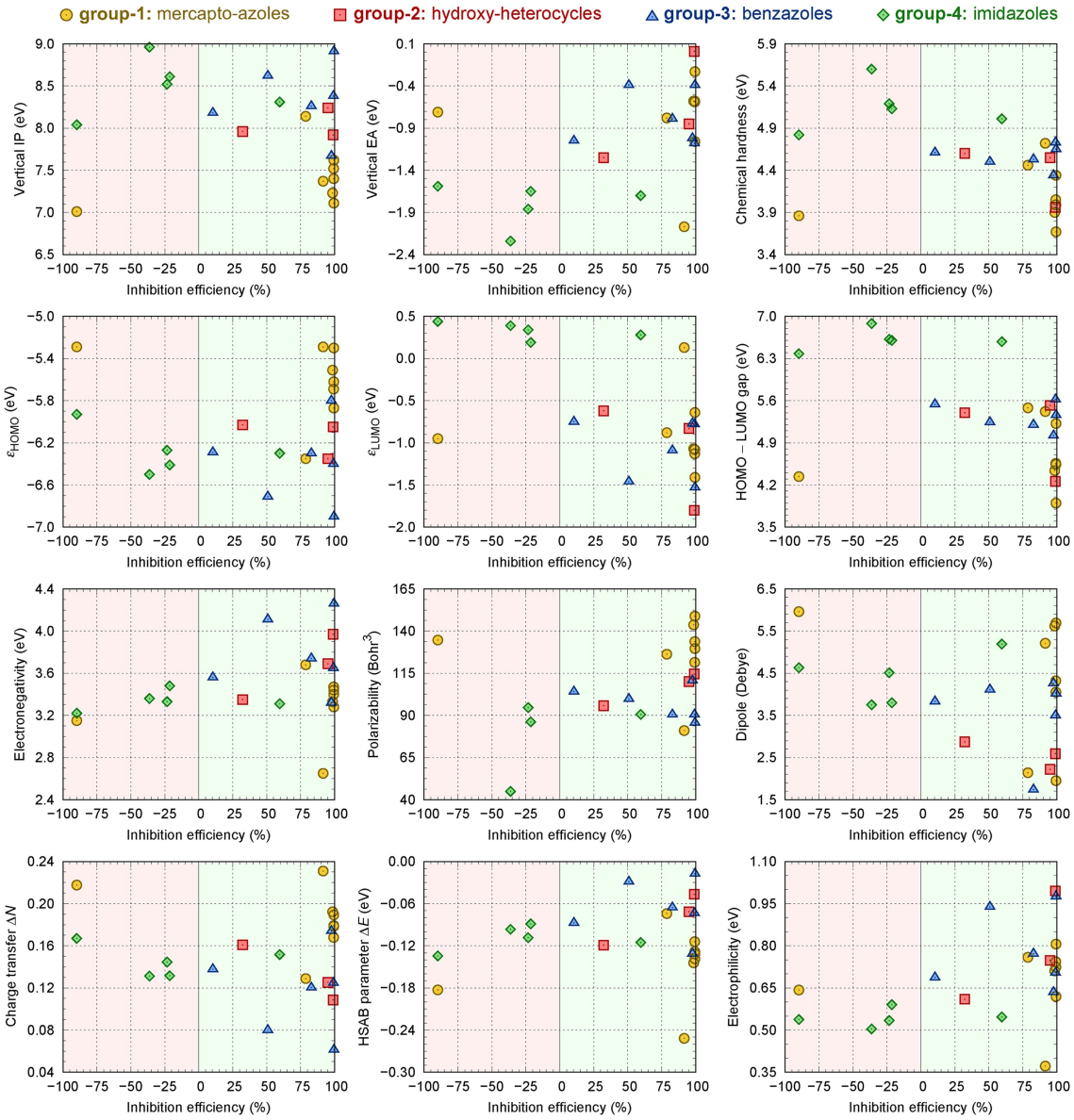

Figure 3.1: Correlations between the experimental corrosion inhibition efficiency and molecular electronic parameters for a set of organic compounds tested as corrosion inhibitors for copper in saline solution. A significant vertical dispersion of points near 100% inhibition efficiency appeared for all the molecular electronic parameters. This implies that a good inhibitor can present almost any value within a relative broad range. All the details about the molecular electronic parameters, set of organic compounds, and numerical values are reported by Kokalj et al. [123]. Adapted from Kokalj et al. [123] with authorization.

ature. Those orbitals tend to react with surface states, thereby enhancing the interaction between the inhibitor and the surface. The E_{HOMO} is associated with the molecule's tendency to transfer electrons to the surface, while the E_{LUMO} is related to its tendency to accept electrons from the surface, e.g. in a transition metal from d-orbitals. Consequently,

the difference between the HOMO and LUMO energies, often referred to as the HOMO-LUMO gap or fundamental gap ΔE, can indicate the strength of the inhibitor-surface interaction in an indirect way. A higher ΔE implies lower reactivity of the molecule with the surface, whereas a lower ΔE suggests higher reactivity.

However, ΔE is not the sole determinant of the inhibitor's reactivity with the surface or its CI performance. Breedon et al. [124] have criticized that correlation by exploring other molecular parameters, such as molecular ionization and deprotonation energies for a set of 28 small organic molecules using DFT and QMC calculations. They found no clear relationship between experimental CI efficiency, the fundamental gap, and other molecular properties. More recently, Kokalj [122] discussed the importance of the molecular electron-donating ability and the fundamental gap in CI for a data set of 22 heterocyclic organic inhibitors for Fe in acidic solutions. A weak bilinear dependence with a volcano-like shape on the fundamental gap was found, but the correlation is too weak to be quantitative. Hence, analyzing only the fundamental gap cannot predict the inhibition efficiency.

Liu et al. [138] studied the inhibition performance of nicotinic acid (NA), nicotinic acid amide (NAA), and 4-methoxypyridine (MP) for the CI of mild steel in acidic solution through experiments and simulations. Their experimental results showed that the inhibitors could prevent the material's corrosion following the trend NAA > NA > MP for CI performance. Then, the CI performance was correlated to molecular properties, such as charge density distributions, HOMO and LUMO energies, and the Hard-Soft Acids and Bases (HSAB) parameters, finding some correlations with their experimental results for CI performance. However, the correlations found, even agreeing with experimental results, should not be generalized to other corrosion inhibitors or materials because, as mentioned before, they can lead to false associations. In this case, the correlations could be more coincidences than true relations.

Another important molecular parameter used in MEPTIC is the dipole moment. This quantity measures the separation of the electric charges within a molecule. There are two arguments for its effect on CI performance. The first one says that a high dipole moment

will enhance the molecule's interaction with the metallic surface, leading to higher CI. The second argument says that a lower dipole moment will favour the molecule accumulation on the surface (the lower dipole moment of the molecule reduces its electrostatic repulsion from the charges on the surface), protecting the material against corrosion. Both arguments could be true, even if they seem to be contradictory. In this sense, the effect of dipole moment on the CI properties is non-trivial and depends on several factors, from electrostatic to intermolecular interactions, as well as the dipole's orientation [123, 142], as shown in Figure 3.1.

The HSAB theory has also been applied in the MEPTIC approach to predict the bonding between the inhibitor and the surface, where the molecule is the electron-donor species (nucleophile), and the metallic surface (assuming metals with d-orbitals) is the electron-acceptor one (electrophile) due to its vacant d-orbitals. Accordingly, the corrosion inhibitor would be adsorbed on the metallic surface by its reactive part and block the active sites on the metallic surface, thus preventing it from corrosion. In this sense, the HSAB theory can help to predict the CI properties of specific molecules, but without any information about the corrosion inhibition mechanism. It can also lead to incorrect conclusions due to the lack of robustness of the models used or because there is no correlation at all between the molecular parameters used and the corrosion inhibition efficiency, as shown in Figure 3.1. The parameters used for HSAB theory, such as Mulliken electronegativity, chemical potentials, nucleophilicity, electrophilicity, softness, hardness, etc., can be calculated using DFT simulations through simple ground-state equations based on the electronic density [123].

The Fukui indices are additional reactivity descriptors that emerge from the HSAB theory. They provide information about which atoms on the molecule tend to lose/gain electrons, thus determining the strength of certain potential bonding sites (reactive sites) on the corrosion inhibitor. Some of these descriptors are the electrophilic (f^+) and nucleophilic (f^-) indices, which indicate the electrophilic and nucleophilic regions of the corrosion inhibitor, hence the affinity to be adsorbed on the metallic surface. The Fukui

indices can be compared for different corrosion inhibitors or molecule derivatives to get insights into which one can perform better as corrosion inhibitor [15, 96, 100, 103, 105, 116, 123, 143–154].

QSAR

The QSAR models can also be used to analyze the dependence of some property of interest (e.g., CI performance) with molecular features. One of the differences between the QSAR models and the MEPTIC approach is that the latter focuses more on the electronic properties of corrosion inhibitors and their correlation with CI. In contrast, the QSAR models are a more versatile modeling approach which can include several molecular descriptors and experimental data to predict the CI. In this sense, the QSAR models are usually more mathematically complex than the MEPTIC ones. Several QSAR models have been applied to different families of organic compounds used as corrosion inhibitors, such as azoles, imidazoles, amino acids, Schiff bases, etc. To evaluate the fitness and statistical significance of a QSAR model, statistical properties such as Pearson's correlation coefficient (R), coefficient of determination (R^2), mean absolute error (MAE), mean square error (MSE), root mean square error (RMSE), the sum of square errors (SSE), etc., are used [127, 155–157].

The main issue with the QSAR models typically used in the CI literature is that only a few show statistical robustness, potentially resulting in false correlations between the CI performance and the computed molecular properties [117]. To identify reliable molecular descriptors for QSAR models, Winkler et al. [126] investigated a data set comprising 100 small organic molecules as potential corrosion inhibitors of Al alloys AA2024 and AA7075. Their findings indicated that molecular electronic properties obtained through DFT (such as electron affinity, ionization potential, E_{HOMO}, E_{LUMO}, among others) lacked sufficient information to generate predictive models for CI performance. However, when these DFT descriptors were combined with other molecular features (e.g., the presence of specific functional groups, molecular topology, van der Waals volume, etc.), along with experimental data, they yielded excellent QSAR models. Winkler's work sets a precedent

demonstrating that molecular properties can be linked to CI efficiency, showing that QSAR models can correlate molecular features with CI performance. However, these models do not provide any information about the mechanism of action of the inhibitor.

Another remarkable example of using QSAR models is the work by Fernandez et al. [158], who studied the CI performance of 28 small organic molecules. They employed a QSAR approach known as comparative molecular surface analysis (CoMSA), which utilizes distributions of electronegativity, polarizability, and van der Waals volume calculated at the DFT level to identify highly effective corrosion inhibitor compounds. The outcomes of their study revealed the identification of five molecules as prototypes and archetypes for corrosion inhibitors. This demonstrates that these properties projected onto the molecular surface (using the Connolly surface model [159]) can predict the CI potential for small organic molecules.

Currently, Artificial Neural Networks (ANN) have emerged as a non-linear technique employed to characterize the connection between molecular descriptors and their corresponding molecular properties in a given dataset [144]. ANN has been used to correlate and predict complex nonlinear relationships without having any knowledge about the underlying mathematical description involved and using an artificial intelligence (AI) approach [160]. An ANN is formed by several simple and highly interconnected processors or neurons (nodes). It is characterized by three main components: node character (processing of the signals by the node), network topology (structure and connections between the nodes), and learning rules (how the weight of the molecular parameters are initialized and adjusted using an algorithm). The nodes in an ANN are usually arranged in three layers: the input, hidden, and output layers [144].

Chen et al. [127] investigated through an ANN the quantitative relationship between structural/molecular features and their experimental electrochemical properties for a data set of 38 corrosion inhibitors. The neural network used was the Bayesian regularization approach, based on a three-layer neural network architecture with an automatic training process to minimize the correlation error. The structural descriptors used in the model

considered molecular features such as the number of atoms, number of non-H atoms, number of rings, among others. The experimental properties considered were the corrosion potential, corrosion current, and anodic/cathodic Tafel slopes. Their results showed that the ANN could predict the electrochemical performance of the corrosion inhibitor compounds they used, with combined experimental and molecular properties, when applied to AA-2024-T3 alloys.

In a recent work by Dai et al. [161], a cross-category corrosion inhibitor database was constructed using an ANN (three-level direct message passing neural network, 3L-DMPNN) model with molecular information that incorporates atomic-level, chemical bond-level, and molecular-level details to predict the CI performance of compounds in specific environments. The model's generalization ability was tested by them in 23 organic molecules from the latest literature studies [127] and 4 molecules tested in the laboratory, finding that the model could accurately predict the CI performance for both highly and slightly efficient corrosion inhibitors at a low computational cost.

In summary, examining the electronic properties of isolated corrosion inhibitors offers insights into their potential interaction with the metallic surface to protect the material from corrosion. However, those analyses are insufficient to conclude that a given molecule might be a good corrosion inhibitor because either using MEPTIC or QSAR approaches often leads to poor or no correlation between the molecule's electronic properties and the experimental CI performance. More advanced QSAR models, when provided with appropriate molecular descriptors, may improve such correlations, but it is always difficult to extend the findings for a given set of molecules to other molecules.

3.2.2 The interaction of the inhibitor with the surface

Addressing the inhibitor's adsorption onto the surface is fundamental in CI modelling. In the CI literature, the adsorption energy (E_{ads}) of the inhibitor on the surface is often used as

a parameter to infer the CI efficiency of inhibitors. For the different methods used, E_{ads} is computed in varying ways, but always referring to how strongly a molecule is attached to a surface and displaces solvent molecules, thus blocking electrochemical activity. Several factors, such as the molecular structure and functional groups of a given inhibitor, may influence its adsorption energy on the metals. That affects the alignment (or configuration) of the inhibitor molecules on the surface and, thus, the adsorption configuration of the molecule on the surface and coverage [98, 103, 109–113, 115, 162–164].

The accuracy of the energies obtained strongly depends on the computational method employed, and emerging methodologies can provide better descriptions of both energetic and structural properties. For instance, in QM simulations the accuracy will depend on the level of theory used in the calculation (e.g. the specific functional used in DFT), while, in MM simulations, on the FF parametrization (AMBER type, reactive force fields, ML FFs, etc.) [79, 165, 166].

In the context of molecular dynamics, to assess the system's energy accurately, it is necessary to consider many different configurations, exploring the local energy minima on the system's PES. Most of the papers found in the literature are unclear whether they use a single configuration of the system (e.g., one adsorption structure obtained by structural optimizations) or consider an average over many MD steps.

Several works in the literature report the adsorption energies for inhibitors in different metallic surfaces by means of QM and MM simulations [14, 95, 107, 149, 162, 167–174]. Thaçi et al. [95] investigated the CI properties of monocarbonyl analogues of curcumin, specifically (2E,5E)-2,5-di-benzylidenecyclopentanone and (2E,5E)-bis[(4-dimethylamino)benzylidene]cyclopentanone, for Cu, using electrochemical measurements, Monte Carlo and MD simulations with classical potentials. Their simulations showed the ability of both inhibitors to be adsorbed on the surface, protecting it from corrosion, where both molecules adopted a configuration parallel to the surface. They performed the structural analysis using the radial distribution functions, which showed peaks in distances from 1 to 3.5 Å, corresponding to chemisorption on the

surface. Kozlica et al. [14] investigated the combined CI performance of MBI and octylphosphonic acid (OPA) on oxidized Cu (Cu_2O) with different OH/O termination, and a model of oxidized Al(111) surface with the equivalent of 2 monolayers of oxygen atoms and hydroxylated termination ($OH/Al_xO/Al(111)$). Adsorption energies of the inhibitors on the Cu surfaces were computed by them using DFT. Their results showed that MBI adsorbed preferably with the thione and thiolate form to the Cu surface, while the thiol form did not take part in the adsorption process due to the lower stability against the thiolate and thione form. In the case of OPA, they found a similar adsorption tendency. For the Al surfaces, the adsorption of the phosphonic group was addressed in a previous work by them [175], showing an adsorption preference for this group instead of the imidazole and thiol ones. In this case, the interactions governing the inhibitor's adsorption on the oxidized surfaces studied are covalent bonds with either O- or OH-terminated surfaces.

Dahmani et al. [90] determined which of the compounds present in the cinnamon essential oil (CiO) is responsible for its experimental CI performance on bare Cu and $CuO_2(110)$ surfaces. Using the major constituents compounds of CiO: trans-cinnamaldehyde (P46), δ-cadinene (P8), and β-Cubebene (P5), and through MD simulations with classical potentials, they found that P8 is interacting most favorably with the $CuO_2(110)$ surface, adopting a parallel adsorption configuration that covers the surface. Their experimental results, particularly using scanning electron microscopy (SEM) and energy dispersive X-ray analysis (EDS), suggested that the presence of the inhibitor protected the metal since the surface was smooth and exempted from all corrosion products. Since their simulations show the molecules are adsorbed to the surface (via MD trajectory analysis), they conclude that it protects the surface. They also analyzed the inhibitors through DFT calculations to determine the molecular properties usually associated with the corrosion inhibition efficiency: HOMO-LUMO energies, electronegativity, and ionization potentials, among others. Their DFT results suggested that P8 and P46 are the compounds with higher corrosion inhibition efficacy. However,

both conclusions about the DFT and MD results and the corrosion inhibition efficiency are weak arguments similar to the other ones found in the corrosion literature, attributing the corrosion protection only to the ability of the molecule to stick to the surface and their value of specific molecular properties calculated in the isolated inhibitors.

Many authors report on Monte Carlo simulations in combination with experimental techniques to predict CI performance [176–183]. Quadri et al. [178] evaluated the CI performance of three N-hydrospiro-chromeno-carbonitriles (INH-1, INH-2, INH-3) on mild steel in acidic solutions performing electrochemical measurements together with DFT and Monte Carlo simulations. The authors found the highest CI performance for INH-3, followed by the INH-2 and INH-1 compounds, which were evaluated through electrochemical impedance spectroscopy. Their Monte Carlo simulations showed that the adsorption energies of the corrosion inhibitors followed the same trend as the CI performance. The adsorption configuration mode for the molecules on the surface was found to be nearly parallel to the surface, using their π-electron-rich centers.

Madkour et al. [181] showed the CI performance for some arylazotriazoles (AATRs) on Cu using electrochemical measurements and Monte Carlo simulations. Their simulations showed that the AATRs adsorbed on the surface with a parallel configuration due to the donation of π-electrons from the aromatic rings, as well as the lone pair electrons from the heteroatoms to the unfilled d-orbitals of the Cu surface. This configuration maximizes surface contact and enhances surface coverage. The experimental results showed that AATRs are good inhibitors for Cu, with an increased CI performance at higher concentrations but decreased with rising temperatures.

The coverage ratio is one of the most important aspects of investigating inhibitors' adsorption mechanisms on metallic surfaces. From the modeling point of view, that can be addressed by either increasing the number of molecules in a simulation box of fixed size or decreasing the box dimensions for a fixed number of adsorbed molecules. In this manner, the adsorption of a given inhibitor on a metallic surface can be investigated as a function of the surface coverage, ranging from low to high concentrations, and potentially leading

to the SAMs formation. However, increasing the inhibitors concentration in experiments does not necessarily guarantee the formation of an ordered SAM layer, but often leads to disordered SAMs. For the SAM case, the lateral interactions between the inhibitors can stabilize the adsorption on the surface. For a given surface with a fixed simulation box size, Figure 3.2 sketches those two adsorption scenarios.

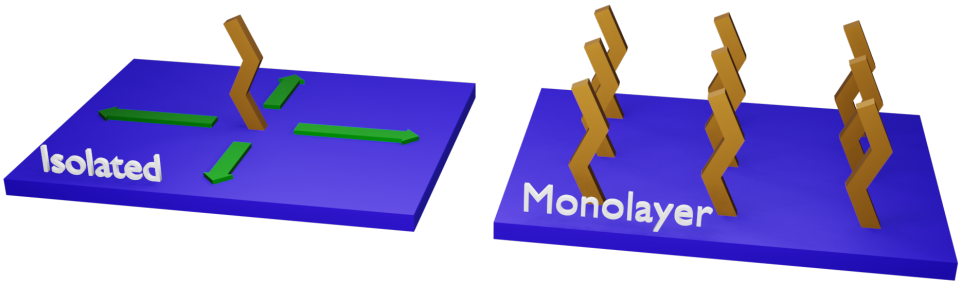

Figure 3.2: Inhibitor adsorption sketch considering the isolated and monolayer cases. The blue surface illustrates the metallic slab of the same size in both cases, showing that more molecules are needed to investigate the self-assembled monolayer (SAM) case. The green arrows indicate the empty lateral space, preventing the molecules from interacting with their images in simulations that apply periodic boundary conditions (PBC), for the case of low coverage adsorption.

Several works using isolated and monolayer adsorption cases are reported in the literature. For example, Vernack et al. [167] investigated the adsorption of 2-mercaptobenzimidazole (MBT) and 2-mercaptobenzimidazole (MBI) on Cu(111) surface via DFT calculations. Using different surface coverages until reaching the SAM formation, they found the most stable adsorption modes (2-atom bonded) of both MBI and MBT on the Cu(111) surface, where the MBI adsorbs more strongly than the MBT due to better lateral interactions in the SAM. The more stable adsorption of MBI would increase its CI performance compared to MBT.

Guo et al. [184] investigated the CI properties of three thiourea derivatives (1-(4-methoxyphenyl)-3-(4-phenylthiazol-2-yl)thiourea, 1-benzyl-3-(4-phenylthiazol-2-yl) thiourea, and 1-(2-hydroxyethyl)-3-(4-phenylthiazol-2-yl)thiourea, named Inh1, Inh2, and Inh3 in Figure 3.3, respectively, from Guo et al. [184]) on Fe surfaces by means of MD simulations with classical potentials to compute adsorption energies. Using this approach, they found that the Inh1 derivative presented strong adsorption for the varying

coverages, followed by Inh2 and Inh3, as shown in Figure 3.3. Their findings show the effect of the coverage in the adsorption energies, where the interactions between the inhibitors are maximized at a certain coverage, increasing its stability on the surface.

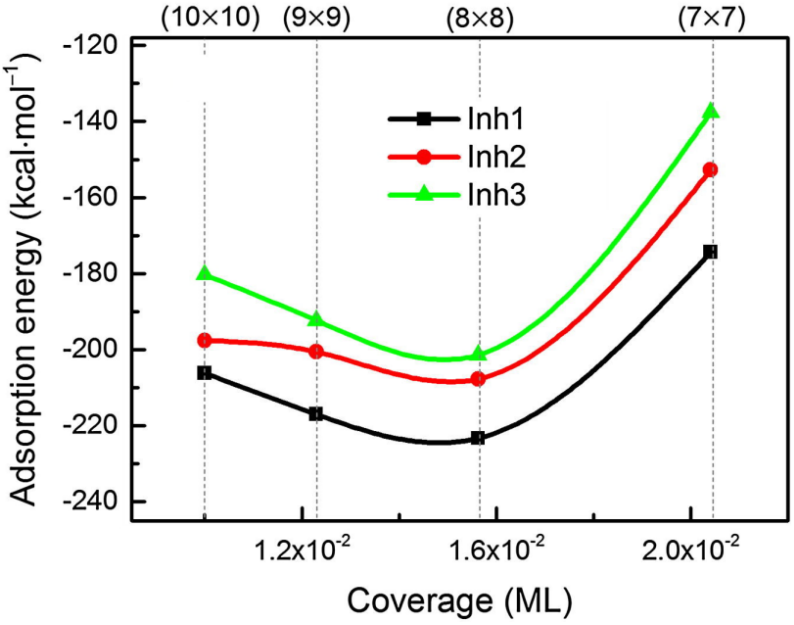

Figure 3.3: Variation of the adsorption energy with the surface coverage. The number of molecules per surface Fe atom is considered as the coverage unit (ML). The size of the supercell is shown at the top of the graphic. Adapted from [184] with authorization.

Chiter et al. [185] provide more insights about the CI properties of MBT monolayers adsorbed on Cu(110) via DFT calculations. Their findings showed that the thione and thiolate MBT are chemisorbed on the surface. The chemisorption leads to a stable and dense monolayer on the surface, which saturates all the Cu surface atoms at a concentration of 3.68 molecule nm^{-2}. The CI performance of the MBT monolayers was evaluated by calculating the Cu vacancy formation energy (the energy cost of creating one Cu vacancy) on the surface, both in the presence and in the absence of the inhibitor. A higher vacancy formation energy suggests a reduced probability of metal dissolution. In this study, their higher Cu vacancy energy for the thiolate case compared with the thione indicates that the thiolate form mitigates the metal dissolution.

In the same regard, Vernack et al. [186] investigated the formation of MBT monolayers on Cu_2O/Cu surfaces using DFT simulations combined with x-ray photoelectron

spectroscopy (XPS) and time-of-flight secondary ions mass spectrometry (ToF-SIMS). Their results showed MBT multilayer formation on the Cu oxide surface, which inhibits the oxide layer growth, as shown in Figure 3.4. The figure depicts the MBT layers' adsorption mechanism on the surface, illustrating the adsorption on both Cu_2O oxide and bare Cu. In the latter case, the adsorption of the MBT multilayers would inhibit the growth of the Cu_2O and the metal redissolution. Their DFT results showed that MBT molecules are strongly bonded to the surface through both S atoms, covered by a weekly bonded multilayer. They also found coadsorbed water between the MBT layers, interacting with the N(H) group via H bonds. Moreover, the adsorption of MBT on the surface inhibits the coadsorption of Cl^-, besides preventing Cu dissolution.

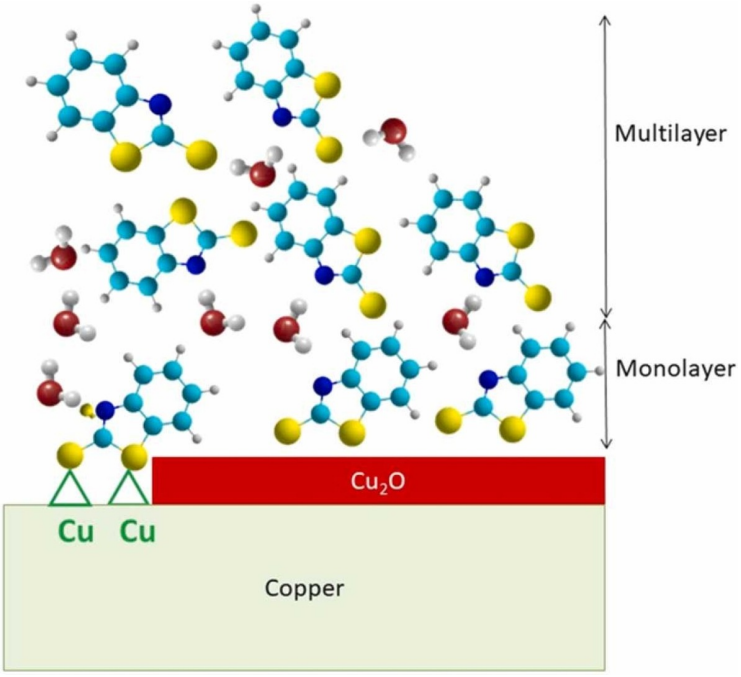

Figure 3.4: Sketch of the adsorption of 2-mercaptobenzothiazole (MBT) layers on the Cu_2O/Cu surfaces, where the adsorption is taking place on both the Cu_2O oxide and the metallic zones. The MBT layers contain water molecules trapped between them. Adapted from [186] with authorization.

The electronic properties can also be used to analyze the adsorption of inhibitors on the metallic surface. One can use the system's electronic density to obtain other quantities such as work functions, the total (DOS) and local (LDOS) density of states, electrostatic potentials, and the electronic density distribution. The work function of a metallic surface

is the minimum energy required to remove an electron from the solid surface to a point in the vacuum just outside the surface. It relates to the electronic energy level and thus with the electrode potential [187]. When the corrosion inhibitor is adsorbed on the metallic surface, there could be a change in the work function related to the adsorption process and intermolecular interactions (e.g., dipole moment) between inhibitors. The modified work function could affect the adsorption of ions on the surface and make less favorable the electron charge transfer to the metal from any of the chemical species present. In this case, when the adsorbate reduces the work function of the system, the adsorption of anions that donate electrons to the metal becomes less favorable. This affects the anodic reaction of the system, and this could be used to evaluate the CI process [163, 188–192].

The DOS allows for understanding how the states of a given atom (or other entity, such as the orbitals) are distributed in terms of energy. It can also provide hints about atoms interacting with each other. LDOS is the space-resolved density of states. This quantity is commonly used in scanning tunneling microscope (STM) analysis as it is directly related to the measured current as a function of the applied voltage and the tip position [193]. One can also assess the interaction between the corrosion inhibitor and the surface by analyzing the DOS [15]. When the corrosion inhibitor is being adsorbed on the surface, the electronic states of the inhibitor start to broaden because of the inhibitor-surface interaction [163].

Several authors have used the DOS to extract information about the CI process [149, 163, 167, 168, 170, 174, 191, 194–196]. Chiter et al. [168], for instance, studied the adsorption of MBI on Cu interfaces (Cu_2O/Cu). The strong adsorption of MBI on the Cu_2O/Cu surface and the formation of chemical bonds were confirmed by the electronic analysis in terms of the DOS and the LDOS. The authors observed drastic changes in both quantities before and after the adsorption process, suggesting the formation of strong bonds between the MBI and the surface. For the isolated MBI, in the thione form, the alignment of the HOMO and LUMO orbitals with respect to the slab's Fermi level suggests an electron donor behavior during the adsorption process. In contrast, the radical thiolate presents both electron donor and electron acceptor behavior. For each form, the DOS

showed that sulfur orbitals were the dominant ones for the states close to the Fermi level, suggesting that the sulfur atom is the most reactive site on the MBI. Once the MBI in both forms is adsorbed on the surface, the strong molecule-surface interactions change the molecule's DOS. These strong changes suggest the formation of covalent bonds between the inhibitor and the surface.

The molecular electrostatic potential (MEP) analysis, defined as the interaction energy between the charge distribution and a test positive charge, provides insights into the charge distribution of the molecule by mapping its value onto the molecule surface, typically the van der Waals volume [197]. The MEP can offer information about how the molecule interacts with the surface, revealing the electron-rich and electron-poor sites. These details allow us to predict potential reactions between the inhibitor and the surface of the molecule charge distribution, leading to a favorable interaction with the surface charges and enhancing its adsorption. Moreover, the molecule's charge distribution, as shown by the MEP analysis, can influence the position of ions in the electrolyte solution and then modify the EDL [190, 198]. For instance, Lgaz et al. [199] investigated the interaction of hydrazone derivates with the Fe surface using the electrostatic potential maps and Mulliken atomic charges, and the nucleophilic and electrophilic regions of the hydrazone derivates could be identified with both quantities. The nucleophilic regions are responsible for interactions with the Fe surface due to their electron-rich properties.

Investigating the interaction between the inhibitors and the metallic surface is an indisputable improvement to QSAR and MEPTIC approaches. That allows for evaluating several properties that offer insights into the molecule's ability to bind to the surface. However, many works use unrealistic surface models or neglect to include crucial ingredients, such as solvent effects. We discuss these issues in the following.

3.2.3 Surface models

The models used to simulate the metallic surface play a pivotal role in CI modeling. Simple surface models typically consist of bare crystalline metallic surfaces oriented according

to specific Miller indices, where the inhibitor molecule binds to the surface according to the different adsorption sites on the surface. Simple surface models neglect essential features of the surface, such as surface crystalline structure, grain boundaries or defects, or are present when the material is in dissolution, such as the formation of oxide layers and other adsorbates on the surface. In all cases, depending on the pH of the media, a native oxide layer (or the corresponding hydroxide) can be formed on the surface, forming a passivated surface. In that case, the surface might become less reactive, increasing its corrosion resistance. Therefore, it is essential to consider more complex metallic surfaces in molecular modeling works to have more realistic models [167, 192, 200, 201].

However, modeling the passivated surface is not straightforward due to the more complicated structural and electronic properties than bare metal surface [196]. Passivated surfaces are often disordered, or present different terminations, and their lattice vectors can have a mismatch with the ones of the metallic surface. That requires using larger supercells to minimize the strain, which increases the computational cost. Furthermore, the inhibitor may have more adsorption modes for passivated surfaces than for bare metals.

A few articles dealing with oxidized surface models are reported in the literature [14, 149, 168, 170, 190, 196, 202–205]. Chiter et al. [168] investigated the formation of MBI monolayers on Cu(111) surfaces covered by an ultra thin $Cu_2O(111)$ film. Both thione and thiolate MBI species formed the monolayers. The SAM formation is favored at high coverages, where the molecules adopt a perpendicular orientation to the surface, enhancing the $\pi - \pi$ interactions between the molecules. Their findings showed that the thiolate monolayer interacts more strongly with the surface than the thione due to the added Cu-C bond. The authors suggested that the MBI-thiolate can replace the H_2O and OH at the oxidized Cu surface due to its higher affinity with the surface, evaluated through its higher adsorption energy than the water/OH adsorption energy.

Chiter et al. [196] studied MBT inhibitors on oxidized copper surfaces: Cu(111) surfaces covered by a layer of $Cu_2O(111)$, where a dense and ordered monolayer perpendicular to the surface was obtained at full coverage, favored over single molecular adsorption

at low coverage. They found that the adsorption induces a reconstruction of the oxide surface's outermost layer, and the results also suggest that both thione and thiolate forms of MBT might substitute H_2O and OH at the $Cu_2O(111)$ surface, forming a protective layer on the surface in an aqueous environment.

Later, Chiter et al. [173] also investigated the adsorption of MBT on locally depassivated Cu surfaces using DFT calculations. The surface model consisted of a Cu(111) surface covered partially with an ultra thin layer of $Cu_2O(111)$. The authors were able to simulate different adsorption zones on the surfaces used: oxide and metallic surfaces, edges, and walls, as shown in Figure 3.5. Their results show how the inhibitor interacts with different surfaces to form an organic film strongly adsorbed on it. Due to the interfacial barrier properties, the organic film can prevent the initiation of localized corrosion. In the different surfaces studied, the most reactive sites were found to be the exposed Cu atoms and the single and doubly unsaturated O atoms of the oxide. The reactive sites for MBT were the S (exo or endo) and N (N or NH) atoms.

Another aspect studied by Chiter et al. [173] was the adsorption energy of MBT. They observed that the MBT adsorption changes with respect to the different zones along the surface. The strength of the adsorption decreases in the following order: oxide edges > oxide surface > metal surface > oxide walls. The adsorption trend was similar for the thione and thiolate species, except for the oxide walls in the latter one. The authors also found that the molecule blocks the most reactive sites, which are the most susceptible to interacting with ions that promote corrosion.

Wang et al. [149] also evaluated the effect of surface morphology, investigating the adsorption energy of imidazole (IMD), benzotriazole (BTAH), and 2-mercaptobenzoxazole (MBO) on the grain boundary of Cu(100) surface. They found that the corrosion inhibitors prefer to adsorb on the grain boundary of the surface, with perpendicular and parallel adsorption modes. In the perpendicular adsorption, the molecules bond to the surface through the azole group. In the parallel one, the bonding occurs through the benzene ring and the azole group.

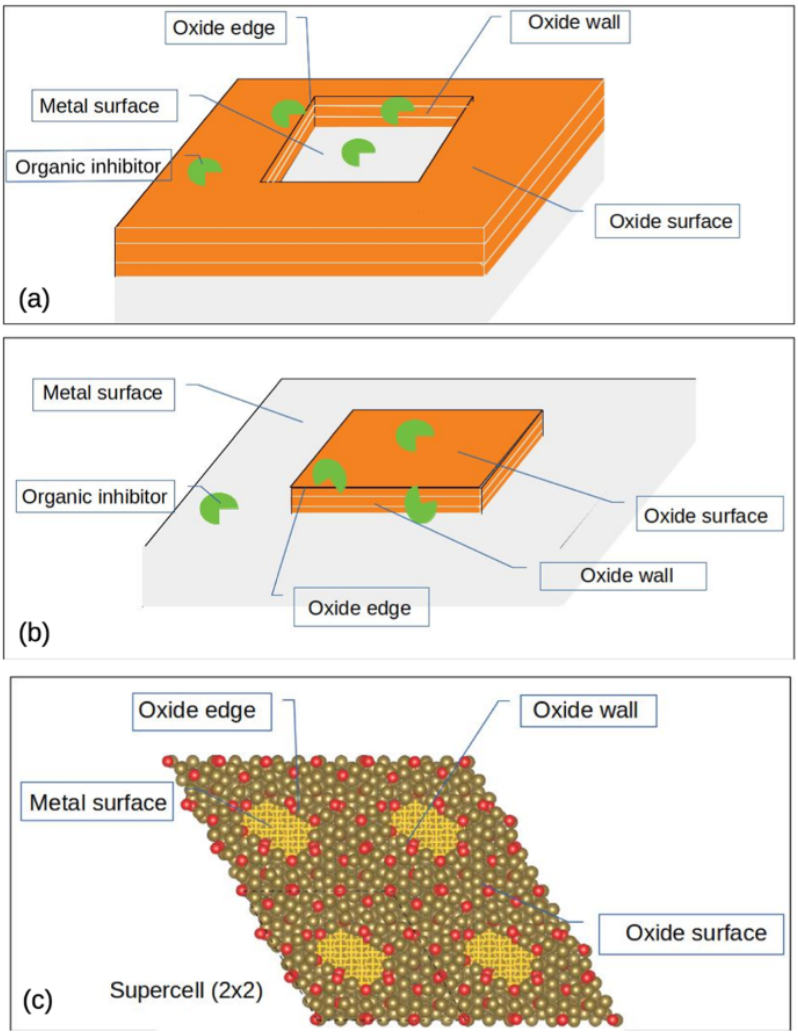

Figure 3.5: Model of the partially depassivated Cu surface. (a) Local depassivation model. The different parts on the surface are also depicted: Cu_2O surface, walls, and edges, as well as the metal surface and the corrosion inhibitor. (b) Incomplete depassivation situation. (c) Locally depassivated surface model, where the different parts on the surface will influence the inhibitors' adsorption. Adapted from [173] with authorization.

Other corrosion products such as Cl, H, and other counterions can also be adsorbed on the surface, and their presence might modify the surface reactivity [143]. The coadsorbed products can also modify the thermodynamics and kinetics of some stand-alone reactions, block the surface's reactive sites, or modify the surface electronic structure [206]. Taylor et al. [207], for instance, investigated how the adsorption of Cl is influenced by the coadsorption of H_2O, OH, and O on the bare surface of some metallic systems: Ni(111), Fe(110), Mg(0001), Zr(0001), and Al(111). The adsorption of Cl is related to its role in

interfering with processes such as the re-passivation or metal dissolution, which can either inhibit corrosion by the growth of passivating oxide phases or accelerate corrosion.

Dlouhy et al. [208] systematically investigated how the co-adsorption of O, OH, H, and Cl affect the adsorption of imidazole on Cu(111) using high-throughput DFT calculations, covering over 400 different adsorption configurations, evaluating the coverage effects, and the distance between imidazole and the co-adsorbates. Their findings revealed an enhancement in the imidazole adsorption in the presence of O and Cl. At the same time, H and OH have negligible impact on the adsorption, even if OH can also diminish it. Furthermore, the higher co-adsorbate concentration on the surface played a stabilizing role in the imidazole adsorption through the formation of hydrogen bonds between the imidazole and the co-adsorbate and the change in the induced work function due to the co-adsorption. The contrary effect was investigated by Chiter et al. [209], where the layers of corrosion inhibitors, long chain n-alkyl carboxylic acids, play a role of protecting a metallic Al surface from the penetration of Cl^-. Their DFT calculations showed that the energy barrier for the Cl^- penetration increases with the thickness of the inhibitor layers and Cl^- concentration.

3.2.4 Effect of anodic and cathodic zones

During the adsorption process of the corrosion inhibitor on the metallic surface, some chemical transformations, such as the making/breaking of bonds, or physical aspects, such as conformational rearrangements, can occur. Some of these chemical transformations are electrochemical reactions. During the corrosion process, there are two different electrochemical zones on the metallic surface exposed to the solvent media where two electrochemical reactions occur: oxidation (anodic reaction) and reduction (cathodic reaction), which are linked together to form a corrosion cell. In the oxidation process, the electrons lost travel to the cathodic site. The anodic reaction is the dissolution of the metal, while the cathodic one depends on what reducible species are in solution but usually is the reduction of the dissolved oxygen gas.

The metal dissolution produces metal cations that can react with the electrolytes and form soluble compounds or insoluble ones (rust) like metal oxide or hydroxide, depending on the electrode potential and pH conditions. In turn, the metal dissolution leads to a mass loss in the material, which can affect its structural resistance. This process is illustrated for steel in Figure 3.6. The Fe dissolution occurs in the anodic site, surrounded by the cathodic site, leading to the rust formation at the pit's edge. Different oxidized Fe compounds form the rust that gets deposited on the material surface.

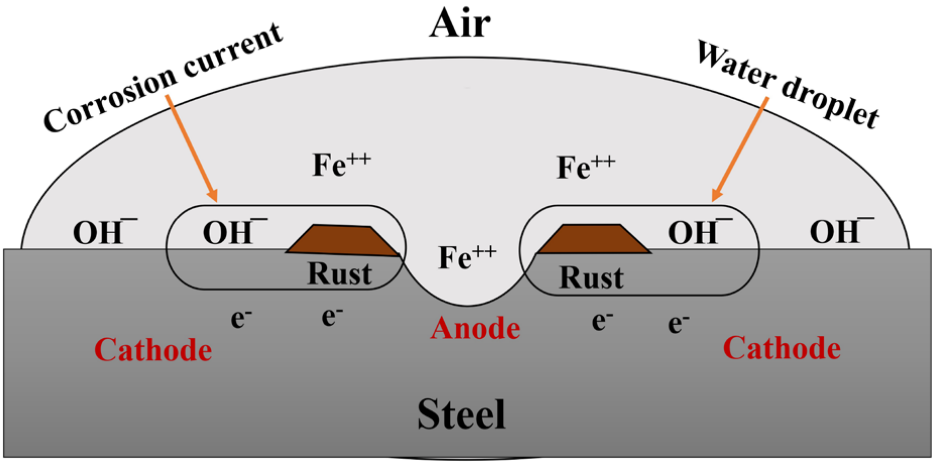

Figure 3.6: Sketch of the corrosion mechanism of steel caused by exposure to water. The anodic and cathodic sites are adjacent, and at the pit's edge, the rust is formed by different oxidized Fe compounds. Adapted from [210] with authorization.

Understanding these fundamental reactions and their kinetics at the nanoscale through molecular modeling might help in proposing inhibitors or even comprehending better the underlying mechanisms of the inhibitors currently used [211]. Some authors have explored these reactions using molecular modeling [123, 149, 202, 204, 205, 212, 213]. Kokalj et al. [190] investigated the adsorption of benzotriazole on Cu_2O and Cu surfaces using DFT, finding that benzotriazole passivates the under-coordinated surface sites, which suffers the corrosion attack. In this case, the adsorption of benzotriazole significantly reduces the metal work function. They also suggested that this effect might potentially result in a reduction of the anodic corrosion reaction, as it is reported in the experiments [190].

To model these processes properly, it is necessary to consider some key aspects, such

as the solvent structure rearrangement due to the dissolution process. Typically, the time scale of these processes is longer than that provided by molecular modeling, especially QM simulations. Some chemical reactions occur on time scales ranging from nanoseconds to milliseconds, while QM simulations are generally limited to tens of hundreds of picoseconds. It is also important to consider the metal-solvent interface, as its characteristics will affect the reactions.

3.2.5 Solvent effects

Solvents play a central role in the corrosion process. Many chemical and physical properties of CI, such as reaction rates, solubility, acidic-basic properties, hydrogen bonds, etc., depend on the solvent media. Thus, it must be considered in CI modeling if one wants to perform simulations as realistically as possible [214]. The most direct way of including the solvent effects is by explicitly adding solvent molecules. Nonetheless, the high computational cost needed for that in QM simulations, not only in terms of the increased number of atoms but also the time scale that should be reached to sample the configurational space satisfactorily (e.g., in MD simulations), is the main reason why the majority of the QM simulations do not explicitly consider solvent molecules. Moreover, when the solvent effects are included in simulations, most of the works only consider pure water, which is not ideal for simulating the actual aqueous solution with electrolytes present in corrosive media. Some authors do go beyond and consider solvents other than pure water [85, 86, 95, 98, 101, 107, 110, 114, 115, 150, 177, 215–221].

A widely used method to include the solvent effect in QM simulations is through continuum/implicit solvent methods, where the solvent is considered a continuum dielectric [222]. This approach can also be used to estimate solvation free energies[2] in chemical reactions [223, 224]. In that manner, quantities such as adsorption energies or descriptors used in MEPTIC/QSAR can be obtained, now including the solvent effects [113, 131, 133,

[2]The solvation free energy estimates the energy involved in taking a solute from a gas phase and inserting it into a liquid/solvated media.

136, 162]. This sort of method, such as the polarizable continuum method (PCM) [225], usually includes only the electrostatic contribution[3] to the solvation energy.

Using this continuum approach to model the solvent, some authors have calculated the adsorption energies of corrosion inhibitors [113, 162]. For instance, Hu et al. [162] investigated the influence of solvent polarity in the adsorption of SAMs on Cu surfaces, incorporating the solvent effects via the COnductor-like Screening MOdel (COSMO) [227]. By simulating various solvents with different polarities, using their respective dielectric constants, they found that the solvent polarity plays a significant role in the formation of dissociated *n*-octadecanethiol (C18S) SAMs compared to the non-dissociated case (C18SH). Their findings indicated that as the solvent polarity increases, the adsorption energy becomes more negative, making the adsorption stronger [162].

Laggoun et al. [113] reported on the adsorption energy of p-toluenesulfonylhydrazide on the Cu surface computed with DFT, including the solvent effects also using COSMO. The authors considered the HCl solution by choosing the dielectric constant accordingly. In that case, all geometries were optimized in the presence of the continuum solvent. They obtained a negative value for the adsorption energy, suggesting that the inhibitor would attach to the surface under the solvation conditions considered.

Some authors compare the inhibitor's solvation free energy with its adsorption energy on a given surface to evaluate if it is likely to be adsorbed on a metallic surface or prefers to be surrounded by the solvent. Gustincic et al. [170], for instance, evaluated that effect using the COSMO model. Although not many details are given, the authors found that the deprotonated forms of the molecules investigated interact more strongly with the solvent (solvation free energies of about -3 eV) than with the surface (adsorption energies of about -2 eV) for the coordinatively saturated site studied. This analysis can provide some initial insights into the solvent effects, and conducting a more comprehensive analysis will allow a deeper understanding of the solvent's role.

Reactivity indices of corrosion inhibitors have also been evaluated under solvent effects

[3] Some continuum solvation models such as the Solvation Model based on Density (SMD) [226] considers dispersion interactions.

via implicit models [98, 103, 110, 113, 115, 116, 184, 228]. For instance, Guo et al. [184] investigated the experimental and theoretical CI performance of thiourea derivatives on carbon steel using COSMO to analyze the solvent effects on some reactive descriptors, such as Fukui indices. The authors found small changes in the charge distribution of the inhibitors compared with the case in vacuum. They concluded that the inhibitors with more negative solvation free energies, i.e., those interacting more strongly with the solvent, will perform worse than those with lower solvation free energies. The solvation free energy trend obtained also follows the adsorption energies trend (computed from MD simulations with classical potentials) for the varying coverages.

Implicit solvent methods could be valuable in understanding the solvent effects on the inhibitor's CI mechanism. Nonetheless, non-electrostatic interactions like the dispersion forces and the explicit interaction between the solvent molecules and the corrosion inhibitor must be included to have a complete description of these effects. In that sense, both QM and MM simulations could describe those effects and interactions. However, to our knowledge, no articles have addressed QM simulations with explicit solvent so far in the CI modeling. Since the computational cost of MM simulations is generally low compared to QM simulations, the inclusion of explicit solvent molecules is commonly reported in works using MM simulations.

For MM simulations, the interactions between the inhibitor, surface, and solvent are typically governed by well-established FF such as the SPC [229], TIP3P, and TIP4P [230] models. Several authors [85, 86, 90, 95, 96, 98, 101, 102, 107, 114, 146, 150, 152, 172, 177, 215–221, 231, 232] reported on MD simulations with classical potentials including explicit water molecules to address some specific aspect of CI. Oukhrib et al. [86], for instance, investigated the CI performance of five pirazolylnucleosides on Cu(111) surfaces in acidic media, using MD with classical potentials, DFT, and Monte Carlo simulations. Their MD results showed that all the molecules adopted a parallel adsorption configuration on the surface. They attributed this adsorption configuration to the enhancement of the bond formation between the inhibitor and the Cu surface due to the electron donation

between the *p*-orbitals from the active sites of the inhibitor to the vacant *d*-orbitals on the Cu surface.

Gao et al. [102] employed weight loss experiments, electrochemical measurements such as electrochemical impedance spectroscopy, and microscope techniques such as atomic force and scanning electron microscopy to evaluate the CI performance of the Papain freeze-dried (PFD) compound. Then, using MD simulations with classical potentials, including 1000 water molecules in the COMPASS FF framework, they proposed that the protonated PFD (PFDH+) can be adsorbed on the Cu(111) surface on a parallel pattern. This parallel adsorption configuration can provide maximum coverage on the surface, protecting the Cu surface from the corrosive media.

The structural features of polyaspartic acid (PASP), polyepoxysuccinic acid (PESA), oxidized starch (OS), and carboxymethyl cellulose (CMC) inhibitors for $CaCO_3$ and $CaSO_4$ were evaluated by Chen et al. [89] using MD simulations with classical potentials and analyzing the coordinates through radial distribution function. The radial distribution functions showed peaks below 3 Å, which represents ionic bonds (chemisorption) between the inhibitor and the surface. When the solvent was included in the simulations, the peak intensity for the radial distribution function decreased. This showed that the water molecules weaken the interaction between the inhibitor and the surface.

As one can see, including the solvent effects is challenging, as a cost-effective and accurate method is needed. A purely QM approach is too computationally expensive, while a purely MM approach might not be accurate enough to account for all the occurring phenomena. To overcome this problem, one can use a hybrid methodology that combines the low computational effort of MM and the high accuracy of QM, the so-called Quantum Mechanics/Molecular Mechanics (QM/MM) method. In that case, the system is split into two subsystems: one described with QM and the rest with MM. The solvent atoms, usually comprising a large number of atoms, can be included in the MM subsystem. The QM system is chosen to be the part of the system that requires a higher accuracy (e.g., where the charge transfer occurs). With that, fewer atoms are considered in the QM subsystem,

which is the most computationally expensive. Thus, larger time scales, as well as a realistic amount of atoms, can be reached. This method is widely applied in biological systems and the area of biosensors [37–44]. However, it is yet to be explored in the context of CI.

3.2.6 Electrodes' potential effects

The last aspect we highlight when investigating the corrosion process is the electrodes' potential effect. Including the electrode potential is essential to describe the electrochemical reactions that take place during the CI process. Moreover, the electrode potential also affects the adsorption of the inhibitor, changing its alignment with the surface. This could change the inhibitor's ability to bond to the metallic surface and the inhibitor-inhibitor interactions that lead to the formation of the subsequent layers adsorbed on the material [211].

When the voltage is applied to metallic electrodes (the working and the reference electrodes in a typical electrochemical cell), we observe the charging of the metal and, consequently, the formation of an electric field between the electrodes, which will induce polarization in the system. The inhibitor's charge distribution will be affected by this polarization, inducing its accumulation and depletion in certain areas. This induced charge distribution has an impact on the structure of the system's EDL, which remains a challenging aspect to characterize correctly in molecular modeling.

Different methodologies are available in the literature for including the electrode's potential in molecular modeling. These approaches involve changing the charges of the electrodes by adding or removing electrons, introducing constant electrical potentials, employing Grand Canonical formulations, or shifting the chemical potential of the electrodes. However, each of these methods comes with some challenges and limitations, which we will discuss in the following [233, 234].

In MM simulations, a common approach to account for the electrode potential involves modeling the induced charges on the metal atoms by external charges in the electrolyte. Gaussian functions centered on the surface atoms represent the induced charge density on

the metal surface atoms. Then, the induced charges are evolved at each simulation step using an extended Lagrangian technique [235, 236]. In that way, the MM simulation can account for the charge in the slab, allowing us to evaluate the response of the electrolyte under those conditions. This approach is able to model applied external voltage differences between different electrodes [237]. It can qualitatively predict the structure of water monolayers on different metal substrates (Cu, Ni, Ag, and Pt) when compared with experiments. However, some adjustments or generalizations are necessary when dealing, for example, with the presence of adsorbates on the surface, or the reconstruction of the metal surface induced by the voltage [237–241].

Reed et al. [241] proposed a similar methodology that uses variable charges to introduce the applied voltage. The model, based on the Siepmann et al. [237] formulation, adjusts the magnitudes of the variable charges on each step of the MD simulation with classical potentials using a variational procedure to keep the potential constant. It has been applied to describe the interfacial structure between two ionic liquids conformed by binary mixtures of molten salts, accurately reproducing the charge distribution within the electrode.

Petersen et al. [238] developed an efficient approach where the electrode polarization by the electrolyte is considered using the image charges method. In this method, the net fluctuating charge is distributed on the surface atoms of each electrode, and an additional charge is added to maintain constant the potential difference. This approach has been applied within the Marcus Theory framework to determine the probability for oxidation and reduction of reactants.

As one recent application of these methodologies, Zhang et al. [240] performed MD simulations with classical potentials of water at electrified graphene interfaces to analyze its structuring, dynamics, and spectroscopic properties. They found that the applied voltage in the simulations dramatically affects the structure and dynamics of water, where positive voltages slow down water's reorientation and translational dynamics. In contrast, an increasingly negative voltage first accelerates the interfacial water dynamics before be-

ing reduced at large negative voltages. They attributed these dynamics to the hydrogen bond exchange.

While all these methodologies offer important insights into the effect of the electrode's potential, the use of empirical models restricts the scope of the results. Ideally, using QM approaches would provide a more accurate understanding of these effects. One of the first attempts to describe the electrodes' potential effects using QM simulations was done by Taylor et al. [242] and Filhol et al. [243] introducing a net surface charge density in the electrodes and maintaining the charge neutrality in the electrochemical cell with a background charge. The induced electric field due to the charged surface at the interface leads to a potential drop in the system, which can be quantified by comparing the Fermi level of the system with a reference electrode far from the interface. This method is called double reference in the corrosion literature. Some other works [244, 245] applied DFT calculations with *a posteriori* corrections to introduce the thermodynamics effects due to the applied voltage. In this last case, even if their findings could be useful to elaborate catalytic mechanisms, the effects of the induced electric field at the interface are still missing [246].

The electrodes' potential effects have also been included in QM methodologies that consider an implicit solvent model. In this regard, Bonnet et al. [247] included the voltage through an external potentiostat added to the system. The electronic charge at the metallic surface was controlled by varying the solvent dielectric constant, as proposed by Otani et al. [248]. Grand canonical approaches are also reported in the literature to include the voltage in the simulations [249–252]. Within these approaches, a remarkable example was carried out by Deißenbeck et al. [251], where a thermopotentiostat approach was developed to compute the dielectric constant of nanoconfined water at constant temperature and electrode potential. Their findings agreed with the experimental observed anisotropic dielectric response in nanoconfined water.

A recent work from Goldsmith et al. [246] investigated the effect of the applied voltage on water-gold interfaces using QM simulations. They used a hybrid explicit-implicit ap-

proach to describe the solvent and fixed charges on the Au surface to modulate the electrode potential. Their results showed that the applied voltage affects the structural properties of water and its orientation. Their results suggested that the water forms at least one structural layer with a higher density than bulk water adjacent to the Au(111) electrode.

One method that can explicitly account for the electrodes' potential is the non-equilibrium Green's functions (NEGF) formalism. In this approach, an open system is considered, and the electrodes can be kept under different chemical potentials. An electric field is naturally established in the system, and the charge accumulation/depletion on the metallic atoms is fully described. Pedroza et al. [233] have recently applied the NEGF approach to investigate the dynamics of a single water molecule under a voltage applied to Au electrodes, as depicted in Figure 3.7. Their findings showed that the water molecule tends to align its dipole moment with the generated electric field in the device. Depending on the sign and magnitude of the applied voltage, either the molecule is attracted or repelled in an asymmetric trend.

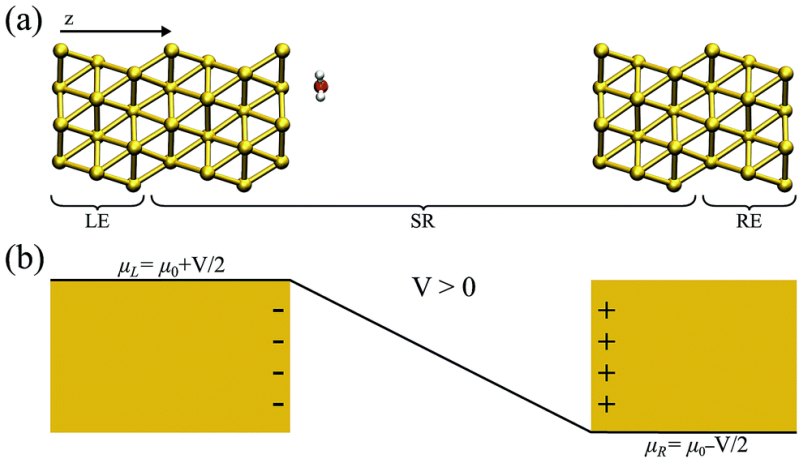

Figure 3.7: (a) A diagram illustrating the metal-water system studied via the non-equilibrium Green's functions formalism employed by Pedroza et al. [233]. The left (LE) and right (RE) electrodes, as well as the scattering region (SR), are denoted. (b) a sketch illustrating the effect of a positive voltage on a parallel plate capacitor. The accumulated charge in each plate, as well as the voltage ramp, are shown. Adapted from [233] with authorization.

Later, Ordejón et al. [253] extended Pedroza et al.'s work to liquid water by considering Au electrodes in contact with 40 water molecules, demonstrating the feasibility of the

method to describe solid-water electrified interfaces. The NEGF can provide a realistic picture of the electrified solid-liquid interfaces, but the computational cost can become prohibitive. A full description of the system (solvent molecules, counter-ions, electrodes, and inhibitors) could require hundreds to thousands of atoms. Multiscale approaches like the QM/MM methods could also overcome those limitations [254]. However, those methods are yet to be applied in the context of CI.

As discussed in the introduction to the advanced simulation of corrosion inhibition it is vital that processes A4-A6 are included in simulations and a major contribution of this review is to highlight methods and strategies to do so. As outlined in section 3.4 the effect of anodic and cathodic zones is critical as it determines the nature of surface charge, surface potential, and the efficiency and nature of inhibitor adsorption. However, the effect of such zones cannot be properly simulated without simulation of both solvent effects (A5) and potential effects (A6). In section 3.5 we review papers that outline how solvent effects may both affect the competition between inhibitor solvation and surface absorption and also the strength of such absorption. The section also outlines the complexity of modeling the solvent effects and the relative advantages of QM and MM methods highlighting the need particularly for MM simulations of selecting appropriate modeling structures and in particular FFs. Section 3.6 highlighted that potential effects can affect the adsorption and alignment of the inhibitor on the metal surface but also the formation of subsequent inhibitor layers. A variety of approaches are outlined but many of these methods have limitations and cannot freely evolve, an emerging approach using NEGF formalism is presented that does permit charges to freely re-arrange. Thus, the review highlights how these complex processes can be integrated into the simulation of corrosion inhibition.

In conclusion, a critical review of the main approaches used in corrosion inhibition (CI) modeling was presented, focusing on gaps found in the literature that need to be addressed to perform more realistic simulations. We highlight six important aspects (A) that a model might consider in order to describe the CI process realistically: (A1) the electronic properties of the isolated inhibitors, (A2) the interaction of the inhibitor with the

surface, (A3) the surface model, (A4) the effect of anodic and cathodic zones on the surface, (A5) the solvent effects, and (A6) the electrodes' potential effects and how it shapes the inhibitor-inhibitor interactions and the monolayer and subsequent inhibitor layers. In this sense, we found that A1-A3 are regularly considered in the reported CI simulation literature, while A4-A6, as well as some more complex surface models in A3, are not.

Most of the CI modeling reported in the literature is mainly intended to support experimental observations. The most common approach for these works is to cover A1 and correlate these properties with experimental CI performance using several correlation techniques. However, the lack of interaction with the surface might not accurately describe the CI processes. To overcome that, some works include explicit interaction between the inhibitor and the surface, using either bare metallic or more complex oxidized surface models, thus addressing A2-A3. The more complete surface models allow us to better represent the interactions between the inhibitor and the surface but also increase the simulation's complexity and computational cost, restricting their use in CI modeling.

As for the solvent effects, the most common approach found was the implicit solvent models, whether the inhibitor is investigated isolated or adsorbed on the surface. The implicit methods can provide a good insight into the solvation process, but they do not consider the explicit interaction between the solvent molecules, inhibitor, and the surface, which is important for the CI process since the inhibitor has to remove some solvent molecules from the interface to get adsorbed on the surface. Explicit solvent methods fit better for this adsorption process, but it makes QM modeling too expensive. In MM methods, such as the MD simulations with classical potentials, the inclusion of explicit water molecules is more common.

Lastly, in terms of the electrodes' potential effects, which are essential to describe the induced surface charges, the polarization of the solvent and electrolytes, as well as the inhibitor-inhibitor interaction to form monolayers and subsequent layers, the reported methods available in the literature usually control the voltage by adding charges to the metallic atoms or using Gran Canonical approaches. In this regard, the non-equilibrium

Green's functions (NEGF) formalism promises to provide an alternative to those approaches, allowing for controlling the voltage explicitly in the simulations, as it is usually done in experiments. However, those methods are yet to be applied in CI modeling.

In summary, a realistic model to describe the CI process should consider the aforementioned A1-A6 key aspects. Including all these effects will lead to a more detailed description of the CI process from the atomistic point of view, which will be determinant in designing corrosion inhibitors. Some of the results that can be obtained from these simulations might be used to feed artificial intelligence (AI) methods and multiscale models to construct the bridge between the nanoscale CI modeling and the continuum scale of the CI processes.

Section 4

MBI adsorption on Cu surface

The adsorption of corrosion inhibitors on the metal surface is one of the critical steps during the CI process. The inhibitors can bind to the surface, interact with other inhibitor molecules, and form layers that cover and protect the surface. These layering formations can also be affected by the different cathodic and anodic zones in the material. Therefore, this chapter investigates the adsorption of 2-mercaptobenzoimidazole (MBI) on the Cu surface under different surface coverage and applied electrode potentials.

MBI is one of the most promising and efficient corrosion inhibitors for Cu, and its use is extensively reported in the literature [255, 256]. However, MBI's inhibition mechanisms are poorly understood and mostly studied via experiments without a detailed examination at the atomistic level. In this work, the strength of the interaction between the MBI and the Cu surface was evaluated in terms of the adsorption energy (E_{ads}), and the nature of the bonding through the electronic structure, evaluated using the density of states (DOS) and the induced charge density (ρ_{ind}) after adsorption. This first model was chosen to investigate the effect of the electrode potential on MBI adsorption independently of the

solvent, and the following chapter describes the cases where both the solvent and electrode potential effects are considered.

4.1 Computational details

Structural optimizations and electronic structure calculations were performed using the DFT formalism, with the SIESTA package [22–24]. The PBE (Perdew-Burke-Ernzerhof) functional [31] was chosen to treat the electron exchange and correlation terms within the generalized gradient approximation (GGA). The electron-core interaction was simulated using Troullier-Martins pseudopotentials in the *psf* format for all chemical species [257]. An optimized DZP (double-ζ plus polarization) basis set was used to describe both the Cu(111) surface and MBI molecule.

The Cu lattice constant was obtained by minimizing the energy of the Cu primitive cell, using a 20×20×20 k-point mesh to sample the Brillouin zone and a 550 Ry mesh cut-off for the real-space grid. A lattice parameter of 2.60 Å was obtained for the optimized Cu primitive cell, which corresponds to 3.67 Å for the Cu conventional cell, in good agreement with the experimental value of 3.62 Å [258], and theoretical results using plane-waves (PW) methods of 3.64 Å [167]. From this optimized primitive cell, the Cu(111) surface models were created using 5 Cu atomic layers, where the two outermost ones were allowed to relax. In contrast, the remaining three bottom layers were kept frozen. The conjugated gradient method was used to relax the atomic positions and lattice vectors for all the structural optimizations.

The surface models investigated were the hexagonal (3×3) and orthorrombic $\left(\begin{smallmatrix} 2 & 3 \\ 2 & -3 \end{smallmatrix}\right)$. The hexagonal surface is formed by five Cu atomic layers, with nine Cu atoms per layer. The lattice constants of the hexagonal slab were $a = 7.785$ Å, $b = 7.785$ Å, and $c = 30.475$ Å. On the other hand, the orthorrombic $\left(\begin{smallmatrix} 2 & 3 \\ 2 & -3 \end{smallmatrix}\right)$ is formed by the same number of Cu layers, with 12 atoms per layer. The combination of different slab shapes and sizes with the number of adsorbed molecules on the surface allowed us to model several coverages,

ranging from low ($\approx$ 1.43 $molecules/nm^2$) to high ($\approx$ 3.7 $molecules/nm^2$) coverage cases. Similar surfaces are reported in the literature [167], and their results were compared with those obtained in this work. The lattice vectors of each surface were kept constant as determined by the Cu bulk lattice constant, allowing only the optimization of the atomic positions. In the structural optimizations, atomic forces below 0.01 $eV/Å^2$ were considered converged. The Brillouin zone of each surface was sampled with a k-mesh grid 6×6×1 for the 3×3 surface, and 3×3×1 for the orthorhombic one. A low electronic temperature of 5 K was specified for the Fermi-Dirac function to account for the occupation of the electronic states. During the adsorption of the molecules on the surface, the van der Waals interactions were described using the D2 Grimme's parametrization [32].

In order to compare our results for the $\begin{pmatrix} 2 & 3 \\ 2 & -3 \end{pmatrix}$ slab and the ones reported in the literature [167], calculations were also performed for the coverage case of 1.43 $molecules/nm^2$, using the Vienna ab-initio simulation package (VASP) [259] which uses the projector-augmented waves (PAW) potentials to describe the inner electrons [260]. PBE-PAW was used as the exchange-correlation functional, and the van der Waals interactions were also considered through the D2 Grimme's dispersion model [32]. An energy cut-off of 540 eV was used to guarantee the accuracy of the calculations. Structural optimizations were performed through a conjugated gradient algorithm until atomic forces in each atom were smaller than 0.01 $eV/Å$. A k-mesh of 6×6×2 was employed for the structural optimization and electronic structure calculations.

The molecular adsorption is considered according to the following equation:

$$nMBI + Cu \rightarrow Cu(MBI)_n, \tag{4.1}$$

where n is the number of adsorbed MBI on the surface, MBI is the isolated molecule, Cu the Cu slab, and $Cu(MBI)_n$ the MBI-Cu adsorbed system. The adsorption energy (E_{ads}) is calculated as follows:

$$E_{ads} = E_{Cu(MBI)_n} - nE_{MBI} - E_{Cu}, \tag{4.2}$$

where $E_{Cu(MBI)_n}$ is the energy of MBI bonded to the Cu surface, nE_{MBI} the energy of the n isolated molecules, and E_{Cu} the energy of the Cu surface. From this definition, the lower (more negative) the E_{ads}, the higher the adsorption stability on the surface. To compare the E_{ads} at different coverages on the surface, E_{ads} was normalized per unit area as follows: $E_{ads,norm} = E_{ads}/A$, where E_{ads} is the previous calculated adsorption energy (Equation 4.2), and A the surface area.

To analyze the change in the charge distribution due to the adsorption, the induced charge density was calculated as follows:

$$\rho_{ind}(\vec{r}) = \rho_{mol+surface}(\vec{r}) - \rho_{surface}(\vec{r}) - \rho_{mol}(\vec{r}), \tag{4.3}$$

where $\rho_{mol+surface}(\vec{r})$ represents the self-consistent charge density of the whole system, and $\rho_{surface}(\vec{r})$ and $\rho_{mol}(\vec{r})$ are the charge density of the isolated surface and molecule, respectively, calculated using the same geometry as for the bonded system. Positive (negative) $\rho_{ind}(\vec{r})$ indicates electron excess (deficit) after the adsorption.

The total and projected density of states (DOS and pDOS, respectively) were calculated for all the systems. The same k-mesh used for the structural optimizations was employed for the (DOS and pDOS) calculations, with a smearing of 0.05 eV. The total DOS ($PDOS_m(\epsilon)$) was projected on each of the MBI molecular orbitals to analyze which orbitals are taking part in the bonding with the Cu surface atoms, which is calculated as follows:

$$PDOS_m(\epsilon) = \sum_{n,k} |\langle \Psi_{n,k} | \Psi_m^{molecule} \rangle| \delta(\epsilon - \epsilon_{n,k}), \tag{4.4}$$

where n, k and $\epsilon_{n,k}$ are the band index, wave vector, and band energies of the molecule adsorbed on the surface.

Electrode potential effects

Once the most stable adsorption modes were determined, the NEGF formalism, as implemented in TranSIESTA [33, 34], was used to include the effect of the electrode potential

in the system. The slab used to create the system setup is shown in Figure 4.1. As is highlighted in the figure, the system is divided into three regions: 1) left electrode, 2) contact region, and 3) right electrode. In the NEGF formalism, the electrodes are considered semi-infinite structures that extend to the semi-infinite direction and are attached to the contact region. The lattice parameters of the electrode are a = 8.989 Å, b = 7.785 Å, and c = 6.357 Å.

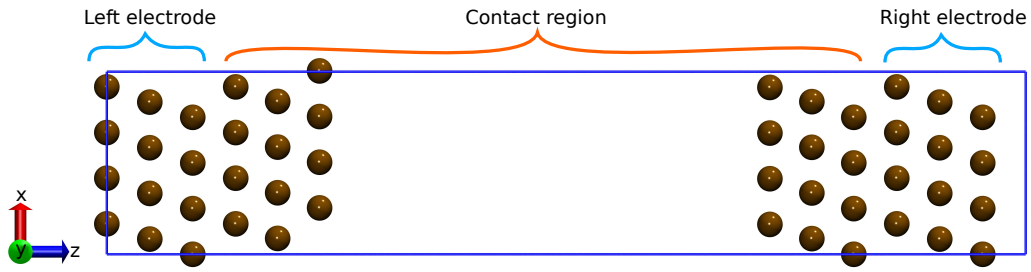

Figure 4.1: system setup for TranSIESTA calculations, using the $\begin{pmatrix} 2 & 3 \\ 2 & -3 \end{pmatrix}$ surface as example.

The electrode calculations were performed at the same level of theory (exchange-correlation functional, pseudopotentials, and optimized basis set) as the MBI adsorption simulation, but using a Brillouin zone with a k-mesh of 3×3×50, and the selected mesh cut-off was 400 Ry. The contact region is formed by six layers of Cu, with the molecule attached to the system's left part. The lattice vectors of the system are a = 8.989 Å, b = 7.785 Å, and c = 45.308 Å, with a distance of 22 Å between the Cu surfaces.

The effect of the voltage was evaluated by doing single point calculations at different voltages, ranging from 1.0 V to -1.0 V, with a step of 0.5 V, using the optimized structure at 0 V. The Brillouin zone was sampled with a k-mesh of 3×3×1. The density matrix (DM) and Hamiltonian matrix elements tolerance were fixed to 10^{-6} and 10^{-3}, respectively. The DOS for all the cases under a voltage was calculated using the TBtrans code, available in SIESTA as follows:

$$DOS(E) = -\frac{1}{\pi N} \sum_{\nu \in \text{atom/orbital}} \Im \mathbf{G}_{\nu\nu}(E), \tag{4.5}$$

where N is the normalization constant, and $\mathbf{G}$ is the Green's function.

The difference in the charge density ($\Delta\rho$) between the calculations at finite voltage and 0 V was calculated to analyze the effect of the voltage in the electronic structure, as follows:

$$\Delta\rho = \rho_V - \rho_{V=0}, \tag{4.6}$$

where ρ_V is the charge density at finite voltage, and $\rho_{V=0}$ is the charge density at 0 V.

Optimization of the basis set

The optimization of the basis set represents an important initial step in MBI adsorption, improving both transferability (the ability to use the basis set in different chemical environments) and quality (accurate representation of the system, e.g., bond distances, electronic structure, adsorption energies, etc.). This was the first step in the MBI adsorption process. For Cu, the basis set used here was previously optimized by Garcia-Gil et al. [261], comprising two floating orbitals added to the standard DZP basis distribution. However, its use can be problematic when adsorbing molecules on the surface due to the relaxation of the atomic positions and the high computational cost. Therefore, from their basis set, the best option for our system was the basis set with an extra *s* shell as a diffuse orbital to the DZP basis. This extra layer of diffuse orbitals for the outermost Cu atoms considerably improves the surface energies and the wave function decay shape, with a small extra cost in the simulation. For Cu, an extra 5*s* orbital was added, with a cut-off radius of 7 *bohr* [261].

For the MBI atoms, a basis set previously reported in the group was the initial basis set used for the optimization process, which will be called the original or non-optimized one. The basis set optimization was performed using the SIMPLEX method [23], which is a minimization method implemented in SIESTA. The cut-off radius, soft confinement potential, ionic charge, and split norm parameters were optimized variationally for each element to obtain the best basis set (in terms of the lowest total energy), using the param-

eters of the non-optimized basis set as a starting point. The optimization was performed with the MBI molecule isolated in the thione form, using its relaxed structure. The isolated molecule was simulated using a cubic cell, with lattice parameters of $a = b = c = 30\,\text{Å}$, at Γ-point. The basis pressure was set to 0 GPa for the optimization process, and the selected mesh cut-off and density matrix tolerance were 400 Ry and 10^{-5}, respectively.

In the optimization process, the basis set parameters were calculated independently, one at a time, keeping the remaining constant with the previous optimized basis set parameters. All the optimizations were performed using the PBE functional [31] and the same Troullier-Martins pseudopotentials [257]. The parameters of the original (non-optimized) and optimized basis set are shown in Table 4.1.

Table 4.1: Parameters of the original and optimized basis set for Cu, Cu outermost layer, C, N, S, and H. r_c is the cut-off radius of each orbital. V_0 and r_i are the parameters for the soft confinement [261]. For the optimized basis set, the optimal split norm parameters of H, C, and N are 0.20000, 0.19558 and 0.18658, respectively. For the optimized S basis set, the split norm parameters are 0.90000 and 0.80000 for the $3s$ and $3p$ orbitals. In the case of the original basis set, the split norm parameters are only specified for the S. The split norm parameters are 0.80000 for both $3s$ and $3p$ orbitals.

					r_C *(bohr)*				V_0 *(Ry)*			r_i *(bohr)*		
	Basis	***Charge (e)***	***1s (1ζ)***	***1s (2ζ)***	***2p (1ζ)***			***s***	***p***	***d***	***s***	***p***	***d***
H	Original DZP	0.46527	4.20357	1.84463	3.52816			99.93138	24.56504	-	2.59932	2.20231	-
	Opt DZP	0.50000	7.00000	0.00000	3.67026			99.50895	47.08569	-	4.565574	0.00000	-
		Charge (e)	***2s (1ζ)***	***2s (2ζ)***	***2p (1ζ)***	***2p (2ζ)***	***2d (1ζ)***						
C	Original DZP	0.35201	5.43077	3.08484	6.83094	3.01366	5.04748	50.37145	13.53326	110.78225	5.22551	6.81234	0.01065
	Opt. DZP	0.24997	7.00000	0.00000	7.00000	0.00000	5.04300	34.14928	29.85023	109.65393	7.00000	6.75460	0.00000
N	Original DZP	0.35201	5.43077	3.08484	6.83094	3.01366	5.04748	50.37145	13.53326	110.78225	5.22551	6.81234	0.01065
	Opt. DZP	0.09625	6.38524	0.00000	6.98866	0.00000	5.14567	49.40746	15.94584	117.07696	5.88648	6.91714	0.01325
		Charge (e)	***3s (1ζ)***	***3s (2ζ)***	***3p (1ζ)***	***3p (2ζ)***	***3d (1ζ); 4p (1ζ)***						
S	Original DZP	-	5.35938	0.00000	6.48147	0.00000	5.57655, 6.51209	-	-	-	-	-	-
	Opt. DZP	0.20000	5.35937	0.00000	6.48146	0.00000	5.57654, 6.51209	0.00000	3p: 9.53000 4p: 102.65000	147.06000	3.07000	3p: 7.00000 4p: 6.06000	6.70000
		Charge (e)	***4s (1ζ)***	***4s (2ζ)***	***3d (1ζ)***	***3d (2ζ)***	***4p (1ζ); 5s (1ζ)***						
Cu	Opt. DZP	0.07400	5.77000	2.19000	5.21000	2.92000	5.49000,-	19.00000	5.10000	5.20000	1.94000	0.26000	2.80000
Cu outermost layer	Opt. DZP	0.07400	5.77000	2.19000	5.21000	2.92000	5.49000, 7.00000	19.00000	5.10000	5.20000	1.94000	0.26000	2.80000

The most significant difference between the non-optimized and optimized basis sets is in the cut-off radius, which are larger for the optimized basis set than the non-optimized. The larger values improve the quality of the basis set but also increase the computational cost. Generally, a rule-of-thumb is to avoid using cut-off radii that are too large or too small for the orbitals. Small cut-off radii lead to a less transferable basis set, with very short orbitals for light elements, inner orbitals or cations [262].

The SIESTA total energy was calculated for the isolated MBI molecule using both non-optimized and optimized basis sets, as well as the SIESTA DZP default. The total energies obtained are shown in Table 4.2. Compared with the standard DZP, the total energies for the original and optimized basis set are more stable by approximately -4 eV. This stabilization in the total energy indicates the excellent quality of the original and the optimized basis sets. The original basis set was optimized previously for organic systems, which is why it performs well in the MBI description.

Table 4.2: Comparison between the SIESTA total energies obtained by the different basis set for the isolated MBI. All the calculations were performed using the PBE as the exchange correlation functional and a mesh cut off of 400 Ry. The basis pressure was set up to 0 GPa.

Basis set	Total energy (eV)
Standard DZP	-2040.448
Original DZP	-2043.814
Opt. DZP	-2044.075

The optimized basis set shows an improvement in the total energy of approximately -0.3 eV compared to the original basis. As mentioned before, the improvement is due to the larger cut-off radii of the orbitals. Thus, the optimized basis set was used for all the calculations presented below.

4.2 Adsorption stability

Firstly, the stability of MBI was evaluated in terms of the relative energy between the tautomers at the same level of theory used in the literature (PBE-D2), finding that the

thione form is more stable than the thiol one by -0.6 *eV* (-13.9 *kcal/mol*). This finding agrees with the results reported in the literature [167]. Then, different initial adsorption sites were sampled on the Cu surface as shown in Figure 4.2. The sites were labeled according to their local symmetry: a top position on the top of one exposed Cu surface atom, a bridge position between two adjacent surface atoms, and two hollow sites, and a two-bonded position depending on the symmetry of the adsorption site.

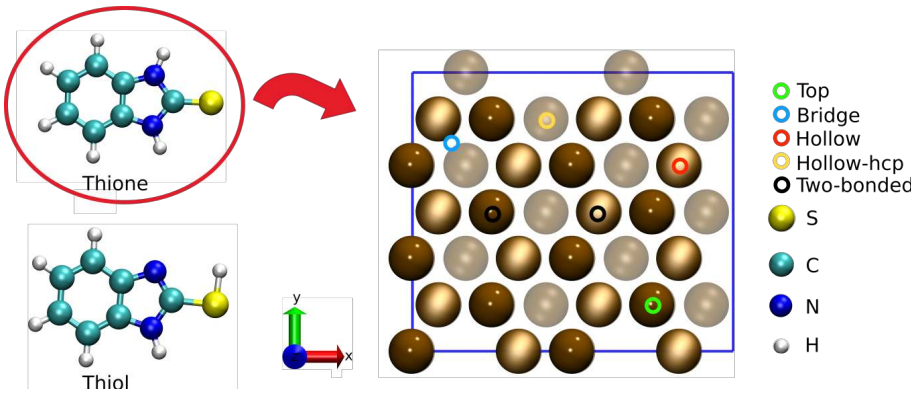

Figure 4.2: Different MBI adsorption sites at Cu surface. The left part of the sketch shows the MBI molecule in its two forms: thione and thiol. Due to its higher stability, the thione form was adsorbed on the Cu surface. Green, yellow, red, and blue open circles represent a top, bridge, hollow positions, and a two-bonded case. Ochre-coloured spheres represent the Cu atoms, and the lighter ochre colour spheres represent the second and third outermost Cu layers.

Different coverage scenarios were considered to investigate the adsorption of MBI on the Cu surface. The first scenario was a low-coverage case, with only one MBI molecule interacting with the Cu surface, in the $\begin{pmatrix} 2 & 3 \\ 2 & -3 \end{pmatrix}$ slab. Several initial configurations were considered, and the three most stable adsorption modes were identified. These modes include a parallel configuration where the molecule lies almost parallel on the surface, a two-bonded case where the molecule is bonded to the surface through the S and NH groups, and a vertical configuration in a hollow position on the surface, with the inhibitor bonded through the S atom. An intermediate coverage was also considered using the MBI molecule in the 3×3 slab, and, finally, the SAM coverage cases, with two MBI molecules adsorbed on both surface slabs. These three scenarios allowed us to understand how the coverage affects the interaction between the inhibitor and the Cu surface. The optimized

structures for these adsorption cases are shown in Figure 4.3.

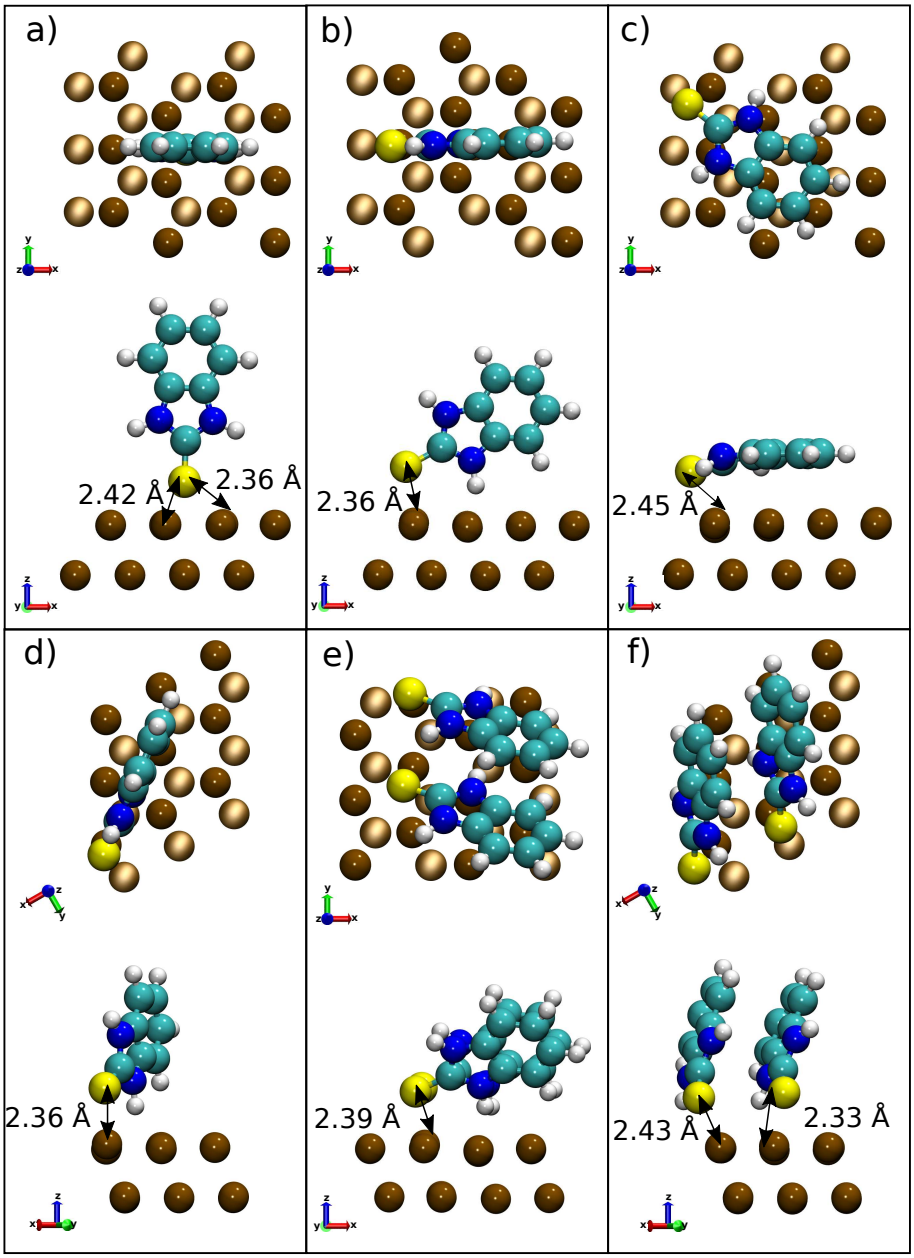

Figure 4.3: Top (above) and side (below) view for the final adsorption structures of MBI on the Cu surface for: a) hollow-$\begin{pmatrix} 2 & 3 \\ 2 & -3 \end{pmatrix}$, (b) two-bonded-$\begin{pmatrix} 2 & 3 \\ 2 & -3 \end{pmatrix}$, (c) parallel-$\begin{pmatrix} 2 & 3 \\ 2 & -3 \end{pmatrix}$, (d) two-bonded-3×3, (e) SAM-3×3, and (f) SAM-$\begin{pmatrix} 2 & 3 \\ 2 & -3 \end{pmatrix}$ cases. White, cyan, yellow, blue, and ochre-colored spheres represent H, C, S, N, and Cu atoms. Lighter color spheres on the top view of each case represent the second outermost Cu layer. The nearest distances between the adsorbed MBI and the Cu surface is shown in the side views. The three innermost Cu layers are suppressed for clarity.

Table 4.3 presents the E_{ads} computed using varying methodologies, along with the results reported in the literature. Comparing their adsorption energies, calculated as shown

in Equation 4.2, we found the parallel case, followed by the two-bonded and hollow cases as the most stable ones on the Cu $\begin{pmatrix} 2 & 3 \\ 2 & -3 \end{pmatrix}$ slab. This trend appears to deviate from the findings reported in the literature [167], which indicated that the most stable adsorption configuration is the two-bonded configuration, followed by the hollow configuration. Additionally, the results reported suggest that the energies of the two-bonded and hollow configurations are within a similar range. In order to further explore this discrepancy, we performed the simulations using the PW methodology implemented in the VASP code [259], which is the same computational code used in [167], at the same level of theory than our SIESTA calculation and the reported one in [167]. The adsorption configurations were recalculated, and the resulting adsorption energies are also presented in Table 4.3. As one can see in Table 4.3, the results found in this work using VASP are also in disagreement with [167].

Table 4.3: E_{ads} as a function of the MBI coverage. The $E_{ads,norm}$ are normalized with respect to the number of MBI adsorbed and surface area (nm^2).

Case	coverage [$molecules/nm^2$]	Surface area [nm^2]	E_{ads} [eV]	$E_{ads,norm}$ [eV/nm^2]	$E_{ads,\,VASP}$ [eV] (reported in [167])	$E_{ads,\,VASP}$ [eV] (This work)
a	1.4	0.70	-0.80	-1.14	-0.76	-0.83
b	1.4	0.70	-1.67	-2.39	-1.37	-0.86
c	1.4	0.70	-2.33	-3.33	-1.87	-0.77
d	1.9	0.52	-1.73	-3.29	-	-
e	2.9	0.70	-1.99	-5.67	-	-
f	3.8	0.52	-2.01	-7.64	-	-

The stability trend on the surface can be explained in terms of the interactions between the MBI and the Cu(111) surface. The interactions between the π orbitals of the aromatic ring and the $3d$ orbitals from the Cu surface atoms are maximized for the parallel structure, which stabilizes the system. Several other works using similar systems reported the parallel adsorption as the most stable one, using DFT or classical potentials [15]. We are, thus, surprised that the results from [167] do not report the parallel adsorption mode as the most stable one. Besides, we found that the stability trend for our calculations was the same in both SIESTA and VASP results, and we cannot find an explanation for the discrepancy between our VASP results and those reported in [167].

In the two-bonded case, the interactions are mainly between the S and NH-group from the MBI and the Cu surface atoms. In this case, the π orbitals of the aromatic ring do

not play an essential role in the adsorption process since the lateral distance between the periodic MBI is too high, not enabling the interactions between molecules and the possible SAM formation. In the hollow case, the primary interaction is between the S and Cu atoms, and the lateral interactions among MBI molecules are also irrelevant due to the distance between periodic images. Also, since only one bond is formed with the surface, the hollow case is expected to be the least stable.

For the higher coverage cases, to better compare the results between the different surface slabs, E_{ads} was normalized for the surface area ($E_{ads,norm}$). The variation of $E_{ads,norm}$ with the MBI coverage is shown in Figure 4.4, and it is also reported in Table 4.3. The previous E_{ads} for the low-coverage cases are also presented for comparison. In Figure 4.4, the cases a-d only consider the adsorption of one MBI on the Cu surface, while e and f represent the adsorption of two MBI molecules in a SAM configuration.

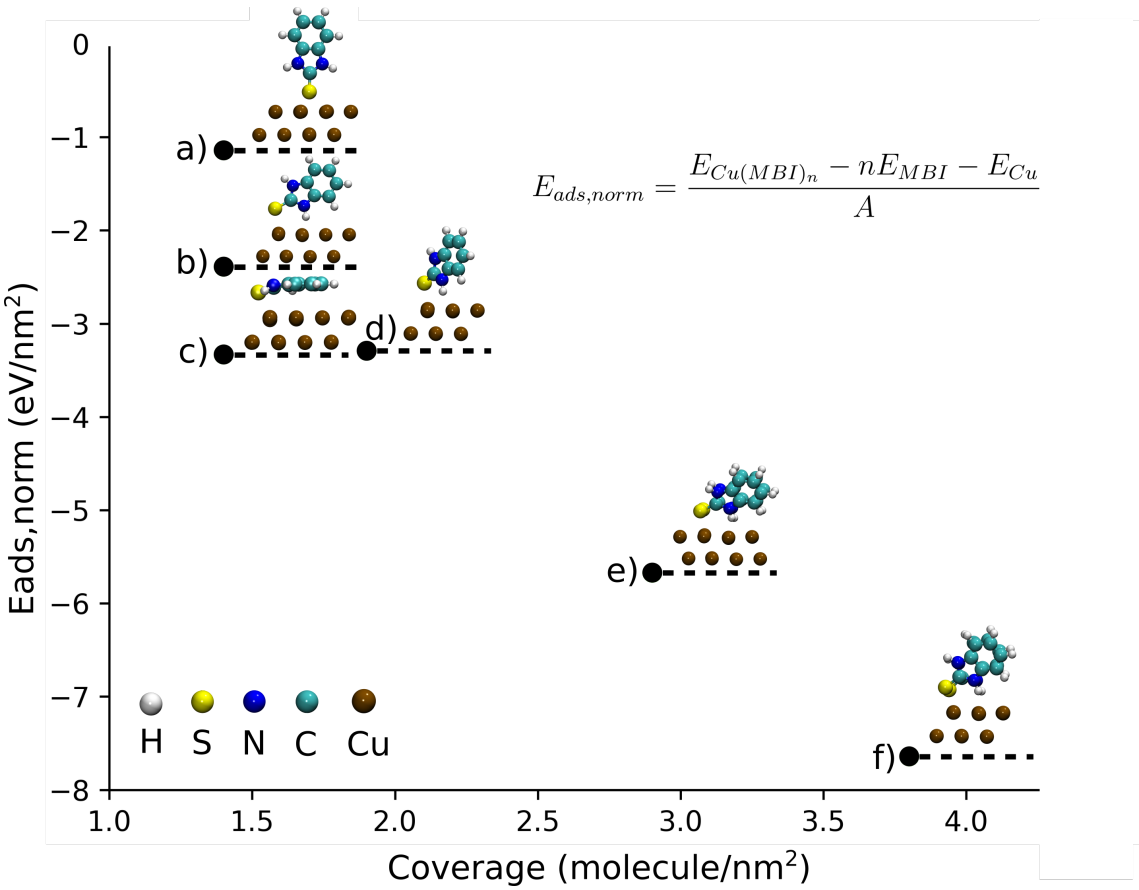

Figure 4.4: Normalized adsorption energies ($E_{ads,norm}$) of MBI on Cu(111) surface as a function of molecular density. The cases (a,b,c,e) belong to the Cu $\begin{pmatrix} 2 & 3 \\ 2 & -3 \end{pmatrix}$ slab, while cases (d) and (f) to the Cu 3×3 slab.

As it can be seen in Figure 4.4, the higher the coverage on the surface, the lower the $E_{ads,norm}$ (more negative), thus stabilizing the system. The lateral π-π interaction between the molecules can explain the stabilization observed for higher coverages, which is enhanced due to the shorter distances between the MBI molecules. The stabilization trend is consistent with the results reported in the literature, where the adsorption energy became more stable with the increasing coverage on the surface [167].

However, in the two-bonded-3×3 case, the more negative $E_{ads,norm}$ is just an effect of the smaller area in this slab compared to the one in the two-bonded case, and not representing an stabilization of the system because of the lateral $\pi - \pi$ interaction. The comparison between the two-bonded-3×3 case and two-bonded case showed a very similar adsorption, where both S-Cu bond distances are approximately 2.36 Å, and the distance between the aromatic rings is 7.86 Å. In this sense, the lateral $\pi - \pi$ interaction is the same in both cases. For the SAM-$\begin{pmatrix} 2 & 3 \\ 2 & -3 \end{pmatrix}$, the S-Cu distance is 2.39 Å, slightly larger than what is observed for lower coverage. This similarity in the S-Cu bonding distances for low and high coverage suggests that the adsorption stabilization observed for the high coverage may not primarily result from the Cu-S interaction but rather the lateral $\pi - \pi$ interaction of the MBI molecules, where the distance between the aromatic rings is approximately 3.34 Å.

The enhancement of the MBI adsorption with the coverage suggests that SAM formation is favoured, potentially protecting the Cu surface from corrosion by forming a physical barrier against the water molecules. In the following section, the electronic structure of the adsorption cases will be discussed to get deeper insights into the adsorption stability on the surface.

4.3 Electronic structure properties

To get more insights into how the MBI electronic structure changes after the adsorption, we analyzed the pDOS before and after the MBI adsorption. The pDOS for the isolated molecule is shown in Figure 4.5. In order to compare the energetic levels between the MBI

and the Cu surface, the Fermi level of the Cu surface was used as a reference. We can observe that the peaks located at around -2.0 eV and -3.2 eV correspond to the HOMO (highest occupied molecular orbital) and HOMO-1 (second highest occupied molecular orbital), and the peaks located at 1.2 eV and 2.0 eV correspond to the LUMO (lowest unoccupied molecular orbital) and LUMO+1 orbitals. The alignment between the HOMO and LUMO orbitals indicates that MBI tends to accept charge density from the Cu surface rather than donate it. The pDOS also reveals that the occupied states near the Fermi level correspond to S, N, and C orbitals, and in the case of S, it indicates that it is most likely to form a bond with the Cu surface atoms.

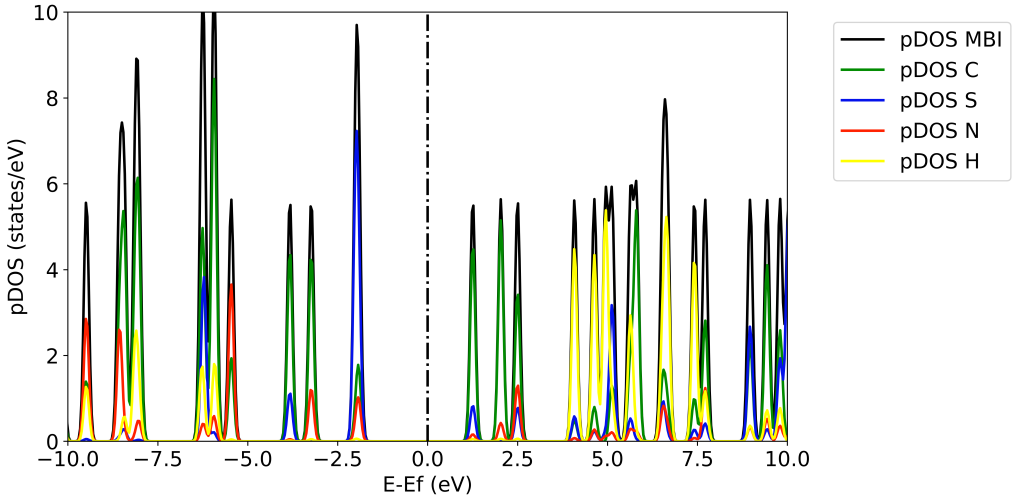

Figure 4.5: Projected density of states (pDOS) for the MBI molecule. In order to compare the energetic levels between the MBI and the Cu surface, the Fermi level (E_F) was aligned to the one of the Cu surface, and normalized to 0 eV. E_F is indicated by a vertical dashed black line.

The electronic structure of all the adsorption cases, in terms of the system's pDOS, is shown in Figure 4.6. In all the cases, the Cu states appear at around -8.0 eV at the valence band and cross the Fermi level, being the higher contribution to the valence band near -2.0 eV due to its 3d states. The drastic change in the MBI's pDOS after the adsorption indicates a strong interaction with the Cu surface. This can be observed in the more broadened and shifted peaks of the pDOS, as well as the appearance of new peaks due to the bond formation between the MBI and the Cu surface. Specifically, these states were mainly associated with C, S, and N for all the cases in both valence and conduction bands.

In all the adsorption cases, the interaction between the MBI electrons and the 3d electrons from the surface also causes states at the system's Fermi level. This states allows the MBI not only to get a charge from the Cu surface but also to donate charge.

The new peaks in the pDOS formed by the bonding with the surface can be observed for the parallel case in energies at around -3.5 eV and are dominated by C states. This peak corresponds to the bond between the π orbitals and the Cu surface orbitals. For the two-bonded case, the peaks at around -2 eV and -3 eV indicate the bonding between the S and NH groups to the Cu surface. The broadening in the peak at 2 eV also shows the higher interaction between the S atom and the Cu surface, compared with the NH group. In the hollow case, the S atom is also strongly bonded to the Cu surface, represented by the peak at around -1.5 eV. The intense peak corresponding to the NH group appears at more negative energies compared with the two-bonded case, indicating its more molecular behaviour and also that it is not taking part in the bond, as can be confirmed by the adsorption geometry shown in Figure 4.6.

In order to understand which MBI orbitals are taking part in the bonding with the surface, we can project the pDOS on the MBI molecular orbitals, as shown in the right-hand plots of Figure 4.6. For the parallel case, the pDOS peak at around -3.5 eV corresponds to the HOMO and HOMO-1 orbitals of MBI, predominantly formed by C and S states. The LUMO and LUMO+1 correspond mainly to C states. We also observed that LUMO and LUMO+1 orbitals appear at the Fermi level, crossing it towards the valence band. In this sense, these orbitals are getting occupied by the electrons that come from the Cu surface. The alignment of these orbitals also confirmed the MBI tendency to accept the electrons of the Cu surface.

In the two-bonded case (Figure 4.6-b), the HOMO is located at energies around -2 eV and corresponds to S states. The strong bond between the S and the Cu surface can be reflected in the position and broadening of this peak at around -2 eV. The HOMO-1 appears at more negative energies, at around -4 eV, and it is formed predominantly by C and S states. In the case of the LUMO and LUMO+1, their location in both the valence

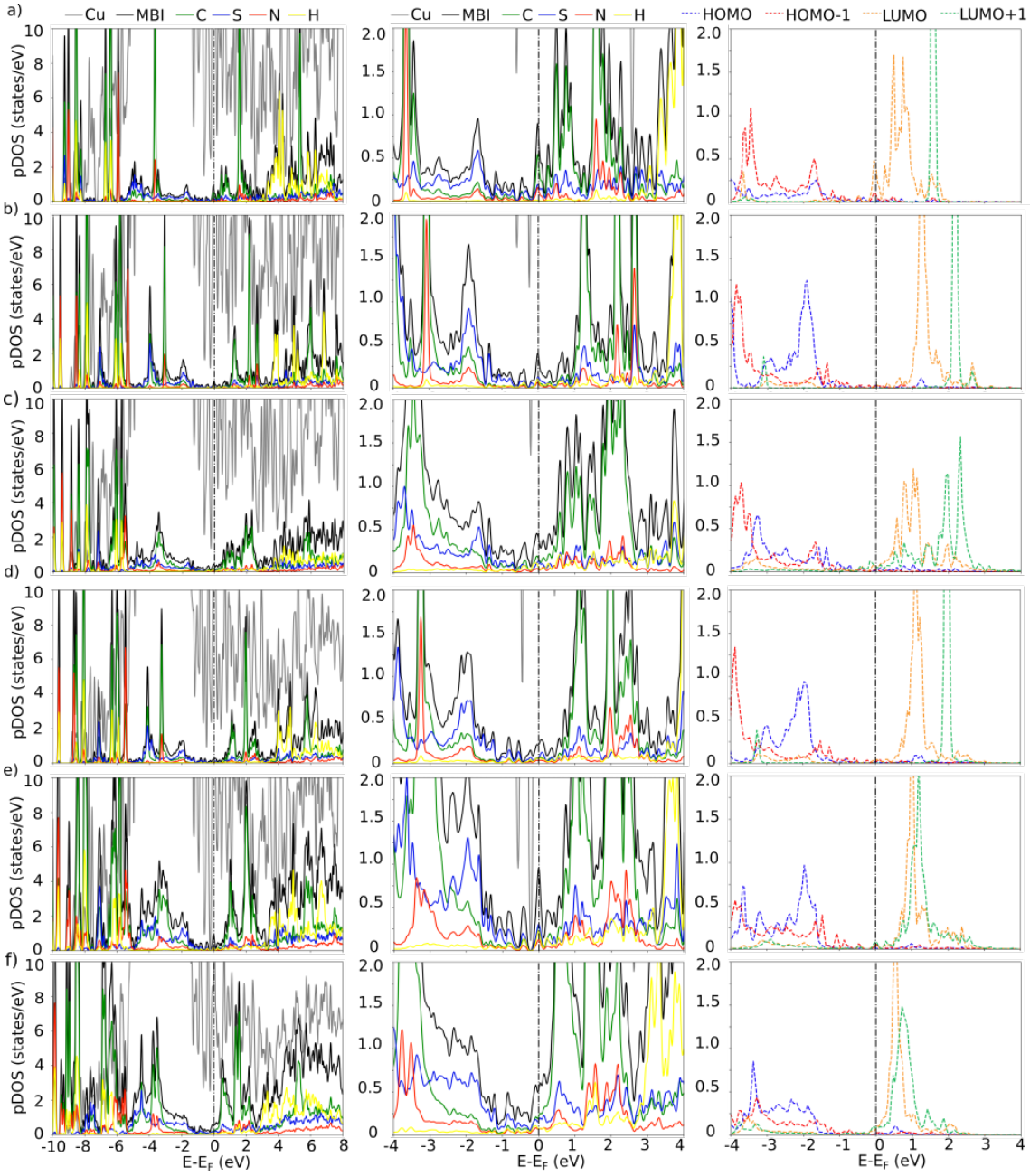

Figure 4.6: Projected density of states (pDOS), and the projections of the MBI molecular orbitals on the pDOS for all the absorption cases in the different slabs: the (a) hollow-$\begin{pmatrix} 2 & 3 \\ 2 & -3 \end{pmatrix}$, (b) two-bonded-$\begin{pmatrix} 2 & 3 \\ 2 & -3 \end{pmatrix}$, (c) parallel-$\begin{pmatrix} 2 & 3 \\ 2 & -3 \end{pmatrix}$, (d) two-bonded-3×3, (e) SAM-$\begin{pmatrix} 2 & 3 \\ 2 & -3 \end{pmatrix}$, and (f) SAM-3×3 cases. The left panels show the pDOS for each adsorption mode, the middle panel a magnified view of the pDOS within the -4.0 to 4.0 *eV* range, and the right panels the projections of the MBI molecular orbitals on the pDOS. The Fermi level (E_F) is normalized to 0 *eV* and indicated in each graph by a vertical dashed black line.

and conduction bands confirms the electro-acceptor behaviour of MBI, partially occupying those orbitals. The LUMO contribution in the valence band is small and very dispersed,

predominantly formed by S states.

On the other hand, the LUMO+1 is formed by N and C states in the valence band. As in the two-bonded case, the HOMO and HOMO-1 orbitals appeared dispersed from energies at around -2 eV to -4 eV and are formed predominantly by S states, which confirms the higher interaction between the S and the Cu surface. In the same regard, the LUMO and LUMO+1 also appear in the valence band, indicating the partial occupation of these orbitals. Particularly in the hollow case (Figure 4.6-a), one considerable contribution of the LUMO appears at the Fermi level.

For the SAM cases (Figure 4.6-e and Figure 4.6-f), their enhanced interaction with the Cu surface can be observed in the broader peaks of the pDOS, comparing the pDOS between the cases at low and high coverages. Also, more states appear at the Fermi level due to the higher interaction with the surface. In both SAM cases, the predominant states in the pDOS, close to the Fermi level, are C and S states. This result confirms the bonding between the SAM and the Cu surface through the S and the lateral π-π in the SAM. A minor contribution to the pDOS also comes from the NH group in the molecules, but as found in the low-coverage cases, it is suggested that the primary interaction with the Cu surface is through the S atom.

Due to the similar adsorption mode on the surface, the pDOS for both SAM cases are comparable. In both cases, a pDOS peak appears around -3.5 eV, and as mentioned before, it is predominantly formed by C and S states. However, slightly broader pDOS peaks can be observed in the SAM-3×3 case, which is in agreement with its higher adsorption energy on the surface. The SAM orbitals projections on the total pDOS show broader orbitals than the low-coverage cases, as shown in Figure 4.6. In both cases, HOMO and HOMO-1 appear as very dispersed states, from energies at around -1 eV towards more negative energies. Those orbitals are predominantly formed by S states, also confirming the bonding between the SAM and the Cu surface through the S atom. LUMO and LUMO+1 orbitals from both SAM cases appear at around 1 eV for the SAM-$\begin{pmatrix} 2 & 3 \\ 2 & -3 \end{pmatrix}$ slab, and 0.5 for the SAM 3×3 case, which are formed mainly by C states. In both cases, LUMO and LUMO+1 orbitals cross

the Fermi level towards the valence band, indicating that they are getting occupied.

The electronic structure can also be analyzed in terms of the induced charge density, $\rho_{\text{ind}}(\vec{r})$, as shown in Figure 4.7, and computed using Equation 4.3. This quantity shows us the redistribution of the electrons due to the adsorption process. The $\rho_{\text{ind}}(\vec{r})$ accumulation indicates the excess of electrons, while depletion indicates the electron deficit in a particular region. The obtained results indicate a strong interaction between the MBI and the Cu surface, as suggested by the accumulation and depletion regions of $\rho_{\text{ind}}(\vec{r})$. Furthermore, the $\rho_{\text{ind}}(\vec{r})$ accumulation in some of the Cu surface atoms and the depletion between the MBI atoms, particularly in the S atoms, denote the charge donation from the MBI orbitals to the Cu unfilled 3*d* orbitals of the surface atoms. In contrast, the $\rho_{\text{ind}}(\vec{r})$ accumulation in some of the atoms of the aromatic ring and depletion on some Cu surface atoms confirm the Cu to MBI electron back-donation from filled 3-*d* bands to unoccupied states of the MBI.

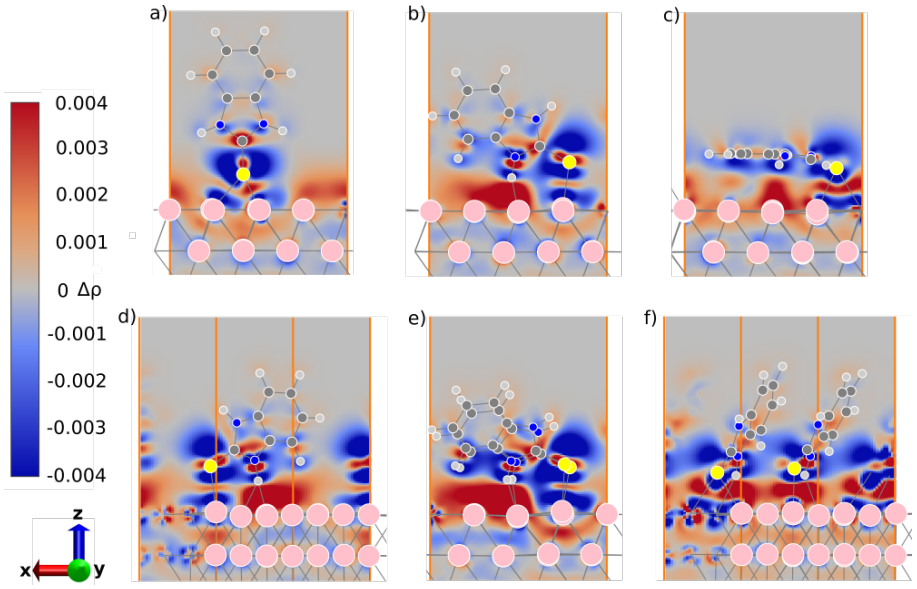

Figure 4.7: Sketch representing the induced charge density $\rho_{ind}(\vec{r})$ in 2D representation for all the adsorption cases. The (a) corresponds to the hollow-$\begin{pmatrix} 2 & 3 \\ 2 & -3 \end{pmatrix}$, (b) the two-bonded-$\begin{pmatrix} 2 & 3 \\ 2 & -3 \end{pmatrix}$, (c) the parallel-$\begin{pmatrix} 2 & 3 \\ 2 & -3 \end{pmatrix}$, (d) two-bonded-3×3, (e) SAM-$\begin{pmatrix} 2 & 3 \\ 2 & -3 \end{pmatrix}$ and (f) SAM-3×3 cases. The color scheme in the left-hand side panel denotes $\rho_{ind}(\vec{r})$ accumulation (red) and depletion (blue). The three innermost Cu layers are suppressed for clarity.

The different MBI adsorption configurations also affect $\rho_{\text{ind}}(\vec{r})$ distribution. In the

parallel adsorption configuration, $\rho_{ind}(\vec{r})$ suggests that the primary interaction with the surface occurs between the π orbitals of the aromatic ring with the d electrons of the Cu surface, in addition to the S atom, as depicted in Figure 4.7. In this scenario, electron donation from the π-orbitals of the aromatic ring to the Cu 3-d states is observed, while Cu to MBI electron-back donation occurs with the S atom. These electron transfers induce structural distortions in the MBI structure. In the two-bonded and two-bonded-3×3 cases (Figure 4.7-b and Figure 4.7-d), MBI to Cu electron donation occurs between the S and N atoms, similar to the parallel case, with electron back-donation from the Cu surface to the S atoms. In the hollow case (Figure 4.7-a), $\rho_{\text{ind}}(\vec{r})$ appears primarily between the S atom and the Cu. In terms of the surface interaction, the additional electron donation from the π orbitals of the ring to the Cu enhances inhibitor adsorption, making the parallel configuration the most stable, followed by the two-bonded and the hollow case, where only a single interaction with the Cu surface is present, which is consistent with the E_{ads} trend.

The $\rho_{ind}(\vec{r})$ in the SAM cases exhibit more intense accumulation/depletion regions compared to low-coverage cases where only one MBI is adsorbed on the surface. Due to their similar adsorption configuration to the two-bonded case, their $\rho_{ind}(\vec{r})$ shows electron transfer between the N and S atoms with the Cu surface: electron back-donation between the S and the Cu, and electron donation between S and N with the Cu surface. Additionally, $\rho_{ind}(\vec{r})$ depletion regions can be observed between aromatic rings, suggesting the lateral $\pi - \pi$ interactions between molecules, which can lead to higher electron donation with the surface, and therefore stabilizing the system. Among the SAM cases, $\rho_{ind}(\vec{r})$ is stronger for the SAM-3×3 case than for the SAM-$\left(\begin{smallmatrix} 2 & 3 \\ 2 & -3 \end{smallmatrix}\right)$ configuration, which also agrees with the adsorption energy trend. In this case, stronger $\rho_{ind}(\vec{r})$ corresponds to more negative (and thus more stable) E_{ads}.

The electronic structure of the MBI adsorption revealed the bond formation with the surface, followed by a charge transfer process. Specifically, there is electron donation from the π orbitals, S and N atoms to the free 3d orbitals of the Cu surface, along with electron back-donation from the Cu 3d orbitals to the π orbitals of the aromatic ring and S atoms.

Furthermore, the electronic structure reflects the surface interaction with the MBI, with more delocalized peaks indicating a stronger interaction with the surface, as revealed by the pDOS and the intensity in the $\rho_{ind}(\vec{r})$. These effects were evaluated under ideal conditions, without the application of any external potential in the system. In the following section, we investigate the effect of the voltage on the adsorption.

4.4 Voltage effect on the MBI adsorption

The role of the voltage is crucial in understanding the corrosion process. It is essential to describe the electrochemical reactions, identify cathodic and anodic zones, and describe the charge redistribution at the interface between the solvent, corrosion inhibitor, and metallic interface. In this section, as an initial exploration, we evaluated the voltage during the adsorption of MBI in a vacuum. This initial exploration provides insights into the fundamental changes in the electronic structure, where only the inhibitor interacts with the surface, where no solvent is included. In this preliminary investigation, the effect of the electrode potential was evaluated using single-point calculations at three different voltages (-1, 0, and 1 V) on the optimized structures depicted in Figure 4.8. The difference in charge density ($\Delta\rho$) was calculated for all the cases using Equation 4.6, and the results obtained are shown in Figure 4.9.

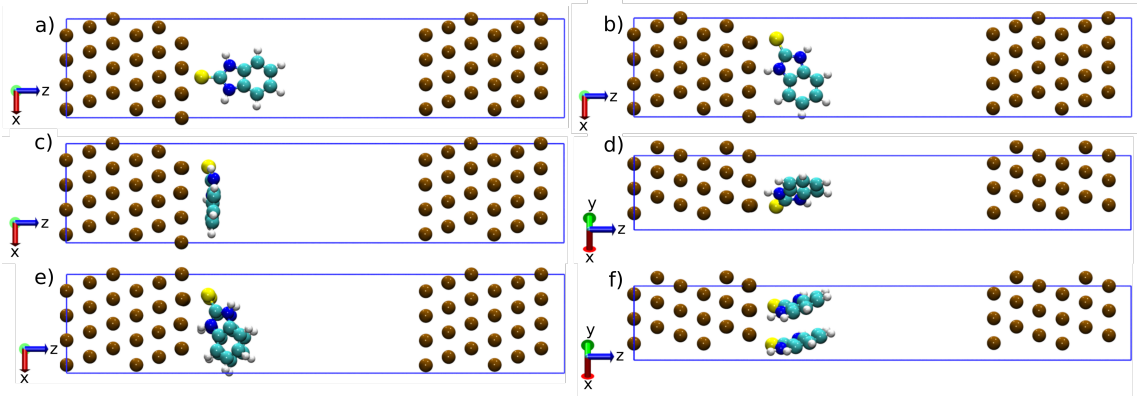

Figure 4.8: Final MBI adsorption cases simulated on the Cu surface: (a) parallel-$\begin{pmatrix} 2 & 3 \\ 2 & -3 \end{pmatrix}$, (b) 3×3, (c) two-bonded-$\begin{pmatrix} 2 & 3 \\ 2 & -3 \end{pmatrix}$, (d) SAM-3×3, (e) hollow-$\begin{pmatrix} 2 & 3 \\ 2 & -3 \end{pmatrix}$, and (f) SAM-$\begin{pmatrix} 2 & 3 \\ 2 & -3 \end{pmatrix}$ cases.

The $\Delta\rho$ results show that applying a positive voltage results in the accumulation of $\Delta\rho$ on the Cu surface and the MBI atoms. This accumulation causes a more negative charge on these atoms, which is especially noticeable near the MBI molecule's edge and the left Cu surface, as shown in Figure 4.9. In parallel adsorption (Figure 4.9-c), the charge accumulation appears on top of the aromatic ring, while in two-bonded (Figure 4.9-b) and hollow (Figure 4.9-a) cases, it is on the hydrogen atoms. In the right Cu surface, the positive voltage induces a $\Delta\rho$ depletion on the Cu surface atoms, causing a more positive charge on them for all cases.

For the negative voltages, the $\Delta\rho$ accumulation/depletion trend is the opposite of that for positive voltages. This is because the chemical potential is inverted on each electrode of the system between positive and negative voltages, inducing the opposite polarization in the system. Negative applied voltages lead to a depletion in $\Delta\rho$ in both the left Cu surface and MBI atoms, resulting in a more positive charge on those atoms. Conversely, the right Cu surface exhibits an accumulation of $\Delta\rho$, indicating a more negative charge on the Cu surface atoms. In the case of the SAMs (Figure 4.9-e and Figure 4.9-f), a similar trend of $\Delta\rho$ accumulation and depletion is observed. Positive voltages predominantly lead to a $\Delta\rho$ accumulation on both the left Cu surface and SAM-MBI atoms, with $\Delta\rho$ depletion on the right Cu surface. In this scenario, SAM-MBI and the left Cu surface predominantly accumulate a more negative charge, similar to what is observed in low-coverage cases, particularly on the edge of the SAM.

The response of $\Delta\rho$ to positive and negative voltages is similar for both voltages, and the shape of the distribution depends on how the molecule is adsorbed, indicating the different electronic structure induced for the adsorption. However, it is surprising to see the $\Delta\rho$ accumulation and depletion at the edge of the MBI, whether under positive or negative voltages and at all coverages. The charge build-up at the edge of the molecule/SAM can have an impact on the adsorption of more MBI molecules, which can affect the formation and stability of other MBI layers or the interaction with water molecules and electrolytes in saline dissolution [164]. It is also noted that $\Delta\rho$ is only present for the exposed Cu

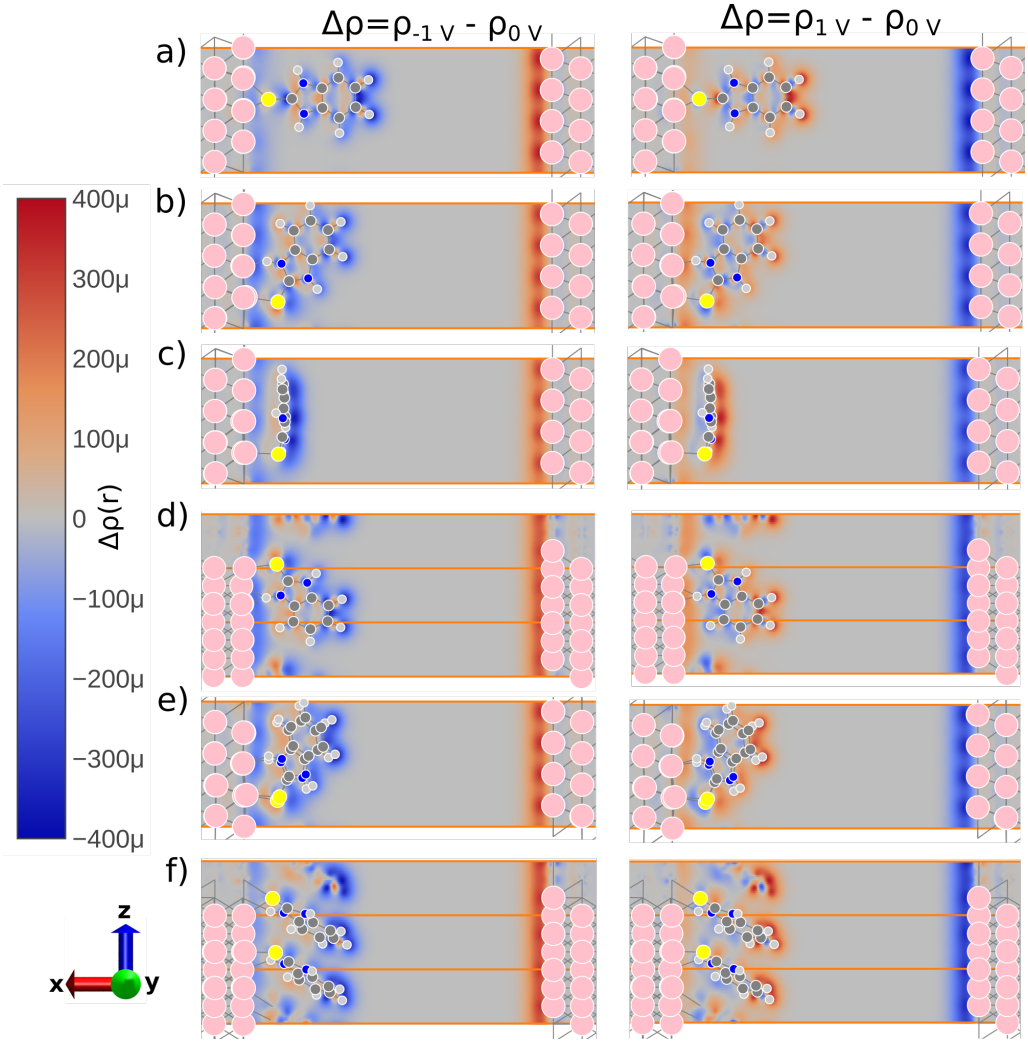

Figure 4.9: Charge density difference ($\Delta\rho$) in 2D between the cases at finite V (ρ_V) and zero voltage ($\rho_{V=0}$) for all the the adsorption cases. The figure displays the $\Delta\rho$ for the hollow-$\begin{pmatrix} 2 & 3 \\ 2 & -3 \end{pmatrix}$, (b) two-bonded-$\begin{pmatrix} 2 & 3 \\ 2 & -3 \end{pmatrix}$, (c) parallel-$\begin{pmatrix} 2 & 3 \\ 2 & -3 \end{pmatrix}$, (d) 3×3, (e) SAM-$\begin{pmatrix} 2 & 3 \\ 2 & -3 \end{pmatrix}$ and (f) SAM-3×3 cases. The red and blue colors indicate charge accumulation and depletion, respectively. Pink, yellow, cyan, blue, and white-colored spheres represent the Cu, S, C, N, and H atoms, respectively. The four innermost Cu layers on both sides of the system are suppressed for clarity.

surface atoms and the MBI/SAM structures and not in the inner Cu layers. This agrees with classical electrostatics, where the metal layers screen the induced $\Delta\rho$.

The effect of the applied voltage can also be observed in the pDOS for all the cases, as shown in Figure 4.10. Within the NEGF method, the pDOS can be derived from Green's function, as illustrated in Equation 4.5. At 0 V, the pDOS obtained from DFT and NEGF should exhibit similar behaviours. However, disparities from the distinct approaches and approximations employed in DFT and NEGF yield non-identical pDOS plots. Nonethe-

less, as previously mentioned, the advantage of the NEGF method lies in its ability to allow us to account for the voltage effects.

The pDOS for all the cases exhibits a displacement towards positive or negative energies according to the voltage sign. Specifically, positive voltages shift the pDOS towards more positive energies, while negative voltages shift it towards more negative energies. This shift in the pDOS is determined by the applied voltage, related to the chemical potential in each electrode ($V/2$), as shown in Equation 2.25.

For both negative and positive voltages, the pDOS shape resembles that observed at 0 V, where the contributions from different atoms appear at the same range of energies when considering the $\pm\, V/2$ shift. The intensity of some of the pDOS peaks changed with the voltage, but this effect can be more attributed to the broadening of the electronic state rather than the applied voltage. The fact that both positive and negative voltages induced a shifted same shape in the pDOS may account for the symmetrical response observed in the induced change in $\Delta\rho$ due to the voltage, as shown in Figure 4.9.

Overall, the changes in the electronic structure, analyzed by the $\Delta\rho$ and the DOS under a voltage, due to the applied voltage indicate a charge redistribution on the system, where the charge gets localized at the MBI's edge, and not between the MBI and the surface, as it would be expected for these systems. This charge redistribution is symmetrical with respect to the voltage and the pDOS for the different voltages. In the following section, as a complement to this theoretical study of MBI adsorption, some experimental results regarding the structure of the MBI layers adsorbed on Cu will be described.

4.5 Conclusions

In this chapter, DFT calculations were performed to simulate the adsorption of MBI, in the thione form, on the Cu surface under different coverages and voltages. Using the $\left(\begin{smallmatrix} 2 & 3 \\ 2 & -3 \end{smallmatrix}\right)$ Cu slab, it was determined the stability trend with respect to the adsorption energy on the surface at low coverage, finding that the parallel adsorption is the most stable one,

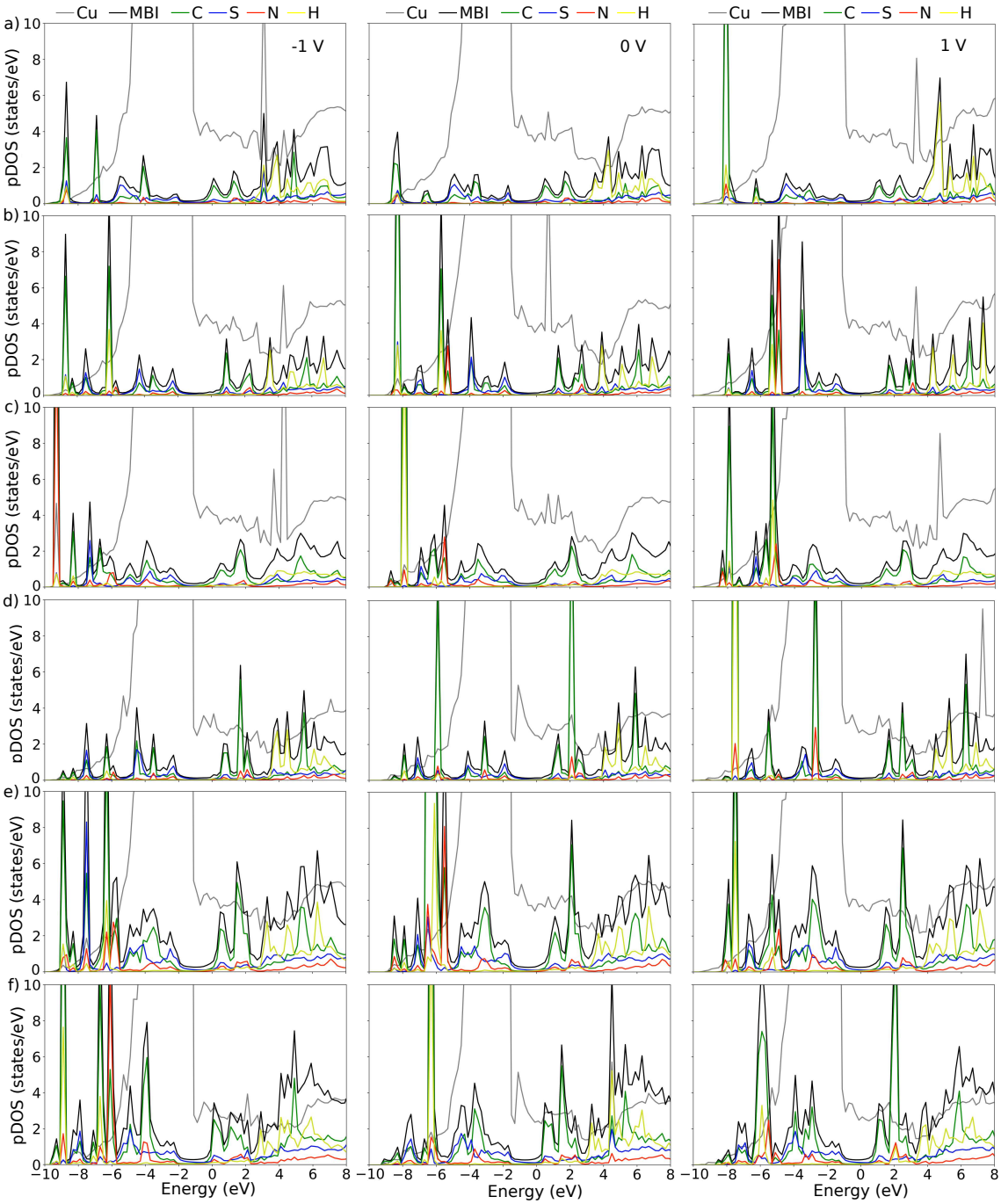

Figure 4.10: Projected density of states (pDOS) calculated at finite V and zero voltage. The figure shows the pDOS calculated at -1, 0 and 1 V for the (a) hollow-$\begin{pmatrix} 2 & 3 \\ 2 & -3 \end{pmatrix}$, (b) two-bonded-$\begin{pmatrix} 2 & 3 \\ 2 & -3 \end{pmatrix}$, (c) parallel-$\begin{pmatrix} 2 & 3 \\ 2 & -3 \end{pmatrix}$, (d) two-bonded-3×3, (e) SAM-$\begin{pmatrix} 2 & 3 \\ 2 & -3 \end{pmatrix}$, and (f) SAM-3×3 cases. The left-side column shows the cases at -1 V, the central column the cases at 0 V, and the right-side the cases at 1 V.

followed by the two-bonded, and the hollow cases. The stability trend showed that the $\pi - d$ interaction between the aromatic ring and the Cu surface stabilizes the adsorption.

The electronic structure in the low-coverage cases showed the ability of MBI to accept

the charge from the Cu surface, which might be linked to the electronic states crossing the Fermi level. The charge transfer was also corroborated through the induced charge density $\rho_{ind}(\vec{r})$, which showed that MBI donates and accepts electronic charge density from the surface depending on its adsorption mode on the surface, due to the electron donation and back-donation processes, which occur mainly through the aromatic ring, S, and N atom. Moreover, the $\rho_{ind}(\vec{r})$ also reflected the intensity of the interaction between the MBI and the surface, indicating the formation of a chemical bond between both, in agreement with the findings based on the E_{ads}.

The MBI coverage on the Cu surface also played an essential role in stabilizing the adsorption of the inhibitor. In this case, higher adsorption energies (more negative) were found for the SAM cases, where the $\pi - \pi$ interactions between inhibitor molecules enhanced the adsorption on the surface. This enhancement was also observed with a higher delocalization of the pDOS peaks in the MBI-SAM cases and where more MBI states appeared at the Fermi level, increasing the charge transfer between the SAM and the surface. The $\rho_{ind}(\vec{r})$ also displayed the stronger interaction between the SAM structure and the surface, suggesting the formation of the chemical bond between both.

Finally, the effect of the voltage on the MBI adsorption reveals an accumulation and depletion of the charge density difference ($\Delta\rho$) between the cases at a finite voltage (ρ_V) and the case at 0 V ($\rho_{V=0}$). In this sense, positive voltages induced an accumulation of $\Delta\rho$ on the left Cu surface and the MBI atoms and a $\Delta\rho$ depletion on the right Cu surface atoms. Negative voltages induced the opposite: $\Delta\rho$ depletion on the MBI and left surface and $\Delta\rho$ accumulation on the right Cu surface. The $\Delta\rho$ was primarily located on the outermost part of the adsorbed MBI and both Cu surfaces. This charge build-up at the edge of the MBI could affect the formation and stability of subsequent layers of adsorbed inhibitors and the interaction with water molecules.

In all the cases, both negative and positive applied voltages have a similar response, and the corresponding induced $\Delta\rho$ distribution shape can be related to the intrinsic interaction between MBI and the Cu surface, where the MBI adsorption mode affects the

electronic structure of the Cu surface. Moreover, the pDOS also displayed a symmetrical response concerning the voltage, displacing the pDOS peaks according to the voltage to more positive or negative energies.

In conclusion, the results obtained in this study, which examined changes in the electronic structure as a function of the applied voltage and the MBI coverage on the surface, provide an essential proof of concept for the methodology used in capturing the voltage effects on the MBI adsorption on the Cu(111) surface. However, it is necessary to include the solvent effects in combination with the electrode potential for a more comprehensive and realistic description of the corrosion inhibition process. These effects can uncover the fundamental aspects necessary to realistically simulate the corrosion inhibition process, paving the way for understanding what properties a molecule must have to be a good corrosion inhibitor. The following section will discuss the solvent and electrode potential effects using the QM/MM-NEGF molecular dynamics approach.

Section 5

Electrode potential and solvent effects

In this chapter, the complete methodology employed in this project was applied to the MBI adsorption on Cu. As mentioned in section 1.4, this methodology (QM/MM-NEGF molecular dynamics) represents an innovative approach to describe CI processes, and it is applied here for the first time to study the particular case of MBI on Cu. The main objective and the research question to be answered is the importance of including the solvent and electrode potential in corrosion modelling.

In the previous chapter chapter 4, the simulations revealed that the electrode potential induces a charge redistribution on the inhibitor and the electrodes when a finite voltage is applied without the solvent. The polarization induced by the voltage causes a charge build-up at the inhibitor's edge, which can potentially affect the adsorption of subsequent inhibitor layers in the material. However, there was no information about the effects of this polarization induced by the voltage on the solvent molecules, which were not considered in our simulations. As mentioned in subsection 3.2.5, the solvent plays a central role in the corrosion process, tunning many chemical and physical properties of the inhibitor and

facilitating chemical reactions and electrochemical process, among others [48]. Therefore, the solvent effects, besides the electrode potential effects, should also be considered in the CI modelling to provide a more complete description of the CI process. In the following, the computational details about the methodology employed and the results of this approach will be introduced. As the literature indicates, including electrode potential and solvent effects in CI modelling is typically not addressed in CI modelling, representing a gap in the literature [48]. This methodology promises to provide a useful approach in describing the CI process and is a step forward for a complete atomistic description of CI.

5.1 Computational details

Initial MBI and SAM structure on Cu

The surface model investigated was the Cu(111)-5×6 orthorrombic slab, composed by five atomic Cu layers with 30 atoms each. The surface was constructed similarly to those slabs reported in section 4.1, using the optimized parameters of the bulk primitive cell to construct the surface unit cell with the Atomic Simulation Environment (ASE) [263], a software package written in Python to set up and analyze atomistic simulations. The surface unit cell was transformed into the Cu(111)-5×6 slab using the corresponding translation matrix **P**, which for the 5×6 slab corresponds to $\mathbf{P} = \begin{pmatrix} 5 & 0 & 0 \\ 0 & 6 & 0 \\ 0 & 0 & 1 \end{pmatrix}$. This matrix will replicate the surface unit cell 5 times in the **x** direction, 6 times in the **y** direction, and once in the **z** direction. The vacuum distance chosen to simulate the surface was 22 Å, as the other Cu slabs in section 4.1. The lattice constants of the slab supercell were a = 12.972 Å, b = 13.481 Å, and c = 30.475 Å.

Three cases were investigated: no molecule adsorbed (bare Cu), a low coverage case (one MBI adsorbed on the Cu surface), and a high coverage case (six MBI molecules forming a SAM structure). The bare Cu surface allowed us to investigate the interaction between the Cu surfaces and the H_2O molecules to validate the correct representation of H_2O in

the system. The MBI initial structure was taken from the optimized two-bonded-3 × 3 adsorption configuration in the low coverage case. This adsorption mode was chosen in order to corroborate how the stability changes when the solvent is included in the simulations and, in this case, to determine if the two-bonded remains in this configuration or if it changes to the parallel adsorption case, which was observed as the most stable one in dry conditions at low coverage (case c in Figure 4.3). Finally, the high coverage case with six MBI adsorbed allowed us to investigate a saturation case where the surface is completely protected from interacting with H_2O.

For the SAM, the six MBI molecules were adsorbed on the Cu surface, following an array similar to the one reported in [167] to reproduce a SAM structure. Both Cu-5×6 slab and the system with the adsorbed SAM were optimized using the same level of theory used for the previous MBI adsorption configurations at low coverage, as explained in section 4.1 (same functional, optimized basis sets, pseudopotentials, van der Waals approximation and convergence criterion). The Brillouin zone was sampled using a 3×3×1 k-mesh grid.

5.2 QM/MM methodology

The first step in the QM/MM methodology was to include the liquid water in the simulations. To do so, the c lattice constant of the previous Cu-5×6 slab was increased to a larger value, 78 Å, to ensure that the number of H_2O molecules is sufficient to represent the appropriate density of liquid H_2O (1 g/cm^3). The lattice vectors of the new Cu-5×6 slab were a = 12.972 Å, b = 13.481 Å, and c = 78 Å. Also, an extra layer of Cu atoms was added to the Cu-5×6 slab to have 6 Cu layers in the system. This extra layer was added for the subsequent NEGF calculation.

The H_2O molecules were introduced in the simulation cell using the GROMACS solvate tool [264]. For the Cu bare surface, the low, and the high coverage cases, the number of H_2O molecules introduced in the simulation box was 347, 338 and 309.

We start our simulations by first performing a pre-equilibration of the system to the

desired pressure and temperature. This was done with molecular dynamics in the NPT (isothermal-isobaric) ensemble, using classical potentials for the whole system (water, MBI and the Cu slab), in order to afford sufficiently long simulation times to equillibrate the system properly. The GROMACS code [264] was used in these simulations. The temperature was set to 300 K and controlled using a Nose-Hoover thermostat, while the pressure was set at 1 bar and controlled using a Berendsen barostat. In the NPT calculation, the $\vec{a}$ and $\vec{b}$ lattice vectors were constrained during the simulation, while the $\vec{c}$ was allowed to relax. Also, the atomic positions of both Cu and MBI systems were kept fixed during the equilibration process. The total simulation time was set to 1 ns. After the NPT equilibration, once the optimized $\vec{c}$ was determined, an NVT (canonical ensemble) calculation was performed to further equilibrate the temperature at 300 K, using the optimized $\vec{c}$ vector in the simulation box. In this last NVT simulation, the total simulation time was set to 2 ns. The SPC force field model described the H_2O molecules in all the cases.

After the NPT and NVT runs, equilibrated geometries extracted from the simulation were used as the starting point for performing the QM/MM-NEGF molecular dynamics under different voltages: -1, 0 and 1 V. The QM/MM-NEGF molecular dynamics were performed using the SIESTA package. Cu and MBI atoms were described as the QM atoms of the systems, while the H_2O molecules were the MM ones. The non-bonded interactions between the MBI atoms and the Cu surface were described using van der Waals parameters. An annealing dynamics was conducted in the system, with a target temperature of 300 K and a relaxation time to reach the temperature of 20 fs. The mesh cut-off was defined as 200 Ry, and the Brillouin zone was sampled at the Γ point. An electronic temperature of 20 meV was chosen to determine the occupations of the electronic states. The density matrix was used as the mixing quantity during the self-consistent cycle, with a mixing weight of 0.01. The tolerance selected for the density matrix was $9x10^{-4}$.

For the NEGF part of the simulations, the electrodes were simulated using a 1×1×3 supercell, with lattice vectors of $a = 2.5944$, $b = 4.4936$, and $c = 6.354$ Å. A mesh cut-off of 400 Ry was used, and the Brillouin zone was sampled using a 5×3×50 k-points mesh.

The electrode was replicated by $5 \times 3 \times 1$ to match the supercell used. The same level of theory was used in all the PBE functional calculations, with the van der Waals described using the D2 parametrization and the optimized basis set described in section 4.1.

Table 5.1: σ [Å] and ϵ [$kcal/mol$] parameters used for the van der Waals QM/MM interactions in the quantum mechanics/molecular mechanics (QM/MM) calculations.

Element	σ	ϵ
C benzene	3.550	0.070
H benzene	2.420	0.030
C imidazole	3.485	0.0860
N imidazole	3.331	0.1700
H imidazole	1.096	0.0158
S thiol	3.550	0.250
C thiol	3.500	0.066

Structural descriptors such as the H_2O density profiles (ρ_{H_2O}), and the distribution of angles defining the orientation of the water molecules were evaluated as averages during the molecular dynamics runs under the different concentrations and applied voltages.

We also computed the time evolution of the dipole moment of the water layer during the dynamics. This provides an interesting measure of the response of water to the external perturbations due to the MBI molecules adsorbed on the Cu surface, or the changes of the potential imposed on the Cu electrodes. The module of the total dipole of the water layer $\mu(\mathbf{r})$ was defined as:

$$|\mu(\mathbf{r})| = \left| \sum_i q_i \vec{r_i} \right|, \tag{5.1}$$

where q_i are the classical H_2O MM charges, and $\vec{r_i}$ the atoms position vector.

The electronic structure was analyzed through the evolution of the net Hirshfeld charges along the dynamics, defined as:

$$\Delta Q_x = \sum_{i=0}^{N_x} (Q_{v,i} - Q_{f,i}), \tag{5.2}$$

where $Q_{f,i}$ is the final Hirshfeld charge of the i atom in the simulation, and $Q_{v,i}$ the Hirshfeld

charge from the isolated i atom (determined by the valence). N_x corresponds to the number of MBI atoms, and the Cu atoms in the left and right side of the device. The ΔQ_x follows the traditional convention, which indicates that positive net Hirshfeld charges mean positively charged atoms, while negative net Hirshfeld charges indicate negatively charged atoms.

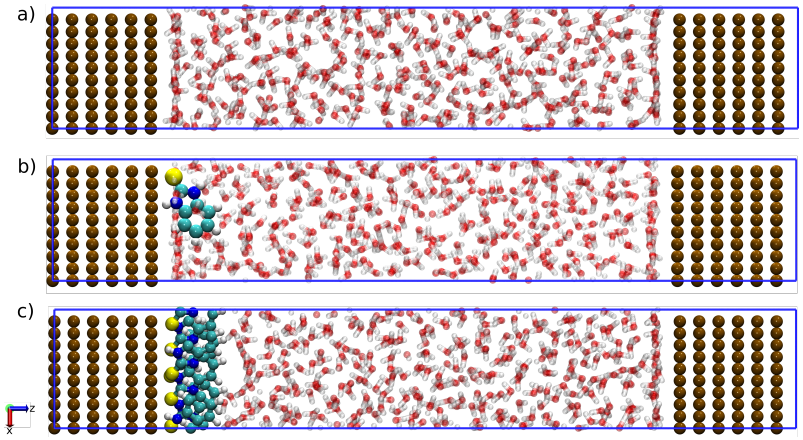

Figure 5.1: Systems used for the non-equilibrium Green's Functions (NEGF) formalism coupled with the quantum mechanics/molecular mechanics (QM/MM) method. a) represent the Cu/H_2O, b) 1-MBI@Cu, and c) 6-MBI@Cu. Ochre, yellow, blue, cyan, red, and white-colored spheres represent Cu, S, N, C, O, and H atoms. Cu and MBI atoms are the QM ones, while the H_2O molecules the MM.

5.3 Water on Cu surface

The first system investigated was the Cu bare surface. This case will help us to understand the fundamental interaction between the H_2O molecules and the Cu surface. In Figure 5.2, the H_2O density profile ρ_{H_2O} is shown for the system calculated at 0 and 1 V. In both cases, ρ_{H_2O} shows a consistent behaviour with the reported results from experimental and theoretical works on the Cu(111) - H_2O interaction. Two peaks near each surface indicate the presence of a layering structure of the liquid, with two well defined layers close to each surface.

For the case at 0 V, the ρ_{H_2O} profile shows two clear peaks around 13 and 16 Å, which correspond to the first and second H_2O layers, respectively. The position of the left-side Cu surface atom exposed to the H_2O is approx. 10.59 Å. This position implies a Cu-H_2O

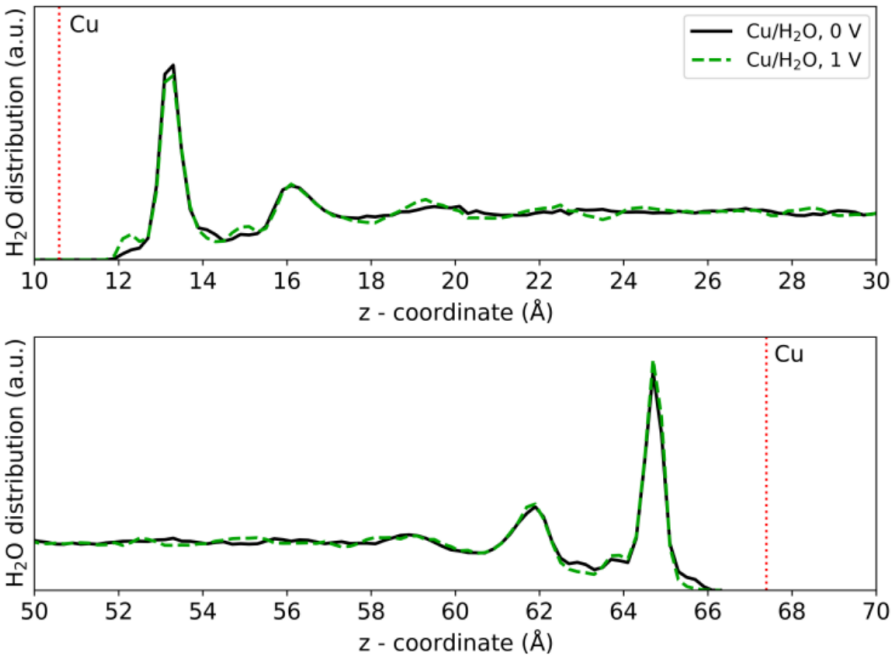

Figure 5.2: H_2O density profile (ρ_{H_2O}) of the Cu/H_2O system averaged in the x and y directions, calculated using the QM/MM-NEGF molecular dynamics. The position of the first Cu layer exposed to H_2O in the left and right of the simulation box is indicated with a red dotted line.

distance of 2.41 Å to the first H_2O layer and 5.41 Å to the second one.

Similar results were obtained for the right-side Cu surface, with defined peaks at 64.7 and 61.8 Å. Considering the position of the first Cu layer on the right-side of the simulation box as 67.39 Å, the Cu-H_2O distances for the first and second H_2O layers were 2.69 Å and 5.59 Å . The results between the left and right sides are similar due to symmetric set-up of Cu left and right sides. Nonetheless, the slight differences between both surfaces can be related to structural effects due to the constraints imposed on the positions of the Cu atoms on the right side during the dynamics. As the MBI adsorption presented below was only performed on the left Cu surfaces, the discussion will focus on the description of the Cu left side.

Far from both surfaces (beyond the two well-defined layers discussed above) the density of water molecules is essentially constant, indicating the convergence towards the unstructured bulk density. The small oscillations in the interior of the bulk are very sensitive to the length of the simulation, tending to disappear for longer simulation times.

We now turn to the more interesting situation in which an external voltage between both Cu electrodes is switched on. For the case at 1 V, the ρ_{H_2O} revealed some subtle but important changes in the H_2O structure. While the overall shape of the density profile is preserved (layering structure near the Cu surfaces and constant density further inside the liquid), small peaks appear at around 12.3 and 14.8 Å from the left surface. These peaks are actually enhancements of small shoulders already present for the 0 V case. They correspond to an enhanced concentration of H atoms at those positions, and originate from rotations of the H_2O molecules to align with electric field generated by the external potential. Since the electrostatic potential is lower on the left Cu electrode, the positively-charge H atoms are attracted towards that electrode, which, in the two layer of the liquid, leads to an increased concentration of H atoms at the left of the main peak of each layer. By the same reason, there is a small depletion of density at the right of the main peak of the layer close to the surface, at around 14 Å.

To gain further insight on the orientation of the water molecules and the effect of the external potential, we now analyze the angular average distributions of the angles of the H_2O molecules during the MD runs. In particular, we show the distribution of the dipole angle (defined as the one between the dipole moment of each molecule and the normal to the Cu surface) and the molecular plane angle (defined as the one formed between the normal to the plane of each molecule and the normal to the Cu surface). These definitions are represented in Figure 5.3.

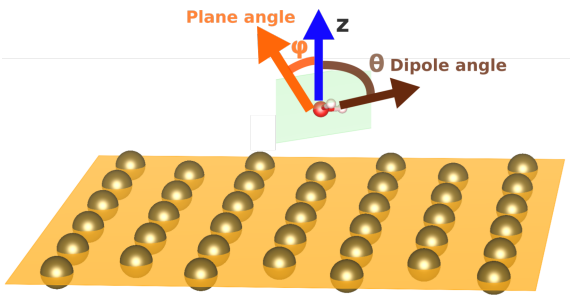

Figure 5.3: Representation of the dipole angle (θ), and plane angle (ϕ) of H_2O molecule. The plane of atoms below the angle's diagram are the Cu(111) surface.

For the analysis of the molecular orientations, the H_2O molecules were divided into

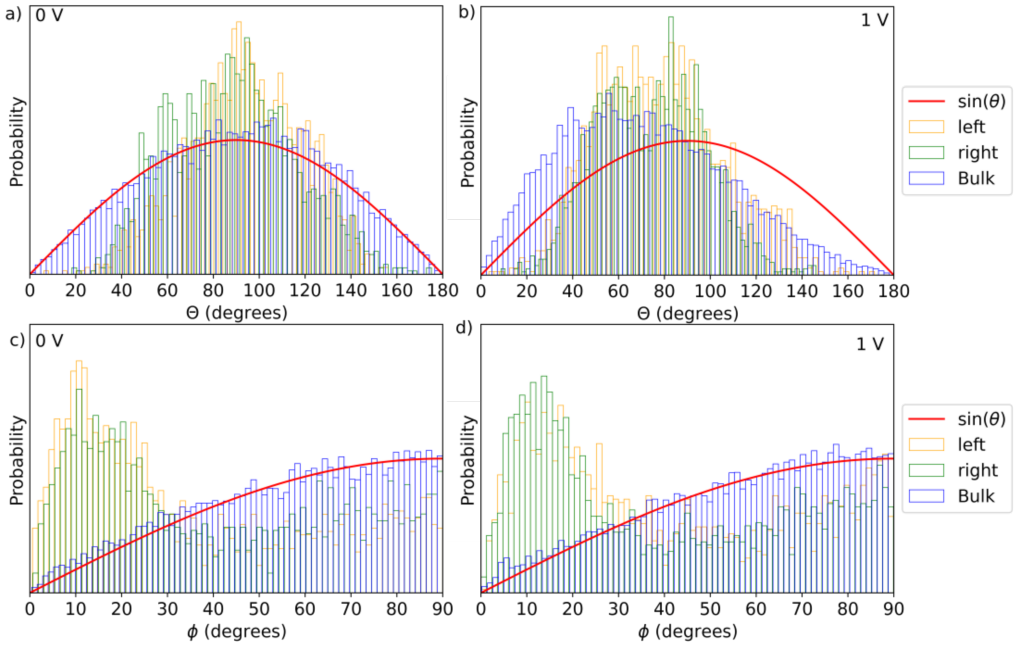

Figure 5.4: Angular distributions of the dipole angle (θ), and the plane angle (ϕ) of H_2O in the Cu bare surface. Two voltages were used in the simulations: (a) 0 V, and (b) 1 V. The left-side, bulk and right-side water layers are represented by yellow, blue and green colors. The red curve indicates a random distribution of water, using the sin(θ) function.

three groups, depending on their distance from the Cu surface, to understand the H_2O orientation as a function of their distance to the Cu surface. The regions were the first layers on the left and right sides, and the centre of the water slab.

In Figure 5.5, the three regions for the 0 V, and 1 eV cases are shown. The colours of each region in the plot correspond to the ones used in

The angular distributions at 0 V for both the dipole and the molecular plane angles for the water molecules far from the surfaces are very close to those corresponding to random directions: centered at 90°, and following closely the expected $sin(\theta)$ shape. This indicates that there is no preferential orientation of the molecules, as it is expected for the bulk liquid. On the other hand, the distributions for the molecules in the first surface layers are significantly different, showing preferential orientations. The dipole angle θ is also centered symmetrically around 90°, but with more weight around that angle than for small ones (θ = 0° or 180°). The deviation from random orientations is even more visible in the molecular plane angle ϕ, which has a large weight on angles in the range from 0°

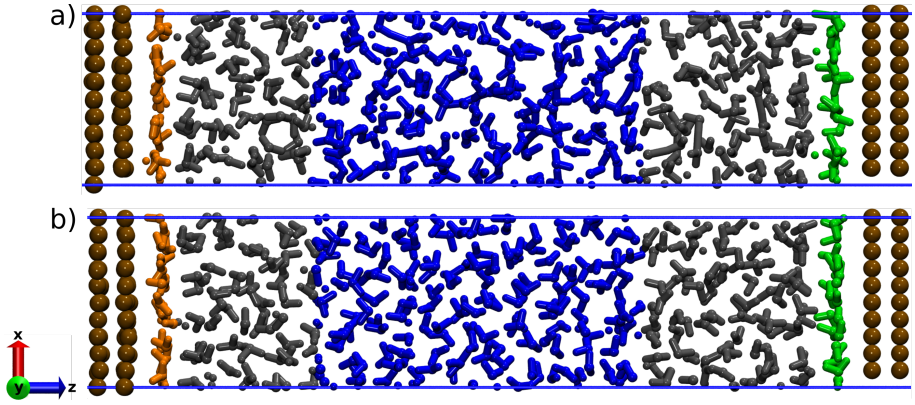

Figure 5.5: Representation of the H_2O layers in the Cu/H_2O case. Brown colored spheres represent the Cu atoms. The H_2O molecules in the first left-side layer are green colored. Yellow, blue and green-colored H_2O molecules represent the left, bulk and right-side H_2O layers. The gray-colored H_2O molecules represent to H_2O molecules in other layers of the system. (a) corresponds to the 0 V case, and (b) to the 1 V case.

to 30°. These deviations on both distributions indicate a preference towards the water molecules laying flat on the surface (corresponding to small ϕ, and to θ close to 90°). This matches well with the know structure on water on noble metals reported in the literature [265]

For the three H_2O layers shows a normal probability distribution, where the left and right H_2O layers displayed a narrower distribution than the water bulk case. The narrower distribution indicates that the water molecules in those layers have more structure than the ones in the bulk case. The wide distribution for the bulk case indicates that the water molecules present a random distribution. These results are aligned with the water density profile, indicating the presence of the layers.

The angular distribution ϕ also shows three distributions for the water layers. For the left and right water layers, ϕ shows a non-uniform distribution, where one part of the angles at between 0 and 40°, and the rest spread in all the range of angles until 90°. The greater water distribution among the smaller angles indicates a more planar water configuration on the surface, with the three atoms lying parallel to the surface. This can be attributed to the alternating charge on the Cu surface, avoiding a preferential interaction with the water atoms. In contrast, the bulk layer displayed a distribution over all the plane angles, with

a higher number of molecules at 90°. This distribution indicates that most of the water molecules in the system are perpendicular to the surface. In this case, the water molecules adopt this configuration to maximize their van der Waals interactions.

We now analyze the changes induced by the external potential. As mentioned, the applied 1 V in the system induces water reorientation, with H's atoms pointing towards the left side of Cu. The angular distributions also reflect the reorientation observed in all the layers. The distribution of dipole angles θ in all the layers is now shifted towards angles smaller than 90°, reflecting the rotation of the molecules towards the direction of the electric field. The distribution of molecular plane angles ϕ is more similar to the one at 0 V, still showing the preferential orientations parallel to the surface for the molecules in contact with the Cu surfaces.

The net Hirshfeld charges were computed and plotted in Figure 5.6 to evaluate the charge redistribution in the system when the voltage is applied. At 0 V, the charges of the electrodes oscillate around zero as expected, since the system is symmetric and the water layer is isotropic, so the net dipole is zero on average, as the molecules are randomly oriented. There are, nevertheless, fluctuations in the total dipole of the water slab, which lead to small opposite charges in both electrodes.

When the voltage is applied, the situation changes dramatically. In the initial step of the dynamics, there is a small unbalance between the charges on the left and right electrodes, consistent with the externally applied voltage of 1 V. At this point, the layer of water molecules is not polarized, as it was equilibrated in an MD simulation with no voltage imposed. As the simulation proceeds, the water molecules start to orient in the direction of the field, until the distribution of angles reaches the equilibrium one discussed above. This leads to a net electric polarization of the water layer, which in turn induces extra (opposite) charges on the two surfaces, that screen the polarization field. Finally, both the water layer polarization and the charges on the Cu electrodes stabilize and oscillate around a value much larger than the initial one. This is consistent with the fact that the surface charges in a capacitor increase as the dielectric constant of the medium between

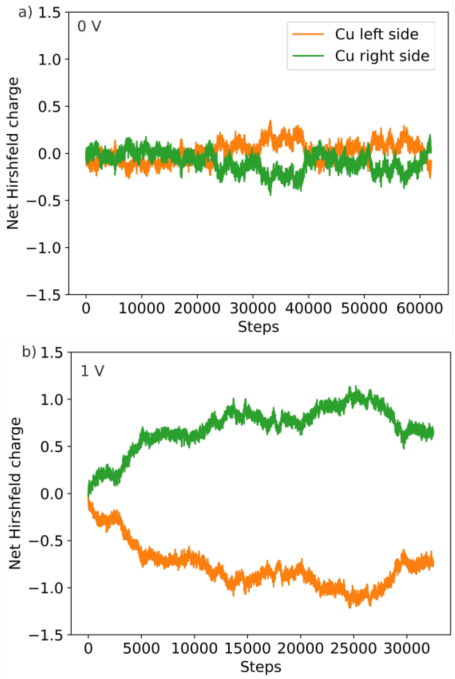

Figure 5.6: Net Hirshfeld charge of the Cu/H_2O system calculated at (a) 0 V, and (b) 1 V. Orange and green solid lines represent the net Mulliken charges for all Cu atoms on the left-side and right-side of the device, respectively. The net Hirshfeld net charges followed the traditional convention, which indicates that positive net Mulliken charges mean positively charged atoms, while negative net Mulliken charges indicate negatively charged atoms.

the plates. As water has a large dielectric constant, the surface charges after equilibration reach much larger values than the initial ones, while maintaining the same fixed potential of 1 V between the plates.

Finally, the average dipole moment, $|\mu(\mathbf{r})|$, was computed for the two voltages. In Figure 5.7, the $|\mu(\mathbf{r})|$ is plotted. For the case with no voltage between the two electrodes, the dipole moment of the water layer is small and oscillates around zero. In contrast, for V=1 V is small in the initial configuration but grows towards a finite value at longer times. The shape of the evolution of the dipole moment with time follows closely that of the charges on the electrodes presented above. As discussed, both quantities are closely related, as the generation of a dipole in water must be followed to screen charges on the electrodes.

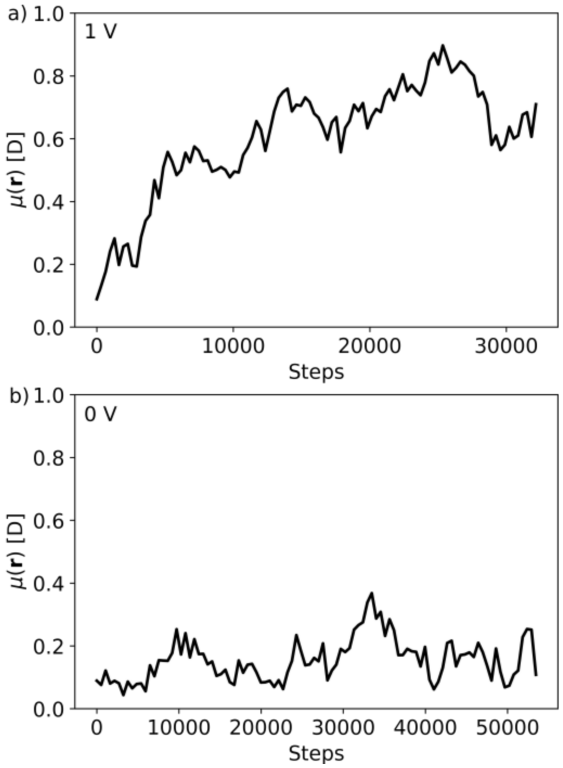

Figure 5.7: Average H_2O dipole moment ($\mu(\mathbf{r})$) in the water layers in the Cu/H_2O system. (a) corresponds to $\mu(\mathbf{r})$ at 1 V, and (b) $\mu(\mathbf{r})$ at 0 V.

5.4 Low coverage of MBI on Cu

Once the voltage effects were evaluated in the Cu/H_2O surface, the adsorption of MBI was considered in the low-coverage case and using the two-bonded configuration of the molecule. For this, the total simulation time for each applied voltage was 56 *ps* and 30 *ps* each for the 0, 1 and -1 V cases, respectively. In auto5.8, the water density profile ρ_{H_2O} is shown for the three voltages studied.

For the 0 V case, the ρ_{H_2O} displays a very similar behaviour to the Cu/H_2O system, showing the water layer positions at similar values. The first H_2O layers appeared around 13 and 16 Å , approximately the same observed for the Cu/H_2O case. In this case, the same positions of the H_2O layers indicate that one adsorbed MBI is not drastically affecting the water layering. Therefore, one MBI cannot displace all the water molecules from the Cu surface and thus physically block the metal from the H_2O. Nonetheless, a small number of

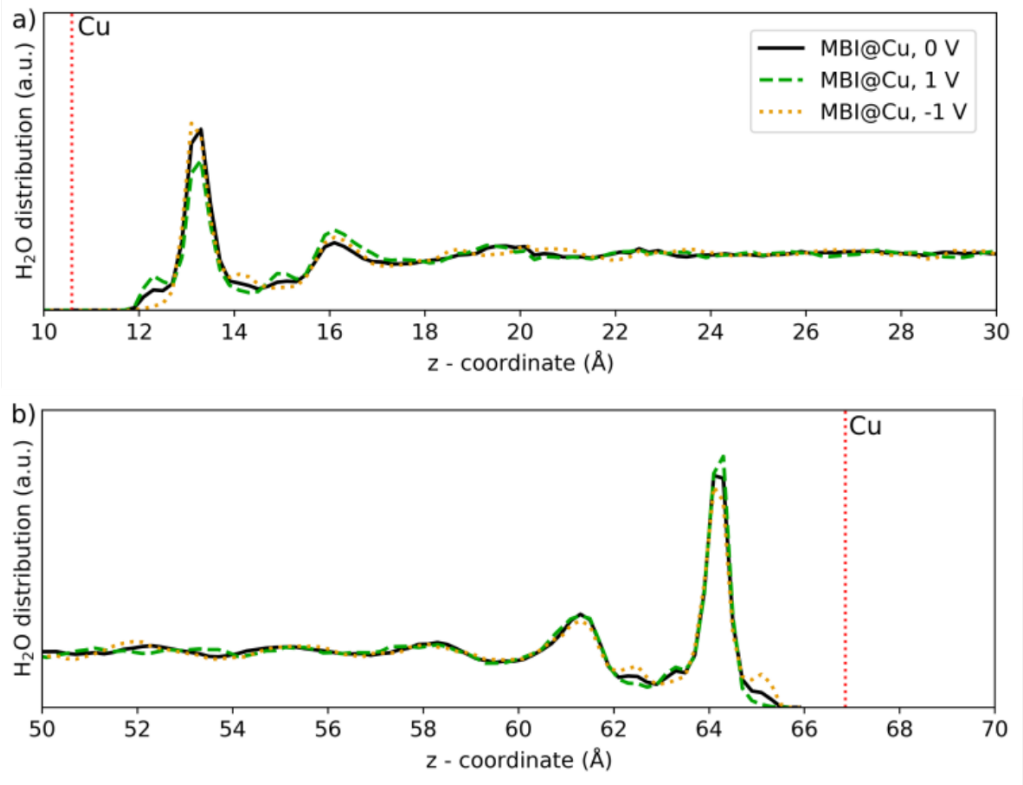

Figure 5.8: H_2O density profile (ρ_{H_2O}) of the MBI@Cu system averaged in the **z** direction, calculated using the quantum mechanics/molecular mechanics (QM/MM) method coupled with the non-equilibrium Green's Function (NEGF) formalism: QM/MM-NEGF molecular dynamics. The first Cu layer exposed to H_2O in the left and right of the simulation box is indicated with a red dotted line.

water molecules are displaced by the MBI, which are reflected in the intensity of the first water layer peak from the left-side surface, compared with the one in the system without MBI, in Figure 5.2

For the 1 *V* and -1 *V* cases, the ρ_{H_2O} indicates the reorientation of the water molecules in the system by the effect of the applied voltage. These water reorientations can be observed by the appearance of new peaks in ρ_{H_2O}. In the 1 *V* case, these new peaks appeared at 12.3 and 14.9Å, and they indicate the H's reorientation towards the left Cu surface, as observed in Figure 5.2.

On the other hand, the -1 *V* case displayed the new peaks near the right-side Cu surface, appearing around 62 and 65Å . Those peaks are due to the water reorientation. With the negative applied voltage on the simulation, this Cu surface is now charged negatively, and this negative charge orients the H's atoms towards the Cu surface.

The polarization in the system was also analyzed in terms of the distributions of the θ and ϕ angles, as displayed in Figure 5.9. The results are very similar to the ones when no MBI molecules are attached to the Cu surface for 0 V and 1 V. For the opposite polarization (V=-1V), the shift of the dipole angle goes in the opposite direction than for V=1 V, as expected.

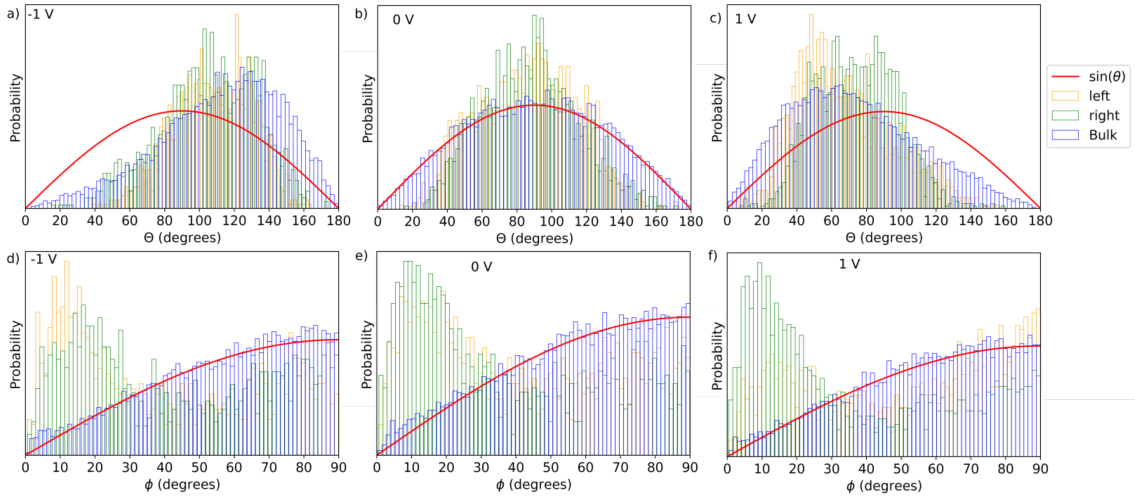

Figure 5.9: Angular distributions of the dipole angle θ (top panels), and the molecular plane angle ϕ (bottom panels) of H_2O in the Cu/H_2O system with a single MBI molecule adsorbed on the left surface. Three voltages were used in the simulations: (a,d) -1 V, (b,e) 0 V, and (c,f) 1 V. The left-side, bulk and right-side water layers are represented by yellow, blue and green colors. The red curve indicates a random distribution of water, using the sin(θ) function.

The water reorientation due to the voltage also induces a charge redistribution in the system, as shown in section 5.3. The net Hirshfeld charges were computed for the system at three voltages, illustrated in Figure 5.10. Again, the results are very similar to those obtained for the case where no MBI molecules are adsorbed on the Cu surface. At 0 V, the net Hirshfeld charges are small in all parts of the system (Cu electrodes and the MBI molecule). The charges on the electrodes oscillate during the dynamics, following the fluctuations of the dipole moment of the water layer. The net charge on MBI was very small, and slightly positive through most of the simulation.

The applied voltages -1 V and 1 V have a similar effect in the charge redistribution to that of Cu/H_2O case. In both cases, the charge on each Cu electrode in the initial steps of the MD run is small and corresponds to the surface charges needed to produce the de-

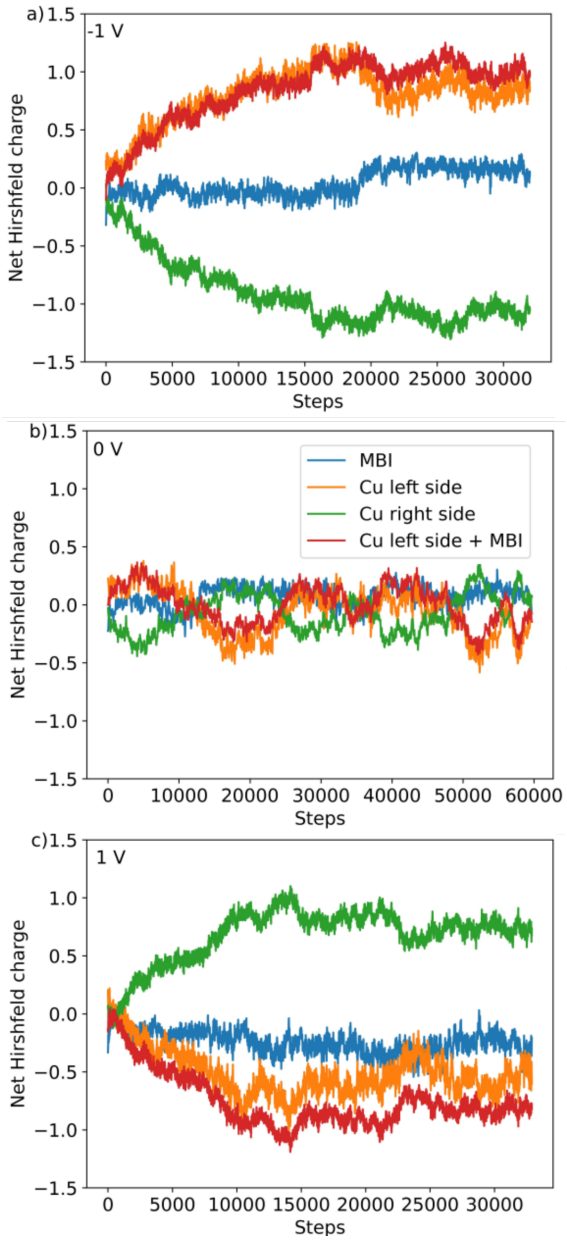

Figure 5.10: Net Hirshfeld charges of the MBI@Cu system calculated at (a) -1 V, (b) 0 V, and (c) 1 V. Orange, green and blue solid lines represent the net Hirshfeld charges for all Cu atoms on the left-side, right-side of the device, and MBI atoms, respectively. The red curve represent the sum of the charge in the left Cu side and the MBI molecule. The net Hirshfeld charges followed the traditional convention, which indicates that positive net Hirshfeld charges mean positively charged atoms, while negative net Hirshfeld charges indicate negatively charged atoms.

sired voltage drop between the electrodes. As the simulation progresses, the water layer between the two electrodes becomes polarized (in opposite directions for the two signs of the external applied potential), which induces extra surface charges to screen the polariza-

tion field. When equilibrium is reached, the left and right electrodes show a charge that oscillates slightly with time around an average value much larger than the initial steps. As in the previous section, this is explained by the large dielectric constant of the water layer present between the Cu plates.

The MBI molecule initially shows a very small charge in all cases. However, this charge becomes somewhat larger during the dynamics due to the interaction of the molecule with the polarized water layer that surrounds it and the interaction with the increasingly more charged left Cu surface. For the case of positive bias (left electrode at negative voltage), the net charge of MBI is slightly positive (around 0.25 electrons). In contrast, for negative bias, the charge is similar but with an opposite sign. This indicates that, in the presence of the dielectric environment, the MBI molecule follows the behaviour of the electrode to which it is bonded and holds part of the surface charge induced to screen the dielectric polarization field.

The dipole moment was also computed for the three voltages, as plotted in Figure 5.11. At 0 V, the dipole molecule in the water molecules is small (0.2 D), as in the Cu/H_2O, and it remains like that along the dynamics, showing an oscillator behaviour, similar to the one obtained for the Hirshfeld charges. When -1 V or 1 V are applied in the system, the initial charge in the Cu electrodes and MBI induces a small dipole moment in the the water molecules, which increases along the dynamics, until it stabilizes at certain value. This indicates that the water is completely polarized because of the applied voltage.

5.5 SAM of MBI on the Cu surface

Finally, for the adsorption of the SAM of MBI molecules on Cu, the ρ_{H_2O} at the different voltages is illustrated in Figure 5.12. The simulation times for the cases at 0, 1, and -1 V are 54 ps, 32 ps, and 21 ps, respectively. ρ_{H_2O} displayed the protection provided by the MBI-SAM to the Cu, not allowing the water molecules to penetrate the SAM structure and interact with the Cu surface. The first H_2O layers appeared around 18.0 and 20.1 Å

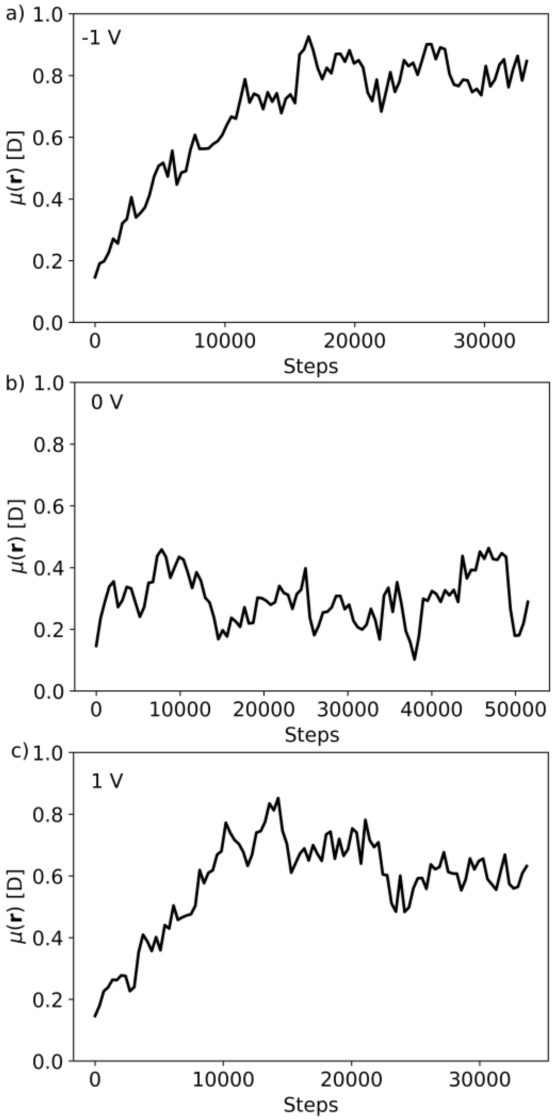

Figure 5.11: Average H_2O dipole moment ($\mu(\mathbf{r})$) in the water layers in the low coverage MBI on Cu system. (a) corresponds to $\mu(\mathbf{r})$ at -1 V, (b) $\mu(\mathbf{r})$ at 0 V, and (c) $\mu(\mathbf{r})$ at 0 V.

regardless of the voltage applied. In contrast to the previous systems, the first H_2O layer is displaced around 9.51 Å from the Cu surface at all the voltages. The small peak around 18.0 Å is due to H_2O molecules that interact with the SAM structure but without entering it.

The right-side Cu surface, where there are no MBI molecules adsorbed, presents a similar behaviour to the previous cases when the voltage is applied in the system: negative potentials charge the right-side Cu surface with a negative charge, which attracts the H

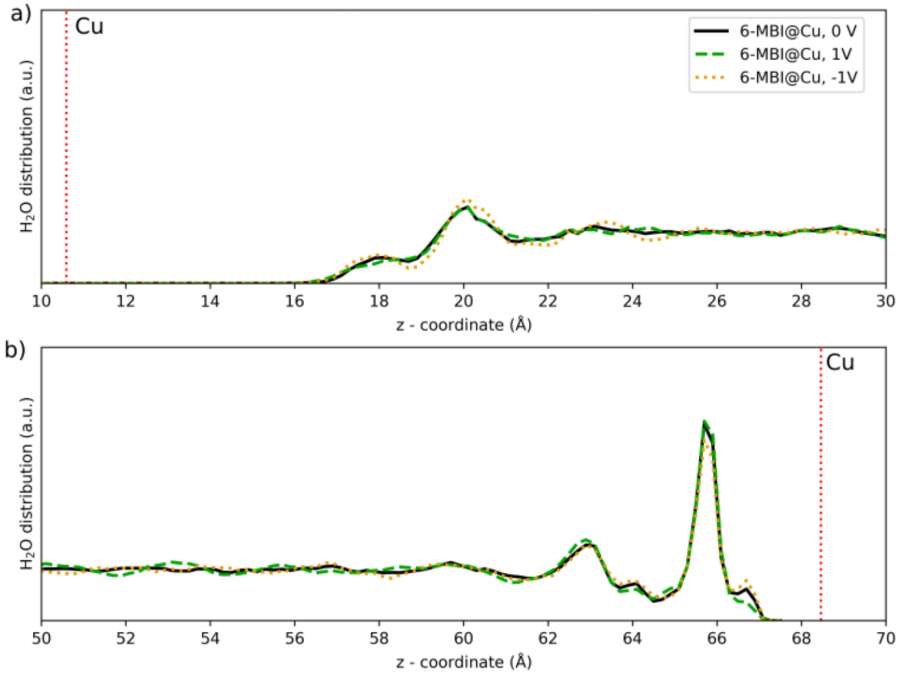

Figure 5.12: H_2O density profile (ρ_{H_2O}) of the SAM@Cu system averaged in the **z** direction, calculated using the quantum mechanics/molecular mechanics (QM/MM) method coupled with the non-equilibrium Green's Function (NEGF) formalism: QM/MM-NEGF molecular dynamics. The surface Cu layers are indicated with red dotted lines.

atoms of the molecules in the first layer, leading to the enhancement of the peak around 67 Å. It is interesting to see that this enhancement of that shoulder also appears at 0 V, in contrast with the cases where no MBI or just one MBI molecules were adsorbed on the left surface. This is an interesting and intriguing observation, as it is not immediately obvious why the chemical composition in the left electrode should affect so much the structure of water on a distant electrode on the right hand side. We will address this issue below.

The distributions of angles is shown in Figure 5.13. For 0 V, the dipole angle θ presents the interesting result that all the layers show a non-symmetric distribution, with a tendency for values larger than 90°, meaning that the water molecules tend to have their dipoles (that is, the hydrogen atoms) oriented towards the right surface. This means that the water layer, even at zero external voltage, has an electric polarization. This is consistent with the observation made above of the pronounced shoulder at the right of the main peak of the water density at the first layer of the right surface. We also note that the deviation from

the random dipole orientations is more pronounced for the water molecules closest to the MBI layer in the left surface, and that this deviation decreases in the bulk layers and is even smaller in the right surface layer.

Concerning the molecular plane angle ϕ, at zero external voltage the distributions for the bulk and right water layers follow quite closely that of random orientations. The water layer at the left surface, in contact with the MBI SAM, does not show a tendency for the molecules to lay flat parallel to the surface, as they did with the clean Cu case. This is because the MBI is softer and allows for more freedom of motion to the water molecules in contact with it. This is supported by the much more smooth density peak of this layer on the MBI SAM compared to that on clean Cu. The right water layer, which is in direct contact with the right Cu surface, in contrast, maintains the strong layering, with the molecules mainly parallel to the Cu surface.

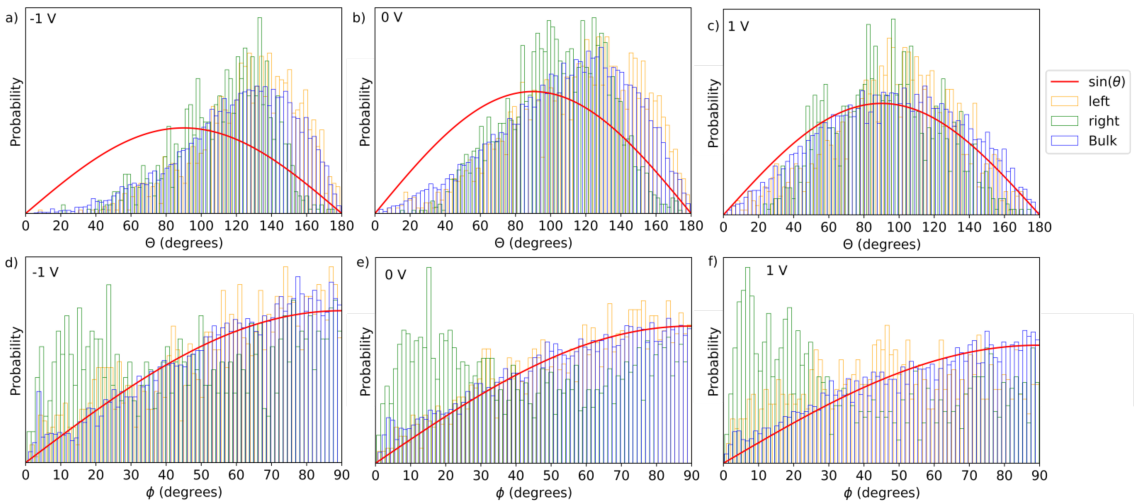

Figure 5.13: Angular distributions of the dipole angle (θ), and the plane angle (ϕ) of H_2O in the MBI SAM adsorbed on Cu surface. Three voltages were used in the simulations: (a,d) -1 V, (b,e) 0 V, and (c,f) 1 V. The left-side, bulk and right-side water layers are represented by yellow, blue and green colors. The red curve indicates a random distribution of water, using the sin(θ) function.

The evolution of the distribution of angles with external applied potential follows what would be expected. The molecules in contact with the right Cu surface maintain their tendency to lay flat on the surface, irrespective of the potential applied. The dipole angle of all the water layers changes with the external voltage, with its distribution shifting towards

larger values (i.e., the dipoles pointing more towards the right surface) for decreasing voltages. For the case of the positive voltage, V=1 V, the distribution becomes close to the random one, with the external potential compensating the tendency of the dipole orientations observed for the 0 V case.

The SAM adsorption also modified strongly the electronic charge distribution in the system. The Hirshfeld charges are shown in Figure 5.14.

To understand the evolution of the charges during the dynamics, we should remember that the initial configuration was obtained from MD simulations using classical potentials both for the water molecules and for MBI and Cu. These classical force fields do not allow for charge transfer between the different components of our system, each of which remains charge neutral. Therefore, these MD simulations include no polarization fields, leading to a water structure with no net dipole moment. Nevertheless, when this geometry is used to start the QM/MM molecular dynamics run, there is a significant charge transfer between the left Cu electrode and the MBI SAM attached to it (with about one electron being transferred from Cu to the MBI layer). The left Cu surface, to which the SAM is attached, loses that charge and becomes positively charged. The opposite Cu surface does not present a significant charge at the beginning of the simulation.

As the dynamics evolve, the water layer becomes polarized as we have seen above, with the dipoles pointing towards the right electrode. Although the reason for the dipoles to align in this particular direction will only be clarified later, the consequence is that the electric polarization developed in the water layer induces charges on the Cu electrodes and the MBI molecules, which screen the polarization field and maintain the voltage between the two electrodes constant. The right electrode develops a negative charge, while the compensating charge on the left is acquired mostly by the MBI layer, with only a small fraction located on the left Cu electrode. This is a surprising result, indicating that the facility of the SAM to acquire charge and screen external fields. When equilibrium is reached, the right Cu surface is left with a net negative charge, the MBI SAM also retains a negative charge (although smaller than the initial one), while the left Cu electrode has a

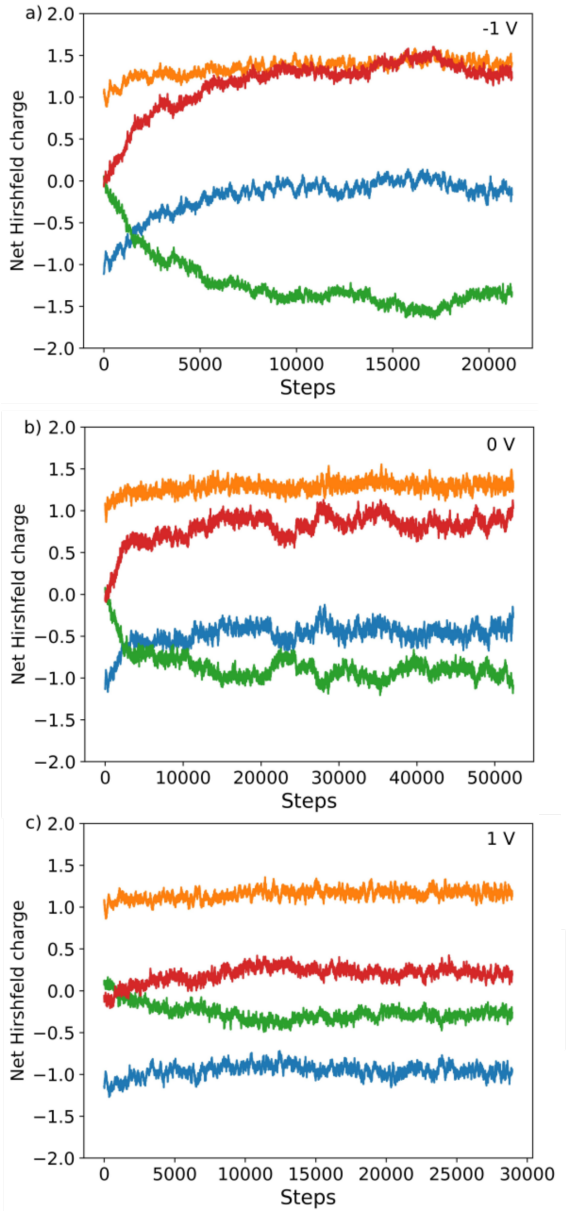

Figure 5.14: Net Hirshfeld charges of the SAM@Cu system calculated at (a) -1 V, (b) 0 V, and (c) 1 V. Orange, green and blue solid lines represent the net Mulliken charges for all Cu atoms on the left-side, right-side of the system, and MBI atoms, respectively. The red curve represent the sum of the charge in the left Cu side and the MBI molecule. The net Hirshfeld charges followed the traditional convention, which indicates that positive net Mulliken charges mean positively charged atoms, while negative net Mulliken charges indicate negatively charged atoms.

positive charge. Again, all this occurs without an external potential being applied to the system, and is due to the polarization developed by the water layer during the molecular dynamics.

To understand the reason for this water polarization developing during the dynamics, we must analyze the charges at the Cu/SAM interface. It could be thought that the small but appreciable charge transfer between the left Cu surface and the MBI SAM could be responsible for the orientation of the water dipoles. However, this charge transfer would induce just the opposite movement of the water dipoles: as the MBI layer is charged with negative charge, the hydrogen atoms of the water molecules would be attracted towards it, therefore moving to the left, which is contrary to our observations. Therefore, there must be another factor that plays a stronger effect on the water dipoles. This turns out to be the intrinsic dipole of the layers of MBI molecules on the surfaces. Isolated MBI has a relatively large dipole of about 4 D. For the SAM, the dipole in the direction perpendicular to the surface is somewhat smaller, but still significant, and points towards the water layer. Therefore, the hydrogen atoms of the water molecules (with a positive charge) are pushed away from the MBI layer, therefore developing the polarization of the water layer we observed above.

With this information, it is now easy to understand the evolution of the charges when an external potential is applied. As all the runs start with the same coordinates, the dynamics of the system now reflect the evolution of the system in response both to the charge distribution among the left electrode and the MBI layer, the dipole present on the MBI layer, and the charges induced on both surfaces by the external potential. When equilibrium is established, the right electrode acquires a negative charge in all cases. As we saw in the analysis of the results for 0 V, this is due to the polarization of the water molecules in response to the dipole moments of the SAM. When the applied potential is negative, this polarization is enhanced, and the accumulation of negative charge in the right electrode becomes larger, too. On the contrary, when the potential is positive, the charge in that electrode is smaller, although, for the case study of V=1 V, the charge is still negative. This is counter-intuitive, as a positive voltage would be expected to induce a positive charge in the right electrode. As we saw before, opposite charges build up on the opposite side, but they are located largely on the MBI SAM rather than in the Cu electrode. Therefore, the

SAM behaves like a metal that screens the external potentials.

The evolution of the dipole moment along the dynamics for the three applied voltage cases also reflects this high polarization induced by the SAM adsorbed on the Cu surface. The polarization in the water can be observed at 0 V, with a curve that is similar to the cases in the MBI@Cu case at low concentration, with an increasing dipole moment along the dynamics. When -1 V is applied in the system, the dipole moment in the water even increases more until it gets to equilibrium and stabilizes. On the contrary, for the case at -1 V, the charge in the SAM does not change along the dynamics, leading to a similar response for the dipole moment, where the dipole moment does not increase along the dynamics

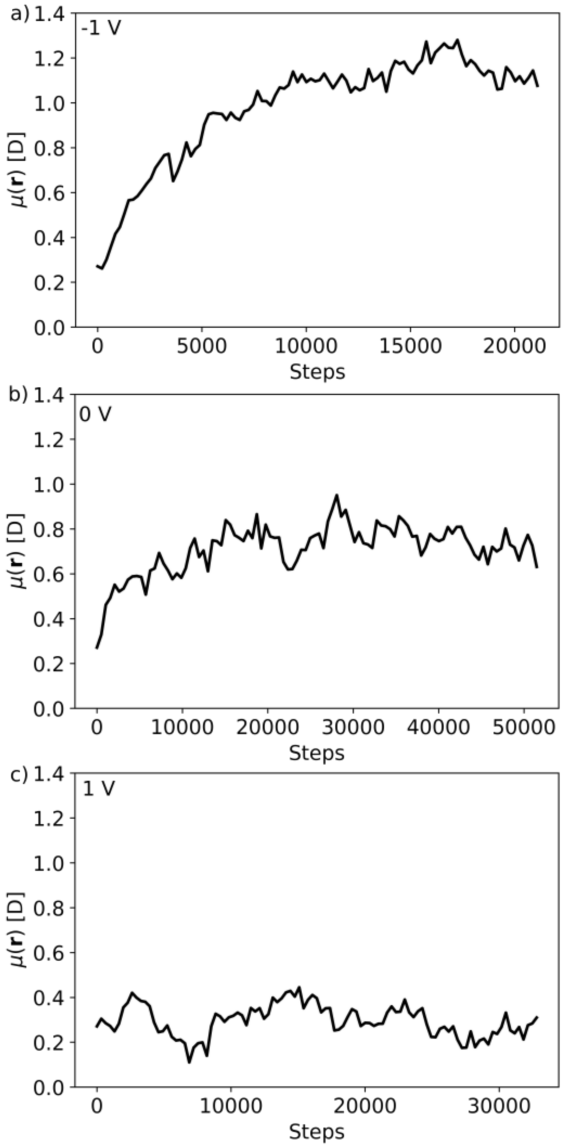

Figure 5.15: Average H_2O dipole moment ($\mu(\mathbf{r})$) in the SAM adsorption Cu system. (a) corresponds to $\mu(\mathbf{r})$ at -1 V, (b) $\mu(\mathbf{r})$ at 0 V, and (c) $\mu(\mathbf{r})$ at -1 V.

5.6 Conclusions

The quantum mechanics/molecular mechanics method (QM/MM) coupled with the non-equilibrium Green's Functions formalism (NEGF) were used to perform QM/MM-NEGF molecular dynamics in order to understand the solvent effects and electrode potential effects in the MBI on the Cu surface under three conditions: a Cu/H_2O surface, low coverage case (1 $molecule/surface$) and a high coverage case (6 $molecule/surface$). The results are

compared with cases where no inhibitor is attached to the surface. The temperature and pressure were calibrated in the systems using classical molecular dynamics, and with their respective final structure, the QM/MM-NEGF molecular dynamics were performed.

The systems described adequately the interaction with H_2O, finding a correct description of the H_2O density profile (ρ_{H_2O}), reproducing two well defined peaks of liquid water for the cases with no MBI and 1 MBI adsorbed on surface. In the MBI adsorption at low concentration and the SAM adsorption systems, the ρ_{H_2O} changed according to the MBI concentration, wherein the low coverage case a slight change in the intensity of the peaks appeared. In the high coverage case, the first H_2O layer was displaced away from the Cu surface, providing a possible mechanism for protecting the surface from corrosion.

In the three systems, the applied voltage reveals important changes in the H_2O structure, enhancing some water molecules peaks because of its aligning with the electric field generated by the external potential. In the systems with MBI, the response of the MBI and SAM follows the behaviour of the electrode which it is bonded and holds part of the induced surface charge to screen the dielectric polarization field. The applied voltage also affects the total dipole moment of the water, showing a close behaviour to the induced charges by the external potential.

The SAM adsorption induces a high polarization in the water that can even be observed at 0 V, with the angular distributions showing a preferential orientation. This adsorption also affects strongly the water structuring, enhancing water peaks close to the electrodes. The reason of this polarization is the high dipole moment present in the SAM layers. The high dipole moment pushed away the hydrogen atoms of the water molecules, developing the observed polarization.

Overall, the results represent an important step toward modelling the corrosion inhibition process and set a precedent for the future use of the QM/MM molecular dynamics to model the critical steps in the corrosion process. This approach includes all the required ingredients, namely the solvent and voltage effects, to realistically simulate the CI process while fully considering the QM character of the electrodes and inhibitor molecules.

Section 6

Inhibitory behaviour and adsorption stability of benzothiazole derivatives as corrosion inhibitors towards galvanised steel

---

This chapter presents a collaborative work with experimental partners from RMIT University to studey the adsorption and corrosion inhibition properties of benzothiazole derivates towards galvanized steel. The chapter's significance lies in the comparison of the adsorption configurations of two different corrosion inhibitors, 2-mercaptobenzothiazole (MBT) and 2-amino benzothiazole (ABT), on electro-galvanized steel (ZE), obtained using DFT simulations, with the experimental results using the X-ray Photoelectron Spectra (XPS) of the system. The different chemical functionalities of both inhibitors affected their adsorption on the surface. Regarding the collaboration, the experimental partners at RMIT

University performed the experimental analysis, while I contributed with DFT simulations. The paper was published in Molecular Systems Design & Engineering [21]. The following section will discuss the theoretical results and use them to analyze the experimental XPS.

6.1 Computational details

DFT simulations were performed using the SIESTA package [22–24]. The Perdew-Burke-Ernzerhof (PBE) [31] functional was chosen to treat the electron exchange and correlation terms within the generalized gradient approximation (GGA). The conjugated gradient method was employed for structural optimization and electronic structure calculations, where atomic forces below 0.01 $eV/Å^2$ were considered converged. An electronic temperature of 25 meV was chosen to smear the electronic occupations with a Fermi-Dirac distribution function. For all the calculations, a tolerance of 10^{-4} was set up for the density matrix as a convergence criterion for the SCF cycles.

Bulk zinc was first studied to obtain the equilibrium lattice parameters $a = b = 2.70$ Å, $c = 4.88$ Å ($\alpha = \beta = 90°, \gamma = 120°$), which are in good agreement with the reported ones in Materials Project database [266]. A mesh cut-off of 600 Ry for the real space integrals and a Monkhorst-Pack k-grid of $30 \times 30 \times 15$ were used for the bulk calculations. The ZE surface was modelled using an orthorhombic 6-layered (4×4)-Zn(0001) slab, which is the predominant grain orientation in the experimental samples, with the lattice vectors of $\vec{a} = 10.800$, $\vec{b} = 9.353$ Å, $\vec{c} = 42.200$ Å, built from an optimized Zn primitive cell. A vacuum layer of 20 Å in the z direction was considered within the slab to prevent interactions among periodic images.

During the optimization of the Zn(0001) slab, the two outermost layers were allowed to relax while the remaining four bottom ones were kept frozen. The Brillouin zone of the surface cases was sampled using a 6×6×1 Monkhorst-Pack k-grid, and the real space integrals were done with a mesh cut-off of 400 Ry.

The structures of both inhibitors are shown in Figure 6.1. For the isolated molecules

(MBT and ABT), structural optimization was performed for each of them using a cubic cell with lattice constant of 30 Å to avoid interaction between periodic images. In this case, the Γ-point was used to sample the Brillouin zone, and a mesh cut-off of 400 *Ry* was chosen for the real space integrals.

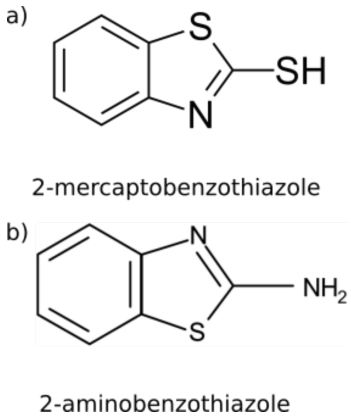

Figure 6.1: The structures of 2-mercaptobenzothiazole (MBT) and 2-aminobenzothiazole (ABT). a) corresponds to MBT, and b) ABT.

Double-ζ basis sets with polarization (DZP) were used to describe the valence electrons of all systems. The basis sets for the different chemical species were optimized variationally to obtain the best basis set (lowest total energy) in terms of the cut-off radius (r_c), soft confinement potential, ionic charge, and split norm parameters [23]. In the case of Zn surface, the inner atoms (second to fifth layers) were simulated using the standard DZP scheme of SIESTA with an energy shift parameter of 0.0001 *Ry* to define the r_c, while the surface ones (first and sixth layer) were simulated with an extra shell of diffuse functions with *s* symmetry to describe better the long decay of the wave functions into vacuum [261]. These diffuse 5*s* orbitals have an optimized cut-off radius of 6.8 *a.u.*.

Troullier-Martins pseudopotentials in the *psf* format were used for the chemical species in the molecules, and norm-conserving pseudopotentials in the PSML format for Zn. During the adsorption of the molecules onto the surface, the van der Waals interactions were described using the D2 Grimme's parametrization which does not pose an additional computational cost over that of the PBE functional. Dipole corrections were applied to avoid the effect of net dipole of the asymmetric slabs. [32, 257, 267, 268].

The molecular adsorption is considered according to the following equation:

$$n\ (\mathrm{MBT/ABT}) + \mathrm{Zn(0001)_{surface}} \rightarrow n\ \mathrm{MBT/ABT} - \mathrm{Zn(0001)_{surface}}, \tag{6.1}$$

where n is the number of molecules adsorbed, (MBT/ABT) is the isolated inhibitor molecule, $\mathrm{Zn(0001)_{surface}}$ is the Zn surface, and MBT/ABT – $\mathrm{Zn(0001)_{surface}}$ is the inhibitor adsorbed system. The adsorption energy (E_{ads}) is calculated as follows:

$$E_{ads} = (E_{n\ \mathrm{MBT/ABT-Zn(0001)_{surface}}} - n\ E_{MBT/ABT} - E_{\mathrm{Zn(0001)_{surface}}})/A, \tag{6.2}$$

where $E_{n\ \mathrm{MBT/ABT-Zn(0001)_{surface}}}$ is the energy of inhibitor bonded to the Zn(0001) surface, $E_{MBT/ABT}$ is the energy of the isolated molecule, $E_{\mathrm{Zn(0001)_{surface}}}$ is the energy of the $\mathrm{Zn(0001)_{surface}}$, and A is the area of the surface ($\mathrm{nm^2}$). From this definition, the lower the value (more negative) of E_{ads}, the higher the stability of the adsorption.

To analyze the change in the charge distribution due to the adsorption, the induced charge density, $\rho_{ind}(\vec{r})$, was calculated as Equation 4.3 in chapter 4. Positive (negative) $\rho_{ind}(\vec{r})$ indicates electron excess (deficit) after the adsorption. The DOS, pDOS, and the projections of the ABT and MBT molecular orbitals on the total DOS were similarly obtained for the system in the chapter 4. The same k-mesh used for the structural optimizations was employed for the DOS and pDOS calculations, with a smearing of 0.05 eV.

6.2 Adsorption modes on the Zn surface

The inhibitor adsorption was evaluated under two different coverages: (1) low - one $molecules/cell \approx 0.98\ molecule/nm^2$ - and (2) high coverage - three $molecules/cell \approx 2.96\ molecules/nm^2$, which correspond to the SAM formation case. To simplify the adsorption model of MBT on the surface, the thione form of MBT was used for the calculations. This approach circumvents the need to model a charged chemical compound (thiolate), which can introduce complications when using periodic boundary methods such as those used

in DFT. Due to its higher stability than the thiol form, the thione form was considered in our analysis as it is reported to have minimal influence on adsorption. Nonetheless, it has been revealed [167] that both tautomeric cases exhibit very similar final configurations, with the only notable difference being the higher E_{ads} values observed in the thiolate counterparts.

Figure 6.2 depicts the different possible adsorption sites presented on the topmost surface plane considered in the simulation for the vertical adsorption of the inhibitor, where either the S atom or the NH_2 group is pointing out to the Zn surface.

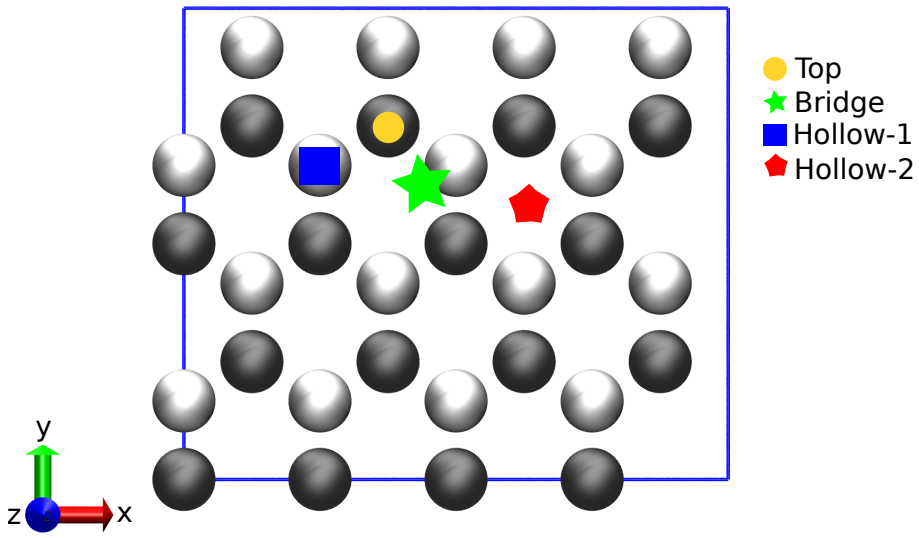

Figure 6.2: Different adsorption sites at the Zn(0001) surface. A top (yellow circle), bridge (red pentagon), hollow-1 (green star), and hollow-2 (blue square) represent the different adsorption sites on the surface. Gray-colored spheres represent the Zn atoms, and a degraded color scale was used to illustrate their position in the slab layers: dark gray means an exposed Zn surface atom, while light gray means an atom in the second and subsequent layers.

The adsorption configurations of both MBT and ABT at low and high coverages are shown in Fig. 6.3 in an energetic diagram showing the adsorption energies as a function of the coverage. The label depends on the atom linked to the Zn surface. In this regard, we found for MBT four different adsorption configurations: one in which one sulfur atom is attached to the surface in a hollow site (S)-Zn, one with the two sulfur atoms linked to the surface (S, S)-Zn, another with the sulfur and the NH bonded linked to the surface (S, NH)-Zn, and a parallel configuration, where the MBT lies nearly horizontal on the Zn

surface, which we will refer to as parallel mode. For ABT, we also found four adsorption cases: a vertical adsorption between the N_2 group and the Zn surface (NH_2)-Zn, a (N, NH_2)-Zn with the NH_2 and the N bonded to the surface, (S, NH_2)-Zn with the NH_2 and the S bonded to the surface, and finally a ABT parallel to the Zn surface.

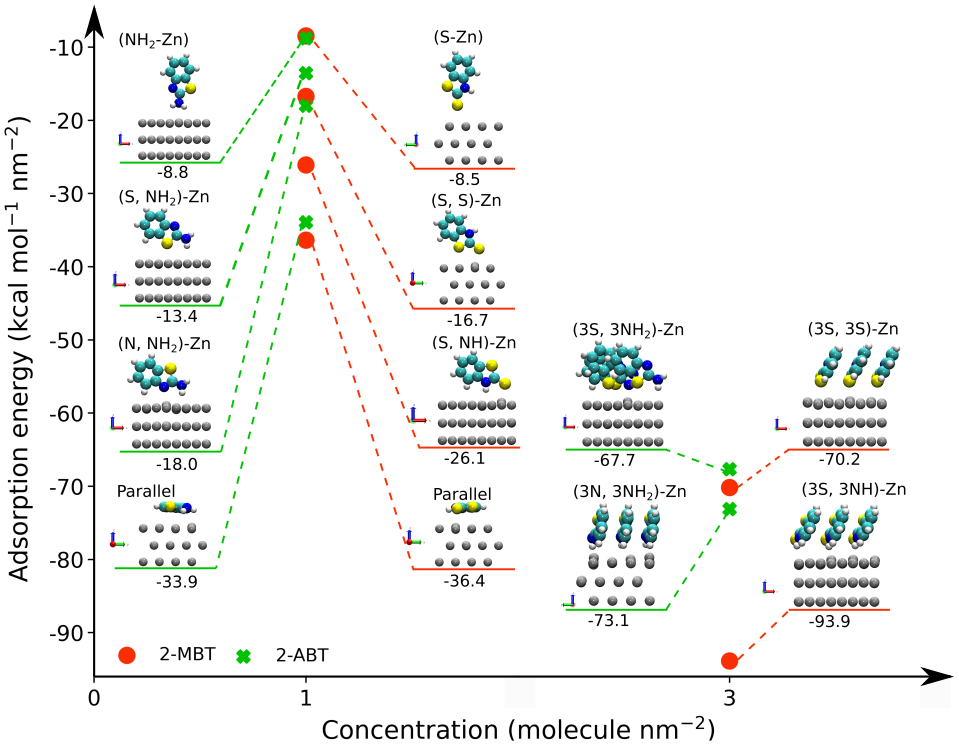

Figure 6.3: Different adsorption configurations of ABT and MBT at low (one *molecule/cell*) and high (three *molecules/cell*) coverage on Zn surface. White, cyan, yellow, blue, and gray colored spheres represent H, C, S, N, and Zn atoms. The orange and green points represent the adsorption energy (E_{ads}) per surface area, which appears below the side view of each structure and is expressed in $kcal\ mol^{-1}\ nm^{-2}$. Some Zn layers are suppressed for clarity.

For the MBT SAM cases, two adsorption modes were found on the surface, which came from the (S, NH)-Zn and (S, S)-Zn modes. In the ABT SAM case, we also found two SAM adsorption modes from the optimized low coverage cases: (N, NH_2)-Zn and (S,NH_2)-Zn. In the following sections, a more detailed analysis of the adsorption of the two inhibitors will be presented.

6.3 Results for MBT

Adsorption stability

The most stable adsorption configurations of MBT at low coverage are shown in Figure 6.4. Among these configurations, the parallel mode exhibits the highest stability, followed by the (S, NH)-Zn, (S, S)-Zn, and (S)-Zn modes. In the parallel, (S, NH)-Zn, and (S, S)-Zn cases, the S atom from the thiol group (exocyclic S) tends to pull out the interacting Zn atom from the surface, at a height of approx 0.24, 0.33, and 0.39 Å, respectively.

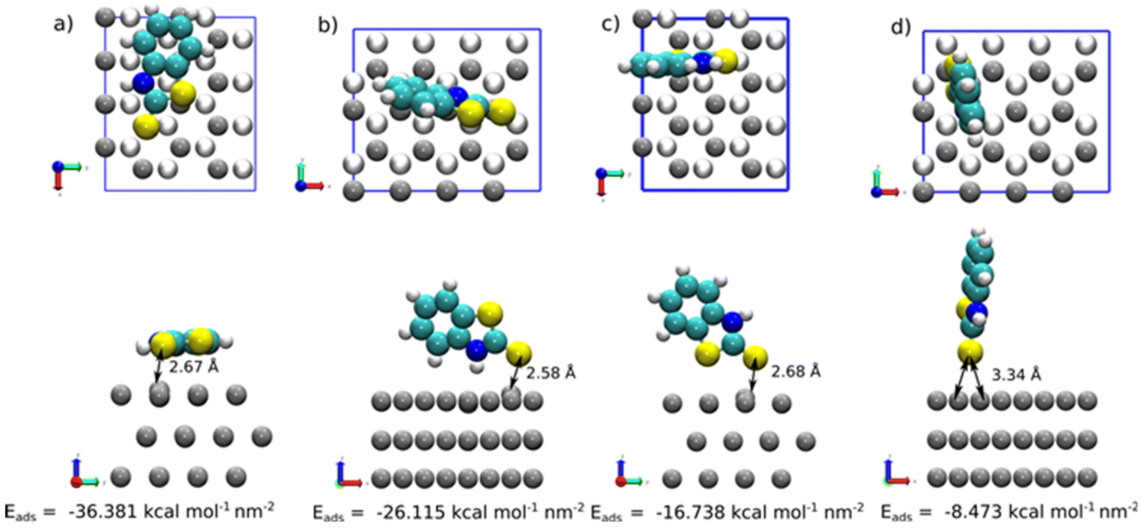

Figure 6.4: Top and side views for the MBT adsorption configurations on Zn surface at low coverage (1 $molecule/nm^2$) obtained for: a) parallel, b) (S, NH)-Zn, c) (S, S)-Zn, and d) (S)-Zn on hollow site cases. White, cyan, yellow, blue, and gray colored spheres represent H, C, S, N, and Zn atoms. On the top view of each case, lighter-colored spheres represent the second outermost Zn layer. The adsorption energy (E_{ads}) for each case is shown below the side view of the structure, which also shows the nearest distances between the adsorbed molecules and the Zn surface. Some Zn layers are suppressed for clarity.

This can be related to the strong interaction between these chemical groups and the metal surface. Except for the parallel case, where the primary interaction is between the π orbitals and the Zn surface states, the displacements in the Zn surface atom, as well as the Zn-S distance can be correlated to the E_{ads} trend, which suggests a stronger interaction in the (S, NH)-Zn case between the exocyclic S and the Zn interacting atom than in the (S,

S)-Zn case. Nonetheless, in the top adsorption, where only the exocyclic S interacts with the surface, the Zn interacting atom is not being pulled out from the surface, presenting the larger Zn-S distance. Additionally, this adsorption configuration is the least stable one, which indicates the role played by the chemical groups in stabilizing the system and making the adsorption more favorable. In contrast to the pulling-out effect, the NH group tends to displace the Zn interacting atom towards the inner Zn layers by approx. 0.15 Å.

The next step was to evaluate the effects of increasing the coverage of molecules in the system, forming a SAM structure. The optimized structures of these adsorption modes are shown in Figure 6.5. At high coverage, the molecules stabilized in a perpendicular orientation towards the surface, with the (S, NH)-Zn and (S, S)-Zn as the most stable geometries, with the (S, NH)-Zn case as the most stable one. The SAM formation on the surface stabilizes the inhibitor adsorption, with more negative adsorption energies E_{ads}'s, compared with the low coverage cases, and as it was shown in chapter 4.

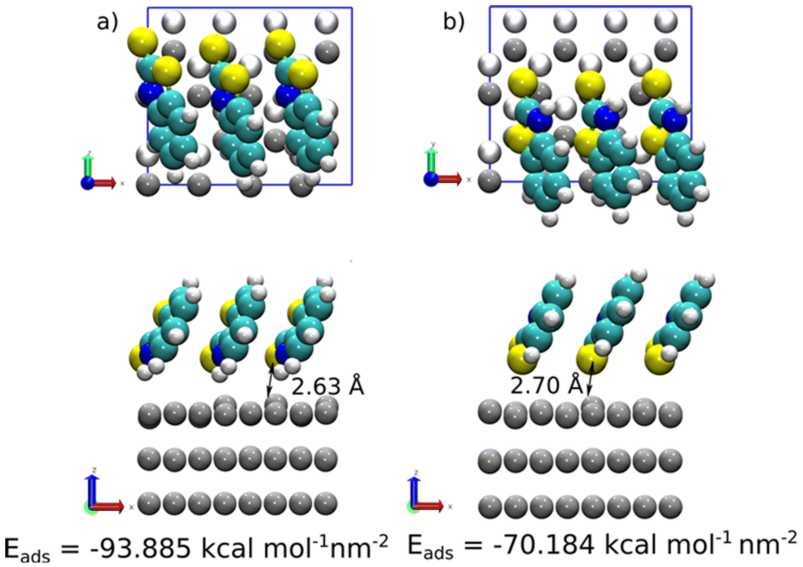

Figure 6.5: Top and side view for the MBT adsorption configurations on Zn surface at high coverage (3 $molecules/nm^2$) obtained for: a) (S, NH)-Zn, and b) (S, S)-Zn cases. White, cyan, yellow, blue, and gray colored spheres represent H, C, S, N, and Zn atoms. On the top view of each case, lighter color spheres represent the second outermost Zn layer. The adsorption energy (E_{ads} $[kcal mol^{-1} nm^{-2}]$) for each case is shown below the side view of the structure, which also shows the nearest distances between the adsorbed molecules and the Zn surface. Some Zn layers are suppressed for clarity.

The stability increases by 5.0 $kcal\ mol^{-1}\ nm^{-2}$ and 6.5 $kcal\ mol^{-1}\ nm^{-2}$ for the case

of (S, NH)-Zn and (S, S)-Zn, respectively. The stabilization can be related to the increase in the lateral $\pi - \pi$ interaction between the molecules, as observed in the MBI adsorption (chapter 4). This can also be confirmed by the displacement of the Zn surface atom, which is displaced by approx. 0.48 and 0.44 Å in the (S, NH)-Zn and (S, S)-Zn cases, respectively. Furthermore, the displacements are higher than those of the low-coverage cases. Finally, the E_{ads}'s of each case are also in agreement with the displacement, with the lower E_{ads} (more stable) for the (S, NH)-Zn than in the (S, S)-Zn.

Electronic structure

The electronic structure for both low and high-coverage cases was investigated in terms of the DOS analysis and the $\rho_{ind}(\vec{r})$ in the system, as in chapter 4. The pDOS and some of the closest molecular orbitals to the Fermi level E_F (HOMO-1, HOMO, LUMO, and LUMO+1) are shown in Figure 6.6.

The HOMO and HOMO-1 orbitals are observed at very similar energies, approximately around -2.2 eV and therefore cannot be distinguished as different peaks in Figure 6.6. Both orbitals exhibit prominent lobes around the exocyclic S atom. Specifically, the lobes are perpendicular to the exocyclic S atom and the aromatic ring for the HOMO-1, while they are parallel to them for the HOMO. Moreover, the pDOS at this energy shows the S atoms as the predominant peak. The LUMO appears at an energy around 0.9 eV, showing predominant lobes around both S atoms, whereas the LUMO+1 at energies around 1.5 eV, with lobes predominantly present around the endo S atom. For both LUMO and LUMO+1 orbitals, at their corresponding energy, the pDOS shows the C states as the predominant ones.

As noted in chapter 4, the shape of the inhibitor orbitals enables particular interactions with the Zn surface states. In Figure 6.7, the pDOS for the different MBT systems at low coverage are depicted. To compare the pDOS of the MBT with the Zn surface, the pDOS of the latter one was normalized with the number of Zn atoms. For all the cases at low coverage, the pDOS of Zn shows the localized character of the 3d orbitals, which appears

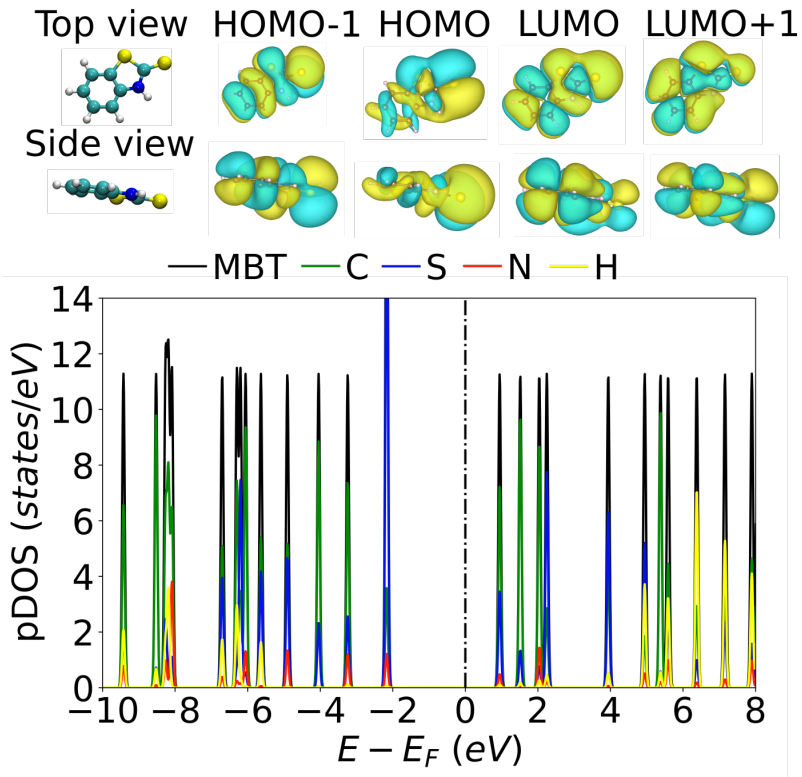

Figure 6.6: Projected density of states (pDOS) for the MBT molecule showing the molecular orbitals corresponding to the HOMO-1, HOMO, LUMO, and LUMO+1 orbitals. The Fermi level (E_F) was aligned to 0 eV and is indicated by a vertical dashed black line.

around -8 eV, and the 4s states, which appear continuously crossing the E_F.

The MBT pDOS for each adsorption configuration displayed a distinct shape close to the E_F, which is influenced by the atom bonded to the surface and the strength of the interaction. To analyze in more detail the peaks near the E_F, Figure 6.8 shows a zoom of the MBT pDOS between -4 and 4 eV, as well as the projections of the MBT's molecular orbitals on the pDOS. In the parallel adsorption, the broader pDOS's peaks near the E_F appeared due to the strong interaction with the surface in both valence and conduction bands. This result was expected due to the similar interaction between the MBI and the Cu surface in the parallel configuration, as explained in chapter 4, but particularly in Zn, due to the position of the 3d band, which is very profound in energy, the interactions are with the 4s orbitals from the surface. The predominant states around the E_F are from S and C states, appearing at -2.5 and 1.0 eV. The states at -2.5 eV are mostly composed of S

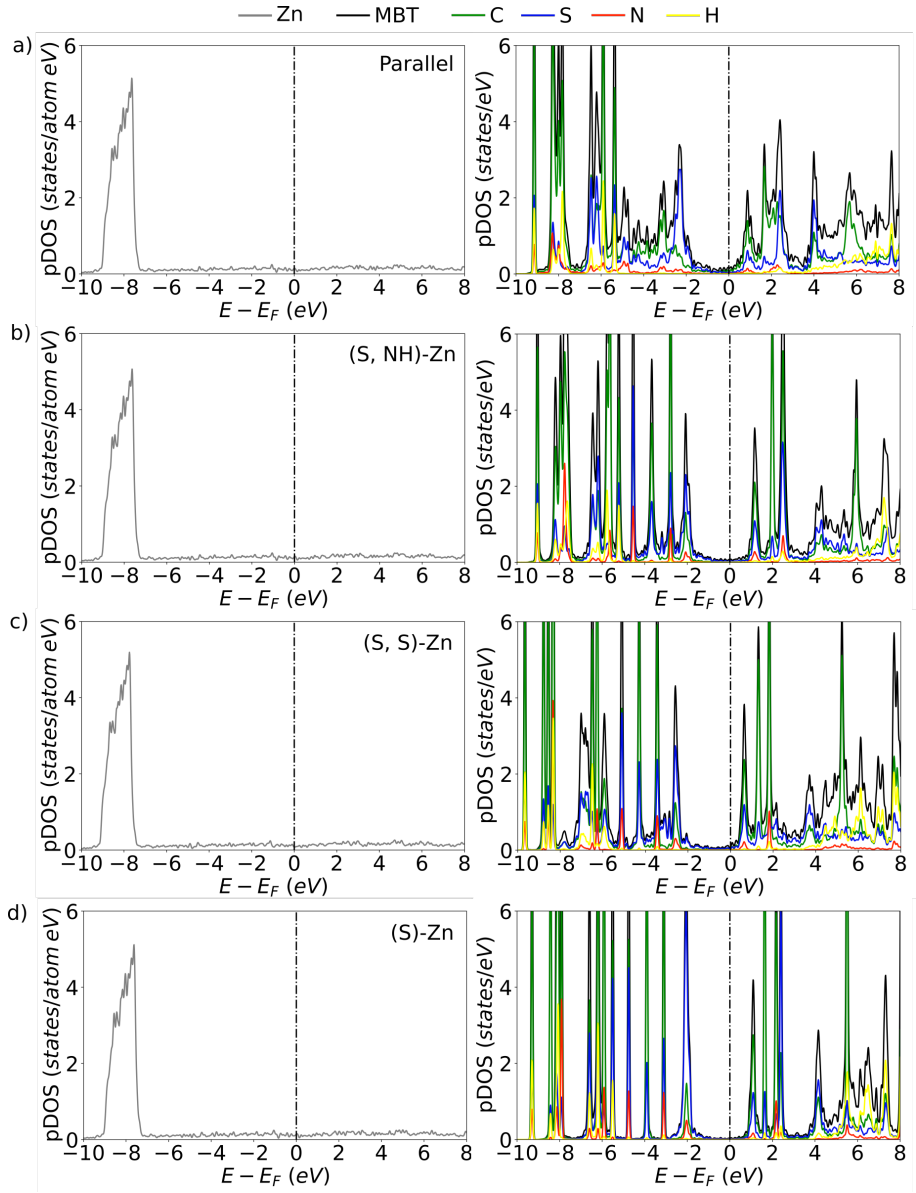

Figure 6.7: Projected density of states (pDOS) of the MBT adsorption configurations on Zn at low coverage (1 $molecule/nm^2$) for (a) parallel case, (b) (S, NH)-Zn, (c) (S, S)-Zn, and (d) (S)-Zn cases. In the first column, the pDOS normalized per Zn atom is depicted for all the cases, whereas the second shows the MBT pDOS, with the corresponding splitting between atoms. The Fermi level (E_F) was shifted to 0 eV and is indicated in each graph by a dashed black line.

states, and their projections indicate that they belong to the MBT HOMO and HOMO-1. In this case, HOMO and HOMO-1 present a similar orbital lobe around the exocyclic S, which in this case enables its bonding to the surface as an extra interaction of the aromatic ring with the surface. The LUMO orbital appeared around 1 eV, mainly composed of C states, and the LUMO+1, which appeared at 1.5 eV, also composed by C states.

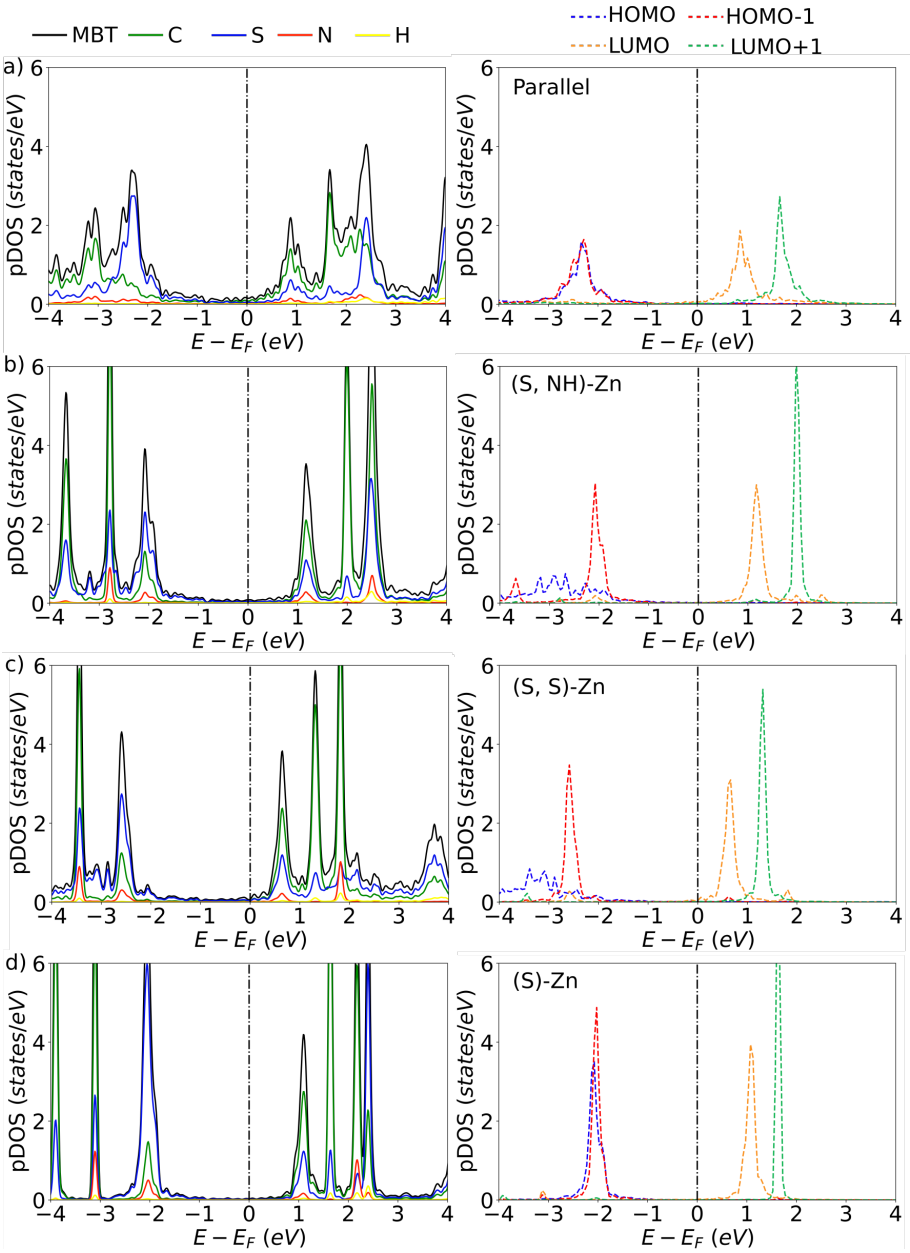

Figure 6.8: Projected density of states (pDOS) of the MBT adsorption configurations on Zn at low coverage (1 $molecule/nm^2$) for (a) parallel case, (b) (S, NH)-Zn, (c) (S, S)-Zn, and (d) (S)-Zn cases. In the first column, the MBT pDOS, with the corresponding splitting between atoms, is depicted for all the cases, whereas the second one corresponds to the projections of the MBT molecular orbitals on the total pDOS. The Fermi level (E_F) was shifted to 0 eV and is indicated in each graph by a dashed black line.

In the (S, NH)-Zn case, due to the weaker interaction in comparison with the parallel case, the pDOS peaks displays sharper peaks. A similar peak than the parallel case appears in the pDOS -2.0 eV, composed mainly for S and C. The peak corresponds to the HOMO-

1, which presents an important lobe in S and facilitates its interaction with the Zn. In contrast, the HOMO appears dispersed along a range of energy, from -4 to -2 eV, which can be attributed to the orientation of the molecular orbital on the MBT atoms. The orientation and shape of the HOMO orbital in the molecule promotes a stronger interaction with the 4s electrons of the Zn, and it spreads out around energies from -4 to -2 eV, and also over the MBT atoms, primary in the C and S atoms.

The distribution of the states in the (S, S)-Zn case is similar to the obtained for the (S, NH)-Zn case but shifted towards more negative energies. This similarity in the pDOS peaks indicates the small reactivity of the endo S, with respect to the Zn, and shows in this case that the bonding with the surface is also established through the exocyclic S. The projections of the molecular orbitals shows the same trend than in the (S, NH)-Zn case, only showing the pDOS peaks shifted to lower energies.

In the vertical adsorption of the (S)-Zn case, the sharper peaks compared with the previous cases aligned with lower adsorption stability found by comparing the adsorption energies E_{ads}. A localized peak around -2.0 eV, mainly formed by S states, belongs to the HOMO-1 and HOMO molecular orbitals from the molecule. The shape and orientation of the orbitals in both HOMO and HOMO-1 states make them very similar toward vertical adsorption. As mentioned above, the higher peak-localized character resembles their not-so-favourable interaction with the Zn states. LUMO and LUMO+1 molecular orbitals appear at energies very similar to the ones reported for the isolated MBT, around 1.0 eV and 1.5 eV, respectively, and showing that they do not take an important part during the bonding of the MBT.

The pDOS for the SAM cases showed in Figure 6.9 demonstrate the higher interaction with the surface with more broadened peaks in both valence and conduction bands. In the (S, NH)-Zn case, the main contributions to the pDOS near the E_F level come from S and C states in both valence and conduction bands. This indicates that the adsorption of the SAM structure on the Zn surface is through the exocyclic S. As in the low-coverage case, the Zn pDOS shows that the inhibitor is mainly interacting with its 4s states, near the E_F

level, and not the 3*d* states, that are located at lower energies around -8 *eV*.

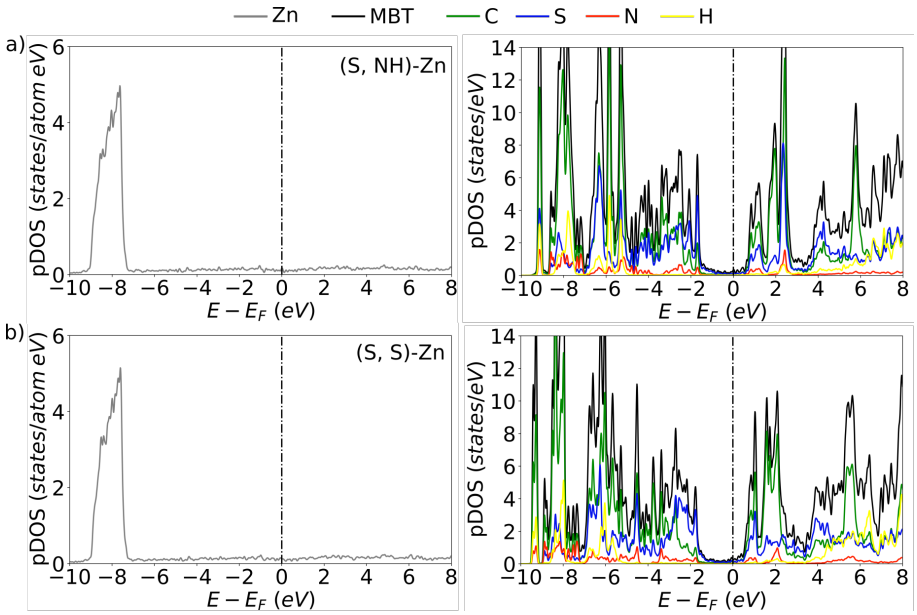

Figure 6.9: Projected density of states (pDOS) of the MBT adsorption configurations on Zn surface at high coverage (3 $molecule/nm^2$) for (a) (S, NH)-Zn, and (b) (S, S)-Zn cases. In the first column, the pDOS normalized per Zn atom is depicted for all the cases, whereas the second one is the MBT pDOS, with the corresponding splitting between atoms. The Fermi level (E_F) was shifted to 0 *eV* and is indicated in each graph by a dashed black line.

The projections of the molecular orbitals for the SAM (S, NH)-Zn case are shown in Figure 6.10. The projections show that the HOMO of the SAM remains at similar energies than in the low-coverage case, around -2 *eV*, and it is composed mainly of S states. However, the HOMO-1 gets spread around energies from -2 to -4 *eV* in the valence band. The spreading of the HOMO-1 can be related to the higher interaction with the surface states and the shape and orientation of the lobs in the orbit. The HOMO-1 orbital resembles the lateral π-π interactions between the inhibitors, and also, the predominant lobs in the exocyclic S can indicate its higher reactivity upon the adsorption. On the other hand, there were no significant changes for the LUMO and LUMO+1 orbitals, which appear around 1.0 *eV*, and they only show the corresponding broadening of the pDOS peaks due to the interaction with the surface.

In the SAM (S, S)-Zn case, a similar behaviour was observed for the pDOS peaks, which show a more dispersed character that agrees with their stronger interaction with the

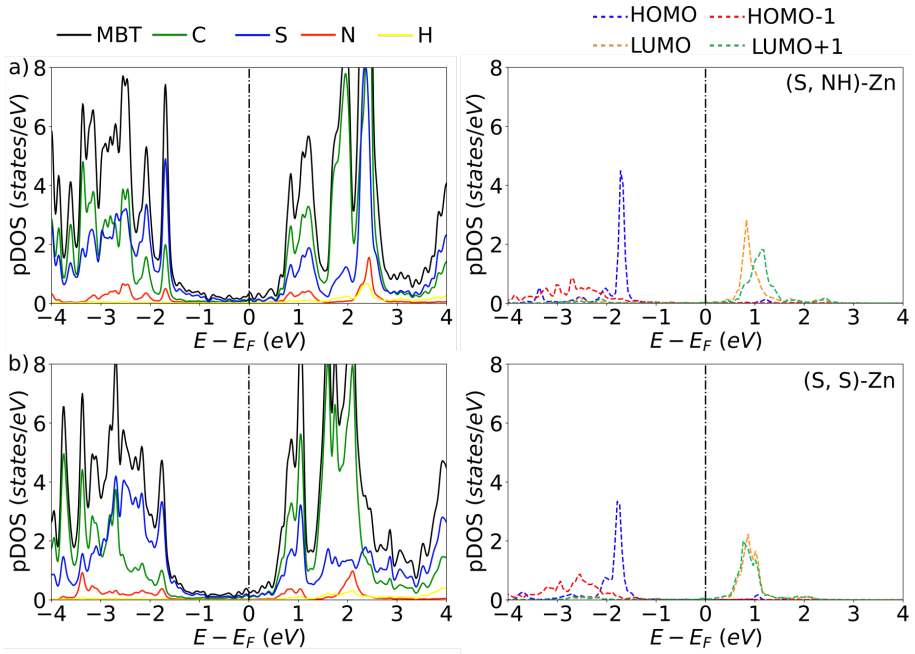

Figure 6.10: Projected density of states (pDOS) of the MBT adsorption configurations on Zn surface at high coverage (3 $molecule/nm^2$) for (a) (S, NH)-Zn and (b) (S, S)-Zn cases. In the first column, the MBT pDOS with the corresponding splitting between atoms is depicted for all the cases, whereas the second one corresponds to the projections of the MBT molecular orbitals on the total pDOS. The Fermi level (E_F) was shifted to 0 eV and is indicated in each graph by a dashed black line.

surface. As in the SAM (S, NH)-Zn case, the main contributions to the pDOS near the E_F correspond to S and C states in both valence and conduction bands. In this case, the projections of the SAM orbitals also showed that the HOMO-1 orbitals are responsible for the interaction with the surface, where the exocyclic S atoms bind to the Zn surface, and it gets spread in energies from -2 to -4 eV. The LUMO and LUMO+1 orbitals, in this case, appear in energies slightly below 1 eV and with both peaks at the same energy. This change can be attributed to higher participation in the bond between the SAM and the surface, but not as important as the HOMO-1 orbital.

The electronic structure was also analyzed in terms of the induced charge density, $\rho_{ind}(\vec{r})$, which was computed for all the cases at low and high coverage to understand the charge redistribution due to the adsorption, as performed in chapter 4. In Figure 6.11, the $\rho_{ind}(\vec{r})$ is depicted for all coverages. The figure's red and blue colours represent the positive (deficit) and negative (excess) induced charge density due to adsorption.

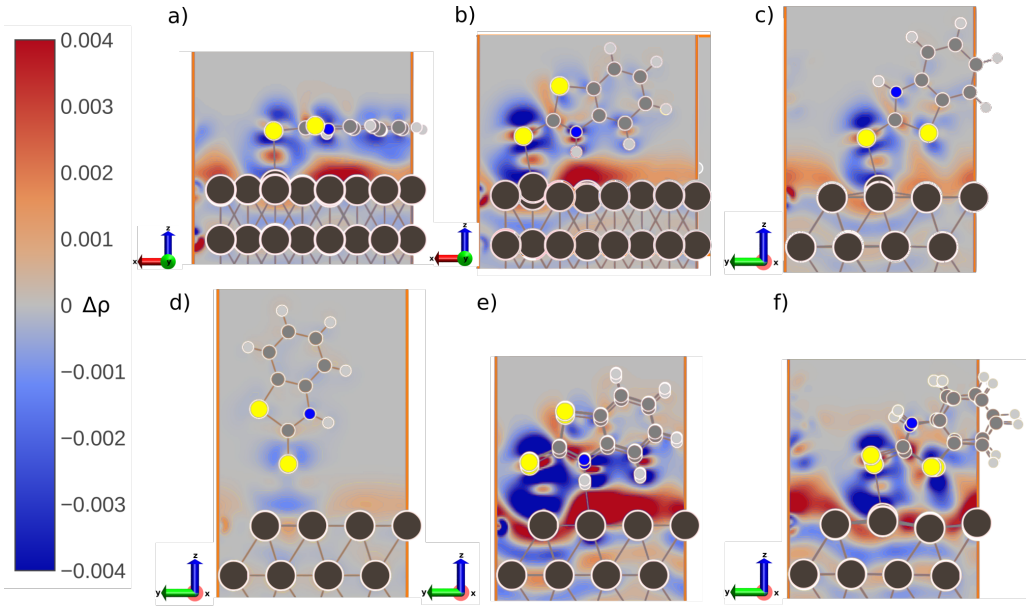

Figure 6.11: The induced charge density ($\rho_{ind}(\vec{r})$) due to the MBT adsorption on Zn surface for the (a) parallel, (b) (S, NH)-Zn, (c) (S, S)-Zn, (d) (S)-Zn, (e) (S, NH)-Zn (SAM case), and (f) (S, S)-Zn (SAM case) adsorption cases on Zn(0001) surface. Pink, blue, yellow, light, and dark gray-colored spheres represent the atoms of Zn, N, S, H, and C. Blue (red) colors represent a deficit (excess) of electrons

The $\rho_{ind}(\vec{r})$ for the parallel case confirms the formation of a chemical bond between the S atom and the Zn surface atom. Since the $\rho_{ind}(\vec{r})$ accumulation is present between the S atom and the Zn, it can be concluded that the chemical bond formed corresponds to a covalent one. The interaction between the aromatic ring and the surface can also be observed in the negative $\rho_{ind}(\vec{r})$ around the atoms of the aromatic ring and the positive $\rho_{ind}(\vec{r})$ above the Zn surface atoms close to the aromatic ring, and no sharing of electrons is observed, indicating a non-covalent interaction.

In the (S, NH)-Zn case, the covalent bond between the S and the Zn is also observed, besides the positive $\rho_{ind}(\vec{r})$ induced by the formation of this bond on the surface. $\rho_{ind}(\vec{r})$ also confirmed that the interaction between the NH group is not as intense as the one induced by the exocyclic S. The covalent bond formation between the exocyclic S and Zn also appeared in the (S, S)-Zn case, being mostly the only interaction presented in the system, as the $\rho_{ind}(\vec{r})$ slightly changed for the other endo S, and as was also observed for

the top adsorption, where there is a slightly negative $\rho_{ind}(\vec{r})$ around the S atoms, without the formation of chemical bond.

In the SAM cases, a higher redistribution of $\rho_{ind}(\vec{r})$ can be observed in the system, but as in the low-coverage cases, the main feature observed was the negative and positive $\rho_{ind}(\vec{r})$ around the exocyclic S and Zn, indicating the formation of the covalent chemical bond between them, in the three molecules that composed the SAM. Also, a positive $\rho_{ind}(\vec{r})$ is observed between the aromatic rings, particularly in the thiazole ring of the molecule, which shows the enhanced π-π lateral interactions of the inhibitors, compared with their corresponding modes at low-coverage. In the SAM (S, NH)-Zn case, besides the covalent bond formation, there is also the non-covalent interaction between the NH and H's of the rings with the Zn surface, as in the low-coverage case. Similarly, in the (S, S)-Zn case, the endo S does not show chemical bond formation with the surface.

The different $\rho_{ind}(\vec{r})$ patterns in all the cases suggest that the most reactive atoms in the MBT are the exocyclic S, which induces the covalent bond formation, the aromatic ring and the NH group. The endo S does not appear to have a strong effect in the MBT adsorption, as the other parts of the molecule. The conjunction of all these interactions with the lateral π-π determined the stability of the MBT adsorption on the surface.

6.4 Results for ABT

Adsorption stability

The stability trend for low coverage ABT adsorption in terms of E_{ads}, as one can see in Figure 6.3, also shows the parallel case as the most stable one, followed by the (N, NH_2)-Zn, (S, NH_2)-Zn, and (NH_2)-Zn cases. The final adsorption configurations at low coverage for the ABT adsorption are shown in Figure 6.12. As in the case of MBT, the higher stability for the parallel adsorption can be related to the interactions between the Zn surface states and the aromatic ring π electrons of the molecule. It is remarkable the higher stability

of the (N, NH_2)-Zn against the (S, NH_2), where even if the two N groups could compete (and thus "screen" each other) for the adsorption sites, the (N, NH_2)-Zn is most favorable one. Finally, in the vertical adsorption case (NH_2)-Zn, the E_{ads} value suggests a weak interaction with the surface, as in the MBT case, probably leading to physisorption.

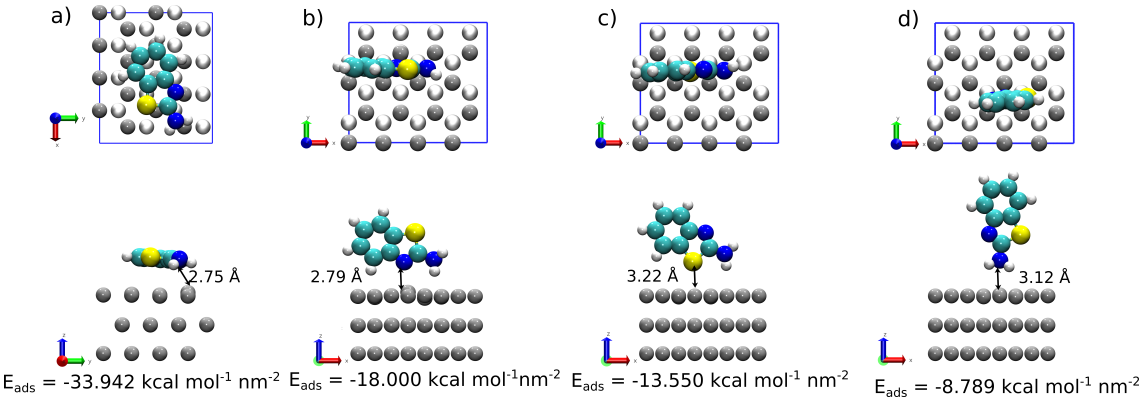

Figure 6.12: Top and side view for the final adsorption configurations at low coverage (1 $molecules/nm^2$) obtained for ABT on Zn surface: a) parallel, b) (N, NH_2)-Zn, c) (S, NH_2)-Zn, and d) (NH_2)-Zn on top site cases. White, cyan, yellow, blue, and gray colored spheres represent H, C, S, N, and Zn atoms. On the top view of each case, lighter color spheres represent the second outermost Zn layer. The adsorption energy (E_{ads} [$kcalmol^{-1}nm^{-2}$]) for each case is shown below the side view of the structure. The nearest distances between the adsorbed molecules and the Zn surface are shown in the side views. Some Zn layers are suppressed for clarity.

The pulled-out effect in the low-coverage case shows a displacement of approx. 0.21 Å for the Zn surface atom by the N in the ring in the parallel case, where the H atoms of the NH_2 group are also displacing by approx. 0.1 Å the interacting Zn surface atoms towards the inner layers. In the (N, NH_2)-Zn case, the N of the aromatic ring displaced the Zn surface atom by 0.35 Å, while the H atoms in the NH_2 move it towards the inner Zn layers by 0.17 Ådue to the repulsion between the atoms. For the (S, NH_2) and (NH_2)-Zn, we did not observe this pulled-out effect on the Zn surface atom, but the repulsion between the H's in the NH_2 and the surface.

The high-coverage cases forming a SAM are shown in Figure 6.13. The stability trend determined by the E_{ads} shows the (S, NH_2)-Zn case as the most stable one. As we observed in the MBT SAM case in the previous section, the presence of the other ABT molecules also enhanced the $\pi - \pi$ interaction between the SAM molecules and, thus, the adsorption

on the surface. Due to the $\pi - \pi$ stacking interaction, each ABT molecule gains -6.2 $kcal\ mol^{-1}\ nm^{-2}$ in the (N, NH_2)-Zn case, and -9.1 $kcal\ mol^{-1}\ nm^{-2}$ in the (S, NH_2) one.

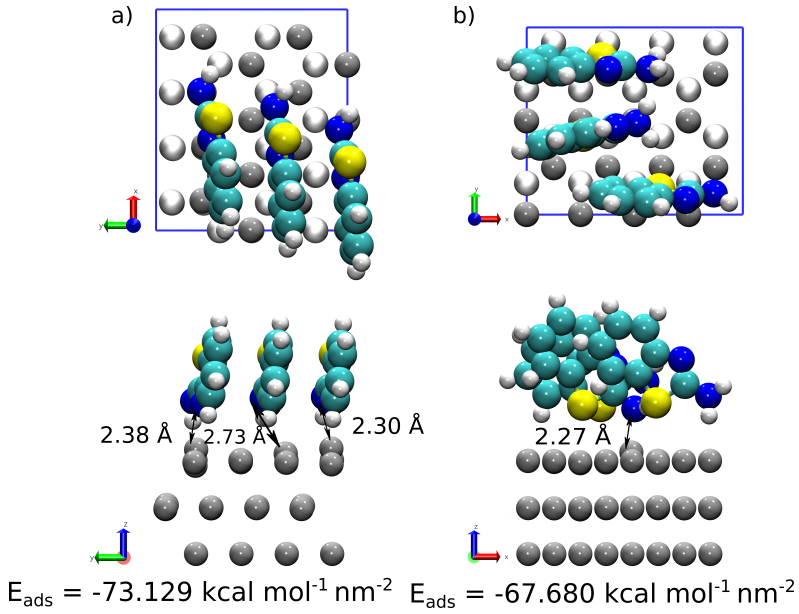

Figure 6.13: Top and side view for the optimized adsorption structures at high-coverage (3 $molecules/nm^2$) obtained for ABT on Zn(0001): a) (N, NH_2)-Zn and b) (S, NH_2)-Zn cases. White, cyan, yellow, blue, and gray colored spheres represent H, C, S, N, and Zn atoms. On the top view of each case, lighter color spheres represent the second outermost Zn layer. The adsorption energy (E_{ads} $[kcalmol^{-1}nm^{-2}]$) for each case is shown below the side view of the structure. The nearest distances between the adsorbed molecules and the Zn surface are shown in the side views. Some Zn layers are suppressed for clarity.

The $\pi - \pi$ stacking interaction enhances the pulling-out effect in the Zn atom from the surface. The Zn surface atom is displaced from the surface by approximately 0.49 Å in the (N, NH_2)-Zn, and 0.44 Å in the (S, NH_2)-Zn cases. We also observed some repulsion between the Zn surface atoms near the H atoms of the NH_2 group. For the (N, NH_2)-Zn case, the Zn surface atoms are displaced by 0.29 Å towards the inner layers. This effect is less intense than in the low coverage adsorption, where the Zn surface atom is displaced towards the inner layers by 0.17 Å. In the case of (S, NH_2)-Zn, the repulsion between the H's of the NH_2 and the Zn surface atoms was similar to the low coverage case, with a displacement of approx. 0.1 Å towards the inner layers, but the repulsion between the molecules in the SAM leads to a more disorganized structure, where those H atoms in the NH_2 seem to play a crucial role.

Electronic structure

The pDOS and the frontier molecular orbitals of isolated ABT are shown in Figure 6.14. As in the MBT case, the pDOS peaks present a localized character, where the main contributions near the E_F are due to C states in both the valence and the conduction bands. The molecular orbitals plotted present a typical aromatic character, with delocalization of the electrons around the aromatic ring, similar to the obtained by the MBT case in section 6.3. The difference between both inhibitors is the exocyclic amine NH_2 group in ABT and the exocyclic S in MBT. Comparing both molecular orbitals around these exocyclic atoms (Figure 6.6 vs. Figure 6.14), particularly the HOMO and HOMO-1, show larger lobs for the exocyclic S than the NH_2, which can lead to a lower reactivity of the lower one upon adsorption on the surface.

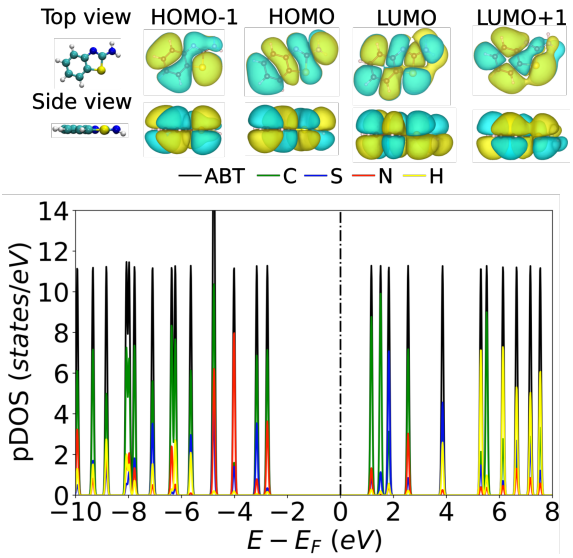

Figure 6.14: Projected density of states (pDOS) of the isolated ABT molecule, showing the molecular orbitals corresponding to the HOMO-1, HOMO, LUMO, and LUMO+1 orbitals. The Fermi level (E_F) was aligned normalized to 0 eV. E_F is indicated by a vertical dashed black line.

The pDOS for the low-coverage systems is depicted in Figure 6.15. As in the MBT case, the pDOS of the Zn states were normalized by the number of atoms to be compared with the rest of the states. The pDOS also reveals a similar behaviour to the MBT case for Zn states, with the 3d states appearing around -8.0 eV, and the contribution of the 4s

states crossing the E_F level.

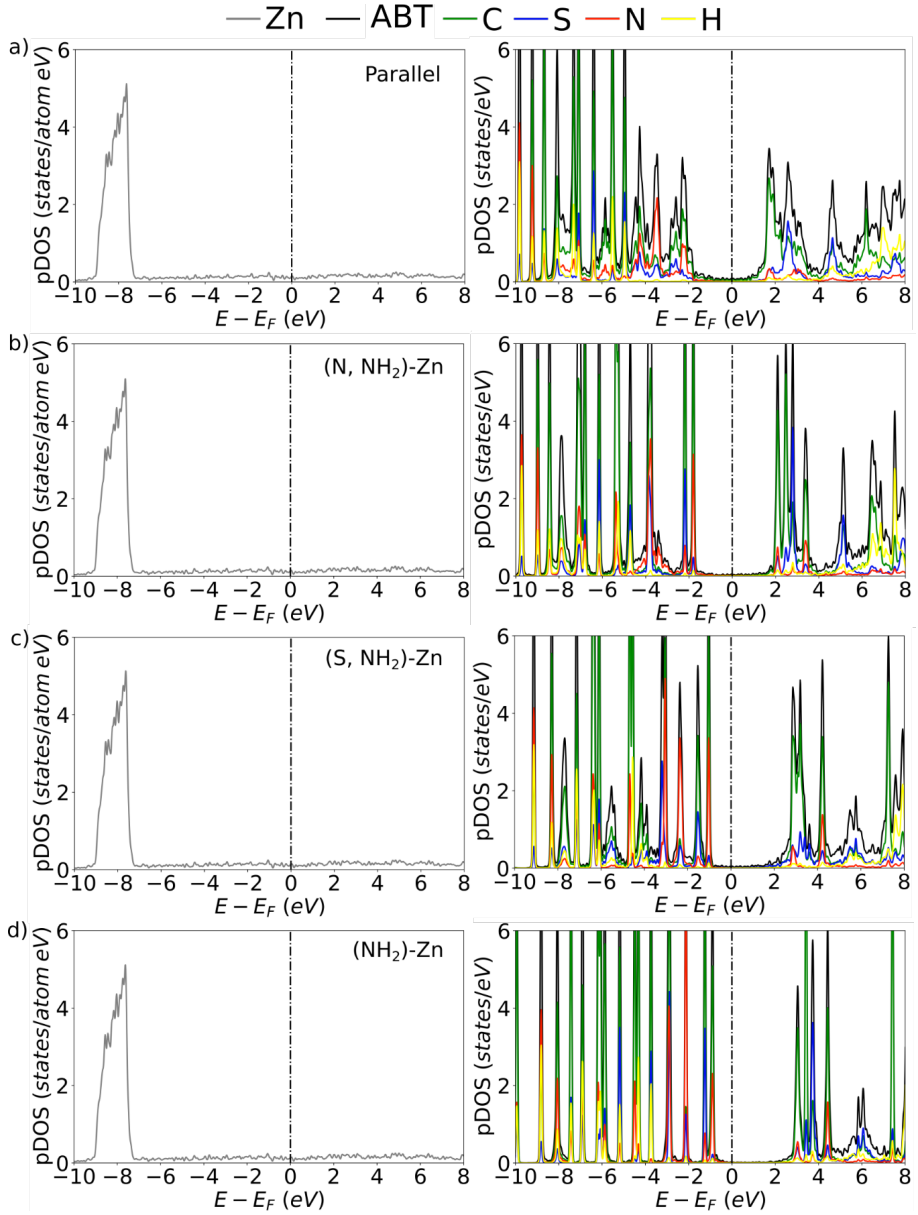

Figure 6.15: Projected density of states (pDOS) of ABT adsorption configurations on Zn surface at low-coverage (1 $molecule/nm^2$). (a) corresponds to the parallel case, (b) (N, NH_2)-Zn, (c) (S, NH_2)-Zn, and (d) (NH_2)-Zn cases. In the first column, the pDOS normalized per Zn atom is depicted for all the cases, whereas the second one is the ABT pDOS, with the corresponding splitting between atoms. The Fermi level (E_F) was shifted to 0 eV and is indicated in each graph by a dashed black line.

As shown in chapter 4 and section 6.3, the shape of the peaks in the pDOS reflects the strength of the interaction between the molecule and the metal. In this sense, the parallel configuration presents the pDOS peaks with a larger broadening than the vertical

adsorption, which presents smaller adsorption energy and, therefore, a weaker interaction with the surface. The pDOS peaks for the parallel case near the E_F mainly correspond to C states, appearing around -2.5 eV in the valence band and 2.0 eV in the conduction band. The projections of the ABT molecular orbitals, depicted in Figure 6.14, show that the HOMO and HOMO-1 form the pDOS peaks at -2.5 eV and -3.0 eV. Those pDOS peaks are mainly formed by C states. The projections showed peaks more broad for the HOMO-1 and HOMO, appearing at a similar range of energies as in the isolated ABT. The large broadening indicates the interaction between the π and surface states. This broadening also appears for the LUMO and LUMO+1 states, with both peaks almost at the same energy, around 2 eV.

In the (N, NH_2)-Zn case, the pDOS peak at -2.0 eV corresponds mainly to C and N states, and the one at -2.5 eV, formed by S and C states. Those peaks are similar in energy and shape to the ones of the isolated ABT, and the projections of the ABT orbitals show that they belong to the HOMO and HOMO-1 orbitals, respectively. On the other hand, the LUMO and LUMO+1 orbitals, mainly formed by C states, appear to shift towards more positive energies than in the parallel and isolated molecule cases.

A similar behaviour appeared for the (S, NH_2)-Zn and the (NH_2)-Zn cases, where the LUMO and LUMO+1 orbitals appeared at higher energies. In both cases, the pDOS peaks in the valence band are also shifted towards higher energies, appearing around -1.0 eV for the HOMO and -1.5 eV for the HOMO-1 orbitals. The energy shift may be related to the adsorption stability determined by the E_{ads}, showing that the more significant the shift in the LUMO and LUMO+1 orbitals, the less stable the adsorption. This change in LUMO and LUMO+1 orbitals also indicates a tendency for less electron affinity in the ABT.

The pDOS of Zn and ABT states for the high-coverage cases are plotted in Figure 6.17. In the (N, NH_2)-Zn case, the predominant peaks in the valence band close to the E_F level correspond mainly to C and N states, with the first peaks appearing at -2.0 eV in the valence band and 1.5 eV in the conduction band. The pDOS peaks in the valence band correspond to the HOMO and HOMO-1 orbitals, as shown in Figure 6.18. On the other hand, LUMO

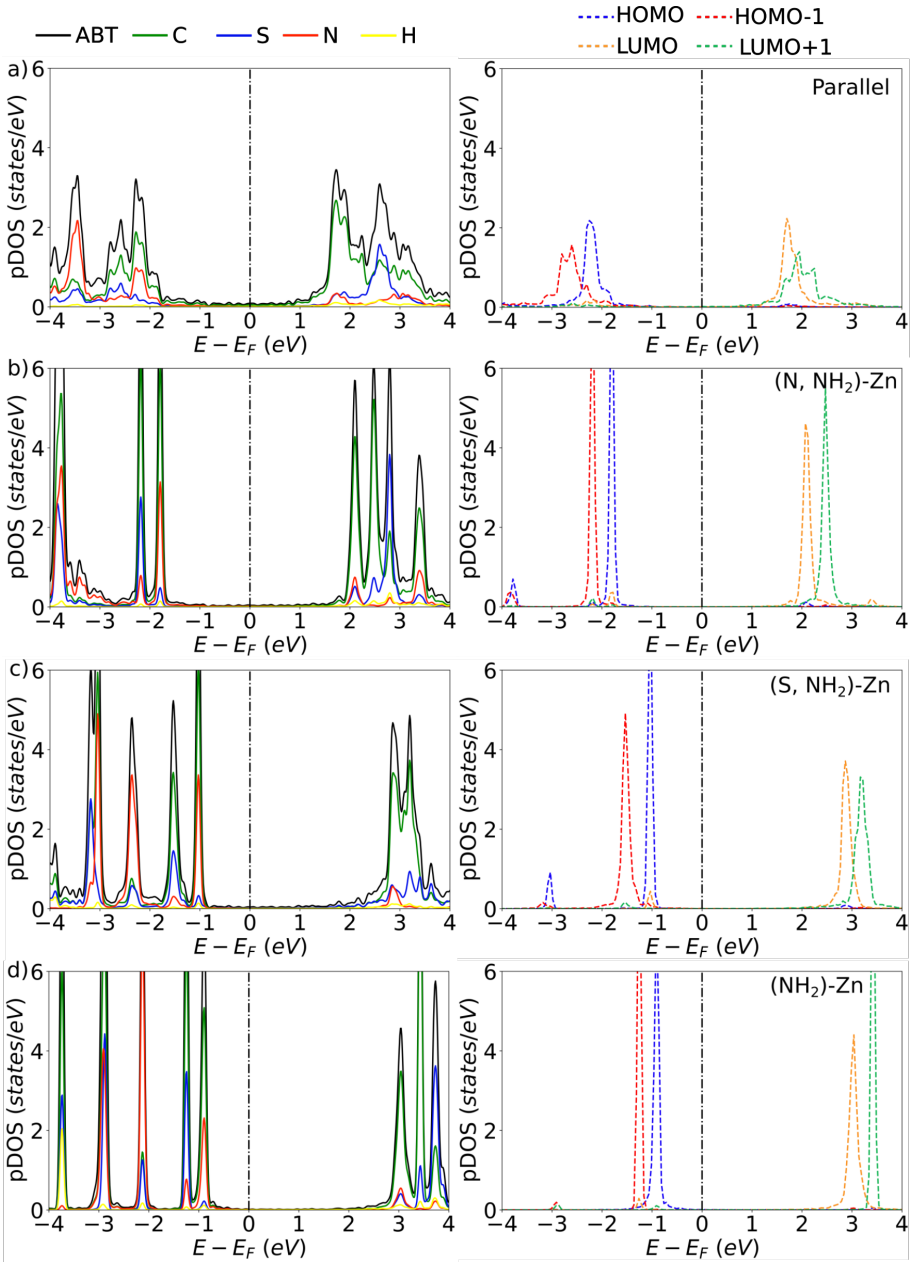

Figure 6.16: Projected density of states (pDOS) of ABT adsorption configurations on Zn at low-coverage (1 $molecule/nm^2$) for the a) parallel, b) (N, NH_2)-Zn, c) (S, NH_2)-Zn, and d) (NH_2)-Zn cases. In the first column, the pDOS normalized per Zn atom is depicted for all the cases, whereas the second one represents the projections of the ABT molecular orbitals on the total pDOS. The Fermi level (E_F) was shifted to 0 eV and is indicated in each graph by a dashed black line.

and LUMO+1 appear at energies of around 1.5 eV in the conduction band. Even if some peaks appeared with more broadening than in the low-coverage cases, the presence of very localized peaks in the pDOS could be an effect of the formation of a more distorted SAM adsorption at the surface, as can be seen in Figure 6.13.

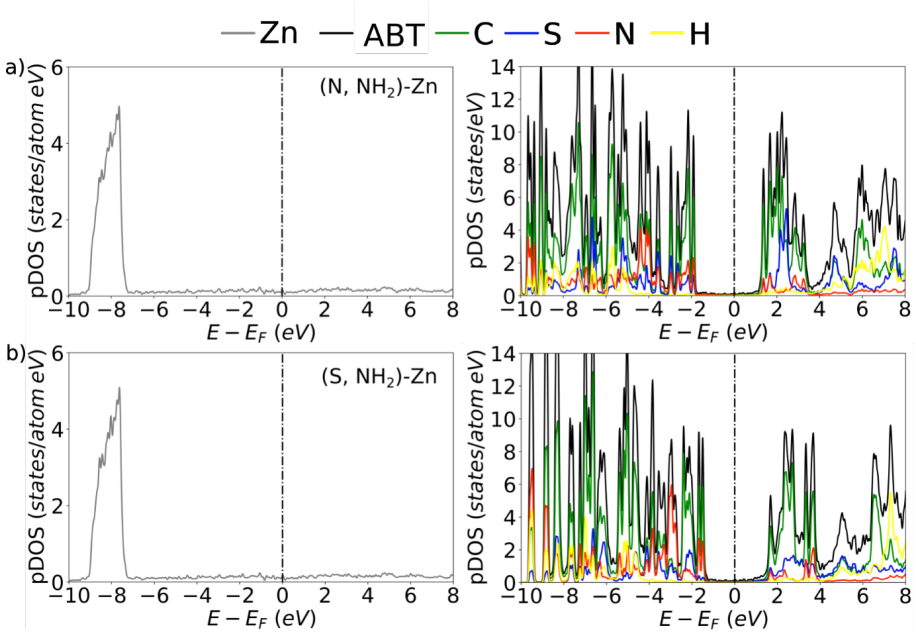

Figure 6.17: Projected density of states (pDOS) of the ABT adsorption configurations on Zn surface at high-coverage (3 $molecule/nm^2$) for a) (N, NH_2)-Zn and b) (S, NH_2)-Zn cases. In the first column, the pDOS normalized per Zn atom is depicted for all the cases, whereas the second one is the ABT pDOS, with the corresponding splitting between atoms. The Fermi level (E_F) was shifted to 0 eV and is indicated in each graph by a dashed black line.

The (S, NH_2)-Zn pDOS also presents localized peaks due to the distorted ABT structure on the surface, with the first pDOS peaks in the valence band appearing in energies around -1.5 eV, and corresponding to C and N states. This peak corresponds to the HOMO of the adsorbed ABT structure, and the peak is located next to this one to the HOMO-1 orbital. The LUMO and LUMO+1 orbitals appear from energies close to 1.5 eV and 2.5 eV in the conduction band. The broadening of these orbitals can be related to the more distorted ABT structure on the surface.

The $\rho_{ind}(\vec{r})$ for all the adsorption cases is depicted in Figure 6.19. As in the MBT adsorption, all the adsorption configurations present a different $\rho_{ind}(\vec{r})$ that reflects the interaction with the surface. However, contrary to the MBT case, the formation of a covalent bond between the NH_2 group and the surface was not observed for ABT. This result underlined the higher reactivity of the exocyclic S against the Zn surface, compared with the NH_2 group.

In the parallel case, the adsorption of the molecule leads to a physisorption on the

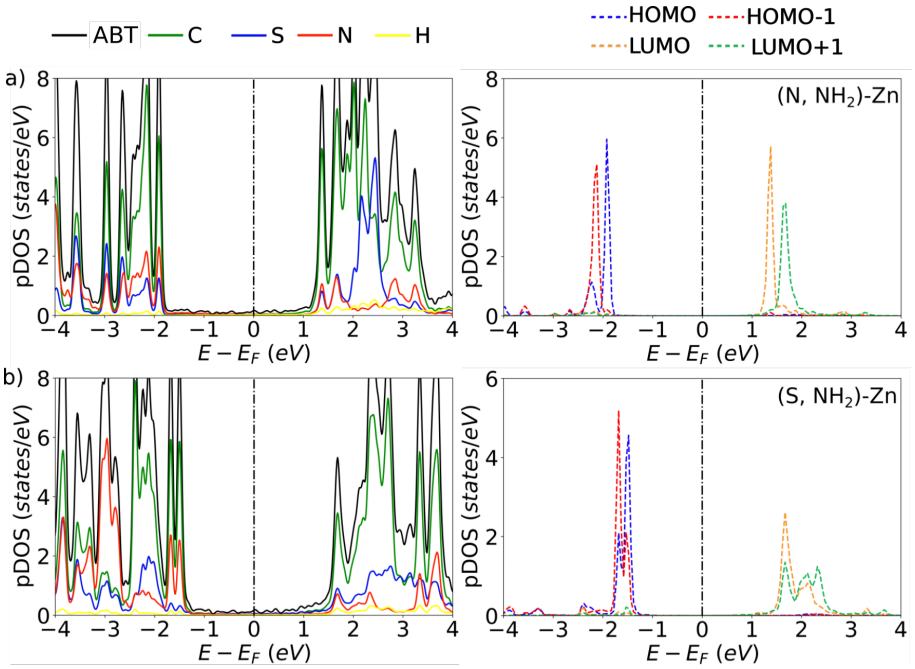

Figure 6.18: Projected density of states (pDOS) of the ABT adsorption configurations on Zn surface at high-coverage (3 $molecule/nm^2$) for a) (N, NH_2)-Zn b) (S, NH_2)-Zn cases. In the first column, the MBT pDOS is plotted with the corresponding splitting between atoms, and in the second one, the projections of the molecular orbitals of the ABT adsorbed on Zn. The Fermi level (E_F) was shifted to 0 eV and is indicated in each graph by a dashed black line.

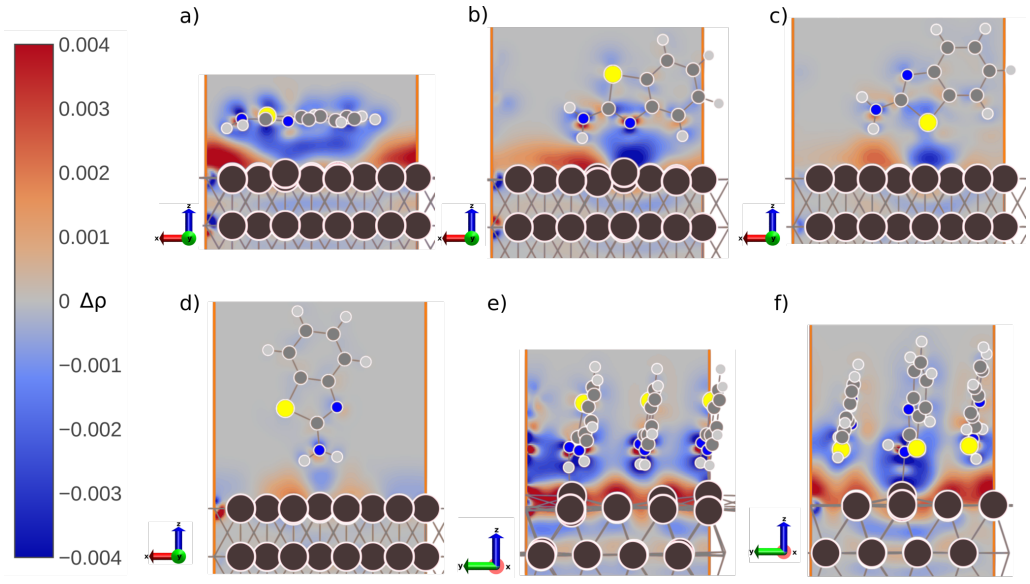

Figure 6.19: The induced charge density ($\rho_{ind}(\vec{r})$) due to the ABT adsorption on Zn surface for a) parallel, b) (N, NH_2)-Zn, c) (S, NH_2)-Zn, d) (NH_2)-Zn, e) (N, NH_2)-Zn (SAM case), and f) (S, NH_2)-Zn (SAM case) cases. Brown, blue, yellow, light, and dark gray-colored spheres represent the atoms of Zn, N, S, H, and C. Blue (red) color represents deficit (excess) of $\rho_{ind}(\vec{r})$.

surface, with a non-covalent interaction between the π electrons of the ABT and the Zn surface states. In the (N, NH_2)-Zn case, the primary interaction is through the N of the aromatic ring, which induces negative $\rho_{ind}(\vec{r})$ on the Zn surface interacting atom, but without the formation of a chemical bond. However, this interaction is strong enough to pull out the surface plane of the Zn atom.

In the (S, NH_2)-Zn case, there is positive $\rho_{ind}(\vec{r})$ on the atoms below the NH_2 group, and negative $\rho_{ind}(\vec{r})$ around the S atom and the Zn surface atoms below it. However, as shown in the previous case, the interaction does not lead to forming a chemical bond. Finally, the last adsorption configuration at low coverage, the (NH_2)-Zn, shows a slightly $\rho_{ind}(\vec{r})$ on its atoms and the Zn surface, indicating its weaker interaction with the surface, and the non-covalent interactions with the Zn surface.

For the cases at high coverage, the $\rho_{ind}(\vec{r})$ is more intense, indicating a higher interaction with the surface. As the cases at low coverage, there is the formation of a covalent chemical bond between the ABT and the Zn surface in the (N, NH_2)-Zn case, but in the (S, NH_2)-Zn case, due to the distorted adsorption, which gets NH_2 group closer to the Zn surface, there is the slight formation of a covalent bond with the surface. In both (S, NH_2)-Zn and (N, NH_2)-Zn cases, there is positive $\rho_{ind}(\vec{r})$ above the Zn surface atoms and between the atoms of the aromatic rings in the molecules. The last one represents a confirmation of the lateral π-π interaction between the inhibitors; nonetheless, as it is suggested by the distorted structure of the (S, NH_2)-Zn case, the π-π interactions might be weaker than in the MBT high coverage cases.

6.5 XPS measurements

In this section, the experimental XPS spectra for both inhibitors are correlated with the adsorption configuration of the inhibitors on the surface obtained in our DFT calculations. The experimental partners at RMIT University performed the XPS measurements, and the details of the experimental measurements are shown in [21]. From the XPS data , the

chemical environments of S $2p$ and N $1s$ were analysed as fingerprints to determine the bonding states of both inhibitor molecules on the surface. These chemical environments were chosen as the fingerprints due to previous studies suggesting the importance of the heteroatoms in the inhibitor-surface interaction [269].

In Figure 6.20 and Figure 6.21, the XPS spectra for the S $2p$ and N $1s$ of the chemical powder (reference) and the inhibited ZE surface for the MBT and ABT cases, respectively, are shown. In both XPS spectra, the bottom panels show the XPS spectra for each inhibitor in dissolution with metal ions to underlie the interaction between them. In Figure 6.20, the S $2p$ spectrum of the MBT powder was decomposed with two main components, the endocyclic S (S in the aromatic ring) (164.3 eV) and exocyclic S (162.2 eV). Two different N environments can be observed in the spectrum, corresponding to the imine N (C=N) and amine N (C-NH). The imine environment, which corresponds to the thione form, is suggested to be the predominant in the solid state [270], and as indicated by the experimental XPS spectra, particularly the peak component of amine at 400.8 eV. Additionally, oxidised S was also observed in the XPS spectra.

The S $2p$ spectrum for the inhibited ZE surface shows a larger binding energy shift of the exocyclic S (162.6 eV) by +0.4 eV than the reported for the powder. This peak corresponds to the thiolate form, which comes from MBT's thione/thiol form interacting with the Zn atom. Also, in the N $1s$ spectra, one main peak corresponding to the NH group appears at 399.7 eV, which is shifted by 0.7 eV compared with the MBT reference (399.0 eV). This shift in the binding energy corresponds to the bond formation between the N atom and the Zn surface. However, the reduction of the peak's intensity that belongs to the protonated N indicates that the thiolate form predominates during the adsorption. Therefore, the S $2p$ and N 1 s spectra obtained by the experimental partners suggest an adsorption configuration of the molecule where both S and N are bonded to the surface.

The DFT results are aligned with the experimental findings, showing that the most stable adsorption case for MBT is the (S, NH)-Zn configuration, where both S and NH are bonded to the surface. As reported in Figure 6.3, between the two most stable cases,

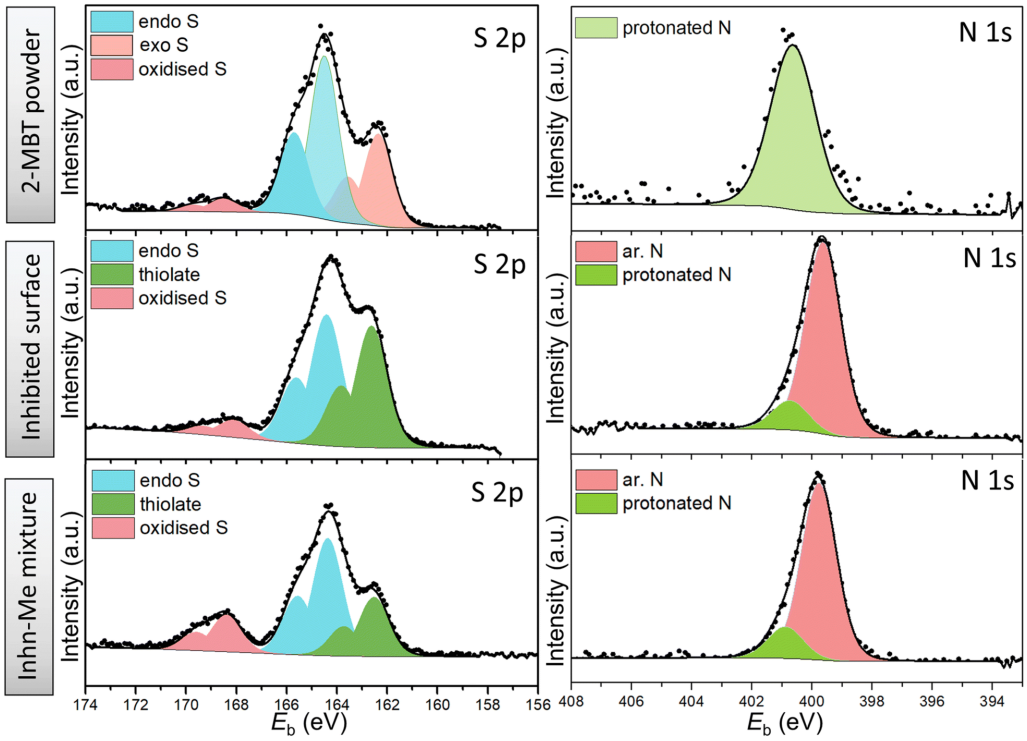

Figure 6.20: High-resolution XPS spectra of S 2*p* and N 1*s* of MBT powder (reference), ZE surface treated with MBT and precipitates of inhibitor solution mixed with $ZnCl_2$. Adapted from [21] with authorization.

the (S, NH)-Zn presents the more negative adsorption energy, which indicates its higher adsorption stability. The electronic structure analysis also showed the formation of covalent bonding between the inhibitor and the surface, which can also be confirmed by the changes in the XPS binding energies of S 2*p* and N 1*s*.

The matching between the experimental and DFT results could have a better match using the thiolate form of the molecule. However, as mentioned in chapter 4, the main difference observed between the adsorption of the thiolate/thione form of the inhibitors is the higher adsorption energies, without dramatic changes in the adsorption geometries [167]. For ABT, the XPS Figure 6.21 shows a change in the binding energy of the S 2*p* peak from the powder (164.1 *eV*) to the ZE substrate adsorption, where the peak is shifted towards lower binding energies (161.9 *eV*). This shift in binding energy suggests the formation of a chemical bond between the S and the Zn surface. However, the N 1*s* peak does not present any changes between the powder and the ZE substrate, indicating no bond formation between the aromatic N and the NH_2 group with the surface.

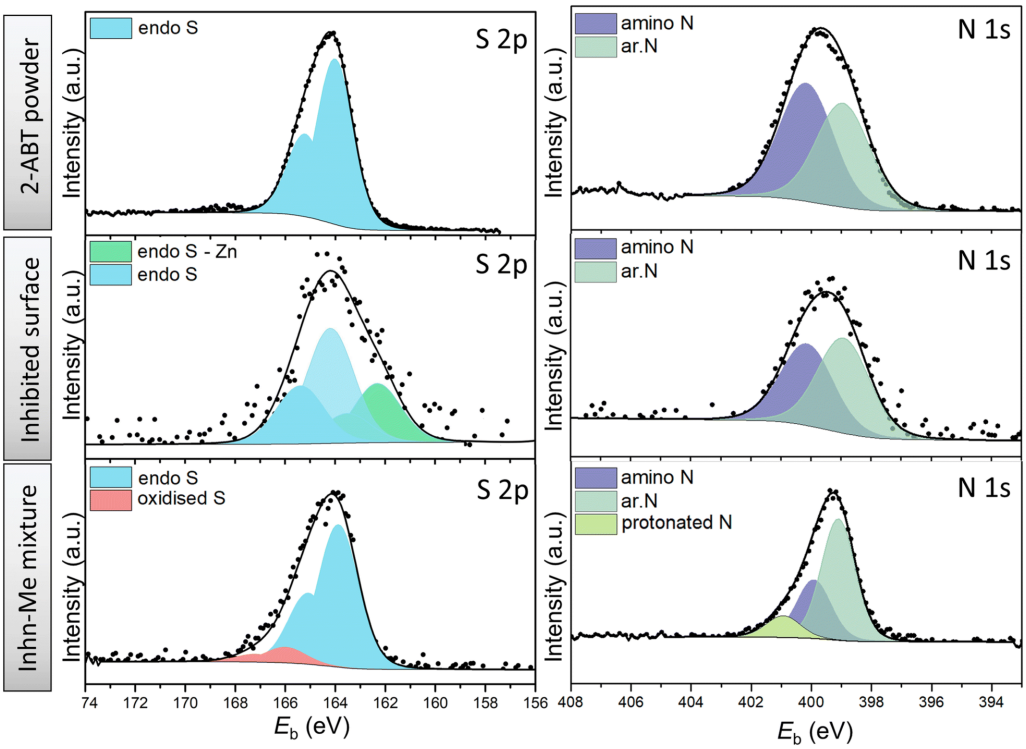

Figure 6.21: High-resolution XPS spectra of S 2*p* and N 1*s* of ABT powder (reference), ZE surface treated with ABT and precipitates of inhibitor solution mixed with $ZnCl_2$. Adapted from [21] with authorization.

On the other hand, our DFT results suggested the (N, NH2)-Zn adsorption configuration as the most stable case on the Zn surface, which is not in agreement with the XPS findings since it indicates the (S, NH_2)-Zn one. However, the difference in adsorption energy between both adsorption configurations is minimal. Therefore, it is complicated to conclude which adsorption configuration is the one observed in the XPS experiment from a theoretical point of view.

6.6 Conclusions

Comparing the results obtained for the two inhibitors at low and high coverage, the adsorption of MBT was found to be more energetically favourable on the Zn surface. Both molecules adopt a parallel configuration at low coverage, where the π orbitals of the ring interact with the Zn surface states. Electronic structure analysis reveals a covalent chemical bond formation in the MBT adsorption case between the exocyclic S and the Zn surface,

contributing to the stabilization of adsorption on the surface. In the case of ABT, only non-covalent interactions are observed.

When the inhibitor coverage is increased on the surface, the molecules adopt a tilted configuration, which is enhanced by the $\pi - \pi$ stacking and contributes to the adsorption stabilization. In the MBT case, the SAM presents an ordered array on the surface, with the (S, NH)-Zn adsorption configuration as the most favourable one on the surface. However, in the ABT case, the SAM formation presents some structural distortions that are more pronounced in the (S, NH_2)-Zn case, and that leads to the formation of a chemical bond between the NH_2 group and the Zn interacting atom. In the ABT adsorption at high coverage, the (N, NH_2)-Zn was found as the most stable one, but close in stability to the (S, NH_2)-Zn case.

The synergy between XPS measurements and DFT results allows for the identification and validation of the inhibitor structure when it adsorbs on the surface. In this case, it was possible to correlate the structure of MBT experimentally and theoretically, thereby obtaining more details at the atomic level that complement both aspects. However, in the case of ABT, the minimal difference between the adsorption energies prevented the correlation of the observed structure with DFT and experimental results from XPS.

Finally, the literature reveals MBT's ability to form complexes with Zn at the experimental pH conditions. The higher displacement of the Zn surface atom by the MBT could provide insights into the formation of these complexes, but an aqueous medium must be considered for that.

Section 7

Discussion, Conclusions and Future Work

7.1 Discussion

In this thesis, firstly, the main gaps present in the corrosion inhibition (CI) modelling are discussed in the literature review chapter. In this regard, six important aspects (A) that the modelling needs to consider in order to describe the CI process realistically were identified: (A1) the electronic properties of the isolated inhibitors, (A2) the interaction of the inhibitor with the surface, (A3) the surface model, (A4) the effect of anodic and cathodic zones on the surface, (A5) the solvent effects, and (A6) the electrodes' potential effects and how it shapes the inhibitor-inhibitor interactions. Aspects A1-A3 are usually considered in the reported CI modelling literature, while A4-A6, as well as some more complex surface models in A3, are not.

Most of the works in the literature are mainly intended to support experimental results.

For these works, the central aspect is to use A1 to correlate these properties with experimental CI performance using several correlation techniques. However, in these works, the explicit inhibitor adsorption on the surface is not considered, which cannot accurately describe the CI processes. Some other works include the explicit interaction between the inhibitor and the surface, using either bare metallic slabs, or more complex surface models, using oxidized surfaces, and thus addressing aspects A2-A3. The more complex surface models better account for the interactions between the inhibitor and the surface but also increase the simulation's complexity and computational cost, restricting the system's size and, therefore, limiting its application to CI modelling.

In the case of the solvent effects, which affects the chemical and physical properties of the inhibitors and electrolytes present in the media, the most common approach reported is the implicit solvent model, where the inhibitor is investigated either isolated or adsorbed on the surface. While these models can offer significant insights into the solvation process, the lack of explicit interaction with solvent molecules is a drawback. The explicit interaction with solvent molecules is an essential part of the CI process since the inhibitor has to remove some solvent molecules from the interface to get adsorbed on the surface. From the modelling part, the MM methods, such as the MD simulations with classical potentials, are commonly used to include the explicit solvent interactions rather than the QM methods, which may become too costly for the explicit description.

Lastly, the electrodes' potential effects are critical to describing the induced surface charges, the polarization between the solvent and the electrolytes, and how this polarization affects the inhibitor-inhibitor interactions in the formation of monolayers or subsequent multilayers. In the literature, the electrode potential effects are typically included by adding charges to the metallic atoms or using Gran Canonical approaches. One alternative to those approaches, allowing for explicit control of the voltage in the simulations, is the non-equilibrium Green's functions formalism. This thesis represents the first attempt at addressing the CI modelling gaps mentioned above, especially for A4-A6.

The system chosen to showcase the new methods was the 2-mercapto benzimidazole

(MBI) inhibitor and the Cu(111) surface. First, the coverage of Cu by the inhibitors was evaluated in terms of the fundamental interaction between the inhibitor and the surface, considering different adsorption sites. The MBI adsorption energies (E_{ads}) were used to compare the stability for the varying coverages.

Using a $\begin{pmatrix} 2 & 3 \\ 2 & -3 \end{pmatrix}$, three different MBI adsorption configurations were found at the surface: parallel, two-bonded, and hollow cases. In terms of the E_{ads}, the adsorption stability indicates that the most stable configuration is the parallel case, followed by the two-bonded and hollow cases. This stability trend can be attributed to the interaction between the π orbitals of the aromatic ring with the $3d$ electrons from the Cu surface, which in the parallel case are maximized due to the adsorption geometry. Between the two-bonded and the hollow cases, the higher number of interactions within the two-bonded case enhances its adsorption compared with the hollow case.

More packed inhibitor coverages enhance the MBI-MBI lateral adsorption. In this sense, it was found that the higher the surface coverage, the more stable (more negative adsorption energies) the system is. This effect can be explained by the lateral π-π interactions between the inhibitors, forming a self-assembled monolayer (SAM).

The changes in the electronic structure after the adsorption were evaluated in terms of the induced charge density ($\Delta\rho_{ind}$) and the projected density of states (pDOS). $\Delta\rho_{ind}$ mainly indicates charge accumulation on the Cu surface atoms and charge depletion on the MBI ones. The depletion is related to the electron donation from the MBI to the Cu surface, which also depends on the adsorption mode of the MBI. The charge donation comes from the aromatic ring and the S atom in the parallel configuration. In the two-bonded, it comes from the S and N atoms; in the hollow case, it comes mainly from the S atom. On the other hand, the charge accumulation comes from the electron back-donation of the Cu surface atoms to the MBI molecule. Comparing the net Mulliken charges after the adsorption, it is observed that the MBI mainly accepted electrons (more negative net charges) from the Cu surface, which ends up losing electrons (more positive net charges) and then suggesting the strength of the electron back-donation.

The distortion on the MBI atoms in all the cases and the changes in $\Delta\rho_{ind}$ indicate the formation of a chemical bond between the inhibitor and the surface. The drastic change in the MBI's pDOS before and after adsorption also indicates the bond formation. More non-localized and dispersed peaks were observed for the parallel case, the most stable case in the $\begin{pmatrix} 2 & 3 \\ 2 & -3 \end{pmatrix}$ slab, and the SAM cases. The projections of the MBI molecular orbitals on the total pDOS in all the cases suggest that the LUMO and LUMO+1 orbitals are getting discharged while the HOMO is getting charged, which is a corroboration of the electron donation and back-donation between MBI and surface.

The influence of the electrode potential on adsorption was evaluated in the final adsorption configurations using the NEGF formalism. This analysis revealed changes in the electronic structure of the system corresponding to the applied voltages. The charge density difference ($\Delta\rho$) between the cases at a finite voltage (-1 and 1 V) and 0 V showed $\Delta\rho$ accumulation (depletion) for the positive (negative) voltage specifically on the left (right) side of the device, where the MBI was adsorbed. Interestingly, the redistribution of charge primarily occurred at the MBI's edge rather than between the MBI and the surface, as anticipated from the DFT results. This charge redistribution could potentially influence the bonding between inhibitors in subsequent layers and, therefore, the formation of inhibitor films at the surface. In contrast, on the right side of the device, the Cu surface displayed $\Delta\rho$ depletion (accumulation) for positive (negative) voltage, exhibiting an opposite trend compared to the left side. This opposite trend is attributed to the inversion of the chemical potentials used to introduce the voltage in the NEGF formalism.

The final step addressed the solvent effects in the MBI adsorption, where the methodology combining the NEGF formalism and the Quantum Mechanics/Molecular Mechanics (QM/MM) method was used. QM/MM-NEGF molecular dynamics were obtained for the 5×6 Cu surface slab under varying coverage conditions: bare surface, a low-coverage with one MBI adsorbed, and a high-coverage case with six MBI adsorbed, and under different applied voltages (-1, 0 and $+1$ V). The dynamics explicitly included water molecules, with their quantity adjusted to match the density of liquid water under standard pressure

and temperature conditions (1 g/cm^3).

The QM/MM-NEGF dynamics revealed the influence of coverage on MBI adsorption. The results showed a stable SAM monolayer formed with six MBI molecules, which prevailed throughout the simulation and the applied voltages. Water structural descriptors, such as the density profiles, dipole moments ($\vec{\mu}$), and angular distributions, were evaluated under the different concentrations and applied voltages. The water density profile indicated a strong layering along the systems' **z**-axis. In the bare surface and with one MBI adsorbed, a water layer is directly in contact with the Cu surface, contrary to the case with a SAM adsorbed, where the first water layer is located at the end of the SAM structure, and therefore suggesting that the SAM plays a role as a physical barrier between the water molecules and the surface, preventing their interaction with the metallic surface.

The dipole moments and angular distribution also revealed the polarization in the water molecules, primarily with the ones located at the inhibitor-surface interface. In the bare surface and with one MBI molecule, the water molecules aligned according to the voltage sign, and in the case of positive voltages, their hydrogen atoms pointed out towards the left Cu surface. Negative potentials induced the opposite effect: hydrogen atoms pointing towards the Cu right surface. Even at 0 V, the simulations with the SAM adsorption showed a polarization, which is evident in the angular distributions and indicates the outstanding charge redistribution caused by the SAM upon adsorption on the surface. The systems were also evaluated through the evolution of the net Hirshfeld charges for the three concentration cases (0, 1, or 6 MBI molecules) in the varying voltages (-1, 0 and $+1$ V). In the bare Cu surface at 0 V, an oscillatory behaviour was observed between the left and right Cu surfaces due to the water molecule's random distribution, which indicated no preferential orientation. In contrast, at 1 V, the applied potential induced negative net charges on the left Cu surface and positive charges on the right Cu surface, influencing the water alignment, with the H's atoms pointing out to the left Cu surface. Similar behaviour was observed in the case of one MBI adsorbed, responding to the induced polarization by the positive potential and negative applied voltage in simulations. For the SAM case, a partic-

ular intense polarization led to charge separation between the left and right Cu surfaces, with the SAM exhibiting a negative charge even at 0 V. At 1 V, net charges on the left Cu surface remained similar, while SAM and right Cu surface charges changed. The SAM presented more negative net charges, and the right Cu surface presented small negative net charges (close to zero). At -1 V, SAM net charges were slightly negative, while more negative for the right Cu surface. In this sense, regardless the sign of the applied voltages, charges in the left Cu surface remained constant, with the sum of net charges between the left Cu surface and MBI molecules opposing in signal to the net charges of the right Cu surface, suggesting MBI and left Cu surface acted as an electrode, and corroborating the effect observed in the MBI adsorption in vacuum under a voltage, where the MBI is acting as a metal and accumulated the induced charge at the molecule's edge.

Finally, a collaboration with experimental partners at RMIT University was carried out, where the adsorption of 2-mercaptobenzothiazole (2-MBT) and 2-aminobenzothiazole (2-ABT) on galvanized steel, using a Zn(0001) model surface, was showcased. Two concentrations at the surface were investigated: a low (1 molecule/nm_2) and high (3 molecules/nm_2) concentration cases, identifying the most stable adsorption modes. The findings showed that parallel adsorption was the most stable configuration for both 2-ABT and 2-MBT inhibitors at low concentrations, while a vertical arrangement, slightly tilted, forming SAM is obtained at higher concentrations. The adsorption enhancement for SAM cases is also attributed to $\pi - \pi$ stacking interactions between the molecules. Experimental results [21] corroborated those findings using X-ray Photoelectron Spectroscopy (XPS), which revealed the bonding between 2-ABT and the Zn through the endo S and the 2-MBT through the endo N and exo S. Electronic structure analysis revealed the inhibitor's charge density donation to the Zn surface. Between 2-MBT and 2-ABT, the latter interacted more strongly with the Zn surface, which could facilitate the formation of complexes with 2-MBT with Zn^{2+} ions.

Therefore, this thesis demonstrated that the proposed QM/MM-NEGF approach significantly advances modelling electrochemistry and can be successfully applied in corrosion

inhibition studies. Some results from these simulations might be used to feed artificial intelligence (AI) methods and multiscale models to construct the bridge between nanoscale CI modelling and the continuum scale of CI processes.

7.2 Conclusions

The main findings of this thesis will be outlined in the following. For the adsorption in a vacuum and the electrode potential:

- Isolated adsorption: π-transition metal surface states interactions favored.
- Charge donation from the inhibitor to the metallic surface.
- Enhanced adsorption with the surface coverage: lateral π-π interactions in the self-assembled monolayers cases.
- Electrode potential: specific response based on the adsorption mode.
  - Electronic charge redistribution in the system due to the applied voltage.
  - Charge accumulation at the corrosion inhibitors could affect the layering stability and interactions with subsequent layers.

For the adsorption with the solvent and electrode potential effects:

- SAM stable physical barrier: prevents interaction with H_2O at all voltages.
- Preferential orientation in the H_2O distribution: induced by the high coverage on the surface (SAM formation) and the voltage.
- Electronic charge in the metallic surfaces are strongly affected by the SAM.

Finally, from the experimental collaboration, the main conclusion is the synergy between the experimental XPS analysis and the theoretical adsorption energies obtained for the inhibitors, which allows us to corroborate and explain how the bonding is between the

corrosion inhibitor and the surface, providing information that cannot be obtained experimentally, such as induced charge densities due to the formation of chemical bonds, as well as charge transfers.

7.3 Future work

In this thesis, the principal results considered the adsorption of MBI on the Cu(111) surface and the adsorption of another two inhibitor molecules, MBT and ABT, on galvanized steel using the Zn(0001) surface as the substrate. Two scenarios were considered in the adsorption of MBI on Cu: a vacuum situation, where no solvent is included in the simulations, and a situation where the solvent is included explicitly. In the first scenario, the plans include the simulation instead of the thione form of MBI, the thiolate one, which has been suggested by XPS analysis [21] as one of the possible MBI forms attached to the Cu surface. This will allow us to compare the adsorption configurations and their energetic among the different inhibitors tautomers.

Another aspect to be improved is the surface model used for the simulations. In our case, due to the novelty of our approach to describing the solvent and electrode potential effects, a simple (but realistic enough) model surface was used to reduce the problem's degree of freedom and corroborate any potential setback of the methodology. However, once the methodology is corroborated with the robust findings of this thesis, more complex systems will be described. In this sense, the evolution of this project considers the modelling of oxide surfaces, which are observed in the experiments.

Finally, different coverages and voltages will be included in the next project. Regarding the former, intermediate concentrations will be investigated to get an idea about the minimum coverage required to protect the surface from the interaction of water molecules. A range of small voltages will be used in the simulations to analyze how the charge is getting distributed when smaller voltages, and in this case, to have a more comparable case with the experimental potentiodynamic studies.

References

1. Raja, P. B. *et al.* Reviews on Corrosion Inhibitors: A Short View. *Chemical Engineering Communications* **203,** 1145–1156 (2016).

2. Chaubey, N., Savita, Qurashi, A., Chauhan, D. S. & Quraishi, M. Frontiers and advances in green and sustainable inhibitors for corrosion applications: A critical review. *Journal of Molecular Liquids* **321,** 114385 (2021).

3. Jiang, Q. *et al.* A Review on Additive Manufacturing of Pure Copper. *Coatings* **11** (2021).

4. Yan, X. *et al.* Microstructure and mechanical properties of pure copper manufactured by selective laser melting. *Materials Science and Engineering: A* **789,** 139615 (2020).

5. Fateh, A., Aliofkhazraei, M. & Rezvanian, A. R. Review of corrosive environments for copper and its corrosion inhibitors. *Arabian Journal of Chemistry* **13,** 481–544 (2020).

6. Habib, K. In-situ monitoring of pitting corrosion of copper alloys by holographic interferometry. *Corrosion science* **40,** 1435–1440 (1998).

7. Tasi, . Z., Petrovi Mihajlovi, M. B., Radovanovi, M. B. & Antonijevi, M. M. New trends in corrosion protection of copper. *Chemical Papers* **73,** 2103–2132 (Sept. 2019).

8. Xu, P., Fu, Q. & Zhao, M. The influence of calcium on copper corrosion and its by-product release in drinking water. *RSC Adv.* **13,** 17842–17855 (26 2023).

9. Xhanari, K. & Fingar, M. Organic corrosion inhibitors for aluminium and its alloys in acid solutions: a review. *RSC Adv.* **6,** 62833–62857 (67 2016).

10. Antonijevic, M. & Petrovic, M. Copper Corrosion Inhibitors. A review. *International Journal of Electrochemical Science* **3,** 1–28 (2008).

11. Winkler, D. A. Predicting the performance of organic corrosion inhibitors. *Metals* **7,** 1–8 (2017).

12. Ma, I. A. W., Ammar, S., Kumar, S. S. A., Ramesh, K. & Ramesh, S. A concise review on corrosion inhibitors: types, mechanisms and electrochemical evaluation studies. *Journal of Coatings Technology and Research* **19,** 241–268 (Jan. 2022).

13. Marinescu, M. Recent advances in the use of benzimidazoles as corrosion inhibitors. *BMC Chemistry* **13,** 1–21 (2019).

14. Kozlica, D. K., Kokalj, A. & Miloev, I. Synergistic effect of 2-mercaptobenzimidazole and octylphosphonic acid as corrosion inhibitors for copper and aluminium - An electrochemical, XPS, FTIR and DFT study. *Corrosion Science* **182** (2021).

15. Kokalj, A. Molecular modeling of organic corrosion inhibitors: Calculations, pitfalls, and conceptualization of moleculesurface bonding. *Corrosion Science* **193,** 109650 (2021).

16. Obot, I. B., Umoren, S. A., Gasem, Z. M., Suleiman, R. & Ali, B. E. Theoretical prediction and electrochemical evaluation of vinylimidazole and allylimidazole as corrosion inhibitors for mild steel in 1M HCl. *Journal of Industrial and Engineering Chemistry* **21,** 1328–1339 (2015).

17. Bockris, J. O. M., Reddy, A. K. & Gamboa-Aldeco, M. E. *Modern electrochemistry 2B: electrodics in chemistry, engineering, biology and environmental science* (1998).

18. Antonijevi, M. M., Mili, S. M. & Petrovi, M. B. Films formed on copper surface in chloride media in the presence of azoles. *Corrosion Science* **51,** 1228–1237 (2009).

19. Kokalj, A., Xie, C., Miloev, I. & Crespo, D. How relevant are molecular electronic parameters for predicting corrosion inhibition efficiency: imidazoles as corrosion inhibitors of Cu/Zr materials in NaCl solution. *Corrosion Science,* 109900 (2021).

20. Deng, Q. *et al.* In-depth insights of inhibitory behaviour of 2-amino-4-methylthiazole towards galvanised steel in neutral NaCl solution. *Corrosion Science* **199,** 110206 (2022).

21. Deng, Q. *et al.* Inhibitory behaviour and adsorption stability of benzothiazole derivatives as corrosion inhibitors towards galvanised steel. *Molecular Systems Design & Engineering* **9,** 29–45 (2024).

22. Soler, J. M. *et al. Journal of Physics: Condensed Matter* **14,** 2745–2779 (2002).

23. Artacho, E. *et al.* The SIESTA method developments and applicability. *Journal of Physics: Condensed Matter* **20,** 064208 (2008).

24. García, A. *et al.* Siesta: Recent developments and applications. *The Journal of Chemical Physics* **152,** 204108 (2020).

25. Born, M. & Oppenheimer, R. Zur Quantentheorie der Molekeln. *Annalen der Physik* **389,** 457–484 (1927).

26. Levina, I. *Quantum Chemistry.* (2014).

27. Thomas, L. H. The calculation of atomic fields. *Mathematical Proceedings of thE Ni/Tio2 Cambridge Philosophical Society* **23,** 542–548 (1927).

28. Hohemberg, P. & Kohn, W. Inhomogeneous Electron Gas. *Physical Review* **136,** B864 (1964).

29. Levy, M. Universal variational functionals of electron densities, first-order density matrices, and natural spin-orbitals and solution of the v-representability problem. *Proceedings of the National Academy of Sciences* **76,** 6062–6065 (1979).

30. Kohn, W. & Sham, L. Self-Consistent Equations Including Exchange and Correlation Effects. *Physical Review* **140,** A1133 (1965).

31. Perdew, J. P., Burke, K. & Ernzerhof, M. Generalized Gradient Approximation Made Simple. *Phys. Rev. Lett.* **77,** 3865–3868 (18 1996).

32. Grimme, S. Semiempirical GGA-type density functional constructed with a long-range dispersion correction. *Journal of Computational Chemistry* **27,** 1787–1799 (2006).

33. Papior, N., Lorente, N., Frederiksen, T., García, A. & Brandbyge, M. Improvements on non-equilibrium and transport Green function techniques: The next-generation transiesta. *Computer Physics Communications* **212,** 8–24 (2017).

34. Brandbyge, M., Mozos, J.-L., Ordejón, P., Taylor, J. & Stokbro, K. Density-functional method for nonequilibrium electron transport. *Phys. Rev. B* **65,** 165401 (16 Mar. 2002).

35. Mao, Q. *et al.* Classical and reactive molecular dynamics: Principles and applications in combustion and energy systems. *Progress in Energy and Combustion Science* **97,** 101084 (2023).

36. Warshel, A. & Levitt, M. Theoretical studies of enzymic reactions: Dielectric, electrostatic and steric stabilization of the carbonium ion in the reaction of lysozyme. *Journal of Molecular Biology* **103,** 227–249 (1976).

37. Rothlisberger, U. & Carloni, P. in *Computer Simulations in Condensed Matter Systems: From Materials to Chemical Biology Volume 2* (eds Ferrario, M., Ciccotti, G. & Binder, K.) 449–479 (2006).

38. Sanz-Navarro, C. F. *et al.* An efficient implementation of a QM–MM method in SIESTA. *Theoretical Chemistry Accounts* **128,** 825–833 (2011).

39. Prasongkit, J. *et al.* Topological Line Defects Around Graphene Nanopores for DNA Sequencing. *The Journal of Physical Chemistry C* **122,** 7094–7099 (2018).

40. de Freitas Martins, E., Scheicher, R. H., Rocha, A. R. & Feliciano, G. T. A multi-scale approach for electronic transport simulation of carbon nanostructures in aqueous solvent. *Physical Chemistry Chemical Physics* **24,** 24404–24412 (2022).

41. de Freitas Martins, E., Amorim, R. G., Feliciano, G. T., Scheicher, R. H. & Rocha, A. R. The role of water on the electronic transport in graphene nanogap devices designed for DNA sequencing. *Carbon* **158,** 314–319 (2020).

42. de Freitas Martins, E., Troiano Feliciano, G., Hendrik Scheicher, R. & Reily Rocha, A. Simulating DNA Chip Design Using All-Electronic Graphene-Based Substrates. *Molecules* **24** (2019).

43. Feliciano, G. T. *et al.* Addressing the Environment Electrostatic Effect on Ballistic Electron Transport in Large Systems: A QM/MM-NEGF Approach. *The Journal of Physical Chemistry B* **122,** 485–492 (2018).

44. Feliciano, G. T. *et al.* Capacitive DNA Detection Driven by Electronic Charge Fluctuations in a Graphene Nanopore. *Phys. Rev. Applied* **3,** 034003 (3 2015).

45. Crespo, A. *et al.* A DFT-Based QM-MM Approach Designed for the Treatment of Large Molecular Systems: Application to Chorismate Mutase. *The Journal of Physical Chemistry B* **107,** 13728–13736 (2003).

46. Wang, J., Cieplak, P. & Kollman, P. A. How well does a restrained electrostatic potential (RESP) model perform in calculating conformational energies of organic and biological molecules? *Journal of Computational Chemistry* **21,** 1049–1074 (2000).

47. Cornell, W. D. *et al.* A second generation force field for the simulation of proteins, nucleic acids, and organic molecules. *Journal of the American Chemical Society* **117,** 5179–5197 (1995).

48. Castillo-Robles, J. M., de Freitas Martins, E., Ordejón, P. & Cole, I. Molecular modeling applied to corrosion inhibition: a critical review. *npj Materials Degradation.* Accepted (2024).

49. de Freitas Martins, E., Pinotti, L. F., de Carvalho Castro Silva, C. & Rocha, A. R. Addressing the Theoretical and Experimental Aspects of Low-Dimensional-Materials-Based FET Immunosensors: A Review. *Chemosensors* **9** (2021).

50. Hill, J.-R., Subramanian, L. & Maiti, A. *Molecular Modeling Techniques In Material Sciences* (2005).

51. Höltje, H., Sippl, W., Rognan, D. & Folkers, G. *Molecular Modeling: Basic Principles and Applications* (2008).

52. Becca, F. & Sorella, S. *Quantum Monte Carlo Approaches for Correlated Systems* (2017).

53. Jorgensen, W. L., Maxwell, D. S. & Tirado-Rives, J. Development and testing of the OPLS all-atom force field on conformational energetics and properties of organic liquids. *Journal of the American Chemical Society* **118,** 11225–11236 (1996).

54. Harder, E. *et al.* OPLS3: a force field providing broad coverage of drug-like small molecules and proteins. *Journal of chemical theory and computation* **12,** 281–296 (2016).

55. Wang, J., Wolf, R. M., Caldwell, J. W., Kollman, P. A. & Case, D. A. Development and testing of a general amber force field. *Journal of computational chemistry* **25,** 1157–1174 (2004).

56. Wang, J., Wang, W., Kollman, P. A. & Case, D. A. Automatic atom type and bond type perception in molecular mechanical calculations. *Journal of molecular graphics and modelling* **25,** 247–260 (2006).

57. Vanommeslaeghe, K. *et al.* CHARMM general force field: A force field for drug-like molecules compatible with the CHARMM all-atom additive biological force fields. *Journal of computational chemistry* **31,** 671–690 (2010).

58. Vanommeslaeghe, K. & MacKerell Jr, A. D. Automation of the CHARMM General Force Field (CGenFF) I: bond perception and atom typing. *Journal of chemical information and modeling* **52,** 3144–3154 (2012).

59. Yu, W., He, X., Vanommeslaeghe, K. & MacKerell Jr, A. D. Extension of the CHARMM general force field to sulfonyl-containing compounds and its utility in biomolecular simulations. *Journal of computational chemistry* **33,** 2451–2468 (2012).

60. Daura, X., Mark, A. E. & Van Gunsteren, W. F. Parametrization of aliphatic CHn united atoms of GROMOS96 force field. *Journal of computational chemistry* **19,** 535–547 (1998).

61. Schuler, L. D., Daura, X. & Van Gunsteren, W. F. An improved GROMOS96 force field for aliphatic hydrocarbons in the condensed phase. *Journal of computational chemistry* **22,** 1205–1218 (2001).

62. Oostenbrink, C., Villa, A., Mark, A. E. & Van Gunsteren, W. F. A biomolecular force field based on the free enthalpy of hydration and solvation: the GROMOS force-field parameter sets 53A5 and 53A6. *Journal of computational chemistry* **25,** 1656–1676 (2004).

63. Horta, B. A., Fuchs, P. F., van Gunsteren, W. F. & Hunenberger, P. H. New interaction parameters for oxygen compounds in the GROMOS force field: Improved pure-liquid and solvation properties for alcohols, ethers, aldehydes, ketones, carboxylic acids, and esters. *Journal of chemical theory and computation* **7,** 1016–1031 (2011).

64. Horta, B. A. *et al.* A GROMOS-compatible force field for small organic molecules in the condensed phase: The 2016H66 parameter set. *Journal of chemical theory and computation* **12,** 3825–3850 (2016).

65. Halgren, T. A. Merck molecular force field. I. Basis, form, scope, parameterization, and performance of MMFF94. *Journal of computational chemistry* **17,** 490–519 (1996).

66. Halgren, T. A. Merck molecular force field. II. MMFF94 van der Waals and electrostatic parameters for intermolecular interactions. *Journal of Computational Chemistry* **17,** 520–552 (1996).

67. Halgren, T. A. Merck molecular force field. III. Molecular geometries and vibrational frequencies for MMFF94. *Journal of computational chemistry* **17,** 553–586 (1996).

68. Halgren, T. A. & Nachbar, R. B. Merck molecular force field. IV. Conformational energies and geometries for MMFF94. *Journal of computational chemistry* **17,** 587–615 (1996).

69. Halgren, T. A. Merck molecular force field. V. Extension of MMFF94 using experimental data, additional computational data, and empirical rules. *Journal of Computational Chemistry* **17,** 616–641 (1996).

70. Abraham, M. J. *et al.* GROMACS: High performance molecular simulations through multi-level parallelism from laptops to supercomputers. *SoftwareX* **1,** 19–25 (2015).

71. Bowers, K. J. *et al. Scalable algorithms for molecular dynamics simulations on commodity clusters* in *Proceedings of the 2006 ACM/IEEE Conference on Supercomputing* (2006).

72. Thompson, A. P. *et al.* LAMMPS - a flexible simulation tool for particle-based materials modeling at the atomic, meso, and continuum scales. *Computer Physics Communications* **271,** 108171 (2022).

73. Case, D. A. *et al.* The Amber biomolecular simulation programs. en. *J. Comput. Chem.* **26,** 1668–1688 (2005).

74. Brooks, B. R. *et al.* CHARMM: the biomolecular simulation program. *Journal of computational chemistry* **30,** 1545–1614 (2009).

75. Huang, J., Lemkul, J. A., Eastman, P. K. & MacKerell Jr, A. D. *Molecular dynamics simulations using the drude polarizable force field on GPUs with OpenMM: Implementation, validation, and benchmarks* 2018.

76. Lin, F. Y. & MacKerell, A. D. Force fields for small molecules. *Biomolecular Simulations: Methods and Protocols,* 21–54 (2019).

77. Hollingsworth, S. A. & Dror, R. O. Molecular dynamics simulation for all. *Neuron* **99,** 1129–1143 (2018).

78. Befort, B. J., DeFever, R. S., Tow, G. M., Dowling, A. W. & Maginn, E. J. Machine learning directed optimization of classical molecular modeling force fields. *Journal of Chemical Information and Modeling* **61,** 4400–4414 (2021).

79. Unke, O. T. *et al.* Machine learning force fields. *Chemical Reviews* **121,** 10142–10186 (2021).

80. Fu, X. *et al. Forces are not Enough: Benchmark and Critical Evaluation for Machine Learning Force Fields with Molecular Simulations* 2022.

81. Rapaport, D. *The Art of Molecular Dynamics Simulation* (2004).

82. Allen, M. & Tildesley, D. *Computer Simulation of Liquids* (1989).

83. Verma, C. *et al.* Molecular dynamics and Monte Carlo simulations as powerful tools for study of interfacial adsorption behavior of corrosion inhibitors in aqueous phase: A review. *Journal of Molecular Liquids* **260,** 99–120 (2018).

84. Taylor, C. D., Chandra, A., Vera, J. & Sridhar, N. Multiphysics modelling, quantum chemistry and risk analysis for corrosion inhibitor design and lifetime prediction. *Faraday Discussions* **180,** 459–477 (2015).

85. Fardioui, M. *et al.* Bio-active corrosion inhibitor based on 8-hydroxyquinoline-grafted-Alginate: Experimental and computational approaches. *Journal of Molecular Liquids* **323** (2021).

86. Oukhrib, R. *et al.* DFT, Monte Carlo and molecular dynamics simulations for the prediction of corrosion inhibition efficiency of novel pyrazolylnucleosides on Cu(111) surface in acidic media. *Scientific Reports* **11,** 1–18 (2021).

87. Alareeqi, S., Bahamon, D., Nogueira, R. P. & Vega, L. F. Understanding the relationship between the structural properties of three corrosion inhibitors and their surface protectiveness ability in different environments. *Applied Surface Science* **542,** 148600 (2021).

88. Liu, A. *et al.* Investigation on the interfacial behavior of polyorganic inhibitors on a metal surface by DFT study and MD simulation. *Applied Surface Science* **541,** 148570 (2021).

89. Chen, X. *et al.* Molecular dynamics simulation and DFT calculation of green scale and corrosion inhibitor. *Computational Materials Science* **188,** 110229 (2021).

90. Dahmani, K. *et al.* Quantum chemical and molecular dynamic simulation studies for the identification of the extracted cinnamon essential oil constituent responsible for copper corrosion inhibition in acidified 3.0 wt% NaCl medium. *Inorganic Chemistry Communications* **124,** 108409 (2021).

91. Kumar, D., Jain, V. & Rai, B. Imidazole derivatives as corrosion inhibitors for copper: A DFT and reactive force field study. *Corrosion Science* **171** (2020).

92. Saranya, J. *et al.* Experimental and computational approaches on the pyran derivatives for acid corrosion. *Colloids and Surfaces A: Physicochemical and Engineering Aspects* **603,** 125231 (2020).

93. Guo, L. *et al.* Multidimensional insights into the corrosion inhibition of 3,3-dithiodipropionic acid on Q235 steel in H_2SO_4 medium: A combined experimental

and in silico investigation. *Journal of Colloid and Interface Science* **570,** 116–124 (2020).

94. Guo, L. *et al.* Multidimensional insights into the corrosion inhibition of 3,3-dithiodipropionic acid on Q235 steel in H_2SO_4 medium: A combined experimental and in silico investigation. *Journal of Colloid and Interface Science* **570,** 116–124 (2020).

95. Thaçi, V., Hoti, R., Berisha, A. & Bogdanov, J. Corrosion study of copper in aqueous sulfuric acid solution in the presence of (2E,5E)-2,5-dibenzylidenecyclopentanone and (2E,5E)-bis[(4-dimethylamino)benzylidene]cyclopentanone: Experimental and theoretical study. *Open Chemistry* **18,** 1412–1420 (2020).

96. Hadisaputra, S. *et al.* Quantum chemical and monte carlo simulation studies on inhibition performance of caffeine and its derivatives against corrosion of copper. *Coatings* **10,** 1–17 (2020).

97. Zhang, J. & Li, H. Inhibition effect and mechanism of 2-(3-bromophenyl)-1-phenyl-1H-benzimidazole on copper corrosion in acidic solution. *International Journal of Electrochemical Science* **15,** 4368–4378 (2020).

98. Farahati, R., Mousavi-Khoshdel, S. M., Ghaffarinejad, A. & Behzadi, H. Experimental and computational study of penicillamine drug and cysteine as water-soluble green corrosion inhibitors of mild steel. *Progress in Organic Coatings* **142,** 105567 (2020).

99. Farahati, R., Behzadi, H., Mousavi-Khoshdel, S. M. & Ghaffarinejad, A. Evaluation of corrosion inhibition of 4-(pyridin-3-yl) thiazol-2-amine for copper in HCl by experimental and theoretical studies. *Journal of Molecular Structure* **1205,** 127658 (2020).

100. Oukhrib, R. *et al.* In silico investigations of alginate biopolymer on the Fe (110), Cu (111), Al (111) and Sn (001) surfaces in acidic media: Quantum chemical

and molecular mechanic calculations. *Journal of Molecular Liquids* **312,** 113479 (2020).

101. Luo, W. *et al.* A combined experimental and theoretical research of the inhibition property of 2-((6-chloropyridazin-3-yl)thio)-N,N-diethylacetamide as a novel and effective inhibitor for Cu in H_2SO_4 medium. *Journal of Molecular Liquids* **314,** 113630 (2020).

102. Gao, L., Peng, S., Huang, X. & Gong, Z. A combined experimental and theoretical study of papain as a biological eco-friendly inhibitor for copper corrosion in H_2SO_4 medium. *Applied Surface Science* **511,** 145446 (2020).

103. Pareek, S. *et al.* A new insight into corrosion inhibition mechanism of copper in aerated 3.5 wt.% NaCl solution by eco-friendly Imidazopyrimidine Dye: experimental and theoretical approach. *Chemical Engineering Journal* **358,** 725–742 (2019).

104. Bhaskaran, Pancharatna, P. D., Lata, S. & Singh, G. Imidazolium based ionic liquid as an efficient and green corrosion constraint for mild steel at acidic pH levels. *Journal of Molecular Liquids* **278,** 467–476 (2019).

105. Belghiti, M. E. *et al.* Computational simulation and statistical analysis on the relationship between corrosion inhibition efficiency and molecular structure of some hydrazine derivatives in phosphoric acid on mild steel surface. *Applied Surface Science* **491,** 707–722 (2019).

106. Zhang, X. Y., Kang, Q. X. & Wang, Y. Theoretical study of N-thiazolyl-2-cyanoacetamide derivatives as corrosion inhibitor for aluminum in alkaline environments. *Computational and Theoretical Chemistry* **1131,** 25–32 (2018).

107. Talebian, M. *et al.* Inhibitive effect of sodium (E)-4-(4-nitrobenzylideneamino)benzoate on the corrosion of some metals in sodium chloride solution. *Applied Surface Science* **447,** 852–865 (2018).

108. Liu, A. *et al.* Theoretical and experimental studies of the corrosion inhibition effect of nitrotetrazolium blue chloride on copper in 0.1 M H_2SO_4. *RSC Advances* **4,** 40606–40616 (2014).

109. Mishra, A. *et al.* Synthesis, characterization and corrosion inhibition studies of N-phenyl-benzamides on the acidic corrosion of mild steel: Experimental and computational studies. *Journal of Molecular Liquids* **251,** 317–332 (2018).

110. Chaouiki, A. *et al.* Exploring deep insights into the interaction mechanism of a quinazoline derivative with mild steel in HCl: electrochemical, DFT, and molecular dynamic simulation studies. *Journal of Adhesion Science and Technology* **33,** 921–944 (2019).

111. Dagdag, O. *et al.* Epoxy pre-polymers as new and effective materials for corrosion inhibition of carbon steel in acidic medium: Computational and experimental studies. *Scientific Reports* **9,** 1–14 (2019).

112. Chaouiki, A. *et al.* New 8-hydroxyquinoline-bearing quinoxaline derivatives as effective corrosion inhibitors for mild steel in HCl: Electrochemical and computational investigations. *Coatings* **10** (2020).

113. Laggoun, R., Ferhat, M., Saidat, B., Benghia, A. & Chaabani, A. Effect of p-toluenesulfonyl hydrazide on copper corrosion in hydrochloric acid solution. *Corrosion Science* **165,** 108363 (2020).

114. Farahati, R. *et al.* Synthesis and potential applications of some thiazoles as corrosion inhibitor of copper in 1 M HCl: Experimental and theoretical studies. *Progress in Organic Coatings* **132,** 417–428 (2019).

115. Habibi-Khorassani, S. M. *et al.* Inhibition of aluminum corrosion in acid solution by environmentally friendly antibacterial corrosion inhibitors: Experimental and theoretical investigations. *Protection of Metals and Physical Chemistry of Surfaces* **53,** 579–590 (2017).

116. Allal, H., Belhocine, Y. & Zouaoui, E. Computational study of some thiophene derivatives as aluminium corrosion inhibitors. *Journal of Molecular Liquids* **265,** 668–678 (2018).

117. Kokalj, A. & Costa, D. in *Encyclopedia of Interfacial Chemistry* (ed Wandelt, K.) 332–345 (2018).

118. Pearson, R. G. Hard and soft acids and bases. *Journal of the American Chemical society* **85,** 3533–3539 (1963).

119. Parr, R. G., Donnelly, R. A., Levy, M. & Palke, W. E. Electronegativity: The density functional viewpoint. *The Journal of Chemical Physics* **68,** 3801–3807 (1977).

120. Parr, R. G. & Pearson, R. G. Absolute Hardness: Companion Parameter to Absolute Electronegativity. *Journal of the American Chemical Society* **105,** 7512–7516 (1983).

121. Geerlings, P., De Proft, F. & Langenaeker, W. Conceptual density functional theory. *Chemical Reviews* **103,** 1793–1873 (2003).

122. Kokalj, A. On the alleged importance of the molecular electron-donating ability and the HOMO-LUMO gap in corrosion inhibition studies. *Corrosion Science* **180,** 109016 (2021).

123. Kokalj, A. *et al.* Simplistic correlations between molecular electronic properties and inhibition efficiencies: Do they really exist? *Corrosion Science* **179,** 108856 (2021).

124. Breedon, M., Per, M. C., Cole, I. S. & Barnard, A. S. Molecular ionization and deprotonation energies as indicators of functional coating performance. *Journal of Materials Chemistry A* **2,** 16660–16668 (2014).

125. Winkler, D. A. *et al.* Towards chromate-free corrosion inhibitors: Structure-property models for organic alternatives. *Green Chemistry* **16,** 3349–3357 (2014).

126. Winkler, D. A. *et al.* Using high throughput experimental data and in silico models to discover alternatives to toxic chromate corrosion inhibitors. *Corrosion Science* **106,** 229–235 (2016).

127. Chen, F. F. *et al.* Correlation between molecular features and electrochemical properties using an artificial neural network. *Materials and Design* **112,** 410–418 (2016).

128. Kokalj, A. & Costa, D. Model Study of Penetration of Cl Ions from Solution into Organic Self-Assembled-Monolayer on Metal Substrate: Trends and Modeling Aspects. *Journal of The Electrochemical Society* **168,** 071508 (2021).

129. Kokalj, A., Xie, C., Miloev, I. & Crespo, D. How relevant are molecular electronic parameters for predicting corrosion inhibition efficiency: imidazoles as corrosion inhibitors of Cu/Zr materials in NaCl solution. *Corrosion Science* **193,** 109900 (2021).

130. Erdogan, S. *et al.* A computational study on corrosion inhibition performances of novel quinoline derivatives against the corrosion of iron. *Journal of Molecular Structure* **1134,** 751–761 (2017).

131. Chen, S., Scheiner, S., Kar, T. & Adhikari, U. Theoretical study on relationship between structure of mercapto-triazole derivatives and inhibition performance. *International Journal of Electrochemical Science* **7,** 7128–7139 (2012).

132. Al-Itawi, H. I., Al-Mazaideh, G. M., Al-Rawajfeh, A. E., Al-Ma'abreh, A. M. & Marashdeh, A. The effect of some green inhibitors on the corrosion rate of Cu, Fe and Al metals. *International Journal of Corrosion and Scale Inhibition* **8,** 199–211 (2019).

133. Khaled, K. F. & El-Sherik, A. M. Validation of a predictive model for corrosion inhibition of API 5L X60 steel in chloride solution. *International Journal of Electrochemical Science* **11,** 2377–2391 (2016).

134. Han, P. *et al.* Synergistic effect of mixing cationic and nonionic surfactants on corrosion inhibition of mild steel in HCl: Experimental and theoretical investigations. *Journal of Colloid and Interface Science* **516,** 398–406 (2018).

135. Obot, I. B., Onyeachu, I. B., Wazzan, N. & Al-Amri, A. H. Theoretical and experimental investigation of two alkyl carboxylates as corrosion inhibitors for steel in acidic medium. *Journal of Molecular Liquids* **279,** 190–207 (2019).

136. Fitoz, A., Nazr, H., Özgür (nee Yakut), M., Emregül, E. & Emregül, K. C. An experimental and theoretical approach towards understanding the inhibitive behavior of a nitrile substituted coumarin compound as an effective acidic media inhibitor. *Corrosion Science* **133,** 451–464 (2018).

137. Jing, C. *et al.* Photo and thermally stable branched corrosion inhibitors containing two benzotriazole groups for copper in 3.5 wt% sodium chloride solution. *Corrosion Science* **138,** 353–371 (2018).

138. Liu, X. *et al.* Nicotinic acid derivatives as corrosion inhibitors for mild steel in hydrochloric acid solutions: an experimental and computational chemistry study. *Journal of Adhesion Science and Technology* **35,** 63–80 (2021).

139. Singh, P., Chauhan, D. S., Chauhan, S. S., Singh, G. & Quraishi, M. A. Chemically modified expired Dapsone drug as environmentally benign corrosion inhibitor for mild steel in sulphuric acid useful for industrial pickling process. *Journal of Molecular Liquids* **286,** 110903 (2019).

140. Liu, Y. *et al.* A Machine Learning-Based QSAR Model for Benzimidazole Derivatives as Corrosion Inhibitors by Incorporating Comprehensive Feature Selection. *Interdisciplinary Sciences: Computational Life Sciences* **11,** 738–747 (2019).

141. Al-Fakih, A. M. *et al.* Quantitative structureactivity relationship model for prediction study of corrosion inhibition efficiency using two-stage sparse multiple linear regression. *Journal of Chemometrics* **30,** 361–368 (2016).

142. Kovaevi, N. & Kokalj, A. DFT study of interaction of azoles with Cu(111) and Al(111) surfaces: Role of azole nitrogen atoms and dipole-dipole interactions. *Journal of Physical Chemistry C* **115,** 24189–24197 (2011).

143. Obot, I. B., Macdonald, D. D. & Gasem, Z. M. Density functional theory (DFT) as a powerful tool for designing new organic corrosion inhibitors: Part 1: An overview. *Corrosion Science* **99,** 1–30 (2015).

144. Ebenso, E. E. *et al.* Molecular modelling of compounds used for corrosion inhibition studies: a review. *Physical Chemistry Chemical Physics,* 9–12 (2021).

145. Kopa Lautar, A., Hagopian, A. & Filhol, J. S. Modeling interfacial electrochemistry: Concepts and tools. *Physical Chemistry Chemical Physics* **22,** 10569–10580 (2020).

146. Xiao, Z. *et al.* Electrochemical studies and molecular dynamics simulation of the interaction between accelerators and Cu surface during the electroplating process. *International Journal of Electrochemical Science* **14,** 4705–4717 (2019).

147. Lgaz, H. *et al.* Exploring the potential role of pyrazoline derivatives in corrosion inhibition of mild steel in hydrochloric acid solution: Insights from experimental and computational studies. *Construction and Building Materials* **233,** 117320 (2020).

148. Suhasaria, A., Murmu, M., Satpati, S., Banerjee, P. & Sukul, D. Bis-benzothiazoles as efficient corrosion inhibitors for mild steel in aqueous HCl: Molecular structure-reactivity correlation study. *Journal of Molecular Liquids* **313,** 113537 (2020).

149. Wang, H. *et al.* DFT study of imidazoles adsorption on the grain boundary of Cu (100) surface. *Corrosion Science* **137,** 33–42 (2018).

150. Asadi, N., Ramezanzadeh, M., Bahlakeh, G. & Ramezanzadeh, B. Theoretical MD/DFT computer explorations and surface-electrochemical investigations of the zinc/iron metal cations interactions with highly active molecules from Lemon balm extract toward the steel corrosion retardation in saline solution. *Journal of Molecular Liquids* **310,** 113220 (2020).

151. Verma, C., Quraishi, M. A. & Ebenso, E. E. Quinoline and its derivatives as corrosion inhibitors: A review. *Surfaces and Interfaces* **21** (2020).

152. Dagdag, O. *et al.* Adsorption and anticorrosive behavior of aromatic epoxy monomers on carbon steel corrosion in acidic solution: Computational studies and sustained experimental studies. *RSC Advances* **9,** 14782–14796 (2019).

153. Guo, L. *et al.* Toward understanding the adsorption mechanism of large size organic corrosion inhibitors on an Fe(110) surface using the DFTB method. *RSC Advances* **7,** 29042–29050 (2017).

154. Palaniappan, N., Cole, I., Kuznetsov, A., Caballero-Briones, F. & Manickam, S. Butylamine functionalized graphene oxide: experimental and DFT studies on the corrosion inhibition efficiency of the MgAZ13 alloy in a 3.5% NaCl environment. *Materials Advances* (2023).

155. Quadri, T. W. *et al.* Quantitative structure activity relationship and artificial neural network as vital tools in predicting coordination capabilities of organic compounds with metal surface: A review. *Coordination Chemistry Reviews* **446,** 214101 (2021).

156. Lukovits, I., Palfi, K., Bako, I. & Kalman, E. LKP model of the inhibition mechanism of thiourea compounds. *Corrosion* **53** (1997).

157. Lukovits, I., Bakó, I., Shaban, A. & Kálmán, E. Polynomial model of the inhibition mechanism of thiourea derivatives. *Electrochimica Acta* **43,** 131–136 (1998).

158. Fernandez, M., Breedon, M., Cole, I. S. & Barnard, A. S. Modeling corrosion inhibition efficacy of small organic molecules as non-toxic chromate alternatives using comparative molecular surface analysis (CoMSA). *Chemosphere* **160,** 80–88 (2016).

159. Connolly, M. L. Analytical molecular surface calculation. *Journal of Applied Crystallography* **16,** 548–558 (Oct. 1983).

160. Cohen, P. & Feigenbaum, E. *The Handbook of Artificial Intelligence: Volume 3* **v. 3** (2014).

161. Dai, J. *et al.* Cross-category prediction of corrosion inhibitor performance based on molecular graph structures via a three-level message passing neural network model. *Corrosion Science* **209,** 110780 (2022).

162. Hu, J. *et al.* Theoretical insights into the solvent polarity effect on the quality of self-assembled N-Octadecanethiol Monolayers on Cu (111) Surfaces. *Molecules* **23** (2018).

163. Guo, L. *et al.* Theoretical insight into an empirical rule about organic corrosion inhibitors containing nitrogen, oxygen, and sulfur atoms. *Applied Surface Science* **406,** 301–306 (2017).

164. Deng, Q. *et al.* Synergistically and sustainably performed inhibitors for galvanised steel against aqueous corrosion. *Corrosion Science,* 110984 (2023).

165. Van Duin, A. C., Dasgupta, S., Lorant, F. & Goddard, W. A. ReaxFF: a reactive force field for hydrocarbons. *The Journal of Physical Chemistry A* **105,** 9396–9409 (2001).

166. Liu, W. *et al.* Molecular dynamics and machine learning in catalysts. *Catalysts* **11,** 1129 (2021).

167. Vernack, E., Costa, D., Tingaut, P. & Marcus, P. DFT studies of 2-mercaptobenzothiazole and 2-mercaptobenzimidazole as corrosion inhibitors for copper. *Corrosion Science* **174,** 108840 (2020).

168. Chiter, F., Costa, D., Maurice, V. & Marcus, P. Adsorption of 2-mercaptobenzimidazole Corrosion Inhibitor on Copper: DFT Study on Model Oxidized Interfaces. *Journal of The Electrochemical Society* **167,** 161506 (2020).

169. Xiong, L. *et al.* Corrosion behaviors of Q235 carbon steel under imidazoline derivatives as corrosion inhibitors: Experimental and computational investigations. *Arabian Journal of Chemistry* **14,** 102952 (2021).

170. Gustini, D. & Kokalj, A. DFT study of azole corrosion inhibitors on Cu_2O model of oxidized copper surfaces: I. Molecule-surface and Cl-surface bonding. *Metals* **8,** 1–27 (2018).

171. Kumar, D., Jain, N., Jain, V. & Rai, B. Amino acids as copper corrosion inhibitors: A density functional theory approach. *Applied Surface Science* **514,** 145905 (2020).

172. Tan, J. *et al.* Electrochemical and computational studies on the corrosion inhibition of mild steel by 1-hexadecyl-3-methylimidazolium bromide in HCl medium. *International Journal of Electrochemical Science* **15,** 1893–1903 (2020).

173. Chiter, F., Costa, D., Maurice, V. & Marcus, P. Corrosion inhibition of locally depassivated surfaces by DFT study of 2-mercaptobenzothiazole on copper. *npj Materials Degradation* **5,** 1–12 (2021).

174. Hu, L., Pan, G., Wang, H., Xu, Y. & Wang, R. The synergistic inhibitory effect and density functional theory study of 2,2'-[[(Methyl-1H-benzotriazol-1-yl)methyl]imino]bisethanol and potassium oleate on copper in H_2O_2 based alkaline slurries. *Colloids and Surfaces A: Physicochemical and Engineering Aspects* **603** (2020).

175. Miloev, I. *et al.* The Effect of Anchor Group and Alkyl Backbone Chain on Performance of Organic Compounds as Corrosion Inhibitors for Aluminum Investigated Using an Integrative Experimental-Modeling Approach. *Journal of The Electrochemical Society* **167,** 061509 (2020).

176. Ouakki, M. *et al.* Insights into corrosion inhibition mechanism of mild steel in 1 M HCl solution by quinoxaline derivatives: electrochemical, SEM/EDAX, UV-visible, FT-IR and theoretical approaches. *Colloids and Surfaces A: Physicochemical and Engineering Aspects* **611,** 125810 (2021).

177. Jmiai, A. *et al.* A new trend in corrosion protection of copper in acidic medium by using Jujube shell extract as an effective green and environmentally safe corrosion

inhibitor: Experimental, quantum chemistry approach and Monte Carlo simulation study. *Journal of Molecular Liquids* **322,** 114509 (2021).

178. Quadri, T. W. *et al.* Chromeno-carbonitriles as corrosion inhibitors for mild steel in acidic solution: electrochemical, surface and computational studies. *RSC Advances* **11,** 2462–2475 (2021).

179. Dehghani, A., Bahlakeh, G., Ramezanzadeh, B. & Ramezanzadeh, M. Potential role of a novel green eco-friendly inhibitor in corrosion inhibition of mild steel in HCl solution: Detailed macro/micro-scale experimental and computational explorations. *Construction and Building Materials* **245,** 118464 (2020).

180. Rbaa, M. *et al.* 8-Hydroxyquinoline based chitosan derived carbohydrate polymer as biodegradable and sustainable acid corrosion inhibitor for mild steel: Experimental and computational analyses. *International Journal of Biological Macromolecules* **155,** 645–655 (2020).

181. Madkour, L. H., Kaya, S. & Obot, I. B. Computational, Monte Carlo simulation and experimental studies of some arylazotriazoles (AATR) and their copper complexes in corrosion inhibition process. *Journal of Molecular Liquids* **260,** 351–374 (2018).

182. Elgendy, A., Nady, H., El-Rabiei, M. M. & Elhenawy, A. A. Understanding the adsorption performance of two glycine derivatives as novel and environmentally safe anti-corrosion agents for copper in chloride solutions: Experimental, DFT, and MC studies. *RSC Advances* **9,** 42120–42131 (2019).

183. Aslam, R., Mobin, M., Zehra, S., Obot, I. B. & Ebenso, E. E. N,N'-Dialkylcystine Gemini and Monomeric N-Alkyl Cysteine Surfactants as Corrosion Inhibitors on Mild Steel Corrosion in 1 M HCl Solution: A Comparative Study. *ACS Omega* **2,** 5691–5707 (2017).

184. Guo, L., Kaya, S., Obot, I. B., Zheng, X. & Qiang, Y. Toward understanding the anticorrosive mechanism of some thiourea derivatives for carbon steel corrosion:

A combined DFT and molecular dynamics investigation. *Journal of Colloid and Interface Science* **506,** 478–485 (2017).

185. Chiter, F., Costa, D., Maurice, V. & Marcus, P. Chemical interaction, self-ordering and corrosion inhibition properties of 2-mercaptobenzothiazole monolayers: DFT atomistic modeling on metallic copper. *Corrosion Science* **209,** 110658 (2022).

186. Tof-SIMS, XPS and DFT study of the adsorption of 2-mercaptobenzothiazole on copper in neutral aqueous solution and corrosion protection in chloride solution. *Corrosion Science* **210,** 110854 (2023).

187. Li, W. & Li, D. Y. Variations of work function and corrosion behaviors of deformed copper surfaces. *Applied Surface Science* **240,** 388–395 (2005).

188. Fingar, M., Lesar, A., Kokalj, A. & Miloev, I. A comparative electrochemical and quantum chemical calculation study of BTAH and BTAOH as copper corrosion inhibitors in near neutral chloride solution. *Electrochimica Acta* **53,** 8287–8297 (2008).

189. Fingar, M. & Miloev, I. Inhibition of copper corrosion by 1,2,3-benzotriazole: A review. *Corrosion Science* **52,** 2737–2749 (2010).

190. Kokalj, A. Ab initio modeling of the bonding of benzotriazole corrosion inhibitor to reduced and oxidized copper surfaces. *Faraday Discussions* **180,** 415–438 (2015).

191. Costa, D., Ribeiro, T., Cornette, P. & Marcus, P. DFT modeling of corrosion inhibition by organic molecules: Carboxylates as inhibitors of aluminum corrosion. *Journal of Physical Chemistry C* **120,** 28607–28616 (2016).

192. Srivastava, V., Salman, M., Chauhan, D. S., Abdel-Azeim, S. & Quraishi, M. A. (E)-2-styryl-1H-benzo[d]imidazole as novel green corrosion inhibitor for carbon steel: Experimental and computational approach. *Journal of Molecular Liquids* **324,** 115010 (2021).

193. Tersoff, J. & Hamann, D. R. Theory of the scanning tunneling microscope. *Phys. Rev. B* **31,** 805–813 (2 Jan. 1985).

194. Li, F., Bai, M., Wei, S., Jin, S. & Shen, W. Multidimension Insight Involving Experimental and in Silico Investigation into the Corrosion Inhibition of N, N-Dibenzyl Dithiocarbamate Acid on Copper in Sulfuric Acid Solution. *Industrial and Engineering Chemistry Research* **58,** 7166–7178 (2019).

195. Gustini, D. & Kokalj, A. A DFT study of adsorption of imidazole, triazole, and tetrazole on oxidized copper surfaces: $Cu_2O(111)$ and $Cu_2O(111)$-w/o-CuCUS. *Physical Chemistry Chemical Physics* **17,** 28602–28615 (2015).

196. Chiter, F., Costa, D., Maurice, V. & Marcus, P. DFT investigation of 2-mercaptobenzothiazole adsorption on model oxidized copper surfaces and relationship with corrosion inhibition. *Applied Surface Science* **537,** 147802 (2021).

197. Orozco, M. & Luque, F. J. *Generalization of the Molecular Electrostatic Potential for the Study of Noncovalent interactions* (eds Murray, J. S. & Sen, K.) 181–218 (1996).

198. Ke, H. & Taylor, C. D. Density functional theory: An essential partner in the integrated computational materials engineering approach to corrosion. *Corrosion* **75,** 708–726 (2019).

199. Assessing corrosion inhibition characteristics of hydrazone derivatives on mild steel in HCl: Insights from electronic-scale DFT and atomic-scale molecular dynamics. *Journal of Molecular Liquids* **308,** 112998 (2020).

200. Wang, D. *et al.* Experimental and theoretical investigation on corrosion inhibition of AA5052 aluminium alloy by l-cysteine in alkaline solution. *Materials Chemistry and Physics* **169,** 142–151 (2016).

201. You, J. & Liu, Z. Atomistic simulation of corrosion protection of Al2Cu aluminum alloy by 8-hydroxyquinoline. *Applied Surface Science* **540,** 148315 (2021).

202. Kokalj, A. & Peljhan, S. Density functional theory study of adsorption of benzotriazole on Cu_2O surfaces. *Journal of Physical Chemistry C* **119,** 11625–11635 (2015).

203. Xiong, S., Liang, D., Ba, Z., Zhang, Z. & Luo, S. Adsorption behavior of thiadiazole derivatives as anticorrosion additives on copper oxide surface: Computational and experimental studies. *Applied Surface Science* **492,** 399–406 (2019).

204. Miloev, I. *et al.* Electrochemical, Surface-Analytical, and Computational DFT Study of Alkaline Etched Aluminum Modified by Carboxylic Acids for Corrosion Protection and Hydrophobicity. *Journal of The Electrochemical Society* **166,** C3131–C3146 (2019).

205. Miloev, I. *et al.* Editors' ChoiceThe Effect of Anchor Group and Alkyl Backbone Chain on Performance of Organic Compounds as Corrosion Inhibitors for Aluminum Investigated Using an Integrative Experimental-Modeling Approach. *Journal of The Electrochemical Society* **167,** 061509 (2020).

206. Castillo-Robles, J. M. & Orgaz, E. Structural and optical properties of Ni atoms and Ni_{55} cluster adsorbed on a rutile TiO_2 (110) surface. *Theoretical Chemistry Accounts* **137,** 31 (2018).

207. Taylor, C. D., Li, S. & Samin, A. J. Oxidation versus salt-film formation: Competitive adsorption on a series of metals from first-principles. *Electrochimica Acta* **269,** 93–101 (2018).

208. Dlouhy, M. & Kokalj, A. How adsorbed H, O, OH, and Cl affect plain adsorption of imidazole on copper. *Corrosion Science* **205,** 110443 (2022).

209. Chiter, F. *et al.* DFT Study of Cl- Ingress into Organic Self-Assembled Monolayers on Aluminum. *Journal of The Electrochemical Society* **170,** 071504 (July 2023).

210. Bazli, L. *et al.* Application of composite conducting polymers for improving the corrosion behavior of various substrates: A Review. *Journal of Composites and Compounds* **2,** 228–240 (2020).

211. Gunasegaram, D. R., Venkatraman, M. S. & Cole, I. S. Towards multiscale modelling of localized corrosion. *International Materials Reviews* **59,** 84–114 (2014).

212. Ke, H. & Taylor, C. D. First-Principles Modeling of the Repassivation of Corrosion Resistant Alloys: Part I. O and Cl Adsorption Energy. *Journal of The Electrochemical Society* **167,** 111502 (2020).

213. Ke, H., Frankel, G. S. & Taylor, C. D. Application of the Chloride Susceptibility Index to Study the Effects of Ni, Cr, Mn and Mo on the Repassivation of Stainless Steels. *Journal of The Electrochemical Society* **167,** 131510 (2020).

214. Burrows, C. J., Harper, J. B., Sander, W. & Tantillo, D. J. Solvation Effects in Organic Chemistry. *The Journal of Organic Chemistry* **87,** 1599–1601 (2022).

215. Huang, H. *et al.* Orderly self-assembly of new ionic copolymers for efficiently protecting copper in aggressive sulfuric acid solution. *Chemical Engineering Journal* **384,** 123293 (2020).

216. Dagdag, O. *et al.* Cyclotriphosphazene based dendrimeric epoxy resin as an anticorrosive material for copper in 3% NaCl: Experimental and computational demonstrations. *Journal of Molecular Liquids* **308** (2020).

217. Ech-chihbi, E. *et al.* Computational, MD simulation, SEM/EDX and experimental studies for understanding adsorption of benzimidazole derivatives as corrosion inhibitors in 1.0 M HCl solution. *Journal of Alloys and Compounds* **844** (2020).

218. Goyal, M. *et al.* Acid corrosion inhibition of ferrous and non-ferrous metal by nature friendly Ethoxycarbonylmethyltriphenylphosphonium Bromide (ECMTPB): Experimental and MD simulation evaluation. *Journal of Molecular Liquids* **315,** 113705 (2020).

219. Laabaissi, T. *et al.* Benzodiazepine Derivatives as Corrosion Inhibitors of Carbon Steel in HCl Media: Electrochemical and Theoretical Studies. *Protection of Metals and Physical Chemistry of Surfaces* **55,** 986–1000 (2019).

220. Lgaz, H. *et al.* On the understanding of the adsorption of Fenugreek gum on mild steel in an acidic medium: Insights from experimental and computational studies. *Applied Surface Science* **463,** 647–658 (2019).

221. Salman, M. *et al.* Chromeno naphthyridines based heterocyclic compounds as novel acidizing corrosion inhibitors: Experimental, surface and computational study. *Journal of Molecular Liquids* **322,** 114825 (2021).

222. Ringe, S., Hörmann, N. G., Oberhofer, H. & Reuter, K. Implicit Solvation Methods for Catalysis at Electrified Interfaces. *Chemical Reviews* **122,** 10777–10820 (2022).

223. de Freitas Martins, Ernane & Pliego, J. R. Unraveling the Mechanism of the Cinchoninium Ion Asymmetric Phase-Transfer-Catalyzed Alkylation Reaction. *ACS Catalysis* **3,** 613–616 (2013).

224. Martins, E. F. & Pliego, J. R. A comprehensive theoretical investigation of the transition states and a proposed kinetic model for the cinchoninium ion asymmetric phase-transfer catalyzed alkylation reaction. *Journal of Molecular Catalysis A: Chemical* **417,** 192–199 (2016).

225. Tomasi, J., Mennucci, B. & Cammi, R. Quantum mechanical continuum solvation models. *Chemical reviews* **105,** 2999–3094 (2005).

226. Marenich, A. V., Cramer, C. J. & Truhlar, D. G. Universal Solvation Model Based on Solute Electron Density and on a Continuum Model of the Solvent Defined by the Bulk Dielectric Constant and Atomic Surface Tensions. *The Journal of Physical Chemistry B* **113,** 6378–6396 (2009).

227. Klamt, A. & Schüürmann, G. COSMO: a new approach to dielectric screening in solvents with explicit expressions for the screening energy and its gradient. *Journal of the Chemical Society, Perkin Transactions 2,* 799–805 (1993).

228. Benhiba, F. *et al.* Combined electronic/atomic level computational, surface (SEM/EDS), chemical and electrochemical studies of the mild steel surface by

quinoxalines derivatives anti-corrosion properties in 1 $molL^{-1}$ HCl solution. *Chinese Journal of Chemical Engineering* **28,** 1436–1458 (2020).

229. Berendsen, H., Grigera, J. & Straatsma, T. The missing term in effective pair potentials. *Journal of Physical Chemistry* **91,** 6269–6271 (1987).

230. Jorgensen, W. L., Chandrasekhar, J., Madura, J. D., Impey, R. W. & Klein, M. L. Comparison of simple potential functions for simulating liquid water. *The Journal of chemical physics* **79,** 926–935 (1983).

231. Chen, S., Zhu, B. & Liang, X. Corrosion inhibition performance of coconut leaf extract as a green corrosion inhibitor for X65 steel in hydrochloric acid solution. *International Journal of Electrochemical Science* **15,** 1–15 (2020).

232. Chauhan, D. S., Mazumder, M. A., Quraishi, M. A. & Ansari, K. R. Chitosan-cinnamaldehyde Schiff base: A bioinspired macromolecule as corrosion inhibitor for oil and gas industry. *International Journal of Biological Macromolecules* **158,** 127–138 (2020).

233. Pedroza, L. S., Brandimarte, P., Rocha, A. R. & Fernández-Serra, M.-V. Bias-dependent local structure of water molecules at a metallic interface. *Chem. Sci.* **9,** 62–69 (1 2018).

234. Coretti, A., Bonella, S. & Ciccotti, G. Communication: Constrained molecular dynamics for polarizable models. *The Journal of Chemical Physics* **149,** 191102 (2018).

235. Sprik, M. & Klein, M. L. A polarizable model for water using distributed charge sites. *The Journal of Chemical Physics* **89,** 7556–7560 (1988).

236. Sprik, M. Computer simulation of the dynamics of induced polarization fluctuations in water. *The Journal of Physical Chemistry* **95,** 2283–2291 (1991).

237. Siepmann, J. I. & Sprik, M. Influence of surface topology and electrostatic potential on water/electrode systems. *The Journal of Chemical Physics* **102,** 511–524 (1995).

238. Petersen, M. K., Kumar, R., White, H. S. & Voth, G. A. A computationally efficient treatment of polarizable electrochemical cells held at a constant potential. *The Journal of Physical Chemistry C* **116,** 4903–4912 (2012).

239. Willard, A. P., Reed, S. K., Madden, P. A. & Chandler, D. Water at an electrochemical interfacea simulation study. *Faraday Discuss.* **141,** 423–441 (0 2009).

240. Zhang, Y., de Aguiar, H. B., Hynes, J. T. & Laage, D. Water Structure, Dynamics, and Sum-Frequency Generation Spectra at Electrified Graphene Interfaces. *The Journal of Physical Chemistry Letters* **11,** 624–631 (2020).

241. Reed, S. K., Lanning, O. J. & Madden, P. A. Electrochemical interface between an ionic liquid and a model metallic electrode. *The Journal of Chemical Physics* **126,** 084704 (2007).

242. Taylor, C. D., Wasileski, S. A., Filhol, J.-S. & Neurock, M. First principles reaction modeling of the electrochemical interface: Consideration and calculation of a tunable surface potential from atomic and electronic structure. *Phys. Rev. B* **73,** 165402 (16 2006).

243. Filhol, J.-S. & Neurock, M. Elucidation of the Electrochemical Activation of Water over Pd by First Principles. *Angewandte Chemie International Edition* **45,** 402–406 (2006).

244. Nørskov, J. K. *et al.* Origin of the Overpotential for Oxygen Reduction at a Fuel-Cell Cathode. *The Journal of Physical Chemistry B* **108,** 17886–17892 (2004).

245. Nørskov, J. K. *et al.* Trends in the Exchange Current for Hydrogen Evolution. *Journal of The Electrochemical Society* **152,** J23 (2005).

246. Goldsmith, Z. K., Calegari Andrade, M. F. & Selloni, A. Effects of applied voltage on water at a gold electrode interface from ab initio molecular dynamics. *Chem. Sci.* **12,** 5865–5873 (16 2021).

247. Bonnet, N., Morishita, T., Sugino, O. & Otani, M. First-Principles Molecular Dynamics at a Constant Electrode Potential. *Phys. Rev. Lett.* **109,** 266101 (26 2012).

248. Otani, M. & Sugino, O. First-principles calculations of charged surfaces and interfaces: A plane-wave nonrepeated slab approach. *Phys. Rev. B* **73,** 115407 (11 2006).

249. Melander, M. M., Kuisma, M. J., Christensen, T. E. K. & Honkala, K. Grand-canonical approach to density functional theory of electrocatalytic systems: Thermodynamics of solid-liquid interfaces at constant ion and electrode potentials. *The Journal of Chemical Physics* **150,** 041706 (2019).

250. Bouzid, A. & Pasquarello, A. Atomic-Scale Simulation of Electrochemical Processes at Electrode/Water Interfaces under Referenced Bias Potential. *The Journal of Physical Chemistry Letters* **9,** 1880–1884 (2018).

251. DeiSSenbeck, F., Freysoldt, C., Todorova, M., Neugebauer, J. & Wippermann, S. Dielectric Properties of Nanoconfined Water: A Canonical Thermopotentiostat Approach. *Phys. Rev. Lett.* **126,** 136803 (13 2021).

252. Hörmann, N. G., Andreussi, O. & Marzari, N. Grand canonical simulations of electrochemical interfaces in implicit solvation models. *The Journal of Chemical Physics* **150,** 041730 (2019).

253. Ordejón, P. & Febrer, P. *Addressing electrified metal-electrolyte interfaces with Non-Equilibrium Green's Functions* in *Bulletin APS* (2021).

254. Ordejón, P., de Freitas Martins, E., Febrer, P. & Pedron, F. *DFT and QM/MM simulations of electrified interfaces using Non-Equillibrium Greens Functions* in *Bulletin APS* (2023).

255. Fingar, M. 2-Mercaptobenzimidazole as a copper corrosion inhibitor: Part II. Surface analysis using X-ray photoelectron spectroscopy. *Corrosion Science* **72,** 90–98 (2013).

256. Fingar, M. 2-Mercaptobenzimidazole as a copper corrosion inhibitor: Part I. Long-term immersion, 3D-profilometry, and electrochemistry. *Corrosion Science* **72,** 82–89 (2013).

257. Troullier, N. & Martins, J. L. Efficient pseudopotentials for plane-wave calculations. *Phys. Rev. B* **43,** 1993–2006 (3 1991).

258. Lide, D. R. *CRC handbook of chemistry and physics* (2004).

259. Kresse, G. & Furthmüller, J. Efficiency of ab-initio total energy calculations for metals and semiconductors using a plane-wave basis set. *Computational Materials Science* **6,** 15–50 (1996).

260. Kresse, G. & Joubert, D. From ultrasoft pseudopotentials to the projector augmented-wave method. *Phys. Rev. B* **59,** 1758–1775 (3 1999).

261. García-Gil, S., García, A., Lorente, N. & Ordejón, P. Optimal strictly localized basis sets for noble metal surfaces. *Physical Review B - Condensed Matter and Materials Physics* **79,** 1–9 (2009).

262. Corsetti, F., Fernández-Serra, M.-V., Soler, J. M. & Artacho, E. Optimal finite-range atomic basis sets for liquid water and ice. *Journal of Physics: Condensed Matter* **25,** 435504 (2013).

263. Larsen, A. H. *et al.* The atomic simulation environmenta Python library for working with atoms. *Journal of Physics: Condensed Matter* **29,** 273002 (June 2017).

264. Abraham, M. J. *et al.* GROMACS: High performance molecular simulations through multi-level parallelism from laptops to supercomputers. *SoftwareX* **1-2,** 19–25 (2015).

265. Pedroza, L. S., Poissier, A. & Fernández-Serra, M.-V. Local order of liquid water at metallic electrode surfaces. *The Journal of Chemical Physics* **142,** 034706 (Jan. 2015).

266. Jain, A. *et al.* Commentary: The Materials Project: A materials genome approach to accelerating materials innovation. *APL Materials* **1.** 011002 (July 2013).

267. García, A., Verstraete, M. J., Pouillon, Y. & Junquera, J. The psml format and library for norm-conserving pseudopotential data curation and interoperability. *Computer Physics Communications* **227,** 51–71 (2018).

268. van Setten, M. *et al.* The PseudoDojo: Training and grading a 85 element optimized norm-conserving pseudopotential table. *Computer Physics Communications* **226,** 39–54 (2018).

269. Sheetal *et al.* An insight about the interaction of Aryl Benzothiazoles with mild steel surface in aqueous HCl solution. *Journal of Molecular Liquids* **354,** 118890 (2022).

270. Silva, A. L. R. & Ribeiro da Silva, M. D. M. C. Energetic, structural and tautomeric analysis of 2-mercaptobenzimidazole. *Journal of Thermal Analysis and Calorimetry* **129,** 1679–1688 (Sept. 2017).